

# Investigations on hybrid organic-inorganic perovskites for high performance solar cells

THÈSE N° 7749 (2017)

PRÉSENTÉE LE 21 JUILLET 2017

À LA FACULTÉ DES SCIENCES DE BASE

LABORATOIRE DE PHOTONIQUE ET INTERFACES

PROGRAMME DOCTORAL EN CHIMIE ET GÉNIE CHIMIQUE

ÉCOLE POLYTECHNIQUE FÉDÉRALE DE LAUSANNE

POUR L'OBTENTION DU GRADE DE DOCTEUR ÈS SCIENCES

PAR

**Norman PELLET**

acceptée sur proposition du jury:

Prof. U. A. Hagfeldt, président du jury  
Prof. M. Graetzel, Prof. J. Maier, directeurs de thèse  
Prof. A. Di Carlo, rapporteur  
Prof. T. Edvinsson, rapporteur  
Prof. C. Ballif, rapporteur



ÉCOLE POLYTECHNIQUE  
FÉDÉRALE DE LAUSANNE

Suisse  
2017



# Abstract

Undoubtedly, perovskite solar cells have become a key player in 3<sup>rd</sup> generation photovoltaics over the last few years. Although it is only in 2012 that the first solid state perovskite solar cell was reported, power conversion efficiencies have increased so rapidly that PSCs are now serious contenders to the well-established and marketed thin-film and wafer technologies. Over the timespan on this work, over 3'000 published articles in peer-review journals have been published. The work that I report in this thesis is merely a small contribution to the gigantic amount of data, models and theories that have been made over the last 4 years. I hope that my modest contribution will be of value to the scientific community.

Over the course of this work, I attempted to approach it from different perspectives. As a result, a wide array of subjects have been treated:

Starting with the fabrication of perovskite solar cells, an innovative way to deposit thin film of perovskite from solution is reported, using a two-step deposition technique. Using this approach, the power conversion efficiency of perovskite solar cells has been increased from 12.3% to over 17% in less than a year.

Subsequently, I looked into the possible compositional variations of the perovskite photo-absorber. This study showed that the cation methylammonium and formamidinium can be used interchangeably using the deposition technique that we have reported on earlier. We showed that a mixture of the two cations leads to a stabilization of the tetragonal perovskite phase and shrinks the optical band gap of the photoabsorber, allowing more photons to be absorbed and converted into electrons.

Following this work, I studied some of the reactivity properties of the phase pure organic inorganic  $\text{CH}_3\text{NH}_3\text{PbX}_3$  ( $\text{X}=\text{Cl}, \text{Br}, \text{I}$ ). Notably, it could be shown that the halide component can be easily exchanged by another one using simple solution based anion exchange reactions.

Later, the power conversion characteristics of perovskite solar cells were investigated. By developing a electronic circuit allowing versatile power point tracking of the solar cells, a new algorithm that deals with the issues specifically related to perovskite solar cells is reported.

A major topic of my work was the study of the frequency resolved dynamics that results for the

---

generation carriers by light. Using a novel way to measure the intensity modulated spectral response of perovskite solar cells, I was able to identify some of the key limiting factors that cap the power conversion efficiency of the devices. A numerical model that answers to the laws of carrier dynamics was assembled and used as a tool to better understand perovskite solar cells.

Finally, I reported on a way to deal with the end of life of perovskite solar cells. Some of the relevant regulatory framework in the European Union that deals with the recycling of solar panels are highlighted. Using the concept of "upcycling", a way to recycle the valuable components of the solar cell in an efficient way was outlined.

Key words: Photovoltaics, Solar Cells, Perovskite, Hybrid Organic Inorganic Perovskite, Mesoscopic, Maximum power point tracking

# Résumé

La technologie des cellules solaires au perovskites hybrides fait partie de la 3<sup>ème</sup> génération des technologies photovoltaïques et, depuis quelques années, est au centre d'intenses recherches scientifiques. Malgré que la première cellule solaire utilisant ce pigment a été décrite en 2012, l'efficacité de ces cellules a progressé si rapidement que cette technologie est désormais une véritable concurrente aux autres technologies bien établies dans le marché, telle que les technologies cristallines (silicium) et celles de couche mince (CIGS et CdTe).

Au cours des travaux rapportés dans cette thèse, plus de 3'000 articles scientifiques sont parus dans des revues scientifiques *peer-reviewed*. Les travaux décrits dans cette thèse ne sont qu'une petite contribution à la quantité gigantesque de données, modèles et théories qui ont été publiés au cours de ces quatre dernières années. J'espère que ma contribution honnête servira dans l'intérêt de la communauté scientifique.

Durant le cours de mes travaux, j'ai tenté de ne pas concentrer mon attention sur un sujet très particulier aux cellules solaires au perovskite, mais plutôt d'aborder cette technologie sous différents aspects.

En commençant par la fabrication des cellules solaires au perovskite, une nouvelle technique de dépôt en couches minces du matériau photo-absorbeur a été rapportée. En utilisant une technique à deux étapes, l'efficacité de ces cellules solaires a été améliorée de 12.3% à plus de 17% en moins d'une année.

Les propriétés structurales de la couche perovskite ont ensuite été abordées. Les travaux rapportés ici montrent que les cations méthylamine et formamidine peuvent être utilisés interchangeablement. En utilisant un mélange des deux cations, la phase tétragonale du perovskite peut être stabilisée, tout en diminuant la largeur de bande interdite, permettant à plus de photons d'être absorbés et convertis en électrons.

Par la suite, j'ai étudié quelques-unes des propriétés réactives de la phase pure  $\text{CH}_3\text{NH}_3\text{PbX}_3$  ( $X=\text{Cl}, \text{Br}, \text{I}$ ). Plus spécifiquement, il a été démontré que la composante halogénée du perovskite peut être facilement échangée par un autre halogénure en utilisant une simple réaction à échange d'anion.

---

Enfin, j'ai étudiée les propriétés des cellules solaires au perovskite à générer de la puissance. En développant un circuit électronique permettant le suivi du point à la puissance maximum, un nouvel algorithme qui règle les problèmes liés à l'hystérèse des cellules au perovskite a été décrit.

Une majeure partie de mon travail traite de l'étude de la dynamique fréquentielle qui résulte de l'absorption de la lumière. En utilisant une nouvelle méthode de mesure de la réponse fréquentielle des cellules solaires en modulant la puissance optique à haute fréquence, j'ai été capable de déterminer certains des aspects limitant la conversion d'énergie solaire en énergie électrique. Un modèle numérique qui répond aux lois des mouvements de charges a été réalisé et utilisé pour mieux comprendre les cellules solaires au perovskite.

En dernier lieu, j'ai rapporté de la manière de gérer la fin de vie des cellules solaires. Certains aspects légaux de l'Union Européenne traitant du recyclage des panneaux photovoltaïques et notamment de la gestion de ces composés dangereux ont été soulevés. En utilisant le concept de valorisation des déchets, une nouvelle manière de récupérer les composés essentiels de ces cellules solaires a été décrit.

Mots clefs: Photovoltaïque, Cellules solaires, Perovskites, Perovskite organique-inorganique hybride, Mésoscopique, Suivi du point à puissance maximale

# Zusammenfassung

Perowskitbasierte Solarzellen sind in den letzten Jahren zu einem der Hauptakteure unter den Solarzellentechnologien der dritten Generation aufgestiegen. Obwohl erst 2012 die erste Festkörperperovskitsolarzelle beschrieben wurde, hat sich der Wirkungsgrad so schnell verbessert, dass die Perowskitzellen heute ernstzunehmende Rivalen der etablierten Wafer-basierten bzw. Dünnschicht solarzellen sind. Während der Zeitspanne, die diese Arbeit umfasst, wurden mehr als 3000 Artikel in peer-reviewten Journalen veröffentlicht. Die Ergebnisse, die ich in dieser Dissertation präsentiere sind lediglich ein kleiner Beitrag zu der gigantischen Menge von Daten, Modellen und Theorien welche in den letzten vier Jahren gesammelt und aufgestellt wurden. Ich hoffe, dass mein bescheidener Beitrag wertvoll für die Wissenschaftsgemeinschaft sein wird.

Während meiner Arbeit habe ich versucht, meine Aufmerksamkeit nicht nur auf ein einzelnes Thema mit Bezug auf Perowskitsolarzellen zu richten, sondern die Technologie von verschiedenen Blickwinkeln aus zu betrachten. Demzufolge wurde eine grosse Bandbreite an Themenbereichen behandelt.

Anfangen mit der Fabrikation von Perowskitsolarzellen wird ein innovatives, sequentielles, zweistufiges Verfahren zur Aufbringung dünner Perowskitschichten beschrieben. Mittels diesem Verfahren konnten wir den Wirkungsgrad der Perowskitsolarzellen innerhalb eines Jahres von 10.2% auf über 17% verbessern.

Danach untersuchte ich detaillierter mögliche kompositionelle Varianten der Perowskitschicht. Wir konnten zeigen, dass die Kationen Methylammonium und Formamidinium mit dem vorher beschriebenen Aufbringungsverfahren ausgetauscht werden können. Wir zeigen, dass eine Mischung der beiden Kationen zur Stabilisierung der tetragonalen Perowskitphase führt und gleichzeitig die optische Bandlücke verkleinert, somit mehr Photonen absorbiert und zu Elektronen umgewandelt werden können.

Als nächstes habe ich die reaktiven Eigenschaften phasenreiner organisch-anorganischer  $\text{CH}_3\text{NH}_3\text{PbX}_3$  ( $\text{X}=\text{Cl}, \text{Br}, \text{I}$ )-Perovskite untersucht. Bemerkenswerterweise konnte gezeigt werden, dass die halogeniden Komponenten in einer einfachen Anionenaustauschreaktion gegeneinander ausgetauscht werden können.

---

Neben Faktoren, die zur Entwicklung des Wirkungsgrades der Solarzellen beitragen, habe ich mich mit frequenzangeregten Dynamiken die in Ladungsträgererzeugung resultieren, beschäftigt. Mittels eines neuartigen Verfahrens zur Messung der Intensitätsmodulation der Farbmempfindlichkeit von Perowskitzellen, konnte ich einige, den Wirkungsgrad beeinträchtigende, Schlüsselfaktoren identifizieren.

Zu guter Letzt wird die Entsorgung von Perowskitsolarzellen besprochen. Neben rechtlichen Aspekten zur Entsorgung von Solarzellen in der EU wird unter dem Gesichtspunkt des 'Up-cyclings' ein effektives Verfahren zur Wiederverwertung wertvoller Bestandteile der Solarzellen vorgestellt.

Stichwörter: Photovoltaik, Solarzellen, Perowskite, organisch-anorganische Hybridperowskite, Mesoskopische Solarzellen, Photovoltaics, Solar Cells, Perovskite, Maximum power point tracking



# Contents

<b>Abstract (English/Français/Deutsch)</b>	<b>i</b>
<b>1 Introduction</b>	<b>1</b>
1.1 Hybrid perovskite solar cells . . . . .	2
1.2 Structure of perovskite solar cells . . . . .	2
1.2.1 Mesoscopic hybrid perovskite solar cells . . . . .	3
1.2.2 Flat hybrid perovskite solar cells . . . . .	4
1.2.3 Fully-mesoporous, hole transporter free solar cells . . . . .	4
1.3 Electronic processes in perovskite solar cells . . . . .	4
1.4 Steady-state characterization . . . . .	6
1.4.1 Reference solar spectrum . . . . .	6
1.4.2 Voltage sweep measurements . . . . .	7
1.5 Components of typical perovskite solar cells . . . . .	10
1.5.1 The compact metal oxide blocking layer . . . . .	10
1.5.2 The mesoscopic scaffold . . . . .	10
1.5.3 The perovskite absorber . . . . .	11
1.5.4 The hole transporting layer . . . . .	14
1.5.5 Back-contact . . . . .	15
1.6 Motivation and procedures . . . . .	15
<b>List of figures</b>	<b>1</b>
<b>2 Sequential deposition as a route to high-efficiency perovskite solar cells</b>	<b>19</b>
2.1 Introduction . . . . .	19
2.2 Motivation . . . . .	20
2.3 Sequential deposition of $\text{CH}_3\text{NH}_3\text{PbI}_3$ . . . . .	21
2.4 Kinetics of the reaction . . . . .	22
2.5 X-ray diffraction . . . . .	23
2.5.1 Fabrication of perovskite solar cells . . . . .	25
2.6 Optimization of the crystal size . . . . .	28
2.6.1 Control of the crystal size . . . . .	28
2.6.2 Influence over the light harvesting . . . . .	30
2.6.3 Influence over the hole transport . . . . .	30
2.6.4 Influence over the photovoltaic performance . . . . .	31

## Contents

---

2.7	Conclusion and outlook . . . . .	32
<b>3</b>	<b>Mixed organic cation perovskite solar cells</b>	<b>33</b>
3.1	Motivation . . . . .	33
3.2	Introduction . . . . .	34
3.3	Mixed methylammonium-formamidinium hybrid perovskites . . . . .	34
3.4	XRD characterization . . . . .	36
3.5	AC impedance spectroscopy . . . . .	36
3.6	Optical absorption . . . . .	38
3.7	Photoluminescence . . . . .	38
3.8	Device performance . . . . .	39
3.9	Light harvesting and internal quantum efficiency . . . . .	40
3.10	Lifetime measurements . . . . .	42
3.11	Conclusion and outlook . . . . .	43
<b>4</b>	<b>Ion exchange reactions of hybrid organic-inorganic perovskites</b>	<b>45</b>
4.1	Motivation . . . . .	45
4.2	Introduction . . . . .	45
4.3	Results and discussion . . . . .	47
4.3.1	$\text{CH}_3\text{NH}_3\text{PbBr}_3$ to $\text{CH}_3\text{NH}_3\text{PbI}_3$ . . . . .	50
4.3.2	$\text{CH}_3\text{NH}_3\text{PbI}_3$ to $\text{CH}_3\text{NH}_3\text{PbBr}_3$ . . . . .	51
4.3.3	$\text{CH}_3\text{NH}_3\text{PbCl}_3$ to $\text{CH}_3\text{NH}_3\text{PbBr}_3$ . . . . .	52
4.3.4	$\text{CH}_3\text{NH}_3\text{PbBr}_3$ to $\text{CH}_3\text{NH}_3\text{PbCl}_3$ . . . . .	54
4.3.5	$\text{CH}_3\text{NH}_3\text{PbCl}_3$ to $\text{CH}_3\text{NH}_3\text{PbI}_3$ . . . . .	54
4.3.6	$\text{CH}_3\text{NH}_3\text{PbI}_3$ to $\text{CH}_3\text{NH}_3\text{PbCl}_3$ . . . . .	56
4.4	Growth and halide exchange of perovskite nanowires . . . . .	56
4.5	Conclusion and outlook . . . . .	57
4.6	Additional figures . . . . .	58
<b>5</b>	<b>Maximum power point tracking of perovskite solar cells</b>	<b>61</b>
5.1	Motivation . . . . .	61
5.2	Introduction . . . . .	61
5.3	Maximum power point tracking . . . . .	63
5.3.1	Perturb and Observe algorithm . . . . .	63
5.4	Optimal performance through poling . . . . .	67
5.5	Voltage poling and collection efficiency . . . . .	70
5.6	Stabilizing the MPPT algorithm at fast speeds . . . . .	70
5.7	Example of ageing tests . . . . .	72
5.8	Conclusion and outlook . . . . .	73
<b>6</b>	<b>Intensity-modulated frequency response of perovskite solar cells</b>	<b>75</b>
6.1	Motivation . . . . .	75
6.2	The IMVS and IMPS experiment . . . . .	76

6.3	Discretization of the model . . . . .	78
6.3.1	Carrier transport and storage . . . . .	78
6.3.2	Continuity equation . . . . .	78
6.3.3	Carrier generation . . . . .	80
6.3.4	Carrier recombination . . . . .	82
6.3.5	Electronic and ionic charge storage . . . . .	83
6.3.6	Displacement capacitance . . . . .	85
6.4	Experimental procedure . . . . .	86
6.4.1	Instrumentation . . . . .	86
6.5	Assembling the equivalent circuit . . . . .	91
6.5.1	Most basic equivalent circuit . . . . .	95
6.5.2	Ionic transport in $\text{CH}_3\text{NH}_3\text{PbI}_3$ . . . . .	96
6.5.3	Prior knowledge and working assumptions . . . . .	97
6.6	Flat-film perovskite solar cells . . . . .	98
6.6.1	Experimental dimensions . . . . .	98
6.6.2	The equivalent circuit . . . . .	99
6.6.3	Simulations of the IMVS response . . . . .	102
6.6.4	Simulations of the IMPS response . . . . .	119
6.7	Results . . . . .	126
6.7.1	Data treatment . . . . .	126
6.7.2	Typical IMVS spectra . . . . .	127
6.7.3	Typical IMPS spectra . . . . .	135
6.7.4	IMPS spectra with complex charge transfer components . . . . .	136
6.7.5	Thickness dependence . . . . .	136
6.7.6	The p-type dopant in Spiro-MeOTAD . . . . .	139
6.7.7	The influence of the LiTFSI additive in Spiro-MeOTAD . . . . .	142
6.8	Conclusion and outlook . . . . .	143
<b>7</b>	<b>Recycling of perovskite solar cells</b>	<b>145</b>
7.1	Motivation . . . . .	145
7.2	Introduction . . . . .	145
7.2.1	The end-of-life of solar panels . . . . .	146
7.2.2	PV panel composition . . . . .	146
7.2.3	Regulatory framework . . . . .	147
7.2.4	The Waste of Electrical and Electronic Equipment Directive . . . . .	149
7.2.5	Financing . . . . .	149
7.2.6	Collection the PV panels waste . . . . .	151
7.2.7	Waste treatment, recovery and recycling . . . . .	151
7.2.8	Waste shipment . . . . .	152
7.2.9	Waste disposal . . . . .	152
7.2.10	Valuable device components of perovskite solar cells . . . . .	153
7.3	Results and discussion . . . . .	156

## Contents

---

7.3.1	Photoanode . . . . .	156
7.3.2	Back contact . . . . .	156
7.3.3	Lead in solvents . . . . .	157
7.3.4	Fate of spiro-MeOTAD, dopants and additives . . . . .	159
7.3.5	Device performance . . . . .	160
7.4	Encapsulation . . . . .	160
7.5	Conclusion and outlook . . . . .	161
<b>8</b>	<b>Conclusion</b>	<b>163</b>
<b>9</b>	<b>Methods summary</b>	<b>167</b>
9.1	Device fabrication . . . . .	167
9.1.1	Sequential deposition . . . . .	167
9.1.2	Single-step deposition . . . . .	169
9.2	Device characterization . . . . .	169
9.2.1	Voltage sweep measurements . . . . .	169
9.2.2	IPCE response . . . . .	170
9.3	Kinetic measurements . . . . .	170
9.3.1	Sequential deposition . . . . .	170
9.3.2	Halide exchange reactions . . . . .	170
9.4	Optical spectroscopy . . . . .	171
9.4.1	Single pass absorption . . . . .	171
9.4.2	Photoluminescence . . . . .	171
9.4.3	Scatter-free absorption spectra . . . . .	172
9.4.4	Fluorescence lifetime measurements . . . . .	172
9.5	Water purification . . . . .	172
9.6	ICP-MS . . . . .	172
9.7	Structural characterization . . . . .	173
9.8	X-ray fluorescence . . . . .	173
<b>A</b>	<b>Implementation of the IMVS / IMPS pre-amplifier</b>	<b>175</b>
A.1	Implementation of the anode sink . . . . .	175
A.1.1	Numerical Simulation . . . . .	176
A.2	Implementation of the cathode driver . . . . .	176
A.3	Implementation of the Howland current pump . . . . .	176
<b>B</b>	<b>Fitting numerical simulations</b>	<b>179</b>
B.0.1	The constant phase element . . . . .	179
<b>C</b>	<b>Implementation of the IMVS / IMPS pre-amplifier</b>	<b>183</b>
C.1	Implementation of the anode sink . . . . .	183
C.2	Implementation of the cathode driver . . . . .	184
C.3	Implementation of the Howland current pump . . . . .	184

<b>D Design and assembly of the MPPT tracker</b>	<b>185</b>
<b>E Certificate of power conversion efficiency</b>	<b>201</b>
<b>Acknowledgements</b>	<b>203</b>
<b>Bibliography</b>	<b>230</b>
<b>Curriculum Vitae</b>	<b>231</b>



# 1 Introduction

With an energy demand on the sharp rise driven by largely populated countries such as China or India, societies face with unprecedented challenges to meet sufficient energy production[1]. With growing concerns about climate change and global warming, notably from the high emission of greenhouse gases such as carbon dioxide and methane, we are faced with the challenge to not only shift our current energy sources to cleaner ones, but also to install capacities designed to meet the future needs. The development of renewable energy sources is widely expected to satisfy both. Energy production using renewable sources is currently growing faster than all other means of production[1]. However, renewable energies traditionally suffer from prohibitive costs, which is why the market share is still widely dominated by the use of fossil fuel (gas, oil and coal combined). Indeed, in 2013, only 14% of the total energy production originated from renewable sources[2]. Among all available renewable energy sources (wind, hydropower, geothermal, biomass and solar but excluding nuclear fusion), solar energy is the only viable candidate for supplying all the energy required by our growing population: there is more energy from the sun incoming on the planet in one hour than our yearly energy requirements in 2001:  $4.3 \times 10^{20}$  Joules vs  $4.1 \times 10^{20}$  Joules[3]. However, in 2014, only 1% of the global electricity production was met by photovoltaics[4], despite a compound 43% annual growth between 2000 and 2014[5]. Some countries have more actively promoted the development of photovoltaics, and PV electricity production now accounts for 7.1% of the total demand in Germany[4]. There are many hindrances that must be met to bring PV installations to double digit numbers, which include cost but also the accessibility of commodity materials (glass, aluminum, copper, plastic, ...) and critical materials[5]. Today, most of the PV market is shared between wafer technologies (silicon monocrystalline and polycrystalline) and thin film technologies (CdTe and CIGS). However, these technologies suffer prohibitive costs and issues related to material scarcity. For example, providing 100% of our electricity needs by 2050 using only crystalline silicon would require 1.3x more silicon and 1.5x more aluminum that have been extracted since 1900[5]. Using more abundant and highly absorbing materials greatly alleviates the problems linked to ore extraction and material usage. For example, the deployment of 25 TW PbS quantum dot solar only requires the equivalent of 22 days of lead mining and only 6 hours of sulfur production, and these figures are even lower

for perovskite solar cells.[5].

### 1.1 Hybrid perovskite solar cells

The first report of lead and tin based halide perovskite structures dates back from 1893 with the syntheses of  $\text{CsPbBr}_3$  and  $\text{CsPbI}_3$ [6]. However, it is only in 1958 that their structures were identified as perovskites by Møller[7], who also identified the photoconductive nature of their single crystalline forms, suggesting semiconducting behavior. The first report of an organic-inorganic lead halide perovskite structure dates from Weber, who was first to introduce the methylammonium cation methylammonium ( $\text{CH}_3\text{NH}_3\text{I}$ ) as an alternative for  $\text{Cs}^+$ . Over the last 20 years, the electronic, structural and processability properties of organic-inorganic lead halide perovskites were investigated primarily by Mitzi[8, 9, 10, 11, 12, 13, 14, 15, 16, 17, 18, 19, 20, 21, 22, 23, 24, 25, 26, 27, 28, 29, 30, 31, 32] but only gained significant attention in the last couple of years for their stunning photovoltaic performances. In particular, the small-cation based three-dimensional perovskite have been found to perform best. Their structure involves lead centers ( $\text{Pb}_2^+$ ) surrounded by corner-sharing halide octahedra ( $\text{I}^-$ ,  $\text{Br}^-$  or  $\text{Cl}^-$ ). The interstitial sites are occupied by the small organic cations ( $\text{CH}_3\text{NH}_3\text{I}$  or  $\text{H}_2\text{N}=\text{CHNH}_3\text{I}$ ) or by cesium ( $\text{Cs}^+$ ) surrounded by 12 halides[33]. Thorough structural characterizations have been performed by Mitzi[27], Kanatzidis[34] and White[35]. Methylammonium lead iodide ( $\text{CH}_3\text{NH}_3\text{PbI}_3$ ), in particular, is exhibiting fascinating optoelectronic properties, among which its narrow band gap (1.55 eV, onset at 800 nm[35]) and high charge diffusion length (100 nm to 1  $\mu\text{m}$ [36, 37, 38]) makes it an ideal candidate as a photo-active layer in solar cells. Such appealing properties are the result of low exciton binding energies (30 meV)[39] and high mobilities[34, 39]. The potential of  $\text{CH}_3\text{NH}_3\text{PbI}_3$  as a photoactive material was first recognized by Kojima[40] in 2009, who applied it in the form of nanoparticles to form the photo-absorbing layer in dye-sensitized solar cells[41]. However, rapid performance degradation was witnessed, as a result of the hydrolysis of  $\text{CH}_3\text{NH}_3\text{PbI}_3$  and its partial dissolution in the acetonitrile-based electrolyte. Combined with poor conversion efficiencies (3.8%), his work and others[42] were largely overlooked by the community until 2012, where the first solid-state perovskite solar cells appeared[43, 44, 45]. By replacing the liquid electrolyte by the solid state, p-type hole conductor spiro-MeOTAD, previously used in solid-state dye sensitized solar cells[46], superior performances could be achieved (10.9%). At the time, these architectures were similar of the ones of solid-state DSSCs, where  $\text{TiO}_2$  was used as a n-type layer, spiro-MeOTAD as a p-type layer, and  $\text{CH}_3\text{NH}_3\text{PbI}_3$  sandwiched in the two as the photogenerating layer. The rise of organic-inorganic perovskite-based materials was set.

### 1.2 Structure of perovskite solar cells

All hybrid perovskite are constructed using bottom-up processes on transparent conductive oxide coated glass. However, structural differences can significantly differ, such that they can be classified into three distinct categories.



## 1.2. Structure of perovskite solar cells

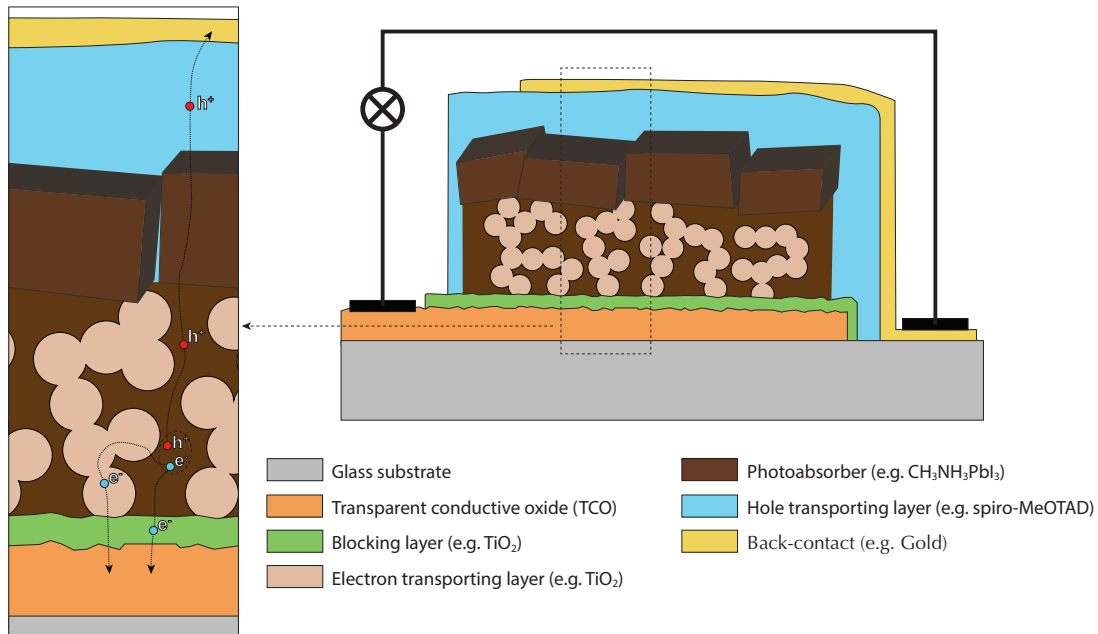


**Figure 1.1:** Schematic cross-section of a typical mesoscopic perovskite solar cell, comprising of a glass substrate coated with a transparent conductive oxide (TCO). In a typical cell architecture, a blocking layer of  $\text{TiO}_2$  is deposited by aerosol spray pyrolysis, followed by a solution-route deposition of a mesoscopic  $\text{TiO}_2$  film. The porous network is infiltrated with  $\text{CH}_3\text{NH}_3\text{PbI}_3$  or a related perovskite using a solution deposition. This process also generates a highly crystalline capping layer of variable thickness. A hole transporter is then deposited on top by spin-coating, followed by the thermal evaporation of a counter-electrode.

### 1.2.1 Mesoscopic hybrid perovskite solar cells

The leading class of hybrid perovskite solar in terms of power conversion efficiency and stability are based on a mesoscopic n-type  $\text{TiO}_2$  film deposited on the conductive glass coating with a thin, compact  $\text{TiO}_2$  layer. The titanium dioxide acts as an electron transport layer and selectively blocks the holes. The mesoporous film generally consists of anatase nanoparticles (18-30 nm) forming a porous 100-200 nm thick film. The  $\text{TiO}_2$  film is infiltrated by  $\text{CH}_3\text{NH}_3\text{PbI}_3$  (or a related hybrid perovskite) deposited from solution. In most cases, a thick and compact 200-250 nm layer of  $\text{CH}_3\text{NH}_3\text{PbI}_3$  caps the electron transporting layer. A thin hole transport layer is then deposited on top of the perovskite layer to provide selectivity for the holes and block the electrons. Most hole transport materials consist of doped Spiro-MeOTAD with additives (LiTFSI and 4-tertbutylpyridine)[47], but variations thereof have been widely reported, notably copper thiocyanate ( $\text{CuSCN}$ )[48, 49, 50, 51] or poly-triarylamine derivatives (PTAA)[52, 53, 54]. The device assembly is terminated by thermally evaporating a 40-200 nm top layer of gold or silver. Research is greatly active towards the optimization of each layer, such that certified power conversion efficiencies have quickly raised from 14.1% to 22.1% in less than three years[55].

### 1.2.2 Flat hybrid perovskite solar cells

Although the hybrid-perovskite PV field was introduced using mesoscopic substrates, the successful fabrication of flat hybrid-perovskite heterojunction solar cells have also been widely reported[56, 57, 58, 59, 60]. Various electron transporting layers can be used, such as the traditional TiO<sub>2</sub> blocking layer, zinc oxide or PCBM, in which case the perovskite must be deposited by thermal evaporation. In particular, the use of SnO<sub>2</sub> as the ETL has attracted significant attention for in view of their increased stability and efficiency[61, 62]. The rest of the device remains the same as in mesoscopic solar cells.

### 1.2.3 Fully-mesoporous, hole transporter free solar cells

At the opposite of flat hybrid perovskite solar cells are fully mesoporous solar cells. They are fabricated through the sequential printing of a TiO<sub>2</sub> mesoporous layer, a mesoporous inorganic spacer (ZrO<sub>2</sub> or Al<sub>2</sub>O<sub>3</sub>) and a mesoporous back-contact (usually graphite-based). The three layers are sintered together and infiltrated by the hybrid perovskite material from solution, which fills the pores of all three layers. There is no selectivity for the hole extraction, which must be transported through the perovskite layer towards the carbon back-contact. Therefore, the functioning of the device relies on the quick charge transfer of the electrons into the titanium dioxide. Failure to transfer the electrons is synonym of electron-hole annihilation, either in the bulk of the perovskite or at the surface with the carbon and is to be avoided.

## 1.3 Electronic processes in perovskite solar cells

The understanding of the electronic processes are key to design better absorptive materials, electron and hole transporters such that the power conversion efficiency and the stability of the resulting photovoltaic cells can be improved. In particular, isolating the bottlenecks for electron and hole transport or charge transfer are essential to bring the PCE closer to the thermodynamic limit. In particular, hybrid perovskites such as CH<sub>3</sub>NH<sub>3</sub>PbI<sub>3</sub> have been shown to exhibit significant ionic conduction. In fact, in the dark, CH<sub>3</sub>NH<sub>3</sub>PbI<sub>3</sub> is primarily an ionic conductor[63]. This leads to an unprecedented situation in the solar cell community, as this is the first time that ionic conduction need to be included in the device models.

The first step occurs when a photon of light is absorbed in the perovskite layer and generates an exciton. This phenomenon occurs as a function of the depth profile, according to the absorption coefficient of the cell. The generation current can be expressed as:

$$G_i(x, \nu) = (e z_i) I_0 \alpha(\nu) 10^{-\alpha(\nu)x} \quad (1.1)$$

Where

1.  $I_0$  is the light flux

### 1.3. Electronic processes in perovskite solar cells

2.  $\alpha(\nu)$  is the wavelength-dependent absorption coefficient

At room temperature, owing to its binding energy comparable to 1 kT, the exciton readily splits into free charges. This has the direct consequence of splitting the dark Fermi level into two quasi-Fermi levels, out of thermal equilibrium<sup>1</sup>. The electron and the hole flow towards the contacts according to the drift-diffusion equation:

$$J_i^{\text{mass}} = -D_i \frac{\partial c_i(x, t)}{\partial x} - \frac{\sigma_i(x, t)}{z_i e} \frac{\partial \phi(x, t)}{\partial x} \quad (1.2)$$

where  $x$  is the position in the film,  $t$  is the time,  $c$  the concentration,  $\sigma$  the conductivity,  $D$  the diffusion coefficient,  $z$  the charge of the species  $i$ ,  $e$  the elementary charge and  $\phi$  the electric field. Equation 1.2 can be rewritten by making use of the chemical potential of the species  $i$  differentiated by the position  $x$

$$\mu_i = \mu_i^0 + k_B T \ln c_i(x, t) \quad (1.3)$$

$$\frac{\partial \mu_i(x, t)}{\partial x} = \frac{k_B T}{c_i(x, t)} \frac{\partial c_i(x, t)}{\partial x} \quad (1.4)$$

and the Nernst-Einstein relationship

$$\sigma_i(x, t) = z_i e \mu_i(x, t) c_i(x, t) = \frac{(z_i e)^2 c_i(x, t)}{k_B T} D_i \quad (1.5)$$

into

$$J_i^{\text{mass}} = -\frac{\sigma_i(x, t)}{(z_i e)^2} \frac{\partial \tilde{\mu}_i(x, t)}{\partial x} \quad (1.6)$$

where  $\tilde{\mu}_i$  is the electrochemical potential ( $\tilde{\mu}_i = \mu_i + z_i e \phi$ ), and, for electronic carriers, is also known as the quasi-Fermi level. Equation 1.6 is the fundamental transport equation for electron, holes and ionic defects in a semiconductor. Finally, aside from generation and carrier transport, electrons and holes can recombine. Recombination can be a pseudo-first order (mono-molecular recombination) or a second order process (bimolecular recombination), or, if Auger recombination is present, a third order process. In addition, recombination can occur in the bulk of the semiconductor or at an interface with another layer. The recombination rate therefore takes various forms depending on the relevant process. The bookkeeping of the charges is ensured by the continuity equation, which, under non-equilibrium conditions, reads:

$$\frac{\partial J_i^{\text{mass}}(x, t)}{\partial x} = -\frac{c_i(x, t)}{k_B T} \frac{\partial \mu_i(x, t)}{\partial t} + G_i(x, t) - U_i(x, t) \quad (1.7)$$

<sup>1</sup>Local band equilibrium is nevertheless respected: the carrier distribution in each band follows the Fermi-Dirac statistics

Where  $G_i(x, t)$  is the generation rate of carrier  $i$  and  $U_i(x, t)$  its recombination. Electrons undergo a competition between drift-diffusion and recombination and those which did not recombine undergo charge transfer towards one of the electrodes. The charge transfer can also take many forms, depending on whether there is a space-charge layer forming at the interface or if the transfer is purely ohmic. Through careful engineering of the materials, it must be ensured that the electron transport layer has a significant available density of state for electrons and few density of state for holes, and conversely for the hole transport layer. Finally, and this is the third thermodynamic equation describing the current flow is given by Maxwell's displacement current (it has nothing to do with the transport of charged species), which scales with the rate of change of the electric field:

$$J_i^{\text{disp}}(x, t) = -\varepsilon_0 \frac{\partial}{\partial t} \left( \varepsilon(x, t) \frac{\partial \phi(x, t)}{\partial x} \right) \quad (1.8)$$

More insights in the electronics processes of PSCs and their characterization will be given in chapter 6.

## 1.4 Steady-state characterization

### 1.4.1 Reference solar spectrum

All solar cells presented in this thesis are measured using simulated light that matches - as close as possible - the American Standards for Testing of Materials (ASTM) Standard Air Mass (AM) 1.5G reference spectrum, as defined in the ASTM G-173-03 reference. The reference represents the solar irradiation spectra under one specific set of atmospheric conditions and one a surface with a specific orientation: the reference surface is an inclined plane at 37° tilt toward the equator and the sun facing the surface at a 48.19° zenith angle (the sun penetrates through 1.5 times the thickness of the atmosphere, hence the name AM1.5). The air turbidity, water column equivalent, ozone column equivalent and CO<sub>2</sub> concentration are also well defined. The AM1.5G (G is for global) reference combines the contribution of direct and diffuse sunlight. The diffuse sunlight is the hemispherical integration of the scattered light and accounts for around 20% of the global light intensity. The extraterrestrial light is filtered by a series of absorbing and scattering processes. For example, most of the UV light is absorbed by ozone, and water vapor is responsible for much of the infrared absorption (905-940 nm and 1100-1150 nm). The integrated spectral irradiance of the AM1.5G spectra is 1000 W m<sup>-2</sup>. Ideally, the irradiance simulated by artificial light should approach the reference spectral distribution. Deviations from it must be accounted for in a mismatch factor, which in turns depends on the external quantum efficiency of the photovoltaic cell.

### 1.4.2 Voltage sweep measurements

The traditional way to assess the performance of a photovoltaic device is to perform a voltage sweep in photovoltaic mode. This is usually performed using a low impedance voltage source (in the form of a source-measuring unit, SMU) that applies a potential across the device and measures the corresponding current. This measurement can be done in the dark (yielding a dark  $j(V)$  curve) or under light (yielding a light  $j(V)$  curve).

A solar cell usually shows a diodic behavior. In accumulation mode, also called forward bias, electrons are pushed through the anode into the perovskite and recombine with holes injected from the cathode (also called the counter electrode). When there is little potential, electrons and holes have to overcome a large built-in voltage and little current flows through the device. As the potential is increased, the barrier height decreases and an increasing amount of current flows from the anode to the cathode (i.e. from the HTM side to the ETL side, opposite to the electron motion). At the same time, the HTL remains blocking for electrons and vice-versa for the ETL, hence the electrons and the holes injected from the contacts must recombine at an interface or in the bulk of the hybrid perovskite layer. In reverse bias, or in depletion mode, electronic carriers are pulled out of the device (the electrons from the ETL side and the holes from the HTL side). This only increases the built-in voltage, and the only current that flows through the device is due to the minority carriers. This current is the dark reverse saturation current  $J_{0,\text{sat}}$ . Under illumination, a flow of carrier (generating a current  $J_{\text{phot}}$ ) opposes the dark current. The cell becomes a high impedance source (around short circuit) and a low impedance source (around open circuit) and, in the ideal case, answers to equation 1.9

$$J = J_{\text{phot}} - J_{0,\text{sat}} \left( \exp\left(\frac{qV}{k_{\text{B}}T}\right) - 1 \right) \quad (1.9)$$

In practical applications, perovskite solar cells (and third generation solar cells in general) do not follow the diode equation quite perfectly, mostly because current generation, transport and recombination are more complex than in the case of an ideal p-n junction, for which equation 1.9 holds. The recorded current  $j(V)$  is the result of a competition between charge transport and recombination that follow the current generation. It is obvious that when transport occurs much faster than recombination, a lot of the generated charges can be collected. Conversely, if the recombination rate is much larger than the charge transport, only a few or none of those charges can be extracted. How transport and recombination is affected by the device potential is not necessarily straightforward and depends on the materials constituting the solar cell, notably their trap density and the mobility of their carriers.

The current at 0 V is referred to as the short circuit current. Generally, at low bias, transport is significantly faster than recombination. This leads to a high collection efficiency for the electron, and the extracted current is almost voltage independent. When the cell approaches the maximum power point, the quasi-Fermi splitting becomes large enough that the recombination rate decreases and approaches the transport rate. The collected current starts to decrease. At some point, when recombination becomes so much faster than transport that no more charges are extracted, the cell is biased at what is referred to as the open circuit  $V_{\text{oc}}$ . The

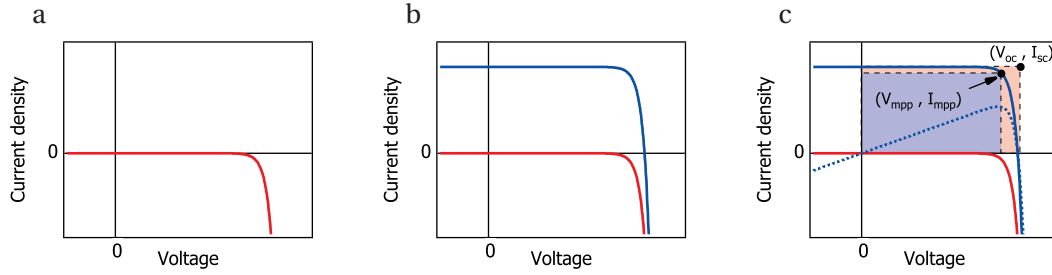


**Figure 1.2:** (a) Example of a typical dark  $j(V)$  characteristics, as described by the ideal diode equation. (b) Example of a typical  $j(V)$  characteristics of a solar cell under light, as described by the ideal diode equation under light. (c) position of the maximum power point. The ratio of the blue area by the orange area yields the fill factor.

value of the open circuit voltage depends on the generation current and the recombination rate, but not on the transport or capacitive properties of the cell. Studying transport and recombination as a function of the cell potential is the focus of chapter 6 of this thesis.

The purpose of a solar cell is to produce electrical work, which time derivative is the electrical power and can be expressed as

$$\frac{dw_{el}}{dt} = P_{el} = V \cdot J(V) \quad (1.10)$$

Evidently, keeping the solar cell at short circuit does not generate any power, nor does keeping it at open circuit. The voltage range at which the cell is generating power is anywhere between 0 V and  $V_{oc}$ . The voltage where the cell generates the maximum possible power is of the highest interest, because it is the one used in the calculation of the power conversion efficiency, the key metric of the solar cell. The voltage at maximum power is found when the differential of the power by the voltage is null:

$$\left. \frac{\partial P}{\partial V} \right|_{V_{mpp}} = 0 \quad (1.11)$$

Hence, the maximum usable power of the solar is defined as the product of the maximum power point voltage and maximum power point current:

$$P_{mpp} = V_{mpp} \cdot I_{mpp} \quad (1.12)$$

The power conversion efficiency of the solar cell is defined as the usable power divided by the input power, in this case the irradiance:

$$\eta = \frac{V_{mpp} \cdot I_{mpp}}{P_{solar}} \quad (1.13)$$

Finally, we introduce the last fundamental measure of the solar cell, the fill factor. It is a geometrical factor that describe how 'square' the  $j(V)$  curve is. It is defined as a function of the

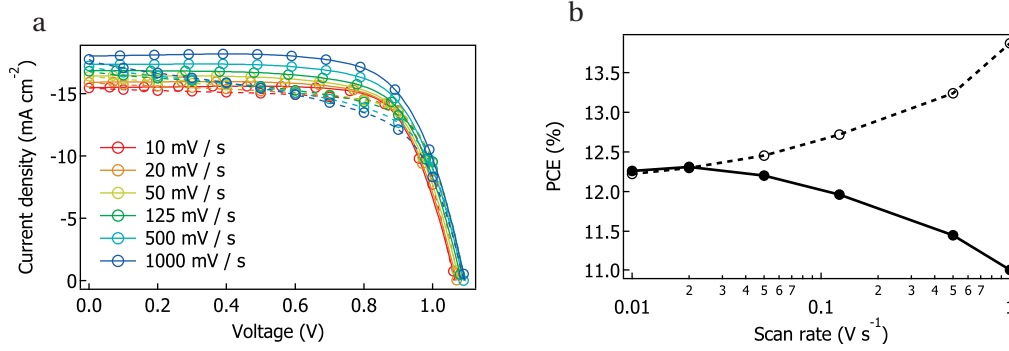


**Figure 1.3:** (a) Voltage sweep measurements of a typical perovskite solar cell at different scan rates illuminated by a simulated AM1.5G solar spectra of  $1000 \text{ W m}^{-2}$  intensity. Solid lines represent the backward scans and dashed lines the forward scans. The cell was equilibrated at  $V_{oc}$  for 10 s before sweeping backward and upon reaching 0 V inverting the scan direction without further delay. (b) Calculated power conversion efficiencies from (a), using the backward scan (dashed line) and the forward scan (solid line) as a function of the scan rate.

open circuit voltage, short circuit current, and maximum power point voltage and current:

$$FF = \frac{V_{mpp} \cdot J_{mpp}}{V_{oc} \cdot J_{sc}} \quad (1.14)$$

Equation 1.13 can be rewritten using the fill factor:

$$\eta = \frac{V_{oc} \cdot J_{sc} \cdot FF}{P_{solar}} \quad (1.15)$$

In practice, determining the power conversion efficiency of perovskite solar cells from voltage sweeps is prone to significant overestimations. It was found that most PSCs have significant hysteresis between the backward scan (from open circuit voltage to short circuit) and the forward scan (from short circuit to open circuit). The magnitude of the hysteresis is known to be affected by both the equilibration time of the cell at  $V_{oc}$  and the rate of the voltage sweep[64]. In figure 1.3 we show the  $j(V)$  curve of a typical perovskite solar cell measured at various scan rates and directions. The corresponding power conversion efficiency is also reported. In this particular case, scanning the device rapidly can lead to an overestimation of the PCE by more than 2% (absolute). The origin of the hysteresis will be discussed in more details in chapter 6. Generally, the maximum power output calculated from the backward  $j(V)$  curve can be substantially larger than the one extracted from the forward scan. Sustained power output using maximum power point tracking measurements can be used to measure the true power output of the device. This is the topic of chapter 5.

### 1.5 Components of typical perovskite solar cells

The following section describes in further detail each of the component of the solar and is intended as a short review of the work that was done in parallel to this thesis by multiple research groups around the world. Similar reviews having been already been written and available in the literature, we will keep this section short but focus on the key aspects of the perovskite solar cells.

#### 1.5.1 The compact metal oxide blocking layer

The blocking layer is directly deposited onto the conductive glass substrate. It should form a compact, continuous n-type contact intending to provide electron selectivity. In other words, it is used to prevent, or rather slow down, the recombination between the electrons injected into the conductive oxide layer and the holes in the perovskite. It is common to use the same material for the underlayer as the one of the mesoscopic scaffold. Most often, the material of choice for the blocking layer is  $\text{TiO}_2$ , deposited by spray pyrolysis, atomic layer deposition or through the sintering of a spin-coated precursor. The goal is to obtain a pinhole-free compact layer[65] that is as thin and as uniform as possible[66]. However, it has been shown than perovskite solar cells also work relatively well with no[67] or ultra-thin[68] hole blocking layers.

Practically, the most frequent technique to deposit  $\text{TiO}_2$  or other metal oxide is by aerosol spray pyrolysis. Spray pyrolysis offers a cheap and accessible way to deposit relatively compact and uniform layers ranging from a few nanometers to micrometers. Alternatives to spray pyrolysis include atomic layer deposition or spin-coating of a  $\text{TiCl}_4$  layer followed by sintering.

$\text{SnO}_2$  blocking layers have also been shown to provide excellent results[61, 62], with reported PCEs over 21% and open circuit voltages above 1200 mV.

#### 1.5.2 The mesoscopic scaffold

On top of the blocking layer is usually deposited a thin mesoporous film made of nanoparticles of a metal oxide (usually  $\text{TiO}_2$ ). Historically, the  $\text{TiO}_2$  mesoporous layer was used in a configuration similar to that of DSSCs, where the perovskite sensitizer was fully infiltrated in the gaps between the particles[42, 40, 47], but today's highest performance devices only contain a thin mesoporous substrate of about 100 nm[69]. The role of the mesoscopic layer is therefore questioned, especially in view of the highly efficient flat film perovskite solar cells. Nevertheless, today's most efficient PSCs still use a mesoscopic scaffold, hence the role of the porous network of the electron transporting layer cannot be overlooked. From the DSSC and ssDSSC perspective, it is known that the  $\text{TiO}_2$  framework provides a high contact area for electron injection. It is used to increase the projected electrode area to boost the dye loading and the external quantum efficiency of both DSSCs and ssDSSCs. In perovskite solar cells, the



## 1.5. Components of typical perovskite solar cells

---

diffusion length of free carriers was estimated between 100 nm and 1  $\mu\text{m}$ [36, 38, 37]. In the former case, the mesoporous scaffold acts as a way for electrons to be collected before they recombine, at least the ones absorbed within the mesoporous layer. Indeed, the collection efficiency can be written as

$$\eta_{coll} = \frac{1}{1 + \left(\frac{d}{L_D}\right)^2} \quad (1.16)$$

where  $d^2$  is the mean square displacement that electrons need to travel towards the  $\text{TiO}_2$  surface, i.e. around 20 nm in the case of most mesoporous layers. For diffusion lengths above 1  $\mu\text{m}$ , we see another potential aspect of the mesoscopic layer, in that it could act as a high surface area electrode that reduces the effective impedance for charge transfer, when compared to a flat electrode (we have  $R_{CT}^\perp \propto A^{-1}$  where  $A$  is the projected surface area).

$\text{TiO}_2$  has historically been the material of choice for the mesoporous substrate[41]. It is semiconductor with a wide band gap of 3.2 eV, hence it only has parasitic absorption in the UV region of the solar spectrum. In addition, it is a non-toxic and cheap material that has found applications in many consumer products, including paint, make-up and skin cream.  $\text{TiO}_2$  is naturally doped by oxygen vacancies and is therefore an n-type material. The exact doping density depends on its crystalline phase and on its processing[65]. There are three naturally occurring phases of  $\text{TiO}_2$ : anatase, rutile and brookite. Although rutile is the thermodynamically most stable at room temperature, brookite and anatase are kinetically stable below 600 °C. DSSCs and PSCs nowadays employ the anatase phase as it usually allows higher performances to be achieved, the reason for which is not clearly established. Even so, there has been reports of successful PSCs that employ the rutile phase[70, 71, 72]. Alternatives to  $\text{TiO}_2$  are also studied, aiming for a higher conductivity and reduced recombinations. Other metal oxide scaffolds have somewhat been successful for PSCs, including  $\text{ZnO}$ [73, 74, 59] and  $\text{ZrO}_2$ [75], but so far perform less efficiently than the  $\text{TiO}_2$  anatase electrodes.

### 1.5.3 The perovskite absorber

The perovskite layer is the layer that is photo-active in the visible region of the spectrum. It is responsible for absorbing photons and generating free charges.  $\text{CH}_3\text{NH}_3\text{PbI}_3$  and related cubic and tetragonal perovskites are direct band gap semiconductors. The pure  $\text{CH}_3\text{NH}_3\text{PbI}_3$  form has a band-gap of 1.57 eV (the optical absorption onset is at 800 nm) and its absorption coefficient ( $10 \times 10^4$  to  $10 \times 10^5 \text{cm}^{-1}$ ) is extremely high throughout the visible spectrum and part of the infrared, similarly to most other direct band-gap semiconductors used in photovoltaics[76]. Depositing perovskite layers with high diffusion lengths is another key aspect in obtaining high power conversion efficiencies. Although the electronic effect of grain boundaries is not yet entirely clear, it is a general goal to obtain larger grain sizes, specifically grains spanning through the whole device thickness. High crystallinity and low defect concentration that can potentially act as trapped state and recombination centers are also pursued

goals. Most organic-inorganic perovskites are deposited from solution and cannot withstand prolonged heating treatments. We briefly review here the various deposition protocols and some of the aspects of compositional engineering that will appear in this thesis.

### 1.5.3.1 Deposition protocols

Tremendous amount of work to control and optimize the deposition procedure of  $\text{CH}_3\text{NH}_3\text{PbI}_3$  was invested since 2012. It is primarily compositional engineering and optimizations of the deposition, rather than fundamental understanding of the electronic properties of the material, that allowed power conversion efficiencies to climb over 22%[55]. Initially,  $\text{CH}_3\text{NH}_3\text{PbI}_3$  was deposited by preparing large concentrations of the precursor materials ( $\text{PbI}_2$  and  $\text{CH}_3\text{NH}_3\text{I}$ ) in a polar solvent, such as  $\gamma$ -butyrolactone (GBL), *N,N*-dimethylformamide (DMF) or dimethylsulfoxide (DMSO), which, upon spin-coating, resulted in uncontrolled crystallization and poor performance output[47, 77, 78].

**1.5.3.1.1 Chloride addition** A simple way to retard crystallization of  $\text{CH}_3\text{NH}_3\text{PbI}_3$  was employed by Lee et al.[45] who added an excess  $\text{Cl}^-$  to the solution using  $\text{CH}_3\text{NH}_3\text{Cl}$ . Further annealing of the as-deposited film was required to form the final absorbing layer. Superior efficiencies of 12.3% were obtained. While the structure  $\text{CH}_3\text{NH}_3\text{PbCl}_x\text{I}_{3-x}$  was initially claimed to be formed and to exhibit enhanced properties, it appears clearly now that chloride addition primarily acts as a crystallization retardant, allowing for bigger grains and better uniformity to be obtained[79]. Indeed, careful crystallographic analysis showed no chloride content in the bulk  $\text{CH}_3\text{NH}_3\text{PbI}_3$  phase[80, 81]. Rather, it appears that chloride induces an amorphous phase of  $\text{CH}_3\text{NH}_3\text{PbCl}_x\text{I}_{3-x}$  which grows into  $\text{CH}_3\text{NH}_3\text{PbI}_3$  above 109 °C[33] and that chloride and iodide cannot co-exist in the crystalline methylammonium lead perovskite.

**1.5.3.1.2 Sequential deposition** The sequential deposition will be the topic of chapter 2. Depositing  $\text{CH}_3\text{NH}_3\text{PbI}_3$  through a two-step process showed superior properties in terms of grain size, coverage and uniformity. After infiltrating  $\text{PbI}_2$  in the nanopores of  $\text{TiO}_2$  and forming a thin capping layer on top of it, lead iodide was converted into  $\text{CH}_3\text{NH}_3\text{PbI}_3$  by dipping the film into a solution of  $\text{CH}_3\text{NH}_3\text{I}$  in 2-propanol. The transformation completes within seconds of the dipping. Large grains of high quality were achieved, and power conversion efficiencies of 15% rapidly obtained. Im et al. showed that the crystal size and growth rate of  $\text{CH}_3\text{NH}_3\text{PbI}_3$  is strongly affected by the concentration of  $\text{CH}_3\text{NH}_3\text{I}$ [82], which in turns affects the light harvesting efficiency and the hole collection rate. Through a careful optimization, conversion efficiencies of 17% were recorded[82].

**1.5.3.1.3 Vapor-assisted deposition** Other methods which overall gained less attention involve partially or totally depositing the perovskite layer through a carrier gas. Leyden et al. have used a multi-zone tube furnace to deposit both  $\text{CH}_3\text{NH}_3\text{I}$  and  $\text{PbI}_2$  from two different sources

## 1.5. Components of typical perovskite solar cells

---

under relatively low vacuum (100 Pa) using a  $N_2$  carrier gas. FTO/TiO<sub>2</sub>/CH<sub>3</sub>NH<sub>3</sub>PbI<sub>3</sub>/Spiro-MeOTAD/Au solar cells with efficiencies of 11.8% were obtained[83]. Alternatively, Chen et al. have demonstrated that vapor-assisted conversion (VASP) of PbI<sub>2</sub> to CH<sub>3</sub>NH<sub>3</sub>PbI<sub>3</sub> was achievable by placing PbI<sub>2</sub>-coated films in a closed petri dish containing CH<sub>3</sub>NH<sub>3</sub>I powder. By heating the dish to 150 °C, MAI vaporizes and converts lead iodide into perovskite. Efficiencies of 16.8% were achieved using this technique[60, 84].

**1.5.3.1.4 Thermal evaporation** Pioneered by Mitzi[11, 9, 30], thermal evaporation of perovskite from its precursors PbI<sub>2</sub> and CH<sub>3</sub>NH<sub>3</sub>I was employed by Malinkiewicz[85] and Liu[86] to deposit CH<sub>3</sub>NH<sub>3</sub>PbI<sub>3</sub> as the photo-active layer in their solar cell. Typically, PbI<sub>2</sub> and CH<sub>3</sub>NH<sub>3</sub>I would be placed in two separate thermal evaporation boats and heated together under vacuum[87]. Teuscher et al. have shown that regulating the chamber pressure using a thermal regulation of the CH<sub>3</sub>NH<sub>3</sub>I source affects the final I/Pb ratio in the device[88]. In addition, it has been shown that PbCl<sub>2</sub> can also be used as a source of evaporation together with CH<sub>3</sub>NH<sub>3</sub>I, to form efficient planar PEDOT/MAPbI<sub>3</sub>(Cl)/PCBM solar cell[89]. Single source evaporation of perovskite single crystals[90] showed that perovskite can be deposited with high level of purity while retaining the proper nominal CH<sub>3</sub>NH<sub>3</sub>PbI<sub>3</sub> stoichiometry. By flash-evaporation of meniscus-coated perovskite films, Longo et al. have shown that single-source evaporation of perovskite could compete well with dual-source evaporation, and power conversion efficiencies up to 12.2% based on a PEDOT/PSS and PolyTPD extraction layers were reported[91].

**1.5.3.1.5 Vacuum flash-assisted deposition** A recent procedure that was utilized to produce high efficiency perovskite solar cell is the vacuum-flash assisted deposition method, which produces shiny, smooth films with large perovskite grains without the need for crystallization agents like an anti-solvent. Efficiencies up to 20.5% have been reported for a 1 cm<sup>2</sup> device using this procedure, paving the way for high-efficiency, large area perovskite solar cells. After spin-coating a perovskite precursor containing Pb<sup>2+</sup>, Br<sup>-</sup>, I<sup>-</sup>, MA<sup>+</sup> and FA<sup>+</sup> in a mixture of DMSO, DMF and GBL, the substrate is placed in a vacuum oven at 20 Pa for 10 s, followed by annealing 100 °C under atmospheric pressure for 30 minutes. The rest of the device fabrication follows the traditional route of Spiro-MeOTAD deposition and gold back-contact evaporation[92].

### 1.5.3.2 Composition engineering

Compositional engineering of perovskite has become a major source of efficiency improvements. It has been shown that bromide and iodide halide can be used interchangeably in the perovskite structure to tune the optical band gap of the absorber[93, 94, 95]. Although bromide-iodide or bromide-chloride can form mixed-phases of intermediate lattice parameters[81, 96], chloride and iodide cannot appear together in the same unit cell. It has also been pointed out by Hoke that some mixtures of Br and I do not sustain strong light illumination and split

into geometrically separated bromide rich and iodide rich phases[97]. Nevertheless, small amounts of bromides have been shown to significantly improve the stability of perovskite solar cells, while not significantly affecting their optical properties[98]. Formamidinium, methylammonium and cesium can also be used interchangeably[99, 100], and a recent study by Sutton showed that cesium can be used to stabilize the  $\alpha$ -phase of the  $\text{CH}(\text{NH}_2)_2\text{PbI}_3$ [101], which otherwise degrades into its non-perovskite  $\delta$ -phase[34, 99]. A tentative explanation of the intrinsic stability of cesium containing perovskite was provided Li et al.[102], who showed that the average ionic radius of mixed cesium and formamidinium cations allowed the Goldschmidt tolerance factor to be kept between 0.8 and 1, a requirement for the stability of the cubic phase of perovskites.

### 1.5.4 The hole transporting layer

In a perovskite solar cell, the hole transporting layer is responsible for selectively transporting holes and blocking electrons. It must be able to match the current generation rate of the perovskite and thus have a sufficiently low resistance. Many materials have been explored for their use as hole transporting materials in perovskite solar cells. Though inorganic p-type semiconductors such as NiO,  $\text{WO}_3$  and  $\text{MoO}_3$  have been somewhat successful as hole transporting layers in PSCs, the most commonly used HTMs are solution-processable p-type organic materials, either molecular or polymeric. In particular, 2,2',7,7'-tetrakis-N,N-di-para-methoxyphenylamine-9,9'-spirobifluorene (spiro-MeOTAD) is the most popular material since its introduction in 1998 by Udo Bach[46]. Its use in solid state dye-sensitized solar cells has been extensively reported and it remains the material of choice for high efficiency perovskite solar cells[69].

Spiro-MeOTAD is an amorphous, wide band gap organic semiconductor with high solubility in organic solvents. It has a glass transition temperature of 121 °C and a melting point at 246 °C[103]. Hole mobilities ranging from  $1 \times 10^{-5} \text{cm}^2 \text{V}^{-1} \text{s}^{-1}$  to  $1 \times 10^{-4} \text{cm}^2 \text{V}^{-1} \text{s}^{-1}$  have been reported. The first oxidation potential of Spiro-MeOTAD was measured at -5.1 eV by photoelectron spectroscopy and electrochemical techniques. The oxidation potential matches well with the valence band of most hybrid perovskite materials, hence the hole transfer between the two should be favored, while conduction band electrons are not energetic enough to reduce Spiro-MeOTAD.

Typically, Spiro-MeOTAD is deposited by spin-coating from a concentrated solution in chlorobenzene or toluene. Interestingly, bare Spiro-MeOTAD leads to very poor device performance. Additives are usually added in the formulation and spin-coated together with the HTM. Typically, those additives are 4-tertbutylamine (4-tBP or tBP) and LiTFSI. In addition, molecular dopants are sometimes used to boost the conductivity of the HTM. The presence of those specific additives originate from the formulation used in solid state dye cells, but their role in PSCs is extremely unclear thus far. 4-tBP is known to adsorb on the metal oxide surface in DSSCs, raising the conduction band position through a local dipole effect, and

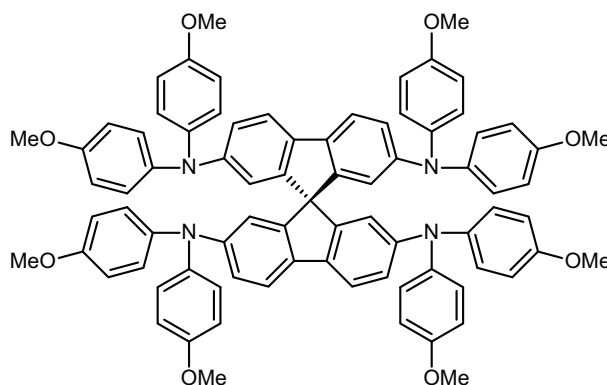


**Figure 1.4:** Chemicals structure of 2,2',7,7'-tetrakis-N,N-di-para-methoxyphenylamine-9,9'-spirobifluorene (spiro-MeOTAD).

effectively slowing down the interfacial recombination. Conversely,  $\text{Li}^+$  ions are known to shift the conduction band of the metal oxide downwards, increase the driving force for electron injection of the dye molecule. Whether such effects occur in PSCs or not, or what their exact role is, remains very unclear: there is surprisingly very few studies unveiling their role in PSCs.

Snaith has shown that LiTFSI has an effect on the hole mobility of Spiro-MeOTAD[104]. Later, it was shown that LiTFSI actually acts as a p-dopant in presence of oxygen, by increasing the rate of photo-oxidation of the HTM[105, 106, 107]. Whether this is the primary role of LiTFSI remains unclear, but avoiding the use of 4-tBP and LiTFSI has so far been challenging. In chapter 6, we will briefly report the effect of the LiTFSI additive on the electronics of the solar cell.

### 1.5.5 Back-contact

Traditional thin film perovskite solar cells are back-contacted with a metallic layer. The material of choice is usually gold, but silver is also widely used for its lower cost and higher reflectivity. However, silver suffers from instability towards  $\text{CH}_3\text{NH}_3\text{PbI}_3$  as it oxidizes into AgI. Semi-transparent contacts using silver nanowires[108, 109] and indium tin oxide counter electrodes sputtered on  $\text{MoO}_x$  were also successfully used to assemble 2-terminal tandem Si/ $\text{CH}_3\text{NH}_3\text{PbI}_3$  solar cells[110, 111].

## 1.6 Motivation and procedures

I started my thesis when the field of hybrid perovskite for photovoltaics had just begun, with only a few articles that were published at the time on this topic. The questions and problematic that were raised in 2013 are entirely different than the ones of 2017. As a consequence, the chapters that I present in this work follow closely the rapid development of the research during this period. Over a four years period, thousands of articles were published on this topic by

## Chapter 1. Introduction

---

over a hundred research groups around the world. In the beginning of 2013, there was a general struggle to fabricate photovoltaic devices with high power conversion efficiencies in a reproducible fashion. The first chapter addresses these problems as we introduced the concept of the sequential deposition. As the power conversion efficiency and reproducibility improved significantly in 2014, we investigated some of the aspects of the chemical composition of the hybrid perovskite layer and its influence on its optical, electrical and photovoltaic properties. While the best formulations for high efficiency PSCs were being adjusted, we discovered that in situ chemical transformation of the perovskite layer were possible through ion exchange. This is the focus of chapter 4. Questions with regards to the stability of the perovskite were raised, particularly in view of the ionic motion that occurs under a constant DC polarization. This issue will be partly discussed in chapters 5 and 6. Finally, as it became clear that perovskite solar cells were approaching a potential marketability, I wished to address some questions that regard the end of life of the solar cells, in particular of the treatment of the waste through efficient recycling. This is the focus of chapter 7.

More specifically, the studies I report in this thesis comprise the following:

In chapter 2, developed in collaboration with Dr. Julian Burschka, we introduced a novel way to deposit  $\text{CH}_3\text{NH}_3\text{PbI}_3$  onto  $\text{TiO}_2$  mesoporous substrates. After depositing  $\text{PbI}_2$  by spin-coating, it was converted into  $\text{CH}_3\text{NH}_3\text{PbI}_3$  by a controlled intercalation reaction. This technique allowed us to gain significant control over the uniformity and the crystallinity of the perovskite layer. We reported a power conversion efficiency of 15%, the highest performance at the time[47]. In parallel to this study, we certified the efficiency of the first perovskite solar cell, referenced in the NREL chart[55]. Following this work, in collaboration with the group of Prof. Nam-Gyu Park, we reported on the control of the perovskite crystal size capping the  $\text{TiO}_2$  layer, also using the sequential deposition. This control allowed us to report further PCE improvements - up to 17%. In chapter 2, it will be shown that the charge collection rate is intimately linked to the size of the cuboids forming the capping layer[82].

In chapter 3, we use the sequential deposition described in the chapter 2 and apply it to the fabrication of mixed methylammonium - formamidinium lead halide perovskites. The strategy of mixing the two cations is to extend slightly the absorption of the perovskite into the infrared. Formamidinium alone is unfortunately not stable as it forms the thermodynamically more stable non-perovskite  $\delta$  phase. We found however that mixing methylammonium and formamidinium in similar quantities can stabilize the  $\alpha$  perovskite phase while leading to a similar gain in spectral absorption. Solar cells assembled using a mixed cation perovskite perform significantly better than the ones assembled with pristine cation lead halide perovskites. This increase in PCE correlated well to a longer excited state lifetime of the mixed cations.

In chapter 4, we explore the reactivity of the perovskite material. We found that even after the formation of  $\text{CH}_3\text{NH}_3\text{PbX}_3$ , the halide can be exchanged by another by simply dipping the film into a solution containing another methylammonium halide in 2-propanol. This reaction exchange was found to occur through different mechanisms depending on which halide in the

solid phase was exchanged by which other halide in the solution. After the halide exchange, the quantum yield for luminescence sharply increases. Chapter 4 also shows that the halide exchange reaction can be used to fabricate  $\text{CH}_3\text{NH}_3\text{PbBr}_3$  and  $\text{CH}_3\text{NH}_3\text{PbCl}_3$  nanowires, which cannot be synthesized through a direct route. We performed halide exchange reactions on their  $\text{CH}_3\text{NH}_3\text{PbI}_3$  counterpart and show complete conversion and preservation of the 1D morphology of the wires.

Chapter 5 discusses the maximum power point tracking of perovskite solar cells. We initially reported on the design of an ageing setup but extended our study to the issues related to the maximum power point tracking of PSCs. In particular, we found that the hysteresis inherent to PSCs advert the convergence of MPPT algorithms under fast tracking conditions. Such issues are expected to also occur in commercial buck-boost converter maximum power point trackers for reasons that are explained in this chapter. A very simple method to stabilize the algorithms is presented. Surprisingly, the highest power output was not obtained when the cell was kept at steady-state, but rather when it undergoes repetitive poling in forward bias. Power outputs higher by as much as +11% compared to steady-state measurements were recorded. Finally, I show one example of stability measurements performed using this home-built ageing setup.

Chapter 6 describes the frequency-resolved dynamics of perovskite solar cells. I begin by expanding the network thermodynamics model to the case of a non-thermal between electrons and holes. An equivalent circuit is assembled, from which the response of intensity modulated photovoltage and intensity modulate photocurrent spectroscopy can be simulated. The principal real and complex features of both techniques for typical perovskite solar cells are discussed and related to the equivalent circuit. For complex cases, non-linear least square fitting of numerically simulated data was performed as a substitute for the missing analytical expression of the IMVS/IMPS response. Finally, we show a few case studies that demonstrate the relevance of these techniques in the characterization of perovskite solar cells.

In the 7th and final chapter, we report on a proof of concept for recycling perovskite solar cells upon their end of life. This work describes a solvent based approach that relies on the orthogonality of the solubility constants of each material to physically separate them from each other. We show that lead ions can be collected with almost perfect orthogonality and that their low residual concentration in the other solvents can be further sequestered using an ion exchange resin. Most importantly, we stress that the mesoporous substrate can be re-used without further heat-treatment, which is a promising pathway to avoid downscaling of the PSC waste.





## 2 Sequential deposition as a route to high-efficiency perovskite solar cells

*This chapter describes an approach to fabricate high efficiency perovskite solar cells using an innovative 2-step route to deposit the  $\text{CH}_3\text{NH}_3\text{PbI}_3$  layer. This work was initiated by Dr. Julian Burschka, who developed the idea, performed the spectroscopic measurements, XRD and SEM characterization. My work was focused on the optimization of the deposition technique, the fabrication of the perovskite solar cells and their certification for the NREL chart[55]. However, the sole reporting of my part of the work without its context would be pointless. The transcript of this manuscript is added to this thesis as a reference, but more information about this work can be found in Dr. Julian Burschka's thesis[103].*

### 2.1 Introduction

Perovskite structures are a class of crystallographic compounds named after the structure of the original perovskite,  $\text{CaTiO}_3$ . The general formula of perovskite materials is  $\text{ABX}_3$  where A and B are cations of different sizes[112] and X is an anion that bonds them together. In the ideal cubic perovskite structure, the B cation is at the center of an octahedral cage formed by the anions. The A cations are located in the interstitial sites and have a coordination number of 12. In the cubic configuration, the  $\text{BX}_6$  are corner-sharing.

Organic-inorganic halide perovskites are a special class of materials that involve a singly charged organic cation in the A site, a doubly charged inorganic one in the B site and a singly charged halide as the X site. Although first column alkali metals are inorganic elements, halide perovskites containing potassium, cesium or rubidium have been extensively reported and are usually included in this class of materials. Organic A-site cations such as methylammonium ( $\text{CH}_3\text{NH}_3^+$ )[9], formamidinium ( $\text{CH}(\text{NH}_2)_2^+$ )[113, 114, 102, 93], ethylammonium ( $\text{CH}_3\text{CH}_2\text{NH}_3^+$ )[115], tetramethylammonium ( $\text{N}(\text{CH}_3)_4^+$ )[116], guanidinium ( $\text{C}(\text{NH}_2)_3^+$ ) and many others have been reported to form hybrid perovskites. The B-site is usually an element in the 4th column element, such as germanium, tin or lead. However, bismuthate[9], nickelate[117, 118, 32, 119, 120, 121, 122, 123], vanadates[119, 121, 122] and others have been reported to also form perovskite structures, in particular when used together with  $\text{Cs}^+$ . The X

## Chapter 2. Sequential deposition as a route to high-efficiency perovskite solar cells

---

site is usually occupied by a chloride, bromide or an iodide, but fluoride-based perovskites are not uncommon.

The size of the A-site cation determines whether the material adopts a three dimensional structure or a two dimensional structure. Cations including methylammonium, formamminium, cesium and rubidium are known to form a 3D structure, while the others arrange in a 2D structure made of flat  $BX_6$  corner sharing structures intercalated with double layers of cations. 2D perovskite structures are significantly more tolerant in terms of the size and type of the organic cations. Integration of large  $\pi$ -conjugated structures have been reported by Mitzi[13]. However, 2D perovskites are usually less attractive as light harvesters because of their wider optical band gap, limiting the potential for a broadband absorption of the solar light.

3D perovskites such as  $CH_3NH_3PbI_3$  have received the greatest attention for their potential use in solar cells. They have become attractive in part because of their near-ideal band gap (1.54 eV[33]) but also owing to their excellent carrier transport properties[36, 38, 37]. In addition, the high solubility of the precursor salts in polar solvents such as N,N-dimethylformamide,  $\gamma$ -butyrolactone and dimethylsulfoxide and the poor solubility of the  $CH_3NH_3PbI_3$  in apolar solvents (chlorobenzene, toluene, hexane, ...) have undoubtedly made them extremely attractive for solution-processed thin film electrochemical devices.

### 2.2 Motivation

The deposition of uniform, thin film perovskite solar cells using solvent-based approaches has, until 2013, been a real challenge. The perovskite film was prepared spin-coating a solution obtained by co-dissolving equimolar salts of  $PbX_2$  and  $CH_3NH_3X$  ( $X=Cl, Br, I$  or mixtures) into a polar solvent. However, the deposition of the perovskite was poorly controlled and resulted in large microstructures of various shapes, dimensions and heights. In addition, there are often large gaps of uncovered  $TiO_2$  in between the structures. In Figure 2.1, we show a top-view scanning electron micrograph of the morphological features of  $CH_3NH_3PbI_3$  obtained by spin-coating the precursor solution onto a  $TiO_2$  covered conductive glass substrate. When N,N-dimethylformamide (DMF) is used as a solvent, large and thick needles grow uncontrolled on the substrate. When GBL is used as the solvent, we observed the formation of islands of various sizes and shapes. In both cases, large gaps of uncovered substrate were found between the perovskite structures.[78] Such gaps are extremely costly in terms of cell performance, mostly for two reasons. In terms of photocurrent density, any uncovered substrate lets visible photons pass unabsorbed, which is a responsible for a reduction of the available photocurrent density. Second, any exposed  $TiO_2$  substrate would come in direct contact with the hole transporting material, which is a potentially very recombinative interface and costs photovoltage.

After this report was published, deposition procedures have been further largely optimized. Even so the deposition that we introduce in this chapter is no longer the one yielding the best conversion efficiencies, it makes the case that control of the deposition technique, the

### 2.3. Sequential deposition of $\text{CH}_3\text{NH}_3\text{PbI}_3$

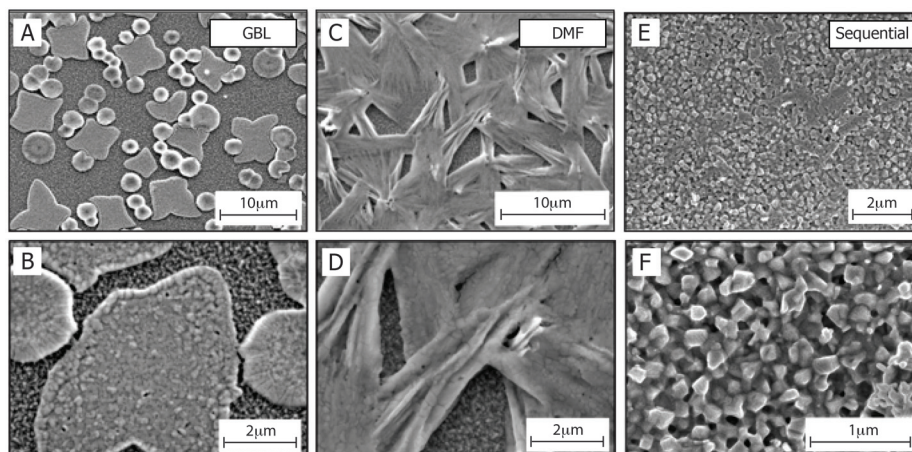


**Figure 2.1:** Comparison between the single-step method and the two-step sequential deposition. (a-d)  $\text{CH}_3\text{NH}_3\text{PbI}_3$  deposited by spin-coating on a FTO substrate using a mixed solution of  $\text{PbI}_2$  and  $\text{CH}_3\text{NH}_3\text{I}$  in (a,b)  $\gamma$ -butyrolactone (GBL) or (c,d)  $N,N$ -dimethylformamide (DMF) solvent. In both cases the surface coverage is low and bare FTO is exposed. (e,f)  $\text{CH}_3\text{NH}_3\text{PbI}_3$  obtained using the sequential deposition method (two steps). The dipping time was 30 s

grain size, the uniformity and the crystallinity were key factors in reaching today's top power conversion efficiencies.

### 2.3 Sequential deposition of $\text{CH}_3\text{NH}_3\text{PbI}_3$

In this work, we have introduced the sequential deposition as a tool to deposit in a highly controlled fashion hybrid perovskite materials. Previously reported by Liang in 1998[16], the sequential deposition involves first the spin-coating of a uniform layer of  $\text{PbI}_2$  onto the  $\text{TiO}_2$  substrate. Following the removal of the solvent (DMF), the  $\text{PbI}_2$ -coated film is dipped into a solution of  $\text{CH}_3\text{NH}_3\text{I}$  in 2-propanol. Upon contact of the lead iodide with the organic cation in solution, a rapid reaction transforms it into  $\text{CH}_3\text{NH}_3\text{PbI}_3$ . The reaction is easy to follow visually, as the yellow color of  $\text{PbI}_2$  quickly transform into a dark brown film, signature of the optical band gap of  $\text{CH}_3\text{NH}_3\text{PbI}_3$ . A schematics of the deposition procedure is shown in figure 2.2. A significant lattice expansion occurs upon conversion: the unit cell of  $\text{PbI}_2$  is  $125.7 \text{ \AA}^3$ <sup>1</sup>, which expands to  $997.9 \text{ \AA}^3$  for the supercell of the I4/mcm phase of  $\text{CH}_3\text{NH}_3\text{PbI}_3$  (containing 4 unit cells). The volume of the perovskite structure is therefore twice the one of  $\text{PbI}_2$ .

The literature contains several examples in which a two-step procedure is used to fabricate nanostructures that are not easily, or not at all, accessible by a direct synthetic route. Ion exchange reactions have, for example, been used to convert dispersed II–V semiconductor nanocrystals into the corresponding III–V analogues while preserving particle size and distribution as well as the initial nanomorphology[124, 125, 126]. As reported, the thermodynamic

<sup>1</sup>ICSD database, collection code 68819

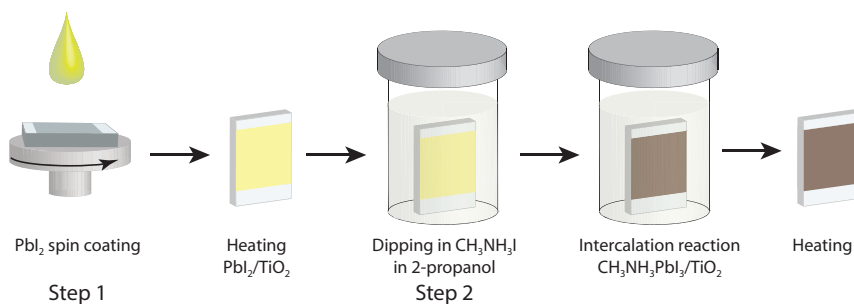


**Figure 2.2:** Schematics of the sequential deposition. First, PbI<sub>2</sub> is deposited onto a TiO<sub>2</sub>-coated TCO substrate by spin-coating, forming a yellow film. Following heating to remove the excess solvent, the film is dipped into a solution of CH<sub>3</sub>NH<sub>3</sub>I in 2-propanol. The color immediately turns dark brown. The sample undergoes an additional heating step as solvent removal.

driving force of such a reaction is the difference in bulk lattice energy for the two materials, and the initial crystal lattice serves as a template for the formation of the desired compound.

As for PbI<sub>2</sub>, the insertion of the organic cation is facilitated through the layered PbI<sub>2</sub> structure, which consists of three spatially repeating planes, I–Pb–I[127]. Numerous literature reports show that strong intralayer chemical bonding, as well as only weak interlayer van der Waals interactions, allows the easy insertion of guest molecules between these layers[128, 129, 130]. In our case, the large energy of formation of the hybrid perovskite, combined with the nanoscopic morphology of the PbI<sub>2</sub> precursor, which greatly enhances the reaction kinetics, finally enables the transformation to be completed within seconds.

## 2.4 Kinetics of the reaction

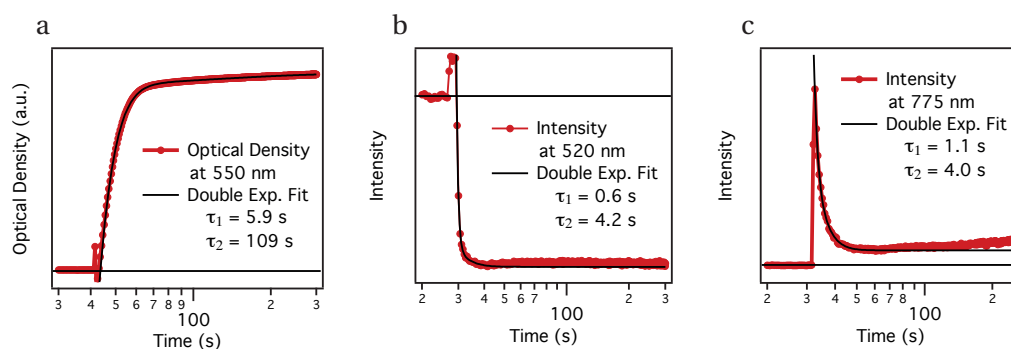


**Figure 2.3:** (a) Changes in the optical density monitored at 550 nm, (b) photoluminescence intensity monitored at 520 nm and (c) photoluminescence intensity monitored at 775 nm of a PbI<sub>2</sub>-coated film upon dipping inside a 10 mgmL<sup>-1</sup> solution of CH<sub>3</sub>NH<sub>3</sub>I in 2-propanol. Plotted versus time. Biexponential fits are added in black.

The kinetics of the conversion were monitored by optical spectroscopy. Upon dipping the

TiO<sub>2</sub>/PbI<sub>2</sub> composite film into a solution of CH<sub>3</sub>NH<sub>3</sub>I in 2-propanol (10 mgmL<sup>-1</sup>), its color changes almost immediately from yellow to dark brown, indicating the formation of CH<sub>3</sub>NH<sub>3</sub>PbI<sub>3</sub>. The dynamics of the formation of the perovskite were followed by absorption spectroscopy. Figure 2.3a shows that the increase over time of the perovskite absorption at 550 nm is practically complete within a few seconds of exposing the PbI<sub>2</sub>-loaded TiO<sub>2</sub> film to the CH<sub>3</sub>NH<sub>3</sub>I solution. A small additional increase in the absorbance, occurring on a timescale of 100 s and contributing only a few per cent to the total increase of the signal, is attributed to morphological changes producing enhanced light scattering. The conversion is accompanied by a quenching of the PbI<sub>2</sub> emission at 520 nm (figure 2.3b) and a concomitant increase in the perovskite luminescence at 775 nm (figure 2.3c). The latter emission passes through a maximum before decreasing to a stationary value. This decrease results from self-absorption of the luminescence by the perovskite formed during the reaction with CH<sub>3</sub>NH<sub>3</sub>I. The traces were fitted to a biexponential function yielding the decay times stated in figure 2.3a–c. We note that the increase in the emission intensity before the quenching in figure 2.3b is an optical artifact that results from opening the sample compartment to add the CH<sub>3</sub>NH<sub>3</sub>I solution.

## 2.5 X-ray diffraction

The green and red curves in figure 2.4 show X-ray powder diffraction pattern measured before and after the TiO<sub>2</sub>/PbI<sub>2</sub> nanocomposite film is brought into contact with the CH<sub>3</sub>NH<sub>3</sub>I solution. For comparison, we also spin-coated the PbI<sub>2</sub> on a flat glass substrate and exposed the resulting film to a CH<sub>3</sub>NH<sub>3</sub>I solution in the same manner as the TiO<sub>2</sub>/PbI<sub>2</sub> nanocomposite. Based on literature data, the PbI<sub>2</sub> deposited by spin-coating from DMF solution crystallizes in the form of the hexagonal 2H polytype<sup>2</sup>, the most common PbI<sub>2</sub> modification. Moreover, the results show that on a flat glass substrate, crystals grow in a preferential orientation along the c-axis, hence the appearance of only four diffraction peaks, corresponding to the (001), (002), (003) and (004) lattice planes (figure 2.4, black curve). For the PbI<sub>2</sub> loaded on a mesoporous TiO<sub>2</sub> film (2.4, green curve), we find three additional diffraction peaks that do not originate from TiO<sub>2</sub>, suggesting that the anatase scaffold induces a different orientation for the PbI<sub>2</sub> crystal growth.

During the reaction with CH<sub>3</sub>NH<sub>3</sub>I, we observe the appearance of a series of new diffraction peaks that are in good agreement with literature data on the tetragonal phase of the CH<sub>3</sub>NH<sub>3</sub>PbI<sub>3</sub> perovskite[35]. However, when PbI<sub>2</sub> is deposited on a flat film (2.4, blue curve) the conversion to perovskite on exposure to the CH<sub>3</sub>NH<sub>3</sub>I solution is incomplete; a large amount of unreacted PbI<sub>2</sub> remained even after a dipping time of 45 min. This agrees with the observation that the CH<sub>3</sub>NH<sub>3</sub>I insertion hardly proceeds beyond the surface of thin PbI<sub>2</sub> films, and that the complete transformation of the crystal structure requiring several hours[16]. A caveat associated with such long conversion times is that the perovskite dissolves in the methylammonium iodide solution over longer periods, hampering the transformation.

---

<sup>2</sup>Inorganic Crystal Structure Database, collection code 68819; <http://www.fiz-karlsruhe.com/icsd.html>

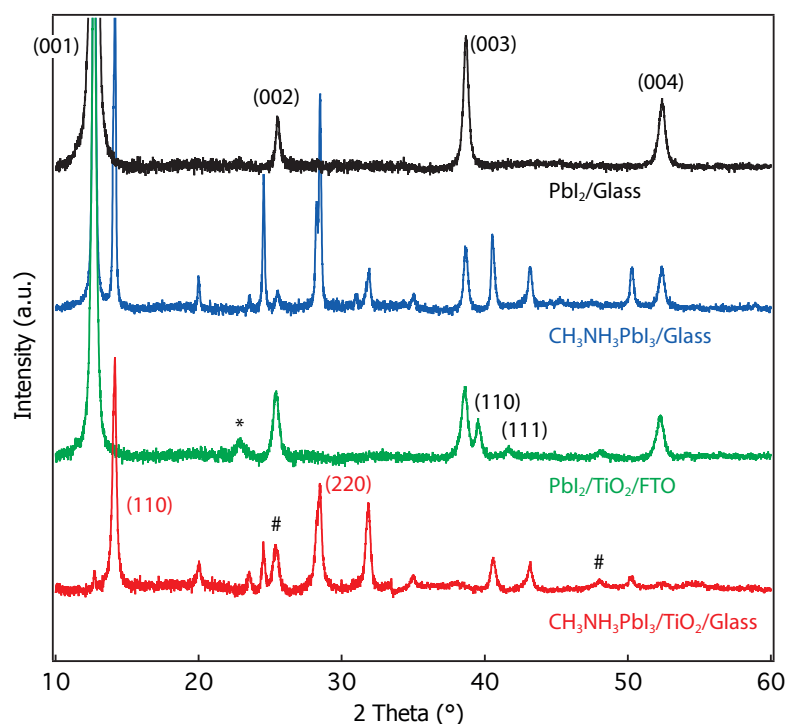


**Figure 2.4:** X-ray diffraction pattern of (a) a  $\text{PbI}_2$  on glass, (b)  $\text{PbI}_2$  converted into  $\text{CH}_3\text{NH}_3\text{PbI}_3$  by sequential deposition onto a glass substrate, (c)  $\text{PbI}_2$  deposited onto a mesoporous  $\text{TiO}_2$  substrate and (d)  $\text{PbI}_2$  converted into  $\text{CH}_3\text{NH}_3\text{PbI}_3$  by sequential deposition onto a mesoporous  $\text{TiO}_2$  substrate. The # symbols indicate  $\text{TiO}_2$  reflections and \* unassigned  $\text{PbI}_2$  reflections.

In striking contrast to the behavior of thin films of lead iodide deposited on a flat support, the conversion of  $\text{PbI}_2$  nanocrystals in the mesoporous  $\text{TiO}_2$  film is practically complete on a timescale of seconds, as is evident from the immediate disappearance of its most intense diffraction peak (the (001) peak) and the concomitant appearance of the XRD reflections for the tetragonal perovskite. When the  $\text{PbI}_2$  crystals are contained within the mesoporous  $\text{TiO}_2$  scaffold, their size is limited to  $\sim 22$  nm by the pore size of the host. Notably, we find that confining the  $\text{PbI}_2$  crystals to such a small size drastically enhances their rate of conversion to perovskite, which is complete within a few seconds of their coming into contact with the methylammonium iodide solution.

Scanning electron micrographs in figure 2.1 show that crystals of  $\text{CH}_3\text{NH}_3\text{PbI}_3$  with a large range of sizes are formed when the perovskite is deposited in a single step from a solution of  $\text{CH}_3\text{NH}_3\text{I}$  and  $\text{PbI}_2$  in  $\gamma$ -butyrolactone or DMF. A key finding of the present work is that the confinement of the  $\text{PbI}_2$  within the nanoporous network of the  $\text{TiO}_2$  film greatly facilitates its conversion to the perovskite pigment. Moreover, the mesoporous scaffold of the host forces

the perovskite to adopt a nanomorphology similar to that of the  $\text{PbI}_2$  precursor.

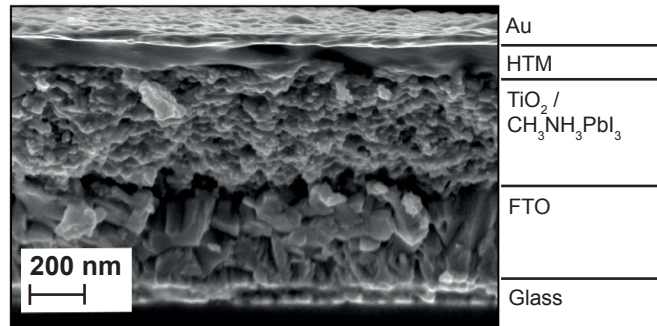


**Figure 2.5:** Cross-sectional scanning electron micrographs of a typical perovskite solar cell assembled by sequential deposition.

Figure 2.5 presents a cross-sectional scanning electron microscopy (SEM) image of the thus-prepared film. The absence of any  $\text{PbI}_2$  crystals protruding from the surface of the mesoporous anatase layer shows that our infiltration method leads to a structure in which the  $\text{PbI}_2$  is entirely contained within the nanopores of the  $\text{TiO}_2$  film.

### 2.5.1 Fabrication of perovskite solar cells

We prepared mesoporous  $\text{TiO}_2$  (anatase) films by spin-coating a solution of colloidal anatase particles onto a 30 nm-thick compact  $\text{TiO}_2$  underlayer. The underlayer was deposited by aerosol spray pyrolysis on a transparent-conducting-oxide-coated glass substrate acting as the electric front contact of the solar cell. Lead iodide ( $\text{PbI}_2$ ) was then introduced into the  $\text{TiO}_2$  nanopores by spin-coating a  $462 \text{ mg mL}^{-1}$  ( $\approx 1 \text{ M}$ ) solution of  $\text{PbI}_2$  in *N,N*-dimethylformamide (DMF) kept at  $70^\circ\text{C}$ . The use of such a high  $\text{PbI}_2$  concentration is critical to obtaining the high loading of the mesoporous  $\text{TiO}_2$  films required to fabricate high performance perovskite solar cells.

We used the sequential-deposition technique to fabricate mesoscopic solar cells employing the triarylamine derivative spiro-MeOTAD as a hole-transporting material (HTM) (figure 1.4). Following a reported concept[131], we use a Co(III) complex as a p-type dopant for the HTM at a molar doping level of 10% to ensure a sufficient conductivity and low series resistance. Figure 2.5 shows a cross-sectional scanning electron micrograph of a typical device. The mesoporous  $\text{TiO}_2$  film had an optimized thickness of around 350 nm and was infiltrated with the perovskite nanocrystals using the above-mentioned two-step procedure. The HTM was subsequently deposited by spin coating. It penetrates into the remaining available pore volume and forms a 100 nm thick layer on top of the composite structure. A thin gold layer was thermally evaporated under vacuum onto the HTM, forming the back contact of the device. We measured the current density  $j(V)$  characteristics of the solar cells under simulated air mass 1.5 global (AM1.5G) solar irradiation and in the dark. Figure 2.6a shows  $j(V)$  curves measured at a light intensity of  $95.6 \text{ mW cm}^{-2}$  for a typical device. From this, we derive values

## Chapter 2. Sequential deposition as a route to high-efficiency perovskite solar cells

Cell n°	$V_{oc}$ (mV)	$J_{sc}$ (mA cm <sup>-2</sup> )	FF (-)	PCE (%)
1	990	17.8	0.70	12.2
2	996	17.7	0.72	12.6
3	971	17.1	0.71	11.7
4	992	17.9	0.73	12.9
5	978	16.3	0.71	11.4
6	962	16.9	0.73	11.9
7	972	18.1	0.68	12.0
8	986	17.4	0.71	12.2
9	963	17.5	0.69	11.5
10	959	17.6	0.66	11.2
<b>Average</b>	<b>977 ± 14</b>	<b>17.4 ± 0.5</b>	<b>0.70 ± 0.02</b>	<b>12.0 ± 0.5</b>

**Table 2.1:** Photovoltaic data for a batch of devices prepared by sequential deposition, measured under a 1000 W m<sup>-2</sup> simulated air mass 1.5 global simulated light

for the short-circuit photocurrent ( $J_{sc}$ ), the open-circuit voltage ( $V_{oc}$ ) and the fill factor of, respectively, 17.1 mA cm<sup>-2</sup>, 992 mV and 73%, yielding a solar-to electric power conversion efficiency (PCE) of 12.9%. Statistical data on a batch of ten photovoltaic devices is shown in 2.1. From the average PCE value of 12.0% ± 0.5% and the small standard deviation, the method has excellent reproducibility, and compared to the deposition procedures that existed at the time this work was being done, yields excellent efficiencies.

Figure 2.6b shows the incident photon to current conversion efficiency (IPCE), which equals the external quantum efficiency (EQE), spectrum for the perovskite cell. Generation of photocurrent starts at 800 nm, in agreement with the bandgap of the CH<sub>3</sub>NH<sub>3</sub>PbI<sub>3</sub>, and reaches peak values of over 90% in the short wavelength region of the visible spectrum. Integrating the overlap of the IPCE spectrum with the AM1.5G solar photon flux yields a current density of 18.4 mA cm<sup>-2</sup>, which is in excellent agreement with the measured photocurrent density, extrapolated to 17.9 mA cm<sup>-2</sup> at the standard solar AM1.5G intensity of 100 mW cm<sup>-2</sup>. This confirms that any mismatch between the simulated sunlight and the AM1.5G standard is negligibly small. Comparison with the absorptance or light harvesting efficiency (LHE) depicted in figure 2.6c reveals that the lower IPCE values in the range of 600 – 800 nm result from the smaller absorption of the perovskite in this spectral region. This is also reflected in the spectrum of the internal quantum efficiency, or absorbed photon to current conversion efficiency (APCE), which can be derived from the IPCE and LHE and is shown in figure 2.6d. The APCE is greater than 90% over the whole visible region, without correction for reflective losses, indicating that the device achieves near-unity quantum yield for the generation and collection of charge carriers.

In an attempt to increase the loading of the perovskite absorber on the TiO<sub>2</sub> structure and to obviate the lack of absorption in the long-wavelength region of the spectrum, we slightly modified the conditions for the deposition of the PbI<sub>2</sub> precursor as well as the transformation reaction. Details are provided in the methods chapter. The  $j(V)$  characteristics of the



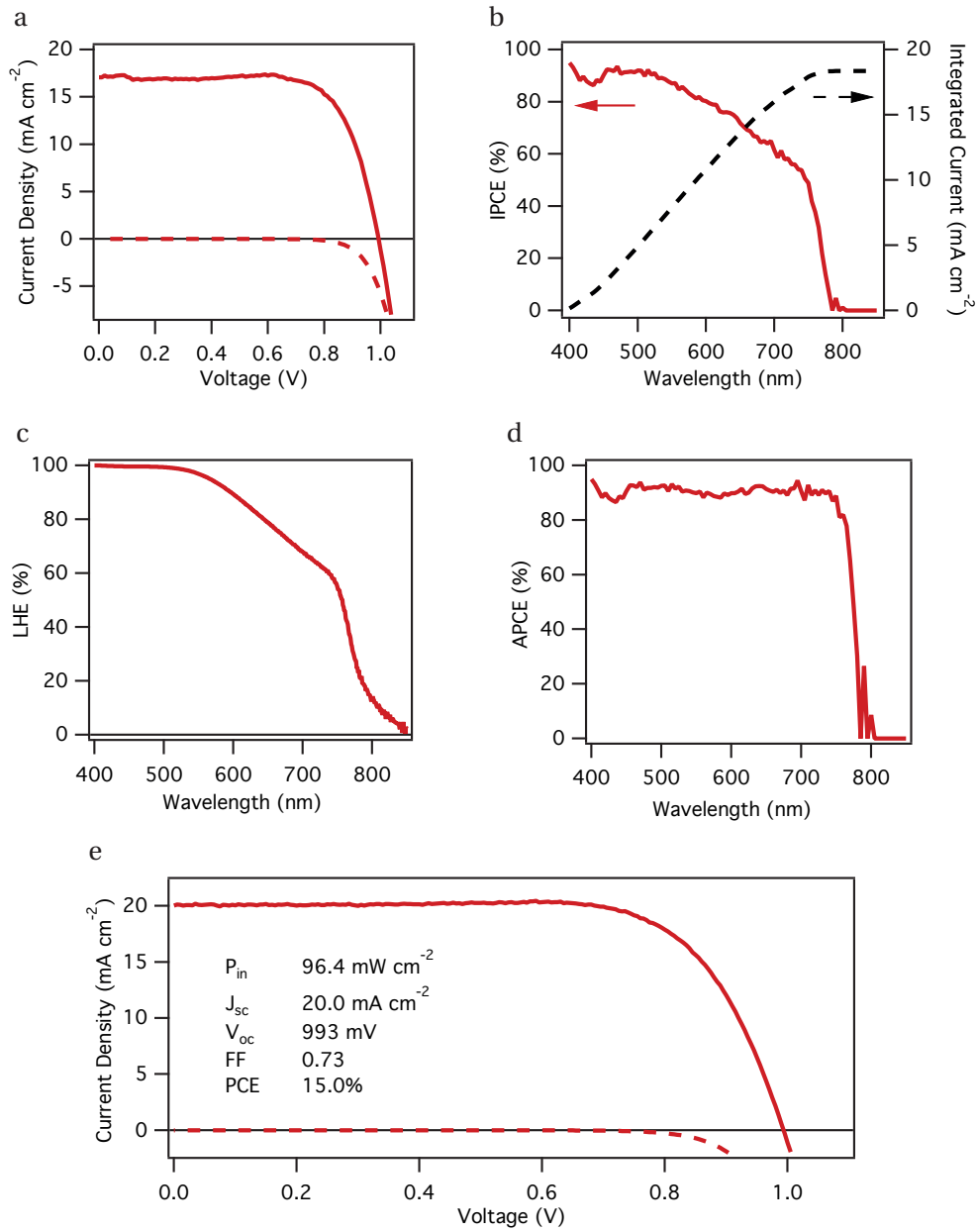


**Figure 2.6:** (a)  $j(V)$  curves for a photovoltaic device measured at a simulated air mass 1.5 global solar irradiation of  $95.6 \text{ mW cm}^{-2}$  (solid line) and in the dark (dashed line). (b) IPCE spectrum. The right-hand axis indicates the integrated photocurrent that is expected to be generated under AM1.5G irradiation. (c) LHE spectrum. (d) APCE spectrum derived from the IPCE and LHE. (e)  $j(V)$  of our champion perovskite device, measured under a simulated air mass 1.5 global solar of  $96.4 \text{ mW cm}^{-2}$

highest performance cell of the series that was fabricated in this manner are depicted in figure 2.6e. From this data, we derive values of  $20.0 \text{ mA cm}^{-2}$  for  $J_{\text{sc}}$ , 993 mV for  $V_{\text{oc}}$  and 0.73 for the filling factor, respectively, yielding a PCE of 15.0% measured at a light intensity of

## Chapter 2. Sequential deposition as a route to high-efficiency perovskite solar cells

---

Intensity $\text{mW cm}^{-2}$	$V_{\text{oc}}$ (mV)	$J_{\text{sc}}$ ( $\text{mA cm}^{-2}$ )	FF (-)	PCE (%)
9.3	901	1.7	0.77	12.6
49.8	973	8.9	0.75	13.0
95.6	992	17.1	0.73	12.9

**Table 2.2:** Photovoltaic performance of a typical perovskite solar cell prepared using the sequential deposition, at different light intensities.

$P_{\text{in}} = 96.4 \text{ mW cm}^{-2}$ . At the time of the publication of this work, this was the highest power conversion efficiency reported so far for organic or hybrid inorganic–organic solar cells and one of the highest for any solution processed photovoltaic device. Several solar cells with PCEs between 14% and 15% were fabricated. One of these devices was sent to an accredited photovoltaic calibration laboratory for certification, confirming a power conversion efficiency of 14.14% measured under standard AM1.5G reporting conditions. Detailed photovoltaic data for this device can be found in appendix E. Compared with the devices from which we took the data shown in table 2.1, these high performance devices benefit from a significantly higher photocurrent, which we attribute to the thicker capping layer present on top of the porous  $\text{TiO}_2$  film, improving the long wavelength IPCE response of the cell.

## 2.6 Optimization of the crystal size

*The acquisition of the photovoltaic data in this section was realized by Dr. J.H. Im and the research group of Prof. Nam-Gyu Park. They are relevant in the sense that they confirm our predictions based on photo-CELIV and LHE measurements that I performed. The photovoltaic data presented in this section originates from our collaborative study, published in a peer-reviewed journal[82].*

Under the leadership of Im[82], we uncovered the significant importance of the layer of  $\text{CH}_3\text{NH}_3\text{PbI}_3$  capping the mesoscopic  $\text{TiO}_2$  film. During the conversion of  $\text{PbI}_2$  into  $\text{CH}_3\text{NH}_3\text{PbI}_3$ , we discovered a significant crystal growth on top of the  $\text{TiO}_2$  layer. Such crystals usually have a cuboid shape of varying size and thickness.

### 2.6.1 Control of the crystal size

We showed that the crystallite size had a direct correlation to the concentration of  $\text{CH}_3\text{NH}_3\text{I}$  into the 2-propanol solution. In figure 2.7, we show top-view scanning electron micrographs of the  $\text{TiO}_2$  film coated with  $\text{CH}_3\text{NH}_3\text{PbI}_3$ , for various concentrations of  $\text{CH}_3\text{NH}_3\text{I}$  in 2-propanol. We found the the mean crystallite size has an inverse dependence on the solution concentration:  $\sim 720 \text{ nm}$  for  $0.038 \text{ M}$ ,  $\sim 360 \text{ nm}$  for  $0.044 \text{ M}$ ,  $\sim 190 \text{ nm}$  for  $0.050 \text{ M}$ ,  $\sim 130 \text{ nm}$  for  $0.057 \text{ M}$  and  $\sim 90 \text{ nm}$  for  $0.063 \text{ M}$ . Smaller crystals can be grown using more concentrated solutions of  $\text{CH}_3\text{NH}_3\text{I}$ , while larger ones can be obtained by reducing it, at the expense of conversion time. However, when the largest crystals are grown, part of the  $\text{TiO}_2$  film becomes uncovered,

## 2.6. Optimization of the crystal size

potentially letting light through unabsorbed and hampering the device performance. It is worth noting that the growth of the capping layer did appear to affect the pore filling. We think that its presence is due to (a) an excess  $\text{PbI}_2$  on top of the  $\text{TiO}_2$  film and (b) the accommodation of the lattice expansion upon conversion of  $\text{PbI}_2$  to  $\text{CH}_3\text{NH}_3\text{PbI}_3$ .

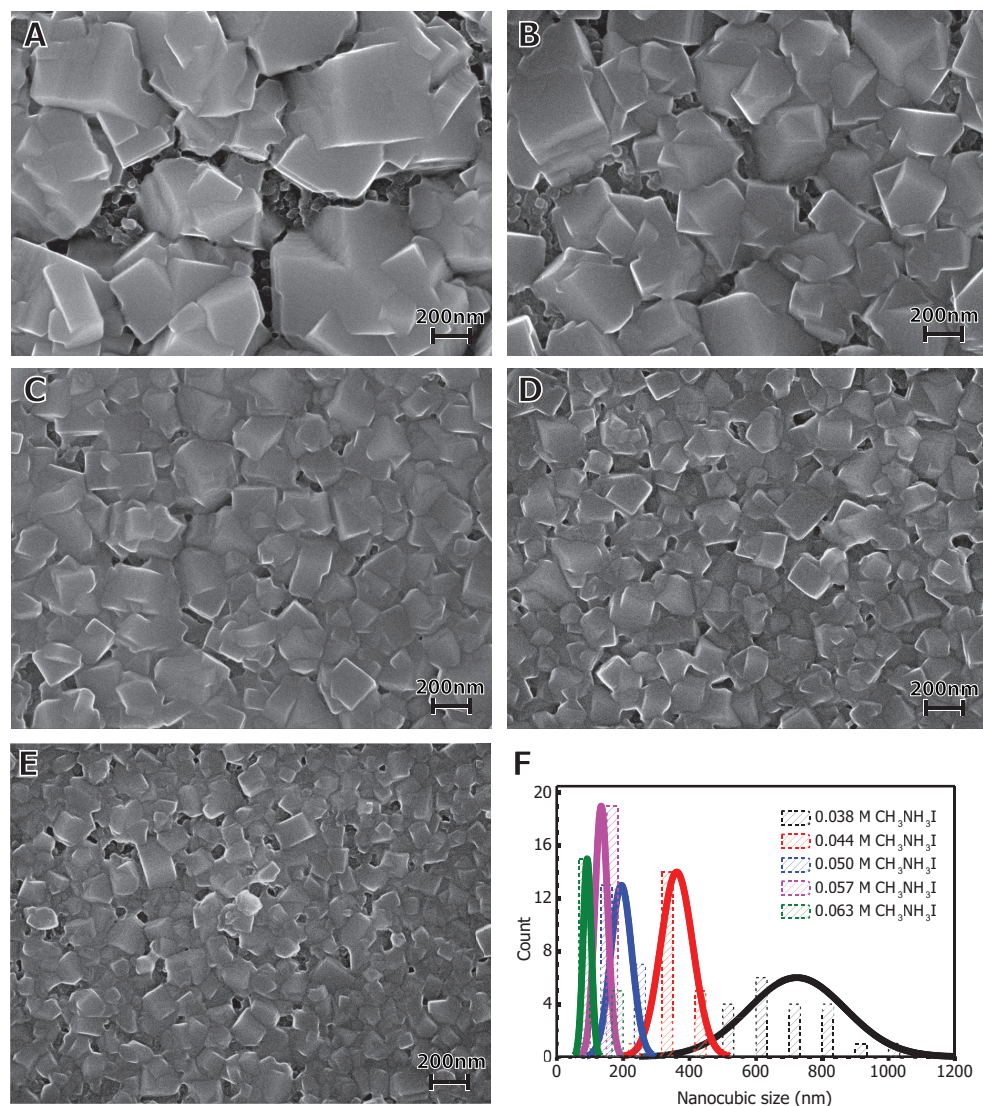


**Figure 2.7:** (a-e) Top-view scanning electron micrographs showing microcomposites of  $\text{CH}_3\text{NH}_3\text{PbI}_3$  deposited onto mesoporous  $\text{TiO}_2$  films, grown using the sequential deposition. The concentration of  $\text{CH}_3\text{NH}_3\text{I}$  in the dipping solution was (a) 0.038 M, (b) 0.044 M, (c) 0.050 M, (d) 0.057 M, (e) 0.063 M. (f) Histogram of  $\text{CH}_3\text{NH}_3\text{PbI}_3$  crystallite size for all five different concentrations. The solid curve represent the fit to a normal distribution.

### 2.6.2 Influence over the light harvesting

We measured the single-pass light harvesting efficiency of the as-grown  $\text{CH}_3\text{NH}_3\text{PbI}_3$  films on  $\text{TiO}_2$  mesoporous layers similar to the ones used in solar cells for films converted with various  $\text{CH}_3\text{NH}_3\text{I}$  concentrations. The results are shown in figure 2.8a. Results show that samples with larger crystals (converted with lower concentrations: 0.032 M and 0.038 M) have flatter LHE spectra over the visible range when compared with the ones with smaller crystals, which correlates well with an increased of the crystal thickness. However, the spacing between the crystals reduces the overall light harvesting efficiency irrespective of the wavelength. For crystals obtained at higher  $\text{CH}_3\text{NH}_3\text{I}$  concentrations (0.044 M-0.063 M), thinner, less scattering crystals form a highly covered film which enhances the absorption of blue photons but decreases the absorption of red photons, according to the absorption spectrum of  $\text{CH}_3\text{NH}_3\text{PbI}_3$ . The data in figure 2.8a shows that, with regards to light absorption, the optimal crystal size is obtained using the 0.038 M or 0.044 M solutions of  $\text{CH}_3\text{NH}_3\text{I}$  in 2-propanol.

### 2.6.3 Influence over the hole transport

We expect that larger crystals can come at the expense of the collection efficiency if the crystal thickness is in the similar order of magnitude as the diffusion length. We carried out qualitative measurements of the rate of the charge transport using charge extraction by linearly increasing the voltage under illumination (photo-CELIV)[132], which has the merit of measuring the overall extraction ability of the whole cell rather than the mobility of a single carrier in a pristine material. We performed photo-CELIV measurements in ambient air over FTO/b- $\text{Al}_2\text{O}_3$ /TiO<sub>2</sub>/ $\text{CH}_3\text{NH}_3\text{PbI}_3$ /spiro-MeOTAD/Au assemblies, where a blocking  $\text{Al}_2\text{O}_3$  underlayer (b- $\text{Al}_2\text{O}_3$ ) on a fluorine-doped tin oxide (FTO) was used to prevent electron collection and selectively collect the holes at the back contact. The photo-CELIV transients are shown in figure 2.8b. We found a qualitative correlation between the crystal size and the rate of collection, as seen by the CELIV transient time, where smaller crystals seem to collect holes significantly faster than the large ones. This can be related to either a higher mobility or simply to the use of thinner crystals<sup>3</sup>. However, the CELIV measurement presented in figure 2.8 are properly normalized, such that the area under the curve amounts to the total quantity of photo-generated carriers remaining after the delay time that precedes the charge extraction. The highest amount of collected charges was obtained for the film grown using the 0.044 M  $\text{CH}_3\text{NH}_3\text{I}$  solution. With the other concentrations, the amount of extracted charges was lower, either due to a decreased light harvesting or to faster recombination, which is also responsible for the broadening of the CELIV signal. We made sure that the generated current never exceeded 20% of the displacement current. Space-charge effects were considered minimal in this regime.

---

<sup>3</sup>In the absence of a perfectly conformal film, the normalization by the film thickness is rather difficult. This is the reason why no quantitative values on the mobility are reported here

## 2.6. Optimization of the crystal size

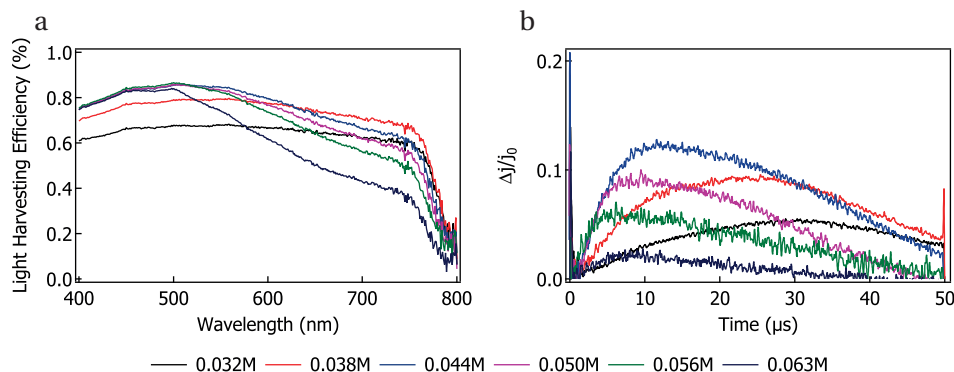


**Figure 2.8:** (a) Light harvesting efficiency spectra of TiO<sub>2</sub>/CH<sub>3</sub>NH<sub>3</sub>PbI<sub>3</sub> films prepared by sequential deposition using solutions various CH<sub>3</sub>NH<sub>3</sub>I concentrations (b) Photo-CELIV transients recorded for devices comprising FTO/bl-Al<sub>2</sub>O<sub>3</sub>/mp-TiO<sub>2</sub>/CH<sub>3</sub>NH<sub>3</sub>PbI<sub>3</sub>/Spiro-MeOTAD/Au depending using various CH<sub>3</sub>NH<sub>3</sub>I concentrations.  $j$ : current;  $\delta j$ : extraction current,  $j_0$ : capacitive displacement current.

CH <sub>3</sub> NH <sub>3</sub> I conc. (M)	V <sub>oc</sub> (V)	J <sub>sc</sub> (mA cm <sup>-2</sup> )	FF (-)	PCE (%)
0.038	1.065 ± 0.009	21.68 ± 0.63	0.709 ± 0.006	16.63 ± 0.35%
0.050	1.090 ± 0.009	21.01 ± 0.37	0.711 ± 0.017	16.27 ± 0.44%
0.064	1.080 ± 0.005	19.27 ± 0.55	0.646 ± 0.012	13.45 ± 0.55%

**Table 2.3:** Photovoltaic performance of perovskite solar cells prepared using the sequential deposition, for various concentrations of CH<sub>3</sub>NH<sub>3</sub>I in the dipping 2-propanol solution.

### 2.6.4 Influence over the photovoltaic performance

Based on the light harvesting efficiency and the dynamics of the charge collection, it is not a surprise that the best performing photovoltaic devices were assembled using an intermediate concentration. The photovoltaic data for perovskite devices assembled using 0.038 M, 0.050 M and 0.064 M is presented in table 2.3. We observe that the short circuit current follows the predictions from the light harvesting efficiency measurement (the highest current is obtained using the 0.038 M solution). In addition, the open-circuit voltage seems to correlate well with the photo-CELIV measurements, where the highest voltage was obtained using the 0.050 M solution, which we think is the sweet spot where charge transport and recombination is optimal.

Using the approach of growing a carefully tailored CH<sub>3</sub>NH<sub>3</sub>PbI<sub>3</sub> capping layer, a record power conversion efficiency of 17% was reported ( $J_{sc} = 21.64 \text{ mA cm}^{-2}$ ,  $V_{oc} = 1.056 \text{ V}$ ,  $FF = 0.741$ ), which is a significant improvement over the initial breaking record of 15% (which was also obtained using a CH<sub>3</sub>NH<sub>3</sub>PbI<sub>3</sub> capping layer) and the average 12.0% power conversion efficiency obtained without the capping layer.

## **2.7 Conclusion and outlook**

The sequential-deposition method for the fabrication of perovskite-sensitized mesoscopic solar cells introduced here provides a means to achieve excellent photovoltaic performance with high reproducibility. The power conversion efficiency of 15% and subsequently of 17% achieved with the best device were amongst the highest for solution-processed photovoltaics and set a new record for organic or hybrid inorganic–organic solar cells at the time of their finding. Our investigations opened new routes for the fabrication of perovskite-based photovoltaic devices, and other preformed mesostructured metal halides have been converted into the desired perovskite by the simple insertion reaction detailed here.

## 3 Mixed organic cation perovskite solar cells

*In this chapter, we describe the use of mixed cations  $\text{CH}_3\text{NH}_3\text{I}$  -  $\text{H}_2\text{N}=\text{CHNH}_3\text{I}$  to extend slightly the band gap of the absorbing perovskite layer. This work is partly derived from a published article in a peer-reviewed journal[99]. At the time of compiling this thesis, most hybrid perovskite compositions still use a mixture of  $\text{CH}_3\text{NH}_3\text{I}$  and  $\text{H}_2\text{N}=\text{CHNH}_3\text{I}$ .*

### 3.1 Motivation

An important target to further improve the performance of perovskite based photovoltaics is to extend their optical absorption onset further into the infrared to enhance solar light harvesting. The optical band gap of  $\text{CH}_3\text{NH}_3\text{PbI}_3$  is slightly wider than the optimal one determined by Schockley and Queisser[133]. For Sn-based perovskites, there is an established correlation between the size of the organic cation in the A site of the  $\text{ABX}_3$  structure and variations of the optical band gap of the perovskite[134]. It is the consequence of the induced tilt of the I-Pb-I bond and the consequent deformation of the  $\text{PbI}_6^{2-}$  octahedron, which alters the electronic band structure of the perovskite absorber. In theory, a 1.5 eV band gap semiconductor can deliver photocurrents up to  $27 \text{ mA cm}^{-2}$  under the standard air mass 1.5 global solar spectrum. This motivates efforts at reducing, even slightly, the optical band gap through structural modifications. However, most organic cations aside from methylammonium and formamidinium are too large to form 3D perovskites and usually arrange into layered structure with much wider band gaps[112]. In this chapter, we show that small band gap reductions can be achieved by using a mixture of formamidinium ( $\text{H}_2\text{N}=\text{CHNH}_3\text{I}$ ) and methylammonium ( $\text{CH}_3\text{NH}_3\text{I}$ ) cations in the A position of the  $\text{APbI}_3$  perovskite structure, leading to an enhancement of short circuit current. The power conversion efficiency of mixed cation PSCs surpass neat  $\text{CH}_3\text{NH}_3^+$  based devices. This is the first time that this concept is applied in perovskite based solar cells. It emerges as a versatile tool to tune the structural, electrical and optoelectronic properties of the light harvester.

### 3.2 Introduction

Hybrid organic–inorganic perovskites employ a variety of organic cation[52, 18, 19, 9, 10, 135, 26, 29]. It has been demonstrated that the size of the organic ammonium cation influences the optical band gap of the perovskite by affecting the M-I-M (M = Sn, Pb) angle[134] or forming insulating barriers between semiconducting  $\text{PbI}_4$  layers[134]. In the latter case, bigger cations usually lead to two-dimensional (2D) perovskite where the  $\text{PbI}_6^{4-}$  octahedra are edge-sharing. 2D iodoplumbate and iodostannate perovskites usually show wider band gaps[8, 136], making them unsuitable for panchromatic absorption of the visible solar spectrum. A variety of organic cations have been shown to affect the band gap by as much as 1 eV in iodostannate perovskites[8]. Theoretically, methylammonium ( $\text{CH}_3\text{NH}_3^+$ ,  $\text{MA}^+$ ) and formamidinium ( $\text{HN}=\text{CHNH}_3^+$ ,  $\text{FA}^+$ ) are sufficiently small cations to form the 3D perovskite, while ethylammonium ( $\text{CH}_3\text{CH}_2\text{NH}_3^+$ ) is known to already form a 2D perovskite[115].  $\text{FASnI}_3$  had previously been described by Mitzi[26], while its Pb analogue had only been recently investigated by Kanatzidis at the time of those findings[34], who reported a significant red-shift of the optical absorption compared to  $\text{CH}_3\text{NH}_3\text{PbI}_3$ . We reasoned that formamidinium offers the potential to lower the band gap of the commonly used  $\text{CH}_3\text{NH}_3\text{PbI}_3$  perovskite to a value of 1.4 eV[133], which is optimal for conversion of standard AM 1.5 sunlight to electricity. We achieved band-gap tuning of  $\text{CH}_3\text{NH}_3\text{PbI}_3$  by the gradual substitution of MA with FA cations and monitored the shift in the optical response. Earlier work on mixed cation perovskites focused on their electronic properties. Thus, Mitzi described a semiconductor-to-metal transition within the series of  $\text{CH}(\text{NH}_2)_2(\text{CH}_3\text{NH}_3)_n\text{Sn}_n\text{I}_{3n+2}$ [135, 14] as  $n$  increases. Mixed cations in three dimensional perovskites have also been prepared in tin halide perovskites, i.e.  $(\text{CH}(\text{NH}_2)_2)_{0.5}(\text{CH}_3\text{NH}_3)_{0.5}\text{SnI}_3$ [20] but their optical or photovoltaic properties were not investigated. In order to tune the band gap of metal halide perovskites, investigations have so far focused on mixing halide anions, e.g. Br/I[136, 94] or Cl/I[118, 10] rather than the cations.

### 3.3 Mixed methylammonium-formamidinium hybrid perovskites

This chapter reports on the use of 3D perovskite of composition  $(\text{MA})_x(\text{FA})_{1-x}\text{PbI}_3$  ( $x = 0$  to 1) as light harvesting material for mesoscopic solar cells. The previously reported sequential deposition method[47] (chapter 2) was used as an effective tool to generate  $(\text{MA})_x(\text{FA})_{1-x}\text{PbI}_3/\text{TiO}_2$  nanocomposites, containing both methylammonium and formamidinium cations in well-defined proportions. We characterize the perovskite films by powder X-Ray diffraction, AC electrical conductivity, absorption and emission spectroscopy and photoluminescence decay. We test fully functional PV devices employing 2,2',7,7'-tetrakis(N, N-di-p-methoxyphenylamine)-9,9'-spirobifluorene (Spiro-MeOTAD) as the hole transporting material (HTM)[131] and a mesoscopic  $\text{TiO}_2$  scaffold (m- $\text{TiO}_2$ ) as a host for the nanostructured perovskite and a compact  $\text{TiO}_2$  film (b- $\text{TiO}_2$ ) as a hole blocking layer. The results show important gains in PV performance from using mixed FA/MA cations based lead iodide perovskite as light harvesters.



### 3.3. Mixed methylammonium-formamidinium hybrid perovskites

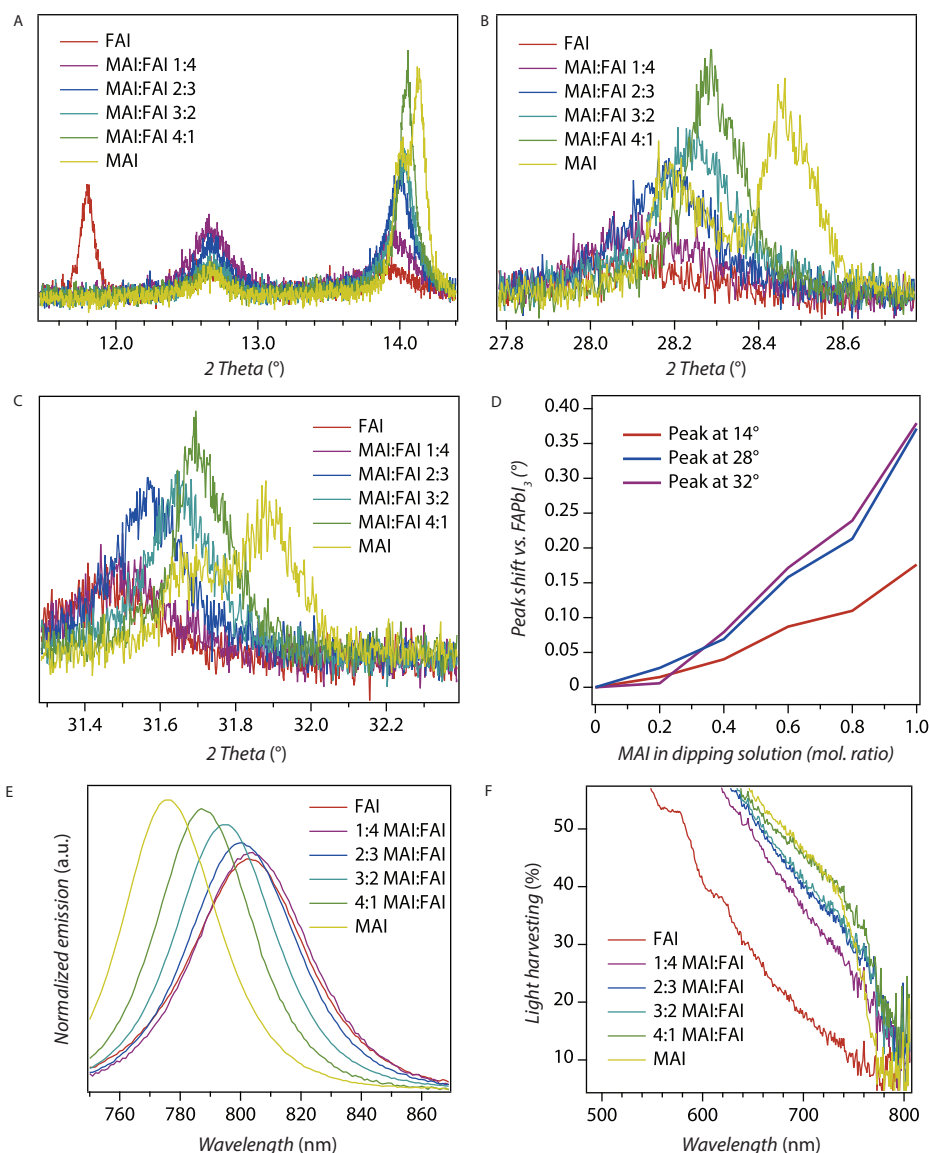


**Figure 3.1:** (a) X-Ray diffraction pattern of the  $(\text{CH}_3\text{NH}_3)_x(\text{HNCHNH}_3)_{1-x}\text{PbI}_3$  thin film perovskite grown by the two-step sequential deposition. The substrate was FTO-coated glass on which a typical 300 nm mesoporous  $\text{TiO}_2$  scaffold has been deposited. Zoom over the  $11^\circ$  to  $14^\circ$  region. The peak at  $14.0^\circ$  shifts to lower reflection angles with FAI intercalation. Remaining  $\text{PbI}_2$  is identified at  $12.8^\circ$ . The peak at  $11.8^\circ$  is assigned to the non-perovskite  $\delta$  phase of formamidinium. A similar effect is seen in the (b)  $31.8^\circ$  peak and (c)  $28.4^\circ$  peak. (d) Summarized peak shift compared to  $\text{CH}(\text{NH}_2)_2\text{PbI}_3$ . Peaks at  $14^\circ$ ,  $28.4^\circ$  and  $31.8^\circ$  are considered. (e) Normalized emission of  $(\text{CH}_3\text{NH}_3)_x(\text{HNCHNH}_3)_{1-x}\text{PbI}_3$  ( $x = 0, 0.2, 0.4, 0.6, 0.8, 1$ ) The emission is shifted further into the red and broadened as  $x$  is decreased. (f) Light harvesting spectra of the different perovskite films taken in an integrating sphere. Note the 20 nm red shift of the absorbance onset for  $(\text{CH}_3\text{NH}_3)_{0.8}(\text{HNCHNH}_3)_{0.2}\text{PbI}_3$  compared to  $\text{CH}_3\text{NH}_3\text{PbI}_3$ . As the formamidinium concentration is increased, the absorbance of the film decreases while no change in the band gap is discernible.

### 3.4 XRD characterization

We conducted powder XRD measurements to investigate the simultaneous intercalation of MA and FA cations. Transparent conducting FTO glass was covered by a thin compact blocking layer of  $\text{TiO}_2$  (b- $\text{TiO}_2$ ) onto which a ca. 300 nm thick mesoscopic  $\text{TiO}_2$  was deposited (m- $\text{TiO}_2$ ). The latter was infiltrated with  $\text{PbI}_2$  by spin coating, which was converted to the mixed cation perovskite  $(\text{MA})_x(\text{FA})_{1-x}\text{PbI}_3$  upon exposing it to a solution of FAI and MAI cations in isopropanol. Results are shown in figure 3.1.

Changes are observed for peaks  $14.1^\circ$  (zoom fig 3.1c),  $20.0^\circ$ ,  $24.4^\circ$ ,  $28.4^\circ$  (zoom Fig 3.1a),  $31.8^\circ$  (zoom Fig 3.1b),  $40.6^\circ$ ,  $43^\circ$ , whose diffraction angles decrease with increasing formamidinium content. This is in keeping with the bigger size of the formamidinium cation expanding the crystal lattice. Figure 3.1d shows the peak shift with respect to the reference  $\alpha$ - $\text{CH}(\text{NH}_2)_2\text{PbI}_3$  peak at  $13.8^\circ$ . Full XRD patterns are shown in figure 3.2. The gradual shift in diffraction angle (that is, not two separate peaks of variable intensities) is a strong indication that a mixed phase of  $\text{MA}_x\text{FA}_{1-x}\text{PbI}_3$  is formed where the two cations are both inserted in the same lattice frame.

Additional reflections specific to  $\text{CH}(\text{NH}_2)_2\text{PbI}_3$  appear at  $11.8^\circ$ ,  $16.25^\circ$ ,  $30.54^\circ$ ,  $32.8^\circ$  and  $41.63^\circ$  and were assigned by measuring spin-coated reference samples produced by a one-step deposition of  $\text{MA}_x\text{FA}_{1-x}\text{PbI}_3$  from N,N-dimethylformamide (figure 3.2b and c). All those features were also present in pure  $\text{CH}(\text{NH}_2)_2\text{PbI}_3$  deposited this way, and are attributed to the yellow  $\delta$ -phase of  $\text{CH}(\text{NH}_2)_2\text{PbI}_3$ [34]. However, the perovskite  $\alpha$ - $\text{CH}(\text{NH}_2)_2\text{PbI}_3$  phase was not produced in this manner as is evident from the lack of a peak at  $14^\circ$ , and even subsequent annealing failed to induce any phase transition  $\delta \rightarrow \alpha$ . The  $\delta$ - $\text{CH}(\text{NH}_2)_2\text{PbI}_3$  gradually disappears as the  $\text{CH}_3\text{NH}_3\text{I}$  concentration is increased. Strikingly, the desired black  $\alpha$ - $\text{CH}(\text{NH}_2)_2\text{PbI}_3$  perovskite phase was formed immediately in substantial proportion relative to  $\delta$ - $\text{CH}(\text{NH}_2)_2\text{PbI}_3$  when the sequential deposition method was applied. In addition, the  $\alpha$ -phase is formed quantitatively already at a  $\text{CH}_3\text{NH}_3\text{I}$  molar ratio as low as 0.2 in the 2-propanol dipping solution, as confirmed by the lack of a diffraction peak at  $11.8^\circ$ . We note here yet another key advantage of the two-step over the single-step perovskite deposition method as it directs the perovskite crystallization to the desired  $\alpha$ -phase upon exposing the  $\text{PbI}_2$  to the  $\text{CH}_3\text{NH}_3\text{I}/\text{H}_2\text{N}=\text{CHNH}_3\text{I}$  mixture in isopropanol.

### 3.5 AC impedance spectroscopy

Since  $\text{CH}_3\text{NH}_3\text{PbI}_3$  displays mixed electronic-ionic conduction[63] we performed impedance analysis to probe the ionic transport in the neat and mixed cation perovskites. A.C. impedance data acquired from all compositions considered here are characterized by a single semicircle (Figure 3.3a) whose capacitance corresponds to the bulk properties of the material (relative dielectric constant  $\epsilon_R \sim 30$ ). A.C. measurements performed at temperature ranging between 30 and  $70^\circ\text{C}$  allow for the determination of the activation energy  $E_a$  of the different samples. Remarkably, as shown in Figure 3.3b, the value of  $E_a$  of the two-phase mixtures (e.g. 0.53 eV for MAI:FAI 2:3 as well as MAI:FAI 3:2) is very close to the activation energy of the FAI single phase

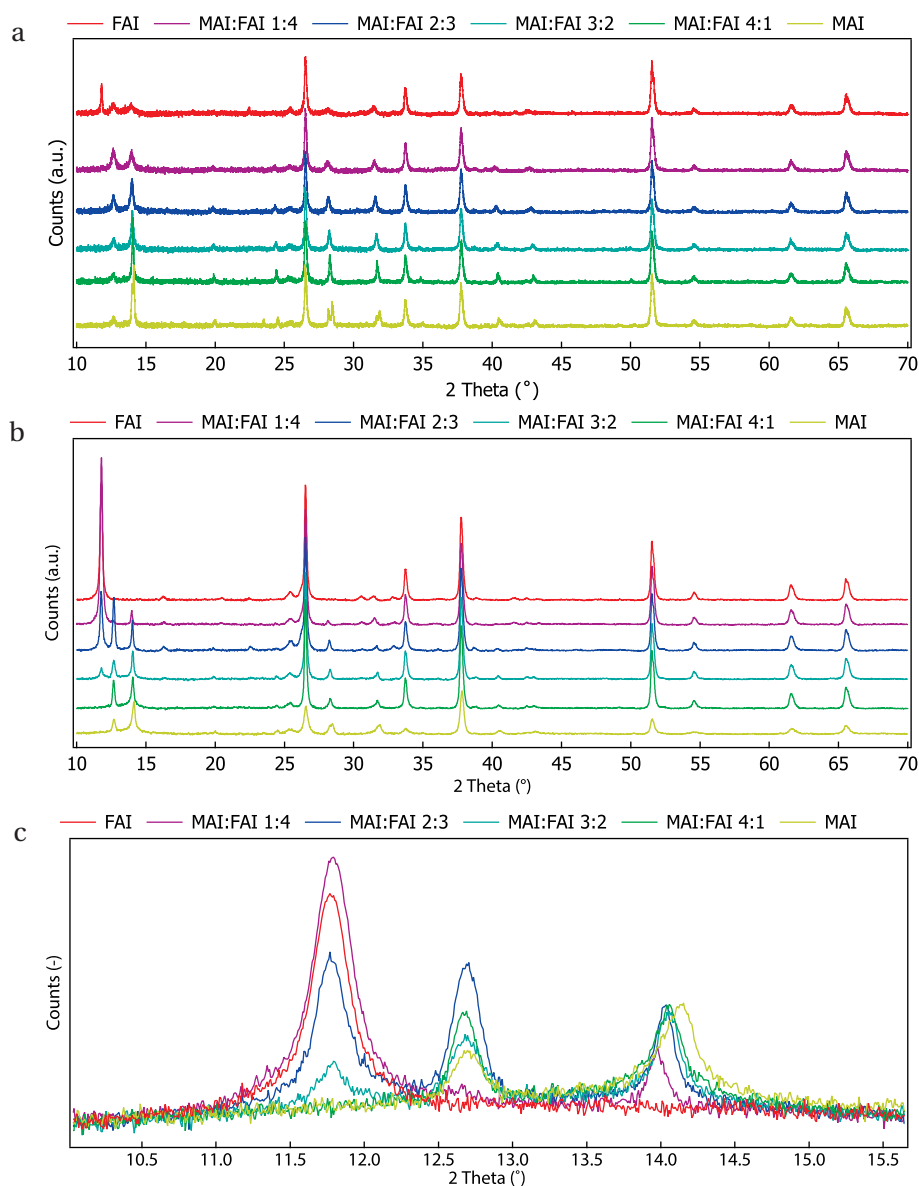


**Figure 3.2:** (a) X-Ray diffraction patterns of mesoporous  $\text{TiO}_2$  films infiltrated with  $\text{MA}_x\text{FA}_{1-x}\text{PbI}_3$  ( $x = 0$  to  $1$ ).  $\text{PbI}_2$  was deposited from a 1.2 M solution in N,N-dimethylformamide for 10 seconds at 6500 r.p.m. After drying at  $80^\circ\text{C}$  for about one hour, the samples were cooled down to room temperature (about  $25^\circ\text{C}$ ) and dipped into a dilute solution of  $\text{CH}_3\text{NH}_3\text{I} / \text{H}_2\text{N}=\text{CHNH}_3\text{I}$  or a mixture thereof in isopropanol where the iodide concentration was  $0.062 \text{ mol g}^{-1}$  2-propanol. The films were dried at  $80^\circ\text{C}$  for one hour before the measurement. (b) X-Ray diffraction pattern of mesoporous  $\text{TiO}_2$  films infiltrated with  $\text{MA}_x\text{FA}_{1-x}\text{PbI}_3$  ( $x = 0$  to  $1$ ). The precursors were mixed in a 20% wt. N,N-dimethylformamide solution and spin-coated over the film before annealing at  $120^\circ\text{C}$  for 10 minutes. (c) Zoom over the  $10\text{-}14^\circ$  region of (b)

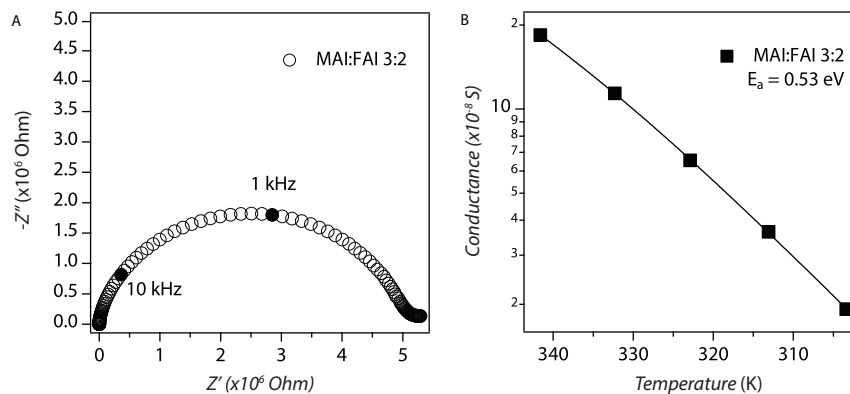


**Figure 3.3:** (a) A.C. conductivity of  $\text{MA}_{0.6}\text{FA}_{0.4}\text{PbI}_3$  measured under argon at 70 °C. (b) Arrhenius plot of the conductance as a function of the temperature for  $\text{MA}_{0.6}\text{FA}_{0.4}\text{PbI}_3$ .

(0.55 eV) rather than the MAI single phase (0.40 eV), suggesting that the electrical conduction properties are dominated by the FAI phase.

### 3.6 Optical absorption

Figure 3.1f shows UV-Vis absorption spectra of the mixed cation lead iodide perovskites  $\text{MA}_x\text{FA}_{1-x}\text{PbI}_3$  for various compositions. Adding only 20 mol %  $\text{H}_2\text{N}=\text{CHNH}_3\text{I}$  in the dipping solution causes the absorption onset of the perovskite to red shift by 20 nm, while maintaining the desired steepness of the absorption edge characteristic of  $\text{CH}_3\text{NH}_3\text{I}$ . As the  $\text{H}_2\text{N}=\text{CHNH}_3\text{I}$  concentration is further increased, the absorbance onset is shifted to longer wavelengths while the absorbance of the film is reduced. Using a ratio of  $\text{CH}_3\text{NH}_3\text{I}:\text{H}_2\text{N}=\text{CHNH}_3\text{I}$  at 4:1 or 3:2 in the isopropanol solution proved to be optimal extending the light absorption of the perovskite into the red while retaining the high absorption coefficient of  $\text{CH}_3\text{NH}_3\text{PbI}_3$ . Note that  $\text{CH}_3\text{NH}_3\text{PbI}_3$  scatters light more strongly than  $\text{CH}(\text{NH}_2)_2\text{PbI}_3$ , as is apparent from the tailing of the absorbance beyond the band gap. This is likely to arise from the smaller size of  $\text{CH}(\text{NH}_2)_2\text{PbI}_3$  crystals compared to their methylammonium counterparts.

### 3.7 Photoluminescence

The normalized near IR photoluminescence (PL) of the  $\text{MA}_x\text{FA}_{1-x}\text{PbI}_3$  ( $x = 0$  to 1) films are shown in Figure 3.1e. A significant 27 nm red-shift in the emission peak from  $\text{CH}_3\text{NH}_3\text{PbI}_3$  ( $\lambda_{max} = 776$  nm) to  $\text{CH}(\text{NH}_2)_2\text{PbI}_3$  ( $\lambda_{max} = 803$  nm) is observed - consistent with the absorption spectrum - along with a noticeable broadening of the emission profile. The gradual shift in emission indicates the formation of a solid solution of  $\text{CH}_3\text{NH}_3^+$  and  $\text{CH}(\text{NH}_2)_2^+$  in the perovskite lattice. The shifts in emission of samples prepared by sequential deposition match the ones observed by the single-step deposition (except for the pure  $\text{CH}(\text{NH}_2)_2\text{PbI}_3$ , which has no  $\alpha$ -phase and a strongly blue-shifted emission when prepared by the one-step deposition),

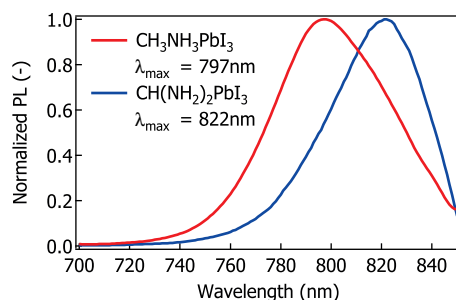


**Figure 3.4:** Photoluminescence spectra of single crystals of (red)  $\text{CH}_3\text{NH}_3\text{PbI}_3$  and (blue)  $\text{CH}(\text{NH}_2)_2\text{PbI}_3$  grown by inverse solubility[137]

suggesting that the intercalated ratio of cations is similar as that of the dissolved cations in the precursor solution. We found that for  $\text{CH}_3\text{NH}_3^+$  rich perovskites compositions, small additions of  $\text{CH}(\text{NH}_2)_2^+$  shift the optical significantly to the red (between 0% and 20%  $\text{CH}(\text{NH}_2)_2^+$ , the band gap shifts by  $\sim 53$  meV). On the contrary, in  $\text{CH}(\text{NH}_2)_2^+$  rich perovskite compositions, the optical band gap is almost independent on the substitution by methylammonium (between 0% and 20%  $\text{CH}_3\text{NH}_3^+$ , the band gap shifts by  $\sim 1 - 2$  nm only). In other words, mixed cation perovskites have a stronger tendency to adopt the  $\text{CH}(\text{NH}_2)_2\text{PbI}_3$  structure than the  $\text{CH}_3\text{NH}_3\text{PbI}_3$  structure (at least in terms of optical transition) and, with regards to the benefits of an extended absorption spectrum, remain competitive with pure  $\text{CH}(\text{NH}_2)_2\text{PbI}_3$ . PL measurements of films prepared by the one-step deposition were complicated by the appearance of the yellow  $\delta$ -phase of the formamidinium iodide[34], which does not manifest itself optically in the  $\text{CH}(\text{NH}_2)_2\text{PbI}_3$  samples prepared by sequential deposition.

To verify that the shift in photoluminescence is a consequence of the material property and not the dielectric interaction between the  $\text{TiO}_2$ -coated film and the perovskite structure, we measured the photoluminescence of  $\text{CH}_3\text{NH}_3\text{PbI}_3$  and  $\text{CH}(\text{NH}_2)_2\text{PbI}_3$  single crystals grown by inverse solubility[137]. In  $\text{CH}(\text{NH}_2)_2\text{PbI}_3$ , the maximum of the PL emission is red-shifted by 25 nm ( $\lambda_{max} = 797$  nm) compared to  $\text{CH}_3\text{NH}_3\text{PbI}_3$  ( $\lambda_{max} = 822$  nm) (figure 3.4), in good correspondence with the values measured on films. We take note that overall both PL peaks are shifted by around 20 nm into the infrared. This observation will be commented in chapter 4.

### 3.8 Device performance

We measured the current (J) - voltage (V) characteristics of the solar cells in the dark and under a simulated air mass 1.5 global standard sunlight. To avoid batch-to-batch variations of photocurrents, cells from the same batch were compared and the  $\text{PbI}_2$ -coated  $\text{TiO}_2$  films were selected at random before dipping in the  $\text{RNH}_3\text{I}$  (R:  $\text{CH}_3^-$  and/or  $\text{NHCH}^-$ ) solutions. In this manner, clear trends in short circuit current densities were reproducibly achieved. The

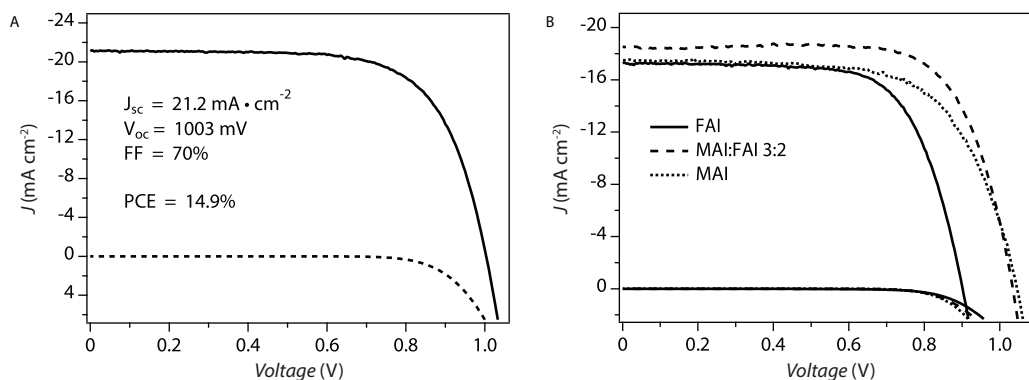


**Figure 3.5:** (a)  $j(V)$  curves of the best performing cell sensitized with  $(\text{CH}_3\text{NH}_3)_0.6(\text{HN}=\text{CHNH}_3)_0.4\text{PbI}_3$  measured under a simulated AM1.5G solar spectrum at  $98.2\text{ mW cm}^{-2}$  (red line) and in the dark (blue line). (b)  $j(V)$  curves for average photovoltaic devices assembled with  $(\text{CH}_3\text{NH}_3)_x(\text{HNCHNH}_3)_{1-x}\text{PbI}_3$  ( $x = 0, 0.6, 1$ ) as the sensitizer. The cells were measured in the dark and under a simulated AM1.5G spectrum at  $98.89\text{ mW cm}^{-2}$ ,  $98.16\text{ mW cm}^{-2}$  and  $98.50\text{ mW cm}^{-2}$  for  $x = 1, 0.6$  and  $0$ , respectively.

dotted trace in Figure 3.5b shows a  $j(V)$  curve for a typical device based on pure  $\text{CH}_3\text{NH}_3\text{PbI}_3$ , from which the short-circuit current density ( $J_{\text{sc}}$ ), open-circuit potential ( $V_{\text{oc}}$ ), fill factor (FF) and power conversion efficiency (PCE) were determined to be  $17.83\text{ mA cm}^{-2}$ ,  $1046\text{ mV}$ ,  $0.655$  and  $12.5\%$  respectively. On average, the devices showed a short-circuit current density of  $17.3\text{ mA cm}^{-2}$  and a PCE of  $12.0\%$ , in excellent agreement with our previously published results[47]. The solid trace in figure 3.5b shows a  $j(V)$  curve obtained from pure formamidinium lead iodide ( $\text{CH}(\text{NH}_2)_2\text{PbI}_3$ ) with  $J_{\text{sc}} = 16.6\text{ mA cm}^{-2}$ ,  $V_{\text{oc}} = 928\text{ mV}$ ,  $\text{FF} = 0.66$  and  $\text{PCE} = 10.5\%$ . The best  $\text{CH}(\text{NH}_2)_2\text{PbI}_3$  based device gave a PCE of  $11.0\%$ , clearly below the average PCE obtained with  $\text{CH}_3\text{NH}_3\text{PbI}_3$ . We tested four different mixed cation perovskite  $(\text{MA})_x(\text{FA})_{1-x}\text{PbI}_3$  of the composition  $x = 0.2, 0.4, 0.6$  and  $0.8$ . Among those,  $\text{MA}_{0.6}\text{FA}_{0.4}\text{PbI}_3$  performed best. The dashed trace in Figure 3.5b shows the  $j(V)$  characteristics of a typical cell, with a  $V_{\text{oc}}$  of  $1027\text{ mV}$ , a  $J_{\text{sc}}$  of  $18.15\text{ mA cm}^{-2}$ , a FF of  $0.715$  and a PCE of  $13.4\%$ . Strikingly,  $\text{MA}_{0.6}\text{FA}_{0.4}\text{PbI}_3$  outperforms the single cation compositions  $\text{CH}_3\text{NH}_3\text{PbI}_3$  and  $\text{CH}(\text{NH}_2)_2\text{PbI}_3$ . Figure 3.5a shows the  $j(V)$  characteristics of the best device, exhibiting a  $J_{\text{sc}}$  of  $21.2\text{ mA cm}^{-2}$ , a  $V_{\text{oc}}$  of  $1.003\text{ V}$  and a FF of  $0.70$  for an overall power conversion efficiency of  $14.9\%$ . In Table 3.1 we report the PV characteristics of a series of other cells sensitized by  $\text{MA}_{0.6}\text{FA}_{0.4}\text{PbI}_3$ .

### 3.9 Light harvesting and internal quantum efficiency

To rationalize the substantial gains in photocurrent observed for the mesoscopic cells based on mixed-cation perovskite light harvesters, we measured their incident photon to current conversion efficiency (IPCE), or external quantum efficiency (EQE), across the visible spectrum. Figure 3.6b shows that the photocurrent onset is shifted by  $20\text{ nm}$  from  $780\text{ nm}$  to  $800\text{ nm}$  to the red for  $\text{CH}(\text{NH}_2)_2\text{PbI}_3$  and  $\text{MA}_{0.6}\text{FA}_{0.4}\text{PbI}_3$  in accordance with the absorbance spectra

### 3.9. Light harvesting and internal quantum efficiency

Cell n°	$V_{oc}$ (mV)	$J_{sc}$ (mA cm <sup>-2</sup> )	FF	Efficiency
1	1025	18.86	0.692	13.71%
1	1033	18.89	0.722	14.52%
1	1033	17.82	0.673	12.93%
1	1039	18.34	0.697	13.57%
1	931	19.87	0.660	12.45%
1	936	19.62	0.696	13.19%
1	951	19.31	0.707	13.39%
<b>Average</b>	$992 \pm 46$	$18.957 \pm 0.66$	$0.692 \pm 0.019$	$13.4\% \pm 0.6\%$

**Table 3.1:** Photovoltaic properties of 8 devices sensitized by MA<sub>0.6</sub>FA<sub>0.4</sub>PbI<sub>3</sub> using either 0.062 M I<sup>-</sup> (first four devices) or 0.050 M I<sup>-</sup> (last three devices) in the dipping bath.

shown in Figure 3.1f. The IPCE spectrum of the MA<sub>0.6</sub>FA<sub>0.4</sub>PbI<sub>3</sub> combines the advantage of a red shifted onset observed for CH(NH<sub>2</sub>)<sub>2</sub>PbI<sub>3</sub> with the steep IPCE rise at the band gap characteristic for CH<sub>3</sub>NH<sub>3</sub>PbI<sub>3</sub>. IPCE values attained with the MA<sub>0.6</sub>FA<sub>0.4</sub>PbI<sub>3</sub> exceed the levels of the two single cation perovskites across the whole visible range attaining close to 90% at 500 nm. Integration of the IPCE spectra (340 nm - 850 nm) over the air mass 1.5 global (AM1.5G) solar emission yielded the short circuit photocurrent densities of 17.0 mA cm<sup>-2</sup>, 16.0 mA cm<sup>-2</sup> and 20.2 mA cm<sup>-2</sup> for CH<sub>3</sub>NH<sub>3</sub>PbI<sub>3</sub>, CH(NH<sub>2</sub>)<sub>2</sub>PbI<sub>3</sub>, and MA<sub>0.6</sub>FA<sub>0.4</sub>PbI<sub>3</sub>, respectively. Figure 3.6a shows the absorptance spectrum for the 3 devices measured with an integrating sphere. For this analysis we removed the gold back contact and cut the films to preserve the active area alone. For wavelengths between 320 nm to 520 nm, the films harvest more than 93% of the incident photons. The remaining few percent are transmitted or lost either by specular reflectance or parasitic absorbance by the FTO. Above 520 nm, the light harvesting efficiency of the films decreases gradually dropping sharply to zero near the band gap of the perovskite. CH(NH<sub>2</sub>)<sub>2</sub>PbI<sub>3</sub> shows the fastest drop in absorbance (red trace) with increasing wavelength and CH<sub>3</sub>NH<sub>3</sub>PbI<sub>3</sub> the slowest (yellow trace), while the mixed cations perovskite (blue trace) lies in-between. A slight red-shift in the band gap is observed from the onset of the absorption, i.e. 787 nm (1.575 eV) for CH<sub>3</sub>NH<sub>3</sub>PbI<sub>3</sub> and 810 nm (1.530 eV) for CH(NH<sub>2</sub>)<sub>2</sub>PbI<sub>3</sub>. Interestingly, MA<sub>0.6</sub>FA<sub>0.4</sub>PbI<sub>3</sub> shows the same band gap as CH(NH<sub>2</sub>)<sub>2</sub>PbI<sub>3</sub>, contrary to our initial expectations. To account for the reflection of the gold counter-electrode, we corrected the absorptance of the films making the following assumptions: (a) the counter-electrode is described by the optical parameters n and k of gold[138], transmission being neglected and a flat interface being assumed, (b) the perovskite film behaves as a Beer-Lambert medium, (c) the parasitic absorptions from oxidized Spiro-MeOTAD, TiO<sub>2</sub> and FTO are negligible, (d) there is no light scattering perovskite capping layer and (e) spiro-OMeTAD has a refraction index of 1.5 with negligible imaginary part. Using these approximations we derived the absorbed photon to current conversion efficiency (APCE) or internal quantum efficiency (IQE) from dividing the IPCE by the absorptance values. Figure 3.6c shows that for MA<sub>0.6</sub>FA<sub>0.4</sub>PbI<sub>3</sub>, high APCE values of 80-85% are maintained throughout the visible spectrum attesting the very high quantum efficiency of carrier generation and collection achieved by the device. This contrasts with CH<sub>3</sub>NH<sub>3</sub>PbI<sub>3</sub> and CH(NH<sub>2</sub>)<sub>2</sub>PbI<sub>3</sub>, which seem to collect less charges produced by red than

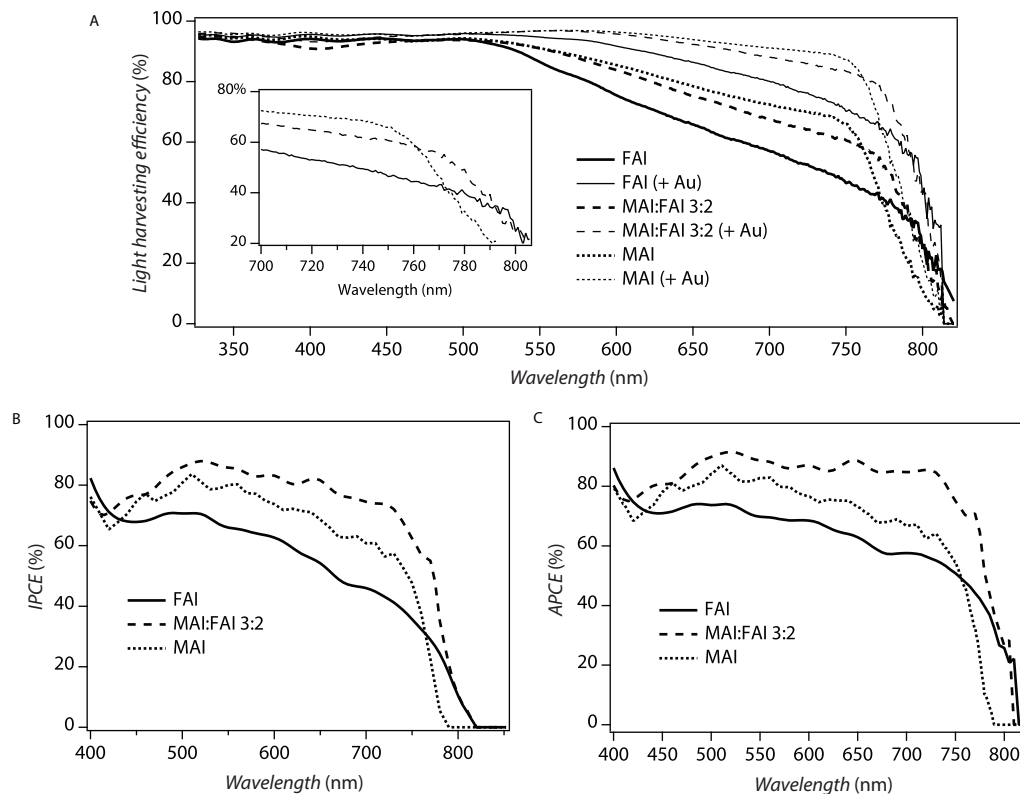


**Figure 3.6:** (a) Light harvesting efficiency of  $(\text{CH}_3\text{NH}_3)_x(\text{HNCHNH}_3)_{1-x}\text{PbI}_3$  ( $x = 0, 0.6, 1$ ). The measurement was performed right after measuring the IPCE and cutting the cell to the active area, after removal of the gold back contact. The measurement has been performed in an integrated sphere to account for diffuse reflectance. The sample was placed successively in the beam and perpendicularly to the beam to compensate for secondary absorption. (b) IPCE spectrum of the three cells. Note the red-shifted IPCE onset above 800 nm for the mixed cations as well as the pure formamidinium lead iodide. (c) APCE spectrum derived from the IPCE and LHE.

blue photons indicating a shorter carrier diffusion length for the single cation perovskite phases.

### 3.10 Lifetime measurements

In order to further substantiate this interpretation we used time-correlated single photon counting as a measure of carrier lifetime of the material, as deposited on glass from solutions of MAI/FAI and  $\text{PbI}_2$  in *N,N*-dimethylformamide (20% wt). The samples were excited by a 406 nm laser diode and their emission recorded at right angle through a double monochromator. All the films were measured over a 200 ns window divided into 1024 channels. Fluorescence lifetimes are displayed in Figure 3.7 for  $\text{MA}_x\text{FA}_{1-x}\text{PbI}_3$  ( $x = 0, 0.2, 0.4, 0.6, 0.8, 1$ ). The time decay of the fluorescence signals was fit to two or three exponentials, the lifetimes for the 3



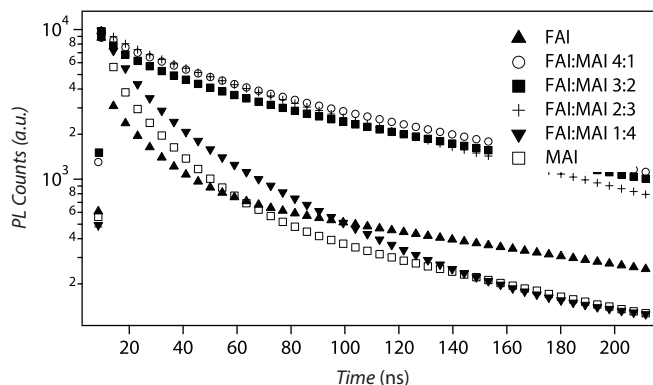


**Figure 3.7:** (a) Fluorescence lifetime for  $(\text{CH}_3\text{NH}_3)_x(\text{HNCHNH}_3)_{1-x}\text{PbI}_3$  spin-coated from a solution of MAI/FAI +  $\text{PbI}_2$  dissolved in N,N-dimethylformamide (20% wt.). The films have been heated at  $80^\circ\text{C}$  for 30 minutes before the measurement. The signals are fitted to three decaying exponential of variable lifetimes.

Lifetime	MAI	MAI <sub>0.4</sub> FAI <sub>0.6</sub>	FAI
1st	2.58 ns	-	17.3 ns
Intensity	11%	-	14%
2nd	17.3 ns	27.6 ns	76.4 ns
Intensity	46%	14%	51%
3rd	103 ns	135 ns	173 ns
Intensity	43%	86%	35%

**Table 3.2:** Fluorescence lifetime and corresponding intensities for  $\text{CH}_3\text{NH}_3\text{PbI}_3$ ,  $\text{FAPbI}_3$  and  $\text{MA}_{0.4}\text{FA}_{0.6}\text{PbI}_3$  fitted with three exponentials, extracted from the traces in Figure 3.7.

components being in the range of 1 - 10 ns, 20 - 70 ns and 100 - 300 ns. Results are reported in table 3.2. Strikingly, 85% of the emission of  $\text{MA}_{0.6}\text{FA}_{0.4}\text{PbI}_3$  decay with a long lifetime of 130 ns, slower than the pure phase perovskites. It also appears that for the mixed cations a double exponential is sufficient to fit the decay kinetics well, since the fast decay observed for the single cations is absent. The prolongation of the lifetime in the mixed cation perovskite is likely to contribute to the better carrier collection efficiency observed with  $\text{MA}_{0.6}\text{FA}_{0.4}\text{PbI}_3$  as it enhances their diffusion length.

### 3.11 Conclusion and outlook

This report was the first of a perovskite-sensitized photovoltaic device based on the mixed cation 3D perovskite  $(\text{MA})_x(\text{FA})_{1-x}\text{PbI}_3$  ( $x = 0$  to 1). The formamidinium cation is presented as a potential replacement for methylammonium in lead iodide perovskites, owing to the red-shifted absorption onset of  $\text{FAPbI}_3$  compared to that of  $\text{CH}_3\text{NH}_3\text{PbI}_3$ . Devices based on  $\text{FAPbI}_3$  were made via sequential deposition and gave PCE of 11.0%, albeit lower than

### Chapter 3. Mixed organic cation perovskite solar cells

---

that of  $\text{CH}_3\text{NH}_3\text{PbI}_3$ MA due to the presence of the yellow  $\delta$ -phase. Using the sequential deposition method and adding 20% MA into the FA dipping bath completely avoids the undesirable formation of the  $\delta$ -phase while maintaining the red-shifted band gap of  $\text{FAPbI}_3$ . The mixed cation perovskite  $\text{MA}_{0.6}\text{FA}_{0.4}\text{PbI}_3$  exhibits superior PV performance to the single cation analogues owing to a greater harvesting and collection of red photons resulting in higher short circuit photocurrents without sacrificing photovoltage. The superior carrier collection efficiency is likely related to the longer exciton lifetime in the  $\text{MA}_{0.6}\text{FA}_{0.4}\text{PbI}_3$  material exceeding 100 ns. Using this technique, we were able to fabricate devices yielding up to 14.9% photon-to-current efficiency under the AM1.5G simulated solar spectrum. The strategy of mixing organic ammoniums opens up new prospects to further improve the photovoltaic efficiency of perovskite-sensitized solar cells by tuning the optical, electrical and morphological properties of the semiconducting sensitizer. It is believed that if the formation of the yellowish  $\delta$ - $\text{FAPbI}_3$  could be fully avoided, the performance of pure  $\text{FAPbI}_3$  will likely surpass  $\text{CH}_3\text{NH}_3\text{PbI}_3$ -based mesoscopic solar devices. In fact, all of the highest efficiency laboratory scale perovskite solar cells are using some mixture of formamidinium and methylammonium, reaching over 21% power conversion efficiencies[69]. It was later shown that the addition of  $\text{Cs}^+$  also plays a role in the stabilization of the  $\alpha$ -phase of  $\text{CH}(\text{NH}_2)_2\text{PbI}_3$ [102], and the deposition mixed cations perovskites by sequential fashion was replaced by an anti-solvent method[54].

## 4 Ion exchange reactions of hybrid organic-inorganic perovskites

*This chapter reports on the reactivity of hybrid organic-inorganic perovskite towards anion exchange reactions. It is primarily based a published article in a peer reviewed journal[81] and on my contribution to two otherwise related article published in peer reviewed journals[139, 140].*

### 4.1 Motivation

The power conversion efficiency on thin film solar cell has typically a tight correlation with morphology control and grain boundary trap state passivation[141, 142, 143, 144]. Morphology control has been one of the key element in advancing the efficiency of hybrid perovskite solar cells[145, 47, 52, 33]. However, it is very typical that the best material formulation for such solar cells is different from pristine  $\text{CH}_3\text{NH}_3\text{PbI}_3$ , such as  $\text{CH}_3\text{NH}_3\text{PbI}_x\text{Br}_{3-x}$ ,  $(\text{MA}, \text{FA})\text{PbI}_x\text{Br}_{3-x}$  or  $(\text{MA}, \text{FA}, \text{Cs})\text{PbI}_x\text{Br}_{3-x}$ , not to mention that there is currently a debate on the benefits of non-stoichiometric perovskites[69, 146, 147]. Getting the best of both worlds (morphology and chemical composition) can sometimes be challenging. This chapter proposes a simple route through which the anion part of the hybrid perovskite (i.e. the halide) can be partially or completely exchanged by another one, while retaining the overall morphology. This technique, although not reported here for cation exchange, can also be employed to exchange the methylammonium by formamidinium cations, while exchanging lead by tin was proven unsuccessful. As an example of application, we show that this technique can be applied to convert  $\text{CH}_3\text{NH}_3\text{PbI}_3$  nanowires into  $\text{CH}(\text{NH}_2)_2\text{PbI}_3$ ,  $\text{CH}_3\text{NH}_3\text{PbBr}_3$  or  $\text{CH}_3\text{NH}_3\text{PbCl}_3$  nanowires.

### 4.2 Introduction

In this chapter, we report on the ionic exchange reactions that the hybrid organic-inorganic perovskites  $\text{CH}_3\text{NH}_3\text{PbI}_3$ ,  $\text{CH}_3\text{NH}_3\text{PbBr}_3$  and  $\text{CH}_3\text{NH}_3\text{PbCl}_3$  undergo in solution. In particular, we found that exchanging a lattice halide ( $\text{I}^-$ ,  $\text{Br}^-$ ,  $\text{Cl}^-$ ) by another can be achieved by exposing a perovskite film of a certain halide to a solution containing the substituting

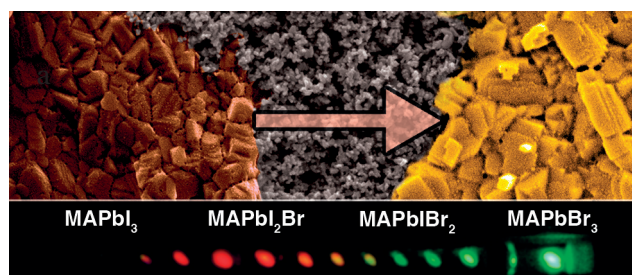


**Figure 4.1:** False color SEM micrograph depicting the conversion reaction from  $\text{CH}_3\text{NH}_3\text{PbI}_3$  (left) to  $\text{CH}_3\text{NH}_3\text{PbBr}_3$  (right) with corresponding photographs capturing the photoluminescence of the film at various time intervals.

halide and the same organic component of the perovskite (in this case, methylammonium or formamidinium). We found that the lattice halide can be completely replaced by the one in solution within minutes after the start of the reaction, with the exception of the substitution of bromide by iodide, which remained incomplete. Surprisingly, the exchange remains fast even for planar perovskite films of several tens of nanometers thick. The kinetics of the substitution reactions have been monitored by in situ photoluminescence, absorption spectroscopy and X-ray diffraction measurements. In this chapter, we show that the halide exchange can be a powerful tool to transform perovskites and enhance their luminescence.

Cation exchanges from solids have been widely reported in the literature, though usually on oxide nanoparticles. Some of those reactions involving a variety of functional materials have been thoroughly reviewed by Clearfield[148]. More recently, multiple reactions involving cation exchange on the nanoscale have been described[125, 126, 149, 150, 151, 152, 153, 154, 155]. For instance, Beberwyck et al. demonstrated the interchange of In, Ga and Cd in arsenide nanoparticles[124]. Similarly, Luther et al. demonstrated the exchange of Cu, Pb and Cd in nanorods[156]. However reactions involving anion exchanges are much scarcer[156, 157]. For instance, Park et al. have described the formation of ZnS hollow nanoparticles through the anion exchange reaction, starting from ZnO nanoparticles[156]. There has been some interest into the partial insertion of halides inside layered oxide perovskites[158, 159, 160, 161, 162]. In fact these reactions proceed via cation exchange as well, as it has been shown that the  $(\text{MX})^+$  fragment is responsible for the halide substitution into the lattice. Partial halide insertion has been achieved for the perovskite  $\text{Sr}_2\text{NiO}_3\text{X}$  ( $\text{X}=\text{F},\text{Cl}$ ) [158] but those reactions were performed at pressures of 6 GPa and at temperatures above 1500 K.

At the time this research was done, there simply did not exist any report on the full anion exchange in inorganic or hybrid perovskites, to the best of our knowledge. This work reports on the substitution of a halide within the three dimensional  $\text{CH}_3\text{NH}_3\text{PbX}_3$  structure. This exchange was found to be strikingly rapid when the perovskite film was contained within a mesoscopic oxide scaffold and was exposed to a solution containing another halide anion. We use the luminescence emission of  $\text{CH}_3\text{NH}_3\text{PbX}_3$  ( $\text{X} = \text{Cl}, \text{Br}, \text{I}$ ) to follow in situ substi-

tution of halides in the perovskite lattice by other halides from solution. We observe that the anion exchange reaction can yield highly luminescent morphologies. Apart from fluorescence we monitor the time course of the anion exchange by X-ray diffraction (XRD) and absorption spectroscopy. We show that gradual substitution on the perovskite lattice can be achieved with Br/Cl and Br/I through in situ halide exchange, while co-insertion of the anions is not observed in the I/Cl system: attempts to partially substitute  $\text{CH}_3\text{NH}_3\text{PbI}_3$  with chloride or  $\text{CH}_3\text{NH}_3\text{PbCl}_3$  with iodide failed. Rather, the formation of two separate phases of  $\text{CH}_3\text{NH}_3\text{PbI}_3$  and  $\text{CH}_3\text{NH}_3\text{PbCl}_3$  was observed. The exchange of chloride by iodide allowed us for the first time to observe a transient blue-shifted photoluminescence of  $\text{CH}_3\text{NH}_3\text{PbI}_3$ , which we attribute to either a transient amorphous phase[163] or to the presence of quantum confined particles formed at the outset of the  $\text{CH}_3\text{NH}_3\text{PbI}_3$  crystal formation[164, 165]. Our observation correlates well with previous experiments performed on halide mixtures: the substitution of iodides for bromides being employed to adjust the band-gap of the perovskite or produce wavelength tunable lasers[36]. The gradual replacement of iodide by bromide blue-shifts the absorption spectra of the resulting mixed-halide structures, resulting from the co-insertion of anions inside the  $\text{Pb}(\text{I}, \text{Br})_6^{4-}$  octahedron that alters the lattice parameter and changes the optical band gap accordingly[94]. This is opposed to creating isolated phases of different halide perovskites, which result in two different luminescence and XRD signals, as was found for  $\text{CH}_3\text{NH}_3\text{Pb}(\text{I}, \text{Cl})_3$  films[145, 166]. Such mixtures had originally been claimed by Snaith and coworkers to be doped forms of  $\text{CH}_3\text{NH}_3\text{PbI}_3$  represented by the widely used chemical formula  $\text{CH}_3\text{NH}_3\text{PbI}_{3-x}\text{Cl}_x$ [45]. Chloride doping has been postulated to boost the performance of perovskite photovoltaics formed via one step precipitation from solution. However so far experimental evidences show lack of Cl/I co-insertion into the perovskite lattice.

### 4.3 Results and discussion

We studied all possible exchange reactions involving the three above-mentioned halides, namely chloride, bromide and iodide. We found that halide substitution takes place at ambient temperature within seconds to a few minutes– except the conversion of bromide to iodide, which was not complete after a period of 1 hour. The anion in the dipping solution always dictates the resulting halide in the perovskite phase, the driving force being the difference of chemical potential of the halides between the reactant and product state of the solid phase. Figure 4.3 shows the luminescence spectra of the bromide and iodide perovskites before and after conversion.

We observe rather complex halide exchange kinetics related to the lattice energy but also by the accessibility and diffusion rate of halides through the lattice. This is corroborated by the variety of structures detected in scanning electron micrographs (figure 4.2). While the Br/I and Cl/Br exchange proceeds gradually - in both directions - with a narrow distribution of halides at all monitored times, the Cl/I exchange occurs via the appearance of a new phase and the concomitant disappearance of the starting one. This is in keeping with the results of Dualeh

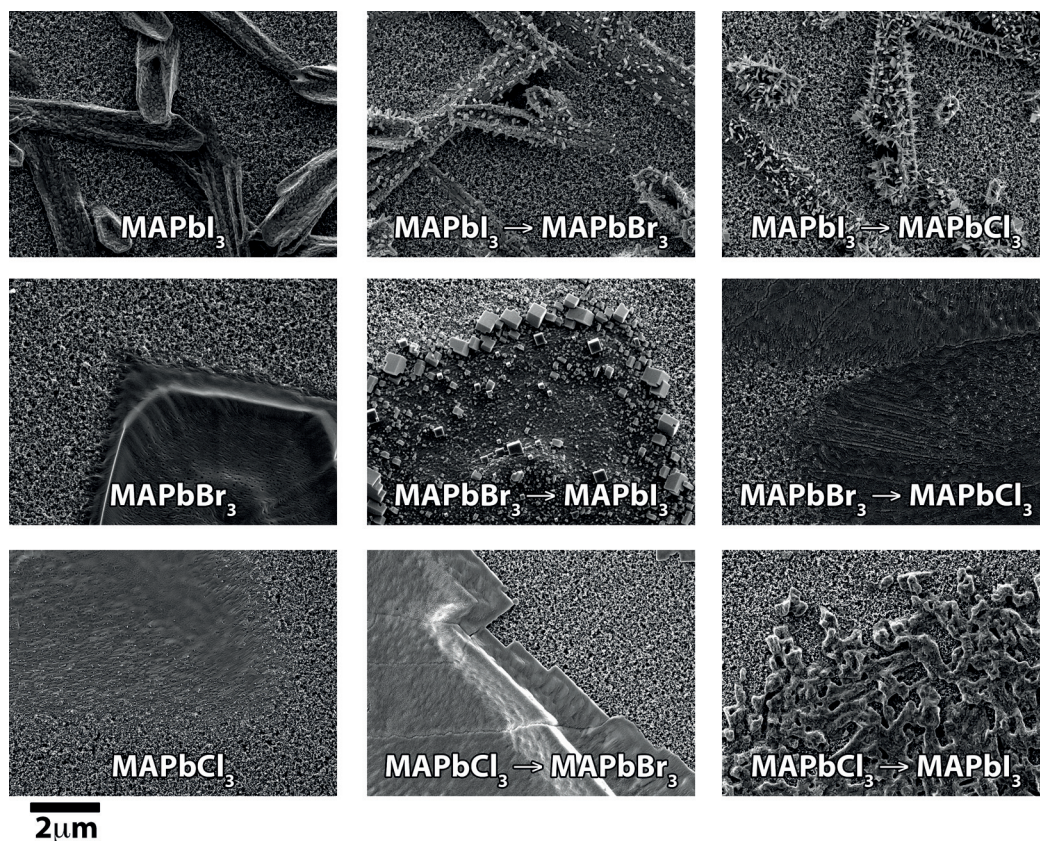


**Figure 4.2:** SEM micrographs illustrating the different halide exchange reactions terminated after 5 minutes. (a) Initial structure of  $\text{CH}_3\text{NH}_3\text{PbI}_3$ . (b)  $\text{CH}_3\text{NH}_3\text{PbI}_3$  converted into  $\text{CH}_3\text{NH}_3\text{PbBr}_3$ . (c)  $\text{CH}_3\text{NH}_3\text{PbI}_3$  converted into  $\text{CH}_3\text{NH}_3\text{PbCl}_3$ . (d) Initial structure of  $\text{CH}_3\text{NH}_3\text{PbBr}_3$ . (e)  $\text{CH}_3\text{NH}_3\text{PbBr}_3$  converted into  $\text{CH}_3\text{NH}_3\text{PbI}_3$ . (f)  $\text{CH}_3\text{NH}_3\text{PbBr}_3$  converted into  $\text{CH}_3\text{NH}_3\text{PbCl}_3$ . (g) Initial structure of  $\text{CH}_3\text{NH}_3\text{PbCl}_3$ . (h)  $\text{CH}_3\text{NH}_3\text{PbCl}_3$  converted into  $\text{CH}_3\text{NH}_3\text{PbBr}_3$ . (i)  $\text{CH}_3\text{NH}_3\text{PbCl}_3$  converted into  $\text{CH}_3\text{NH}_3\text{PbI}_3$

et al. on the solid-phase Cl/I exchange[145]. Small shifts of the luminescence peak in the spectra of  $\text{CH}_3\text{NH}_3\text{PbI}_3$  witnessed during the substitution of chloride by iodide (Figure 4.7 a and d) or vice-versa may reflect a quantum confinement effect occurring within  $\text{CH}_3\text{NH}_3\text{PbI}_3$  nanocrystals whose size is below the Bohr radius of the exciton of 2.2 nm[165]. Such small crystals possibly occur since the chloride / iodide exchange seems to pass through formation of new nuclei (Figure 4.2, 4.12), as a consequence of the lattice mismatch of their respective phases impairing the formation of solid solutions. Alternatively, since luminescence blue shifts were observed even for films with crystal sizes around 30 nm measured by XRD and SEM, Choi et al.[163] suggested that this emission could arise from a highly disordered amorphous perovskite phase, which luminesces at shorter wavelength than crystalline particles.

We monitored the photoluminescence (PL) of the perovskite crystals during the halide exchange reactions and found that its intensity can vary during the conversion by up to two orders of magnitudes. Typically the temporal intensity changes are not gradual. Rather

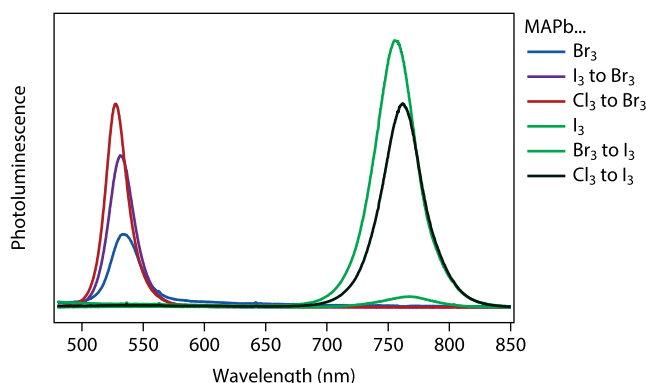


**Figure 4.3:** (a) Absorbance profile of the iodide to bromide exchange performed on a 150nm thick  $\text{CH}_3\text{NH}_3\text{PbI}_3$  evaporated thin film on FTO conductive glass. The traces were fitted to a single exponential decay. A blank sample consisting of bare FTO provided the baseline.

the luminescence shows a steep increase during the first few seconds after contacting with the  $\text{CH}_3\text{NH}_3\text{X}$  ( $X = \text{Cl}, \text{Br}, \text{I}$ ) solution, as we already observed for the insertion of MAI into  $\text{PbI}_2$  [47]. We argued that the fluorescence intensity decay after the first PL spike was due to re-absorption of emitted photons. Additionally, in the current case, the difference may be attributed to better light out-coupling in the case of the IPA/ $\text{CH}_3\text{NH}_3\text{PbX}_3$  interface compared to Air/ $\text{CH}_3\text{NH}_3\text{PbX}_3$ . To investigate this possibility, a mesoporous  $\text{Al}_2\text{O}_3$  film infiltrated with  $\text{CH}_3\text{NH}_3\text{PbI}_3$  was mounted in a quartz cuvette and placed in a spectrofluorometer. The luminescence was detected at 750 nm, slightly below the maximal PL wavelength of  $\text{CH}_3\text{NH}_3\text{PbI}_3$ . After recording the baseline in air for ca. 20 seconds, 2 mL of pure 2-propanol (IPA) were injected in the cuvette. 150 seconds later we added about 2 mL of  $0.05 \text{ mol L}^{-1}$   $\text{CH}_3\text{NH}_3\text{Br}$  in IPA. Results are shown in figure 4.9. After contacting the perovskite with pure IPA, the PL slowly increases by a factor of 15 with no apparent change in the UV-Vis absorption spectrum. After the signal leveled off, we added  $\text{CH}_3\text{NH}_3\text{Br}$  to the cuvette and the PL intensity doubled until reaching a maximum, before dropping due to the formation of  $\text{CH}_3\text{NH}_3\text{PbBr}_x\text{I}_{3-x}$ , which luminesces at shorter wavelengths than 750 nm. We attribute the first rise of PL after contacting with IPA to the release of tensile strengths produced by the sudden removal of DMF during sample preparation. The IPA acts as a solvent for MAI, allowing it to dissolve and re-intercalate locally in a dynamic equilibrium (before dissolving completely) thereby locally recrystallizing the perovskite structures. The subsequent addition of  $\text{MA}^+$  and  $\text{Br}^-$  is thought to help passivate surface states or fill halide vacancies, further boosting the luminescence. In total, we found that the PL intensity can be multiplied by a factor of more than 30 due to a simple IPA/ $\text{CH}_3\text{NH}_3\text{Br}$  bath without much band gap variation. Therefore, all reaction dynamics monitored by luminescence will reflect the combination of solvent and halide exchange effects. Individual reactions are now discussed in the following section, highlighting their salient features.

4.3.1  $\text{CH}_3\text{NH}_3\text{PbBr}_3$  to  $\text{CH}_3\text{NH}_3\text{PbI}_3$ 

Although powder XRD data shows that the bromide and iodide co-intercalate at all considered time with gradually changing stoichiometry, the gradation is not as clear from photoluminescence measurements. A sharp red-shift of the PL is recorded as soon as the reaction has begun. The first recorded data point shows already a PL peak that is centered at 700 nm which, according to Noh et al., should correspond to a I:Br ratio of 0.6736. However from XRD data the actual stoichiometry matches an I:Br ratio of 0.077. We rationalize the strong red-shift in photoluminescence by the presence of local domains of higher iodide content into which mobile carriers drift (along the chemical potential gradient) where they recombine radiatively in the near-IR. Alternatively, formation of a capping layer of  $\text{CH}_3\text{NH}_3\text{PbI}_3$  that shields the emission arising from underlying  $\text{MAPbBr}_3$  could explain the sudden shift in the luminescence peak. As the reaction proceeds, the PL maximum further red-shifts to reach its final position of 753 nm after 1 minute which is still below that of pure  $\text{CH}_3\text{NH}_3\text{PbI}_3$ . X-ray diffraction confirms that  $\text{CH}_3\text{NH}_3\text{PbI}_3$  phase is not pure at this stage of the reaction.

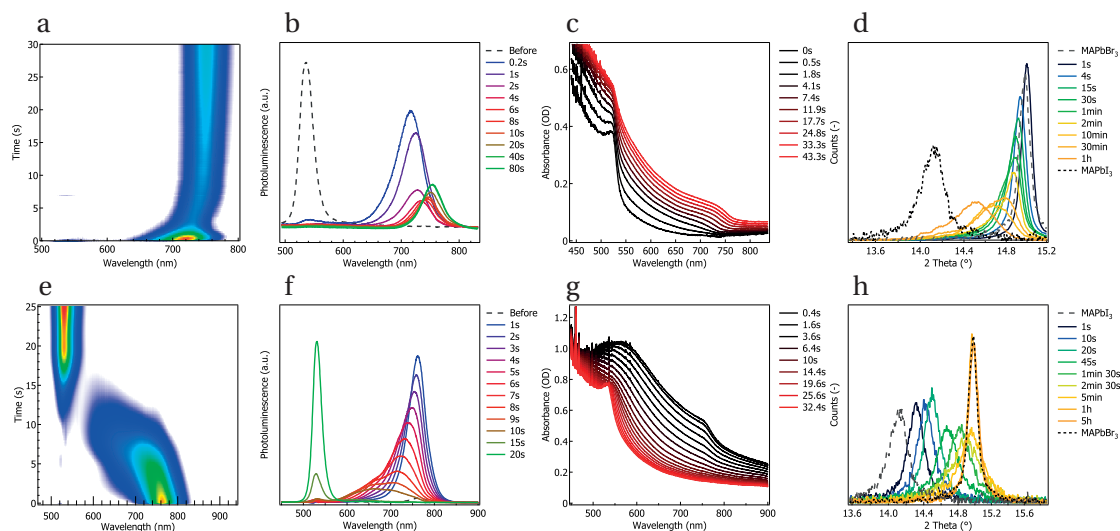


**Figure 4.4:** (a-c) Reaction profile of the  $\text{CH}_3\text{NH}_3\text{PbBr}_3$  –  $\text{CH}_3\text{NH}_3\text{PbI}_3$  interconversion. (d-f) Reaction profile of the  $\text{CH}_3\text{NH}_3\text{PbI}_3$  –  $\text{CH}_3\text{NH}_3\text{PbBr}_3$  interconversion. (a,d) Photoluminescence profile as a function of time. At time  $t = 0$  s, the MAX solution was injected in the cuvette. The sample was illuminated at  $60^\circ$  by a continuous wave 406 nm blue laser and detected at right angle onto the CCD camera. (b,e) change in absorbance due to the transformation reaction. At time  $t = 0$ , the MAX solution was injected into the cuvette. A FTO/ $\text{Al}_2\text{O}_3$  blank was subtracted. (c,f) XRD profile of the reactions. The samples were dipped in MAX for various times and the reaction was quenched in IPA.

We rationalize the strong red-shift in photoluminescence by the presence of local domains of higher iodide content into which free charges drift (along the chemical potential gradient) where they recombine radiatively in the near-IR. Alternatively, a thin layer of  $\text{CH}_3\text{NH}_3\text{PbI}_3$  that shields the absorption and the emission for  $\text{CH}_3\text{NH}_3\text{PbBr}_3$  could explain the sudden shift



in luminescence.

As the reaction time increases, the position of the maximum luminescence further shifts into the red to reach a final luminescence centered close to the full-iodide stoichiometry at 753 nm after 1 minute. There is however no evidence by X-ray diffraction of a full iodide phase at this stage of the reaction and a broad distribution of I:Br stoichiometries is observed (Figure 4.4c)

Even after 1h of reaction, a broad distribution of I:Br stoichiometries is observed (Figure 4.4c). The morphology of the final  $\text{CH}_3\text{NH}_3\text{PbI}_3$  features 100 to 300 nm-sized crystals grown primarily on the edges of the microscopic  $\text{CH}_3\text{NH}_3\text{PbBr}_3$  islands and smaller particles formed inside those islands (Figure 4.2e). The quality of the crystals at the edge of the  $\text{CH}_3\text{NH}_3\text{PbBr}_3$  islands is much better than the ones formed typically by the  $\text{PbI}_2$  to  $\text{CH}_3\text{NH}_3\text{PbI}_3$  conversion via insertion of MAI, which produces polycrystalline particles with many grain boundaries. It is worth noting that at this stage of the reaction, XRD indicates the presence of substantial amounts of the initial methylammonium lead bromide. The bulkiness of the initial  $\text{CH}_3\text{NH}_3\text{PbBr}_3$  islands and the difficulty of the large lattice expansion associated with the substitution of  $\text{Br}^-$  by  $\text{I}^-$  in an already crowded volume (Figure 4.2d) slows down the exchange process along with the lack of thermodynamic driving force. While we observe the appearance of the sharp absorbance onset near 750 nm within the first seconds of the reaction (Figure 4.4b), this still below the band edge of pure  $\text{CH}_3\text{NH}_3\text{PbI}_3$  (Figure 4.4e), which is consistent with only a partial bromide replacement by iodide.

#### 4.3.2 $\text{CH}_3\text{NH}_3\text{PbI}_3$ to $\text{CH}_3\text{NH}_3\text{PbBr}_3$

Just like the bromide to the iodide, the iodide to bromide exchange passes through intermediate halide stoichiometries throughout the experiment, as shown by powder X-ray diffraction measurements (Figure 4.4f). In this direction, the reaction performed at a faster pace than in the reverse direction, possibly due to the higher surface area provided by the  $\text{CH}_3\text{NH}_3\text{PbI}_3$  micro-needles (Figure 4.2a) or owing to the reduction in the lattice parameter, allowing more accessibility through the structure.

A weak 14 nm blue-shift of the luminescence is observed directly after the  $\text{CH}_3\text{NH}_3\text{PbI}_3$  is exposed to  $\text{CH}_3\text{NH}_3\text{Br}$  in solution. The shift correlates to the XRD measurement, which shows an immediate 24% relative shrink in the lattice compared to  $\text{CH}_3\text{NH}_3\text{PbBr}_3$  (1.36% absolute shrink). During the exchange reaction, the PL shifts gradually down to about 609 nm where it vanishes below the setup detection threshold, before appearing suddenly as the pure bromide peak at 535 nm. The lack of luminescence between 535 nm and 609 nm is not indicative of a certain missing stoichiometry, as is evidenced by the continuous shift in the XRD, but the crystals seem to be PL inactive during the exchange of the last iodide (a 2.03 eV band gap corresponds to a Br:I ratio of 0.75 according to Noh et al.[94]). No luminescence occurs until the pure  $\text{CH}_3\text{NH}_3\text{PbBr}_3$  phase is formed, which then gives rise to the 532 nm luminescence peak. This intensity effect was reproduced accurately on samples where the reaction had been

quenched and measured with a more sensitive spectrofluorometer, which suggests that the morphology or the stoichiometry that is PL inactive is a real can be sustained.

The reaction appears to be complete within about 5 minutes, as indicated by the XRD signal (Figure 4.4f). This contrasts with the absorbance and luminescence measurements that show much faster completion. We attribute these differences to heating by the excitation laser or halogen light source during the optical measurements, speeding up the halide exchange. After completion of the reaction, we observe a strong shrinking of both the (110) reflection XRD peak and the 535 nm PL peak. We also noticed that the general morphology of the initial  $\text{CH}_3\text{NH}_3\text{PbI}_3$  crystals has been preserved after complete bromide substitution as the material has crystallized in the shape of the initial micro-needles (Figure 4.2a/b). The absorbance profile of the reaction shows the decrease in absorbance throughout the whole green-red region, including below the band gap of  $\text{CH}_3\text{NH}_3\text{PbBr}_3$  (Figure 4.4e). As the iodide phase disappears, the excitonic peak of  $\text{CH}_3\text{NH}_3\text{PbBr}_3$  gradually emerges near 532 nm nm.

To study whether the iodide to bromide exchange could occur on more compact perovskite films, we deposited  $\text{CH}_3\text{NH}_3\text{PbI}_3$  onto a glass slide using a previously reported procedure[54]. The film thickness was adjusted by varying the concentrations of precursor solutions. The films were then dipped into solutions of  $\text{CH}_3\text{NH}_3\text{Br}$  in 2-propanol of various concentrations and the absorbance kinetics was monitored at 720 nm. The disappearance of the absorbance was fitted to a single decaying exponential to extract the pseudo first order time constant. Results are shown in 4.10. We observe that while the rate of reaction is strongly dependent on the film thickness, it is independent on the bromide precursor concentration within the considered concentrations (5 to  $11\text{mgmL}^{-1}$ ). Therefore we conclude that the exchange is limited by the iodide diffusion within the lattice rather than ionic transport in solution or by the interfacial halide exchange at the crystal surface. The iodide diffusion in the solid occurs most likely via halide interstitials or vacancies.

### 4.3.3 $\text{CH}_3\text{NH}_3\text{PbCl}_3$ to $\text{CH}_3\text{NH}_3\text{PbBr}_3$

The chloride-bromide exchange shows a extremely rapid red-shift of the luminescence, the first luminescence peak being recorded at 500 nm. The position of this luminescence does not match with the X-ray diffraction pattern which show only a small exchange in the first few seconds. We attribute this luminescence shift as a similar effect seen in the bromide to iodide exchange: by converting a high band gap material to a low band-gap material, there is a fast electron and hole diffusion to the low band gap regions of the film faster than the radiative recombinations occur, which shows up as a strongly red-shifted luminescence after only little time. After the conversion of the first thin layer of perovskite, the rest of the halide exchange reaction takes place, dictated by the high concentration of bromide in solution. The band gap of the material further shifts towards the red, until it reaches the expected 530 nm emission ( $E_g \sim 2.3\text{eV}$ ).

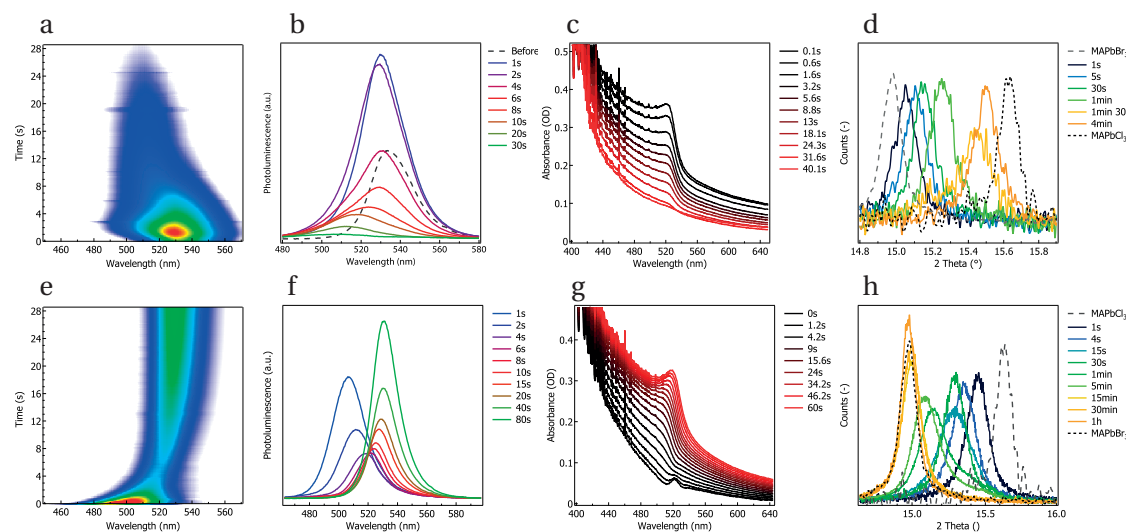


**Figure 4.5:** (a-c) Reaction profile of the  $\text{CH}_3\text{NH}_3\text{PbBr}_3 - \text{CH}_3\text{NH}_3\text{PbCl}_3$  interconversion. (d-f) Reaction profile of the  $\text{CH}_3\text{NH}_3\text{PbBr}_3 - \text{CH}_3\text{NH}_3\text{PbCl}_3$  interconversion. (a,d) Photoluminescence profile as a function of time. At time  $t = 0\text{s}$ , the MAX solution was injected in the cuvette. The sample was illuminated at  $60^\circ$  by a continuous wave 406 nm blue laser and detected at right angle onto the CCD camera. (b,e) change in absorbance due to the transformation reaction. At time  $t = 0$ , the  $\text{CH}_3\text{NH}_3\text{X}$  solution was injected into the cuvette. A FTO/ $\text{Al}_2\text{O}_3$  blank was subtracted. (c,f) XRD profile of the reactions. The samples were dipped in MAX for various times and the reaction was quenched in IPA.

The luminescence of the  $\text{CH}_3\text{NH}_3\text{PbBr}_3$  crystals produced via halide exchange from  $\text{CH}_3\text{NH}_3\text{PbCl}_3$  is about one order of magnitude more intense than the emission of perovskite directly deposited from DMF, suggesting that  $\text{CH}_3\text{NH}_3\text{Cl}$  is participating in the mitigation of surface states, blocking non-radiative recombination pathways. We measured the fluorescence quantum yield  $\Phi_{\text{PL}}$  for  $\text{CH}_3\text{NH}_3\text{PbBr}_3$  crystals formed via the conversion of chloride to bromide, iodide to bromide and via direct bromide deposition in a single step from solution (Figure 4.6a). We note that  $\Phi_{\text{PL}}$  increases by a factor of about 6 when the  $\text{CH}_3\text{NH}_3\text{PbBr}_3$  is prepared by halide substitution from  $\text{CH}_3\text{NH}_3\text{PbCl}_3$ , i.e. 0.85% vs. 0.15% compared to the direct deposition. The increase is less pronounced when the  $\text{CH}_3\text{NH}_3\text{PbBr}_3$  is formed from the iodide, i.e.  $\Phi_{\text{PL}} = 0.31\%$ . Since the latter sample transmitted less light (26% vs 58%), self-absorption of the emitted photons may contribute to the lowering of the external luminescence yield. The increase of the  $\Phi_{\text{PL}}$  observed during the chloride to bromide conversion is mainly due to a decrease of the non-radiative deactivation rate resulting in a longer exciton emission lifetime most likely due to the passivation of surface states. For  $\text{CH}_3\text{NH}_3\text{PbBr}_3$  crystals formed by anion exchange from  $\text{CH}_3\text{NH}_3\text{PbI}_3$  a shorter lifetime was observed in keeping with the lower emission quantum yield.

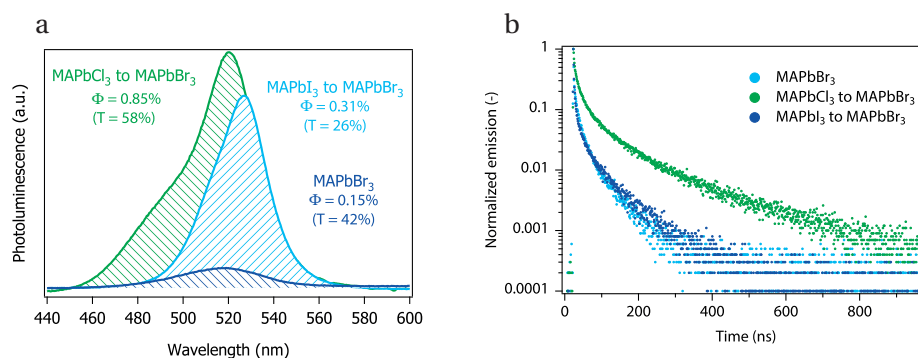


**Figure 4.6:** (a) Quantum yield measurement of  $\text{CH}_3\text{NH}_3\text{PbBr}_3$  films converted from  $\text{CH}_3\text{NH}_3\text{PbCl}_3$ ,  $\text{CH}_3\text{NH}_3\text{PbI}_3$  or directly deposited from *N,N*-dimethylformamide. The transmittance at 406 nm is also specified. (b) Fluorescence lifetime of the  $\text{CH}_3\text{NH}_3\text{PbBr}_3$  films excited at 406 nm.

#### 4.3.4 $\text{CH}_3\text{NH}_3\text{PbBr}_3$ to $\text{CH}_3\text{NH}_3\text{PbCl}_3$

The exchange of bromide to chloride induces a blue shift of the luminescence, corresponding to gradual chloride substitution of the bromide (Figure 4.5d). This is confirmed in the XRD measurement where the  $15.6^\circ$  diffraction peak shifts to higher angles, sign of a lattice compression (Figure 4.5f). After 30 seconds, the luminescence drops beyond the detection limit of the setup but can still be monitored ex situ by the spectrofluorometer (figure 4.11). The luminescence seemingly further shifts to lower wavelength without noticeable interruption. No increase of luminescence at 404 nm over time can then be observed. The bromide and chloride interchange retains very well the initial perovskite morphology in both directions (Figure 4.2f/h).

#### 4.3.5 $\text{CH}_3\text{NH}_3\text{PbCl}_3$ to $\text{CH}_3\text{NH}_3\text{PbI}_3$

The powder XRD data of the chloride to iodide exchange does not show a common intercalation of iodide and chloride in the lattice that would yield a change in the lattice parameter, down to the angular resolution of the X-ray diffraction apparatus (Figure 4.7c). Unlike the Br/I or Cl/Br system where both halides can form solid solutions, the Cl/I exchange produces separate  $\text{CH}_3\text{NH}_3\text{PbCl}_3$  and  $\text{CH}_3\text{NH}_3\text{PbI}_3$  phases. This is confirmed by scanning electron micrographs, where the conversion of chloride to iodide produces new crystals with strongly altered morphology (Figure 4.2g/i).  $\text{CH}_3\text{NH}_3\text{PbCl}_3$  is deposited in broad islands that efficiently penetrate the mesoporous titanium dioxide scaffold. After conversion, the iodide phase has grown on top of the film in a multitude of grains stacked together in an intertwined network. This contrasts with the chloride/bromide exchange which retains the initial structure of  $\text{CH}_3\text{NH}_3\text{PbCl}_3$ .

No luminescence from mixed  $\text{MAPbI}_{3-x}\text{Cl}_x$  compositions could be observed. Rather, the first luminescence peak has a maximum at 756 nm and shifts to 768 nm as the reaction

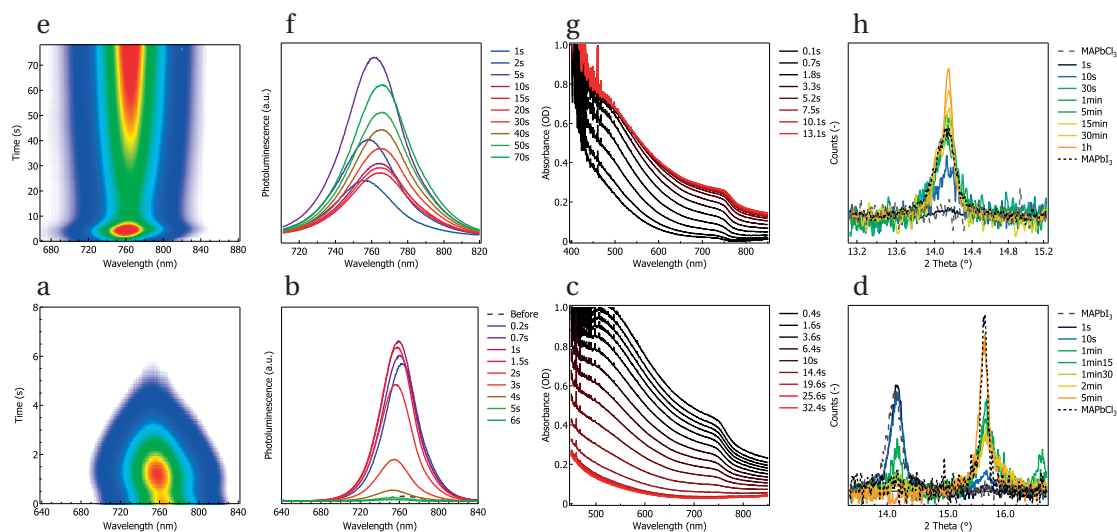


**Figure 4.7:** (a-c) Reaction profile of the  $\text{CH}_3\text{NH}_3\text{PbCl}_3$ –  $\text{CH}_3\text{NH}_3\text{PbI}_3$  interconversion. (d-f) Reaction profile of the  $\text{CH}_3\text{NH}_3\text{PbI}_3$ –  $\text{CH}_3\text{NH}_3\text{PbCl}_3$  interconversion. (a,d) Photoluminescence profile as a function of time. At time  $t = 0$  s, the MAX solution was injected in the cuvette. The sample was illuminated at  $60^\circ$  by a continuous wave 406 nm blue laser and detected at right angle onto the CCD camera. (b,e) change in absorbance due to the transformation reaction. At time  $t = 0$ , the MAX solution was injected into the cuvette. A FTO/ $\text{Al}_2\text{O}_3$  blank was subtracted. (c,f) XRD profile of the reactions. The samples were dipped in MAX for various times and the reaction was quenched in IPA.

proceeds (Figure 4.7a). Similarly, the exchange was performed without  $\text{Al}_2\text{O}_3$  scaffold and stopped on a flat FTO substrate, after either 0.5 seconds or 1 minute by quenching in isopropanol. In this case we observed a red-shift of up to 17 nm of the near IR luminescence maximum (Figure 4.12c). Scanning electron micrographs of the as-deposited  $\text{CH}_3\text{NH}_3\text{PbCl}_3$  are shown in Figure 4.12a. The  $\text{CH}_3\text{NH}_3\text{PbCl}_3$  appears amorphous at high resolution. After 0.5s dipping time however, we observe the growth of 20-30 nm size  $\text{CH}_3\text{NH}_3\text{PbI}_3$  crystals nucleating from the  $\text{CH}_3\text{NH}_3\text{PbCl}_3$  (Figure 4.12b). Line broadening analysis by X-Ray diffraction over the (110) reflection places a lower boundary for the crystal size at 32 nm (Figure 4.12d), correlating well with SEM micrographs. The large population of  $\text{CH}_3\text{NH}_3\text{PbI}_3$  crystals would evidently contribute significantly to any PL signal, and therefore we conclude that quantum confinement is unlikely to occur as the reported Bohr exciton radius of  $\text{CH}_3\text{NH}_3\text{PbI}_3$  is much lower (2.2 nm) than the particle size we measured [164, 165]. The observed blue shifted luminescence is therefore tentatively assigned to a transient  $\text{CH}_3\text{NH}_3\text{PbI}_3$  amorphous phase which is not observed by XRD, as it was explained by Choi [163]. As the  $\text{CH}_3\text{NH}_3\text{PbI}_3$  grows more crystalline (shown by the shrinking of the  $14.2^\circ$  reflection, Figure 4.7c), the amorphous phase gradually disappears, which is accompanied by a red-shift of the luminescence.

Considering that a full morphological change is included, the swiftness at which the chlorides are transformed into the iodides is remarkable, indicating a fast halide diffusion rate. We expect that similar mechanisms occur in solid state chloride-iodide exchange, such as the

ones described by Dualeh et al[145]. That  $\text{CH}_3\text{NH}_3\text{PbCl}_3$  is merely present to direct the growth of the  $\text{CH}_3\text{NH}_3\text{PbI}_3$  comes therefore at no surprise to us.

### 4.3.6 $\text{CH}_3\text{NH}_3\text{PbI}_3$ to $\text{CH}_3\text{NH}_3\text{PbCl}_3$

The  $\text{CH}_3\text{NH}_3\text{PbI}_3$  to  $\text{CH}_3\text{NH}_3\text{PbCl}_3$  conversion proceeds also rapidly. The 790 nm emission of the iodide disappears within 5 seconds following the exposure of the film to  $\text{CH}_3\text{NH}_3\text{Cl}$ . The  $\text{CH}_3\text{NH}_3\text{PbI}_3$  PL peak initially blue-shifts by 13 nm as it converts into  $\text{CH}_3\text{NH}_3\text{PbCl}_3$ . It appears that this effect is similar to the one observed in the chloride to iodide exchange. However when the reaction is performed in the dark and stopped at various times, we noticed that the exchange was far slower, as it took up to 1 min for all traces of the iodide phase to disappear (Figure 4.7f) as indicated by the X-ray diffraction pattern. The fluence of the laser used in the time-resolved PL measurement is probably responsible for the increased reaction rate as most of its power is absorbed by  $\text{CH}_3\text{NH}_3\text{PbI}_3$  and dissipated into heat locally. Similarly, the absorbance measurement shows that the reaction is somewhat slower than observed by time-resolved PL: the absorbance in the green-red region drops uniformly vanishing after 25 seconds only (Figure 4.7e), indicating the disappearance of the iodide phase.

## 4.4 Growth and halide exchange of perovskite nanowires

Directional hybrid perovskite nanowires have been a promising approach not only for solar cells[140, 167], but also photodetectors[168, 169, 170], lasers[171, 114, 172] and light-emitting diodes[173]. We have previously on a growth technique based on a modified two-step conversion of  $\text{PbI}_2$  into extremely directional  $\text{CH}_3\text{NH}_3\text{PbI}_3$  nanowires[140]. Other techniques such as slip coating[169, 174] and evaporation-induced self-assembly[167] we also reported.

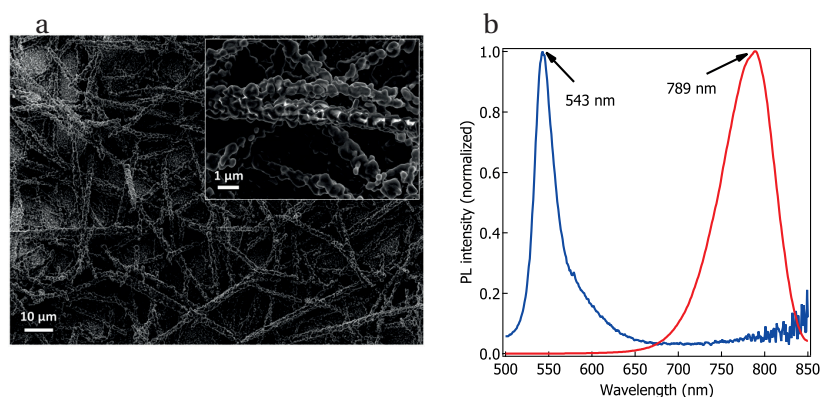


**Figure 4.8:** (a) SEM micrograph of  $\text{CH}(\text{NH}_2)_2\text{PbBr}_3$  nanowires obtained by bromide exchange from  $\text{CH}(\text{NH}_2)_2\text{PbI}_3$  nanowires. (b) Photoluminescence spectra of the originating  $\text{CH}(\text{NH}_2)_2\text{PbI}_3$  and resulting  $\text{CH}(\text{NH}_2)_2\text{PbBr}_3$  nanowires.

In the modified two-step synthesis, a thin-film, uniform  $\text{PbI}_2$  film is exposed to a  $\text{CH}_3\text{NH}_3\text{I}$  solution in isopropanol containing a 1% additional DMF, which is the essential component that is required for nanowire growth. This technique was further used by Zhu[168]. It is believed that directional perovskite nanowires grown in this way are the thermodynamic product of the perovskite two-step conversion. Furthermore, it has become evident that the nanowire growth goes through the intermediate of a DMF-MAI- $\text{PbI}_2$  adduct[139, 175, 176] which structure has yet to be resolved. The formation and re-dissolution of this adduct is believed to drive the preferred growth along one axis. So far, growing nanowires of the cubic  $\text{CH}_3\text{NH}_3\text{PbBr}_3$  phase have been unsuccessful under similar conditions. This underlines the importance of iodine in the nanowire growth, hypothetically relating the thermodynamics of the formation of the adduct to the relative size of the bromide to the iodine anion.

However, we demonstrated that it is possible to apply the solution-based halide exchange reaction to  $\text{CH}_3\text{NH}_3\text{PbI}_3$  and  $\text{CH}(\text{NH}_2)_2\text{PbI}_3$  nanowires to yield  $\text{CH}_3\text{NH}_3\text{PbBr}_3$  and  $\text{CH}(\text{NH}_2)_2\text{PbBr}_3$  nanowires while conserving the general one-dimensional order. However, due to the lattice mismatch of the iodide and the bromide phase, the nanocrystals forming the nanowires have clearly shrunk, leaving gap between them, while still being interconnected. Similarly, the resulting  $\text{CH}_3\text{NH}_3\text{PbBr}_3$  and  $\text{CH}(\text{NH}_2)_2\text{PbBr}_3$  could be converted into their respective  $\text{CH}_3\text{NH}_3\text{PbCl}_3$  and  $\text{CH}(\text{NH}_2)_2\text{PbCl}_3$  phase.

## 4.5 Conclusion and outlook

In this chapter, we described the dynamics of the halide exchange system in methylammonium lead halide films. We showed that all exchange reactions, except the bromide to iodide, can proceed to completion within less than 5 minutes. We showed how the morphology of the films was influenced by those reactions, specifically that the chloride/iodide exchange completely scrambles the crystal shape because both halides do not intercalate together in the perovskite lattice. We also showed that starting from the chloride creates highly fluorescent states for both the iodide and the bromide, although the high fluence of the pump laser may have some responsibility for this effect. We attributed the unusually strong luminescence of wet films to the passivation of surface states or the filling of vacancies by the halides or methylammonium present in solution. Based on this work, we then showed that high aspect ratio nanowires of  $\text{CH}_3\text{NH}_3\text{PbI}_3$  can be efficiently converted into  $\text{CH}_3\text{NH}_3\text{PbBr}_3$  while retaining their overall structure.

## 4.6 Additional figures

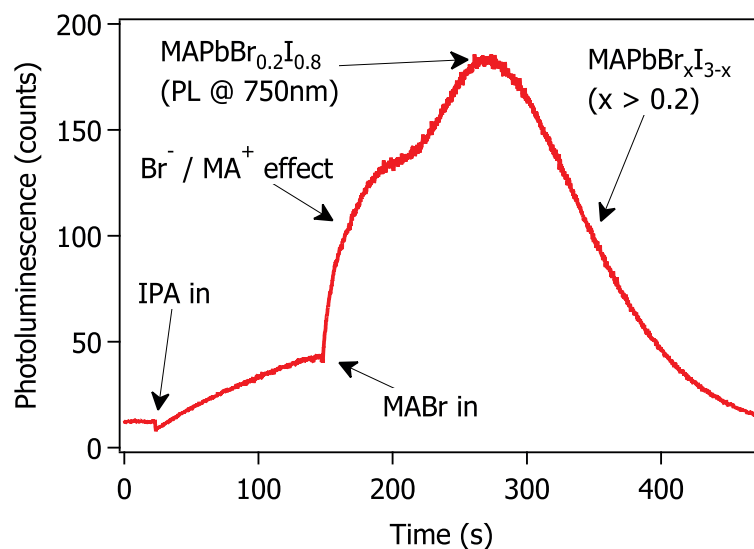


**Figure 4.9:** 2-propanol and  $\text{MA}^+/\text{Br}^-$  effect on the photoluminescence of  $\text{CH}_3\text{NH}_3\text{PbI}_3$  monitored at 750 nm. After 30 seconds, IPA is introduced, leading to a slow increase of the luminescence up to 20 times the original luminescence intensity. After 150 seconds,  $\text{CH}_3\text{NH}_3\text{Br}$  in 2-propanol (0.05 M) is added, increasing the luminescence by a factor of 2. The second peak is due to the formation of the mixed bromide-iodide whose fluorescence peak is located at 750 nm. The conversion kinetics here are much slower than the ones described in the iodide to bromide exchange, as it is limited by the diffusion of  $\text{Br}^-$  into the IPA

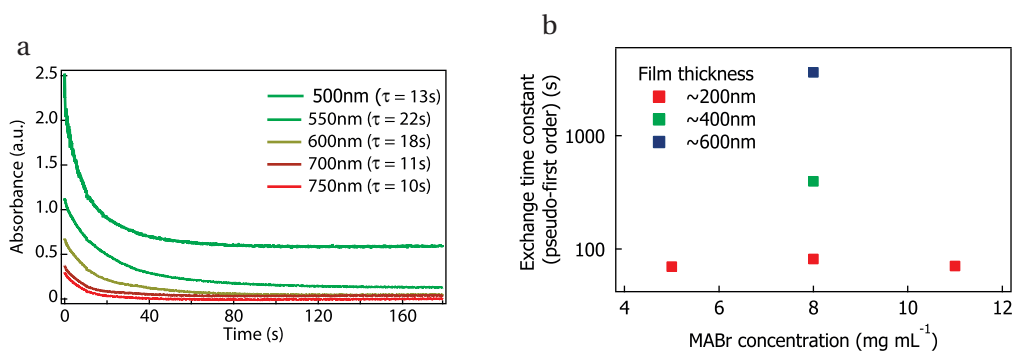


**Figure 4.10:** (a) Absorbance profile of the iodide to bromide exchange performed on a 150 nm thick  $\text{CH}_3\text{NH}_3\text{PbI}_3$  evaporated thin film on FTO conductive glass. The traces were fitted to a single exponential decay. A blank sample consisting of bare FTO provided the baseline. (b) Extracted pseudo first-order time constant as a function of the  $\text{CH}_3\text{NH}_3\text{Br}$  concentration and thickness of a flat  $\text{CH}_3\text{NH}_3\text{PbI}_3$  film deposited through a solution route.



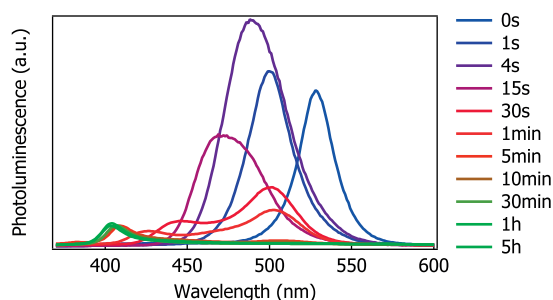


**Figure 4.11:** Photoluminescence spectra of films of  $\text{CH}_3\text{NH}_3\text{PbBr}_3$  undergoing conversion into  $\text{CH}_3\text{NH}_3\text{PbCl}_3$  by an anion exchange reaction. The samples were quenched in 2-propanol after various times and measured on a calibrated spectrofluorometer. The fluorescence at 400 nm belongs to  $\text{CH}_3\text{NH}_3\text{PbCl}_3$ .

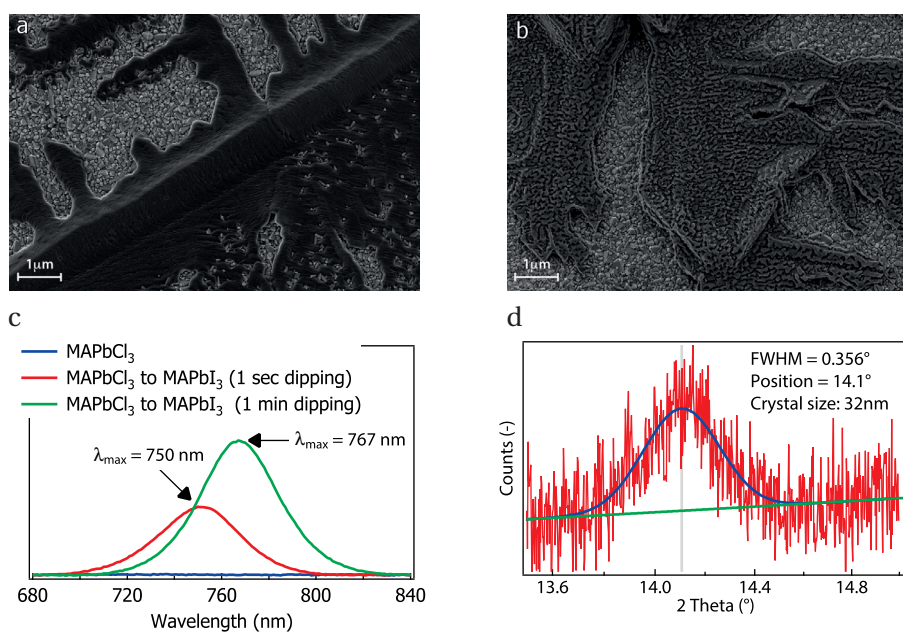


**Figure 4.12:** (a) SEM micrograph of  $\text{CH}_3\text{NH}_3\text{PbCl}_3$  deposited on conductive glass. (b) SEM micrograph of  $\text{CH}_3\text{NH}_3\text{PbCl}_3$  on conductive glass partially converted into  $\text{CH}_3\text{NH}_3\text{PbI}_3$  by dipping in a 0.05 M  $\text{CH}_3\text{NH}_3\text{I}$  solution in 2-propanol. (for 0.5 s) (c) Photoluminescence of  $\text{CH}_3\text{NH}_3\text{PbCl}_3$  before and after its conversion into  $\text{CH}_3\text{NH}_3\text{PbI}_3$  for 0.5 s and 1 min (d) Line broadening analysis of the 14.1° peak after 0.5 s dipping. The Scherrer equation yielded a lower bound for the crystal size of 32 nm.



# 5 Maximum power point tracking of perovskite solar cells

*The following chapter describes strategies, challenges and implementations of maximum power point tracking of perovskite solar cells. The figures and part of the following text is primarily based on an article published in a peer-review journal. The work has been done in collaboration with Dr. Fabrizio Giordano*

## 5.1 Motivation

Together with the surge of the power conversion efficiency of metal halide lead perovskite solar cells over recent years come concerns of long-term intrinsic and extrinsic stability of the hybrid perovskite layer. In particular, their sensitivity to heat, moisture and oxygen have been recognized. Some other problems, such as stoichiometric polarization and phase segregation, are expected when the devices are measured under real working conditions (maximum power point tracking at 60 °C). On the long run, stability will certainly decide on the fate of  $\text{CH}_3\text{NH}_3\text{PbI}_3$  and related lead perovskites for their use in photovoltaic modules. In this chapter, we show an effective and inexpensive strategy to perform ageing tests of perovskite solar cells under maximum power point tracking. For the first time we analyze the issue of power extraction from solar cells exhibiting hysteresis. We show that a standard tracking algorithm such as Perturb and Observe fails to converge to the maximum power point of the solar cell if they exhibit  $j(V)$  hysteresis and we present an effective strategy to stabilize the algorithm. We show that enforcing oscillation in forward bias can boost the mean power output of some perovskite solar cells by more than 10%, in contrast to a reference crystalline silicon solar cell.

## 5.2 Introduction

Stability concerns of 3<sup>rd</sup> generation photovoltaics, such as dye sensitized solar cells (DSSCs)[40], organic photovoltaics or polymer photovoltaics have long been recognized, studied and extensively reported[177, 178, 179, 180, 181, 182]. Yet, when it comes to organic-inorganic

## Chapter 5. Maximum power point tracking of perovskite solar cells

---

perovskite-based systems, stability studies[183, 100] have thus far been largely overshadowed by reports of increasing power conversion efficiencies (PCE)[55].

It is urgent to consider the interplay between stability and efficiency, rather than looking at the two issues separately. Mimicking real-life ageing conditions requires applying a load, preferably dynamic, on the solar cell. Leaving devices at open-circuit or short-circuit are not proper measurements and can lead to misinterpretation of the mechanisms dictating the stability. The test devices could be kept under a constant load, using a Schottky diode to drop a fixed potential, or using a fixed load resistance. They would require being periodically taken out of the light soaking setup for voltage sweep and power conversion efficiency measurements. During the ageing test, the devices would become improperly loaded if small changes in the  $j(V)$  characteristics of the cell occur. Alternatively, devices can be connected to a potentiostat with a maximum power point tracking (MPPT) algorithm or by applying a fixed potential to the cell. In this chapter, we report on the design of a small and inexpensive maximum power point tracker in the form of an electronic board that can handle up to 8 lab-scale devices simultaneously. Appendix D shows the electronic schematics, bill of materials and the microcontroller code. MPPT algorithms come with various levels of complexity and implementation costs and already extensively covered in the literature. However, they are usually tested against well-established PV technologies, such as silicon modules. In this chapter, we demonstrate the issues entailed by this approach when applied to PSCs which, in most cases, show anomalous hysteresis in their  $j(V)$  characteristic[184, 64].

The large chemical capacitance of the PSCs[185] is a challenge for fast power tracking as it interferes with the convergence of the tracking algorithm: standard perturb and observe (P&O) algorithms fail to track the optimal power of perovskite-based cells and lead to large oscillations of the power output. For small-scale laboratory measurements, we apply a simple modification to standard algorithm by introducing two new parameters that stabilize it: the sweep-inverting thresholds, which describe by how much the power has to drop relatively to a previous local maximum before the P&O switches direction. Judicious choices of the algorithm parameters help reducing the oscillations and stabilize the device power output. This implementation in large-scale systems should be addressed from the perspective of power electronics where the power is fed into a buck-boost converter, but the strategy presented here remains valid. A major finding of this study is that for most perovskite solar cells, the best power output is not obtained when the algorithm oscillates closely around the maximum the power point, but rather when large forward voltage poling pulses are applied. In some cases, the mean power output was higher by over 11% when compared to the quasi steady-state situation. This is an unprecedented situation, which does not occur in crystalline silicon solar cells and calls for further studies in the power tracking of perovskite solar cells.

### 5.3 Maximum power point tracking

The power-voltage characteristics of photovoltaic cells are non-linear and strongly affected by illumination, temperature or ageing. Maximum power point tracking control is essential to keep large-scale photovoltaic arrays at peak power. Variations of irradiance and temperature vary with the illumination angle, solar spectrum or partial shading (clouds, dust, ...) and can relatively rapidly shift the optimal working voltage of the solar cell. On a laboratory scale, MPPT is used to confirm the sustained power output of the cell or to perform ageing under simulated outdoor conditions. Perturb and Observe (P&O)[186, 187, 188, 189, 190, 191, 192, 193, 194, 195, 196] and Incremental Conductance (IncCon)[197, 198, 199, 200, 201, 202, 203, 204] are the most popular MPPT methods owing to their effectiveness and ease of implementation. P&O relies on hill climbing: the power output is maximized by constantly perturbing the operating voltage (perturb stage) and recording its effect on the power output (observing stage)[198]. Most of the literature reports on MPPT algorithms aim at improving the steady-state performance, the transient response[191, 205, 206], and the cost of implementation[45]. Aside from P&O, other closed loop algorithms include incremental conductance [207], fuzzy logic[208, 209, 210, 211, 212], neural networks[213, 214, 215], load maximization[216, 217] or ripple correlation current (RCC)[218]. In RCC, the ripple current (or voltage) of the PV array that naturally occurs upon switching of the buck-boost converter is recorded to determine the array conductance[187]. This technique has gained significant traction because of its effectiveness at steady-state and its fast transient response[219, 218], but will fail if the conductance has an imaginary component at the switching frequency due to the capacitive behavior of the module. The issue of the output capacitance in RCC was recognized and approaches to mitigate it by calculating the power-voltage correlation (instead of power-current correlation) have been somewhat successful[220, 221]. However, the chemical capacitance of the perovskite solar cell is (a) much larger than what has been considered[63] in refs. [220, 221] and (b) is not an external capacitor closely placed to the converter, but it is “sandwiched” in between the electron and hole transport layers of the device. As a result, both the power-voltage and power-current correlations have a potentially large out of phase component, which impedes the convergence of the incremental conductance algorithm.

#### 5.3.1 Perturb and Observe algorithm

Perturb-and-observe algorithms are implemented by continuously sampling the current and the voltage of the solar cell. The power is computed and compared to the previously recorded one. If the sign of the differential  $\partial P/\partial V$  is positive, the voltage is increased. If it is negative, the voltage is decreased. Around the maximum point, the algorithm will naturally perform small oscillations. A flowchart of the algorithm is shown in Figure 5.1a. It reads as follows: the current and voltage of the solar cell are sampled at the cycle  $k$ , yielding  $i(k)$  and  $v(k)$ . The algorithm will reject any below noise level voltage or current variation ( $i(k) - i(k-1) < \epsilon_i$  and  $v(k) - v(k-1) < \epsilon_v$ )[222]. The power is computed ( $p(k) = i(k)v(k)$ ) and compared to the previous one ( $p(k-1)$ ). If it has increased, the voltage is incremented by the value

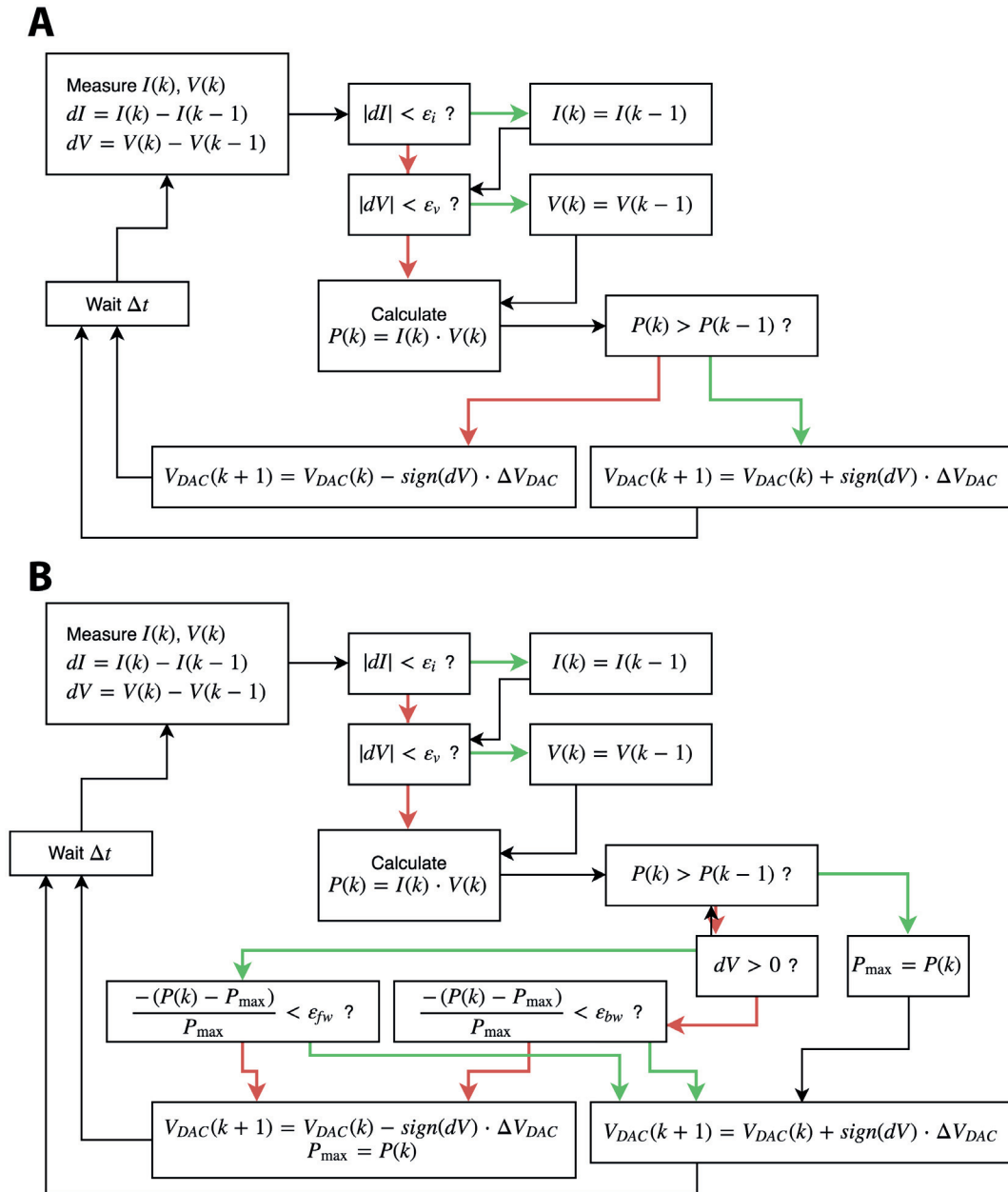


**Figure 5.1:** (a) Standard perturb and observe (P&O) algorithm flowchart for the generic cycle  $k$ , including noise thresholds ( $\eta_i$  and  $\eta_v$ ) to correct the transient behavior of the sampler, non-linearity and noise. In this configuration, the correction of the load is not done through adapting the duty cycle of the buck converter, but through changing the applied voltage driving the solar cell. (b) modified perturb and observe (P&O) algorithm flowchart, including the power thresholds  $\epsilon_{fw-bw}$  and  $\epsilon_{bw-fw}$ . The local maximum power is adapted each time the power increases or when a switch in scanning direction is done. Green arrows are followed when the condition is "true" and the red ones when it is "false"

### 5.3. Maximum power point tracking

sign  $dV \Delta v_{\text{DAC}}$  (the device is biased further into the direction it is currently going). If the power output has decreased compared to the previous one, the direction of tracking is reversed and the bias is incremented by  $-\text{sign } dV \Delta v_{\text{DAC}}$ , where  $v_{\text{DAC}}$  is the algorithm voltage step size. This step is the hill-climbing part of the algorithm. The new local maximum is updated and the cycle  $k + 1$  begins.

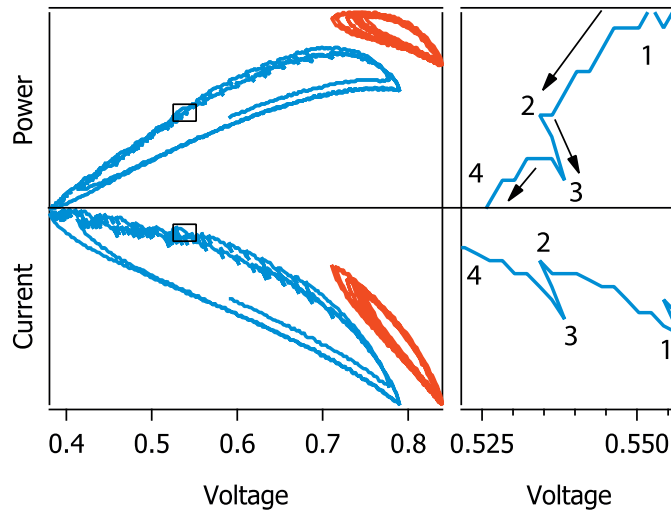


**Figure 5.2:** Blue: P&O algorithm performed without threshold regulation. Orange: Modified algorithm that includes the power threshold regulation, showing reduced oscillations. Arrows represent the scanning direction.

In practice, we found that this somewhat naive implementation yields poor results for the tracking of perovskite solar cells. Below the maximum power point (Figure 5.2, point 1), the power decreases as the voltage is decreased. When the noise threshold is surpassed (Figure 5.2, point 2), the algorithm switches direction, increases the voltage and records a new point (Figure 5.2, point 3). In PSCs, the power at point 3 has usually further decreased, for most positions of the tracker on the  $j(V)$  curve. The algorithm therefore decides to switch again the perturbation backwards (point 4) and the voltage keeps decreasing, diverging from the ideal maximum power point. As a result, large oscillations are created below the actual maximum power point. This power drop between point 2 and 3 confuses the algorithm, led to believe that the maximum power point is at even lower voltage. Similar cycles are repeated again and again at voltages far below the optimal one, until some point at which the voltage is so low that the power doesn't drop anymore upon switching the direction to forward scanning. The voltage then climbs up uninterruptedly until reaching a new maximum power point at higher bias. On average, the tracking is done at a potential lower than optimal and the device undergoes significant voltage oscillations. Significantly decreasing the sampling rate until the phase shift of the cell response is minimal is an effective way to solve the tracking instability, but comes at expense of the transient response.

In an effort to optimize the MPPT P&O algorithm at fast sampling rates, we propose to add

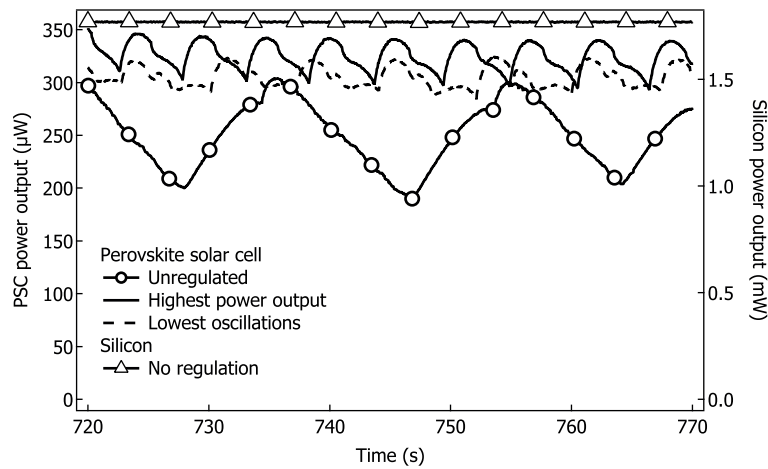


**Figure 5.3:** Maximum power point tracking of a  $\text{CH}_3\text{NH}_3\text{PbBr}_3$  solar cell (circles, dashed, solid) and a crystalline silicon cell (triangles) under various threshold conditions. Circles: No threshold regulation. Dashed: lowest attained oscillation. Solid: highest attained efficiency. The silicon cell was not regulated.

thresholds ( $\varepsilon_{fw-bw}$  and  $\varepsilon_{bw-fw}$ ) below which the power has to drop – compared to the previous local maxima - before switching direction (Figure 5.2, orange trace). Similar concepts have been proposed with the purpose of achieving faster transient response of the P&O[223], but never as a mean to track largely capacitive solar cells. Adding a hysteretic controller forces the voltage sweep further into one direction before switching to backward scan, despite a recorded power drop. When the threshold is set too low, the device will be tracked at a bias lower than optimal (figure 2 and 3), whereas a threshold higher than necessary will induce unnecessary power oscillations that are detrimental to the average power output. Such thresholds are usually not required for currently marketed PV technologies, since the  $j(V)$  relationship of silicon solar cells and most thin film technologies is transient-free at the chopping frequency of most DC-DC boost converters (slower than the RC time constant or the solar cell). Similar oscillations and instabilities have been recognized for the P&O algorithm when illuminations conditions are changing faster than the sampling rate[44], and hysteresis adds to this issue. Figure 5.3 shows an example of MPPT of a conventional bromide perovskite-based solar cell and compares it to a silicon solar cell without regulation (triangular markers). Clearly, the perovskite cell works better with the power inversion threshold (solid and dashed traces) than without (round markers). Figure 5.5 shows the average power output (figure 5.5a) and the oscillation intensity (figure 5.5b) as functions of the inversion threshold. The average power output of the solar cell is not improved by the backward to forward threshold (vertical axis): when the device is switched from scanning forward to scanning backward, the power output always immediately increases. When it is used and set too high, it is actually detrimental to device performance: the device is scanned too far at voltages below VMPP before the scanning direction is inverted. On the other hand we found that the power output is strongly correlated to  $\varepsilon_{bw-fw}$  (the forward to backward threshold, horizontal axis). By preventing the device from switching too easily from forward to backward scan, the algorithm



## 5.4. Optimal performance through poling

leaves sufficient headroom for the power drop that occurs upon switching scanning direction, such that the algorithm is allowed to proceed to higher voltages, where the steady-state power output is higher. Thanks to  $\varepsilon_{fw-bw}$ , the strong oscillations of figure 5.2 and 5.3 can be avoided. Overall, the stabilization improves the power output by over 30% when compared to the non-regulated algorithm. Figure 5.5c depicts the same experiment performed with a reference silicon device, where the absence of hysteresis means that the tracking is done best with the lowest power threshold.

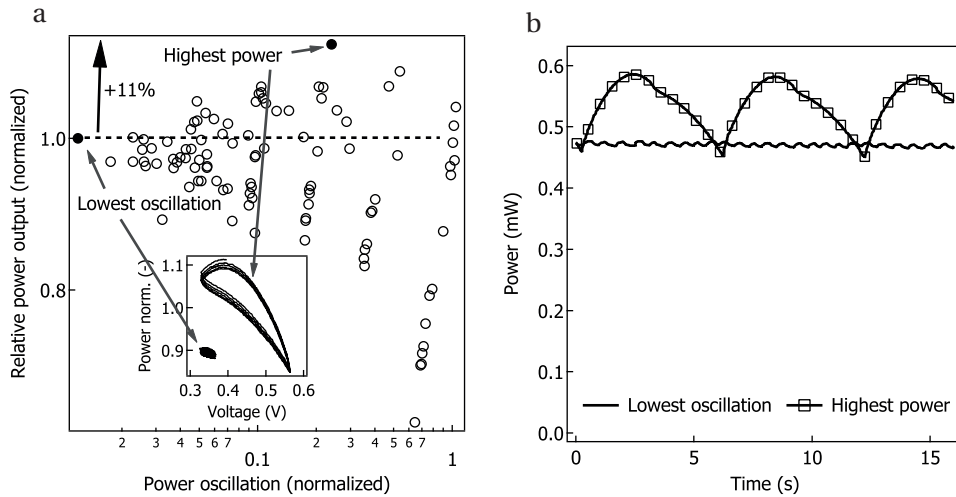


**Figure 5.4:** (a) Mean power output as a function of the power oscillation (normalized to the highest power) for a hole-transporter free perovskite solar with a carbon back-contact, acquired for various sets of voltage inversion thresholds (backward and forward). Each circle represents the power and oscillation obtained for a specific set of thresholds ( $\varepsilon_{fw-bw}$ ,  $\varepsilon_{bw-fw}$ ), using 11 values ranging from 0.8% to 82% (121 points in total). The point with the lowest oscillation (leftmost point, using  $\varepsilon_{fw-bw}=1.28\%$ ,  $\varepsilon_{bw-fw}=0.32\%$ ) and the one with the highest efficiency (topmost point, using  $\varepsilon_{fw-bw}=20.48\%$ ,  $\varepsilon_{bw-fw}=2.56\%$ ) are represented with filled circles. Inset: power-voltage curve for the highest power point and lowest oscillation point as a function of voltage. The order in which the sets were chosen was randomized. (b) Power output plotted versus time for the two sets of thresholds mentioned in point (a).

## 5.4 Optimal performance through poling

Despite effectively stabilizing the algorithm using a set of thresholds, we found that the highest power output from the cell was not given by the set that minimizes the oscillation around the maximum power point. This is unexpected because setting a voltage away from the maximum power point should be sub-optimal. An example of power tracking with different forward to backward thresholds is shown for one device in figure 5.5d (power-voltage curve) and figure 5.3 (power-time curve). The average power output of the cell was found to be higher when it undergoes strong oscillation above the steady-state MPP, compared to the situation where it undergoes the lowest possible oscillation (3% for the cell depicted in figure

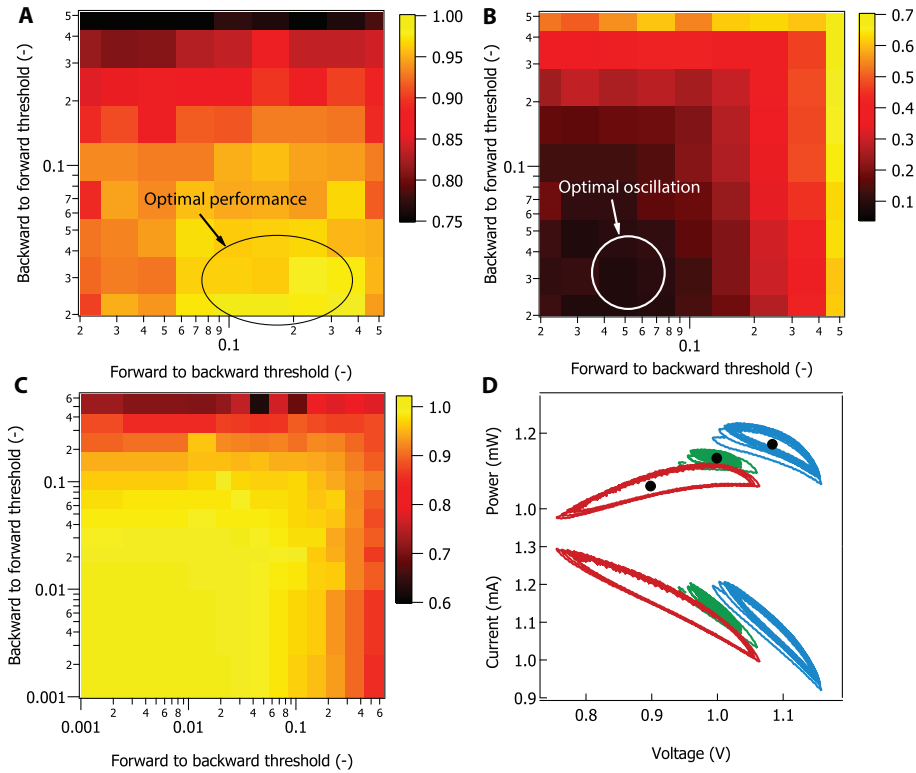


**Figure 5.5:** (a) Normalized power output of a CH<sub>3</sub>NH<sub>3</sub>PbBr<sub>3</sub> solar cell as a function of the power thresholds  $\varepsilon_{bw-fw}$  and  $\varepsilon_{fw-bw}$ . The circled area shows the region where the tracking parameters yield the highest averaged power output over 1 minute. Sampling of the matrix was performed randomly. (b) Peak-to-peak power oscillations of the algorithm (obtained simultaneously with figure 5.5a, normalized to the maximum power output). The circled area shows the region where the tracking parameters are optimal in terms of reduction of the output oscillation. (c) Normalized power output of a reference silicon solar cell as a function of the power thresholds  $\varepsilon_{bw-fw}$  and  $\varepsilon_{fw-bw}$ . The best regulation is obtained with the lowest possible thresholds. (d)  $j(V)$  curves of the device used for figure 5.5a and 5.3b, with different forward and backward power regulations. Red:  $\varepsilon_{bw-fw} = 0.04\%$ ,  $\varepsilon_{fw-bw} = 0.32\%$ , green:  $\varepsilon_{bw-fw} = 0.04\%$ ,  $\varepsilon_{fw-bw} = 2.56\%$  and blue:  $\varepsilon_{bw-fw} = 0.04\%$ ,  $\varepsilon_{fw-bw} = 10.24\%$ . The dots show the average power output of the cell at the average driving voltage.

5.5d and 5.3, and more than 11% for the HTM-free PSC depicted in figure 5.4). Figure 5.5 shows the average power and peak-to-peak oscillation as a function of both thresholds. The circled regions highlight the optimal oscillation (figure 5.5b) and the optimal power output (figure 5.5a) and do not overlap. This improvement reflects the fact that the power conversion efficiency of a PSC measured by a voltage sweep from  $V_{oc}$  to  $J_{sc}$  is usually higher than when swept from  $J_{sc}$  to  $V_{oc}$ . That a similar observation is sustained over large periods of time suggests that the hysteresis is not uniquely a capacitive charging-discharging effect, but that the charge collection efficiency of the cell is positively affected by poling in forward bias, even temporarily.[224] For hole-transporter free solar cells, this effect is even more prevalent. In figure 5.4, we show the mean power output (y axis) as a function of the relative oscillation (x

## 5.4. Optimal performance through poling

axis) for 121 sets of threshold values. When the cell undergoes the lowest recorded oscillation, close to 1% of the power (filled circle marker at the left of figure 5.4), it generates on average 11% less power than the highest one, obtained with more than 20% oscillation (filled circle marker at the top of figure 5.4). The inset in figure 5.4 shows the power-voltage curves for both conditions. The proper threshold was found by randomly sampling a set of possible values. In practice, an adaptive algorithm can be designed in order to converge toward the optimal set of parameters during power tracking.

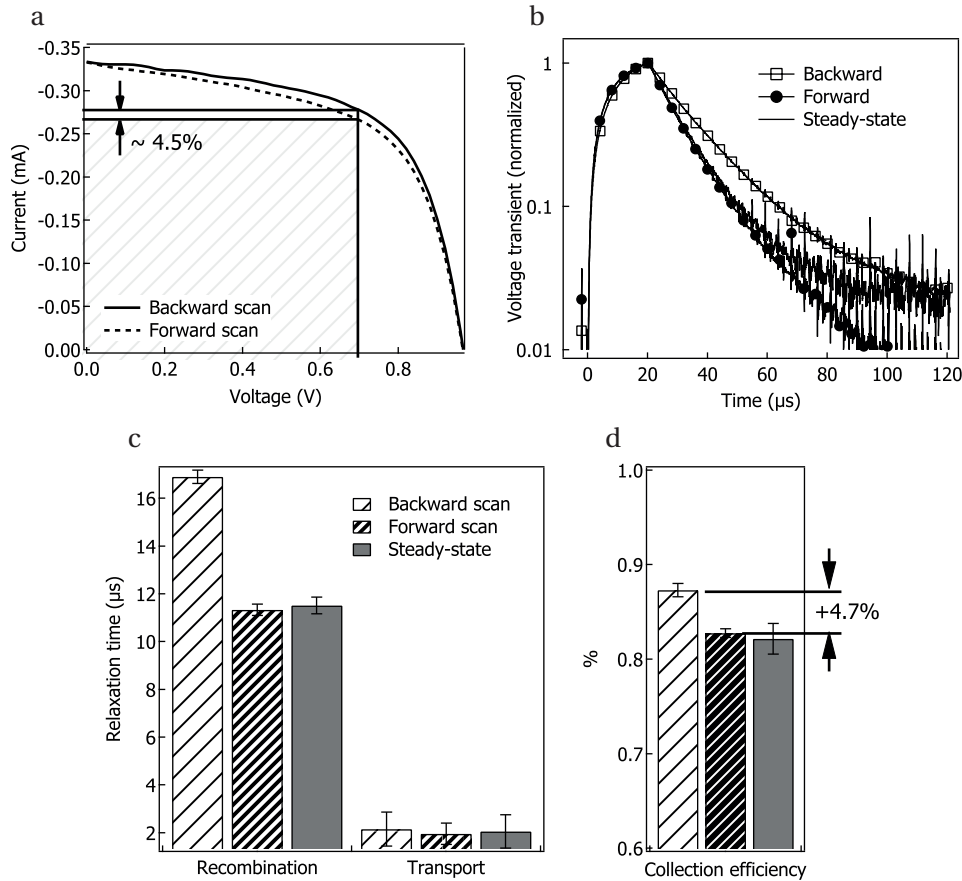


**Figure 5.6:** (a)  $j(V)$  curve for a typical hybrid perovskite solar cell, measured from  $V_{oc}$  to  $J_{sc}$  (backward) and from  $J_{sc}$  to  $V_{oc}$  under an 90% attenuated AM1.5G simulated solar irradiation. The sweep rate was  $200 \text{ mVs}^{-1}$ . (b) Transient photo-voltage traces upon an additional light excitation from a 422 nm laser diode ( $t_{\text{pulse}} = 20 \mu\text{s}$ ). The relaxation was fitted to a mono-exponential decay. The cell was constantly scanned from  $V_{oc}$  to  $J_{sc}$  (square and circle) markers or at steady-state (solid line, no markers). The light was pulsed precisely as the device voltage crosses 700 mV, either in the backward direction (empty squared) or in forward direction (circles). In the steady-state experiment, the cell was kept at 700 mV and the pulse applied periodically. (c) Resulting time constants from the TPV and TPC experiment, measured during the backward scan, forward scan and steady-state. (d) Resulting collection efficiency calculated from  $\eta = 1 - \tau_{\text{TPC}}/\tau_{\text{TPV}}$

## 5.5 Voltage poling and collection efficiency

To validate our hypothesis that polarizing the device in forward bias affects the charge collection efficiency, and that the  $j(V)$  hysteresis is not only an effect of capacitive charging and discharging, we performed transient photovoltage (TPV) and transient photocurrent (TPC) in non-steady state conditions. The TPV and TPC are the time-domain equivalent of IMVS and IMPS, presented in chapter 6. Unlike IMVS and IMPS, the transient technique need not ensure that the cell is in quasi-steady state condition. In our experiment, the device was illuminated by an array of white LEDs such that the generation current was roughly equivalent to the one provided by the  $100 \text{ W m}^{-2}$  AM1.5G reference spectrum (10% sun). The device was constantly scanned from  $V_{oc}$  to  $J_{sc}$  using either a voltage-controlled potentiostatic source or a voltage-controlled galvanostatic source (the exact same instrument as the one presented in chapter 6). The voltage set-point was given by a arbitrary waveform generator such that the voltage was constantly swept back and forth between  $V_{oc}$  and  $J_{sc}$  at a scan rate of  $200 \text{ mVs}^{-1}$ . Upon crossing a certain voltage value (in this experiment, 700 mV), an additional short light pulse of  $20 \mu\text{s}$  provided by a digitally controlled LED photodiode ( $\lambda = 422 \text{ nm}$ ) was directed onto the device. The resulting voltage perturbation and current perturbation was recorded, to yield the electronic transport rate and the recombination rate of the cell[225].

The  $j(V)$  curve of the device is shown in figure 5.6a. At 700 mV, the current difference between the backward and the forward scan was 4.5% (at  $200 \text{ mVs}^{-1}$ ). Confirming the observations from O'Regan[224], we observed that this result correlated well to an increase of collection efficiency during the backward scan when compared to the forward scan. While the transport rate remained largely unaffected by the scan direction, the recombination was significantly slower during the backward one. The overall improvement in collected efficiency was 4.7%, closely matching the value measured by voltage sweep measurements (4.5%).

## 5.6 Stabilizing the MPPT algorithm at fast speeds

The current hysteresis in the voltage sweep of organic-inorganic perovskite-based cells is well recognized, but its origin is still under debate[184, 64, 63]. It appears in both the voltage sweep and in the small signal complex response of the impedance of the solar cell[226]. Figure 5.8 shows the correspondence between the Nyquist impedance spectra of a  $\text{CH}(\text{NH}_2)_2\text{PbBr}_3$  and the corresponding  $j(V)$  Lissajous curves recorded under the same conditions. When the phase is minimum, less hysteresis is observed, which occurs either at high frequencies (above 150 kHz) or at intermediate frequencies (100 Hz to about 2 kHz). Figure 5.8 shows clearly that the condition  $p(t) = p(v(t))$  is generally not respected, even in the small perturbation regime. Although there is active research in limiting or suppressing the hysteresis of perovskite devices, reports of hysteresis-free solar cells mostly rely on slow voltage sweeps. One way to stabilize the algorithm is to reduce the sampling rate such that the cell has time to fully equilibrate at each new point. In figure 5.7a and b, we show the phase (Bode plot) and the impedance (Nyquist plot) acquired from a typical PSC. The usual low frequency Warburg-like feature

## 5.6. Stabilizing the MPPT algorithm at fast speeds

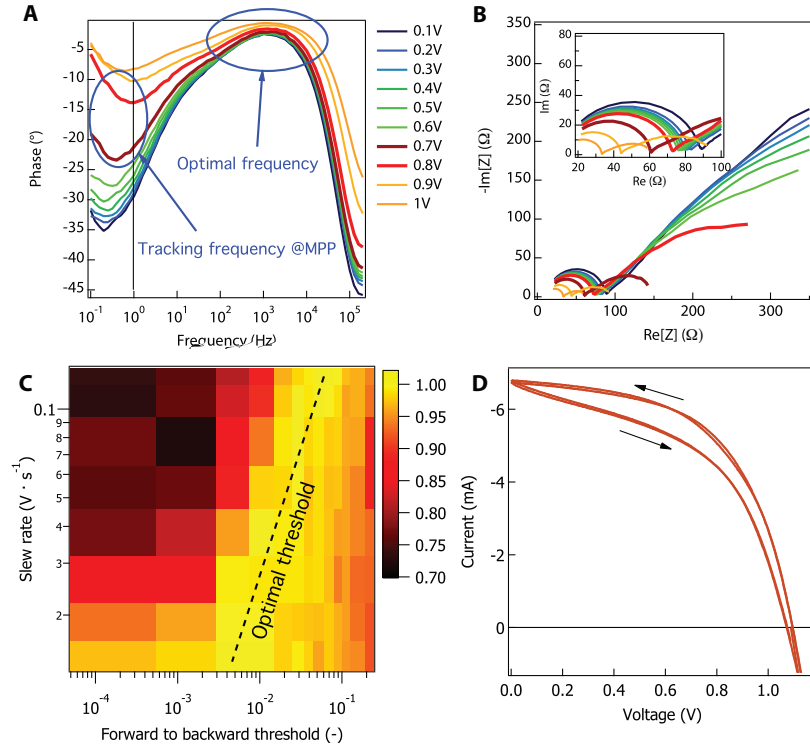


**Figure 5.7:** (a) Bode plot of the impedance phase of an  $m\text{-TiO}_2/\text{CH}_3\text{NH}_3\text{PbI}_3/\text{Spiro-MeOTAD}$  solar cell under an equivalent 10% illumination by a white LED. (b) Nyquist plot of the impedance for the same cell illuminated in the same conditions. (c) Averaged power output of the device under maximum power tracking, using the illumination intensity; plotted as a function of the forward to backward threshold (x axis) and slew rate (y axis). (d)  $j(V)$  relationship of the device scanned in both directions, under illumination, at  $200 \text{ mVs}^{-1}$ .

was previously attributed to ionic polarization in the cell[63]. It spans from about 100 Hz down to less than 0.1 Hz with a phase shift maximum between 0.2 Hz and 1 Hz depending on the bias. The low frequency complex component of the admittance is responsible for the power drop that occurs upon switching the voltage direction and for the failure of standard MPPT algorithms at intermediate frequencies. In figure 5.7c, we show a parametric matrix showing power output as a function of the forward to backward threshold (x axis) and the slew rate (y axis). When the fundamental frequency of the MPP algorithm is out of phase with the slow response of the device, higher power inversion thresholds need to be used to regulate the algorithm. At lower slew rates where the phase of the impedance is close to  $0^\circ$ , the power tracking is stable even with small thresholds. Alternatively, we suggest that the differential conductance could be obtained at frequencies where the phase of the Bode impedance is closest to 0, between the first and the second arc, in this region, the criterion is almost respected and the power gradient can be readily calculated from the ripple current[219]. The slow response of the device will be treated as a slow change in power output and treated accordingly. This sets a frequency window in which DC-DC converters can safely operate using a bandpass filter, but it requires prior knowledge of the frequency response of the photovoltaic

array.

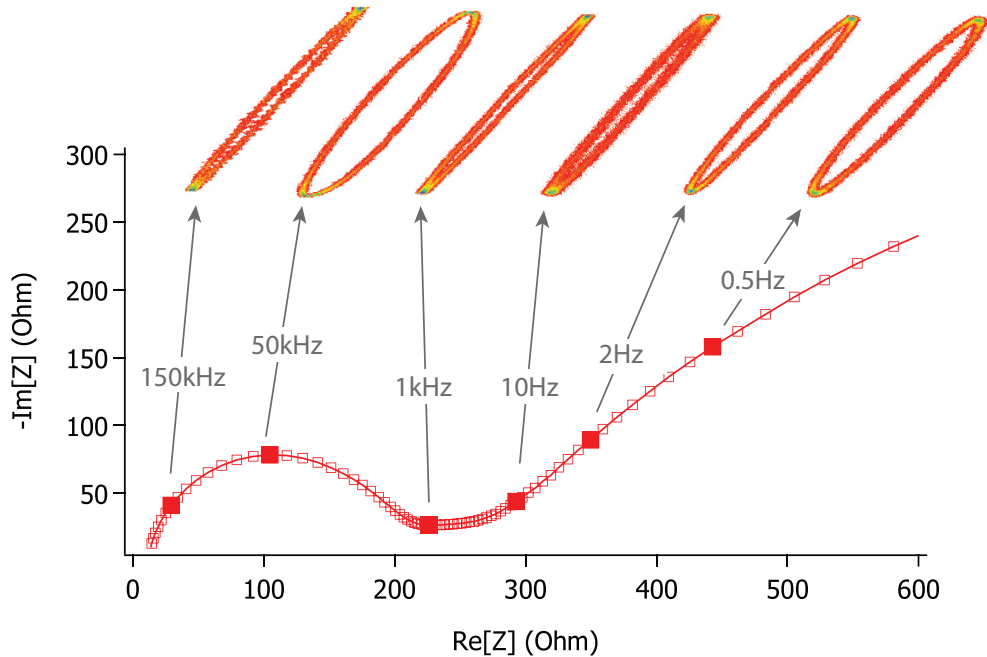


**Figure 5.8:** Nyquist impedance spectra of a  $\text{CH}_3\text{NH}_3\text{PbI}_3$ -based mesoscopic solar cell, measured at 950mV under an equivalent 1 sun illumination. The Lissajous curves (current vs. voltage) corresponding to a sinusoidal perturbation ( $V_{rms} = 22\text{ mV}$ ) under the same measuring conditions (light and DC bias) are shown above for the indicated frequencies

## 5.7 Example of ageing tests

Based on the modified tracking algorithm presented in this chapter, we performed long-term ageing measurements of perovskite cells in a sealed box permanently flushed with a constant flow of Argon (purity 99.998%). In figure 5.9, we show, as an example, the normalized power out of three typical solar cells over 600 hours, comprising a control device and two modified devices. The modification involved the use of hydrophobic PCBM derivatives drop-casted during the deposition of the perovskite layer[227]. Our ageing measurement showed that even when the control devices were aged under argon, the tiny amounts of water content that remains or seeps in destroys the perovskite layer in a matter of days. Adding hydrophobic molecules to the perovskite layer is thought to retard water ingress and hydration of the photoactive layer. In this study, PCBM and the PCBM derivative  $\alpha$ -bis-PCBM were used as the hydrophobic components[227]. The contact angle with deionized water droplets was measured by sessile drop measurement with deionized water droplets. The hydrophobicity of the perovskite layer reflects in the measured contact angle and matches the measured

degradation rate of the perovskite cells over time.

The most stable devices were obtained using the treatment with  $\alpha$ -bis-PCBM, which exhibited less than 4% drop of efficiency over more than 600 hours of measurement, while the control was fully degraded a couple of days only.

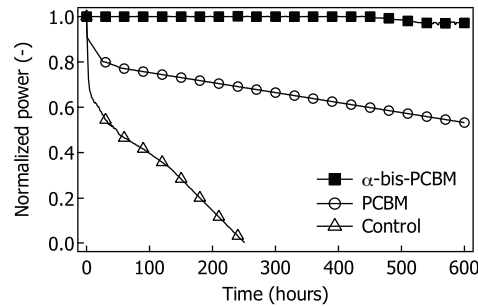


**Figure 5.9:** Normalized power output of three perovskite devices over time. The cells were kept under a constant illumination which power was equivalent to the visible portion of the AM1.5G spectrum at  $1000 \text{ W}^2 \text{ m}^{-1}$ . The devices were sealed in a tight box under a constant argon flow and tracked at maximum power.

## 5.8 Conclusion and outlook

Measuring and improving the stability of perovskite laboratory cell has become an urgent task. Often the means to perform correctly ageing tests on long time scales are lacking within research groups. We have reported the conception and realization of an inexpensive acquisition board capable of maximum power point tracking and  $j(V)$  sweeps and released the schematics in the appendix D. We have shown that tracking the maximum power of a perovskite cell is challenging due to the low frequency response of PSCs. To alleviate the hysteretic response and non-optimal power tracking, an arbitrarily defined power inversion threshold is introduced into the classical perturb-and-observe algorithm, which forces the device into a regime of controlled oscillation that does not necessarily come at the expense of the power output. On the contrary, for HTM-free perovskite devices, improvements of power output by more than 10% were obtained by forcing the solar into oscillation. Such methods could be employed for larger area PV arrays by affecting the duty cycle of the DC-DC in a similar manner.





## 6 Intensity-modulated frequency response of perovskite solar cells

*This chapter describes the use of intensity modulated spectroscopy as a mean to study the electronic motion and mass transport within hybrid organic-inorganic perovskite devices. There is currently very little in the literature about the interpretation, even qualitative, of the intensity modulated response of perovskite solar cells. This work provides the basis for the explanation of the various spectral features we observed and how they correlate to the motion of electronic and ionic carriers inside a perovskite device. Contributions from Dr. Fabrizio Giordano, Dr. Donqin Bi and Dr. Xiong Li are acknowledged.*

### 6.1 Motivation

The function of a solar cell is to convert light into electrical work. The study of the interaction between light and charge carrier densities is therefore a fundamental task that can be fulfilled on various scientific level, ranging from the non-linear interaction of light and matter to terahertz spectroscopy, femtosecond transient absorption spectroscopy, all the way to the basic voltage sweep measurement of the solar cell. Each techniques provide a set of information that is valuable to the scientific community. There is no question that at this date, the thriving research in hybrid-organic perovskite solar cells strongly relies on trial and error. But one could make the case that at some point, deeper understanding of the interplay between the electrically active layers composing the solar cell will have to be gained, whether it is to achieve further efficiency improvements, to improve long-term stability or simply from a scientific interest. Typicall, solar devices are characterized by measuring a voltage sweep and to extract its  $j(V)$  characteristics, namely the open circuit voltage, the short circuit current, the fill factor and eventually the power conversion efficiency. Information can be gained from the analysis of the open circuit voltage with regards to the light intensity, or by fitting the current in the dark to known equations.

However, it is difficult to characterize the inner charge and mass transport, generation and

annihilation of the solar cell from pseudo-steady state measurements such as simple voltage sweeps. The logical next step is to record the cell response in the frequency spectrum, when a small ac field is applied to it. AC impedance spectroscopy (or EIS, for electronic impedance spectroscopy) has been widely used and reported for many kind of solar cells, including dye sensitized solar cells, organic solar cells, polymer solar cells and also for perovskite solar cells. This is therefore not the purpose of this work. In this chapter, we attempt at the study of charge carrier transport and storage when they are induced by light. We must therefore turn to a different set of techniques in the frequency space, which rely on the perturbation of a system at equilibrium by a sinusoidal perturbation in the form of light radiation. Depending on the boundary conditions of the cell (namely, on the impedance of the biasing circuit), these techniques are named IMVS and IMPS, for Intensity Modulated PhotoVoltage Spectroscopy and Intensity Modulated PhotoCurrent Spectroscopy. In this chapter, we explain how to relate the equivalent circuit of a cell to its observed frequency response. When possible, we write down the analytical expression to which the experimental data can be fitted. When not, we either process through the fitting of numerical simulations or simply qualitatively. Special attention will be given to low frequency components. A major drawback of IMPS and IMVS so far is that they are measured uniquely at short circuit and open circuit, respectively. A major part of this work was spent on the development of a pre-amplifier electronic circuit that enables any arbitrary biasing of the cell in both potentiostatic and galvanostatic mode. By forcing a potential across or a current through the cell, we ensure tight frequency-independent boundary conditions that allows the measurement of IMPS and IMVS as a function of voltage. To the best of our knowledge, this is the first report of potential-dependent IMVS and IMPS.

In addition to the well-developed network thermodynamic equations that describe charge and mass transport and storage, we extend those equations to the case where generation and recombination occur, and identify how to alter existing models to account for non-steady state electron and hole concentrations.

### 6.2 The IMVS and IMPS experiment

Part of the electronic and ionic processes that determine the  $j(V)$  characteristics of the photovoltaic device occur in the 1 MHz-DC frequency window and can be probed through the electrical leads of the device. Processes that do not directly yield to quasi-Fermi level changes cannot be probed electrically, such as exciton splitting or charge injection and have to be probed through optical means (such as pump-probe spectroscopy, terahertz spectroscopy or electro-absorption). When the internal processes of the cell affect the Fermi levels near the contacts, their effect can be probed by electrical techniques. They include electron-hole recombination, electron transport and mass transport.

Circuitual linearization using common circuit elements can be a good approximation of the device under quasi steady-state regime, yielding information about the competition between charge transfer, transport and recombination. Such circuits have been successfully used to

represent not only spatial but also thermodynamic displacement of mobile species, (electrons but also ionic carriers). While the Poisson equation, Fick's diffusion law and the Maxwell equation of displacement can be treated analytically or numerically, it is often simpler to construct an equivalent circuit using combinations of resistors and capacitors that answer Kirchhoff's laws of impedance. However, solar cells are inherently non-linear devices and fixed values of resistances and capacitances would not describe the solar cell behavior across its voltage range. In this situation, the solar cell model has to be linearized, that is the capacitances and resistances are given single values that are valid within the approximation of the linearization. It is common to perform such linearization as function of the electrodes electrochemical potential difference (the voltage across the device leads).

One way to achieve the quasi-steady-state conditions in a photovoltaic device is to apply small perturbations to the system in equilibrium, using either Dirac pulses or sinusoidal perturbations around the equilibrium condition. The latter is the fundamental idea behind AC impedance spectroscopy, which resolves the complex impedance of the device under test (DUT) as a function of frequency around a DC voltage point. An AC impedance spectrometer is configured to drive the DUT with a small AC voltage and record the current flowing through the device. The complex division of the ac voltage by the ac current yields the complex impedance.

In intensity-modulated spectroscopy, it is a light modulation, rather than a voltage perturbation, that is applied to the cell, using a fast LED or a CW laser diode. IM spectroscopy has been made popular by Frank[228] and Peter[229] in the late 90's owing to its ability to describe accurately the processes in dye-sensitized solar cells[229, 228, 230, 231]. It has been particularly useful in the description of the transport and recombination of photo-generated charges, which can not be directly accessed by impedance spectroscopy without some arbitrary assignment of the spectral features. In this technique, a DC light source is used to create the steady-state condition. A small AC photon flux is added on top of the DC component. The AC light is absorbed by the active layer and puts the electron and hole quasi-Fermi levels out of equilibrium. The Fermi levels equalize throughout the active film (dependent on the carrier mobility), through the transport layers (dependent on the charge transfer resistance) and finally propagate towards the electrodes (dependent on the carrier mobility in the transport layers), where it can be probed in the form of a voltage or a current, yet with a phase lag and an amplitude loss when compared with the generation current. By recording the phase and amplitude of the output signal and reconstructing the frequency spectrum, one can extract valuable information about the efficiency of the charge collection, which is affected by a wide variety of parameter, such as layer thicknesses, charge mobilities, charge transfer resistances, trap state distribution, ... To the best of our knowledge, equivalent circuits of perovskite solar cells for IMVS and IMPS have so far never been reported.

In this chapter, we begin by reviewing the standard network thermodynamic equations that describe the motion of charged species in an electrochemical device and their equivalent circuit elements. We then look more specifically into some of the equations that are specific to a solar cell outside of thermal equilibrium, namely generation and recombination. We

lay down the necessary equations that describe such processes and relate them to circuit elements.

Based on such understanding, we assemble various equivalent circuits that correspond to different cell architectures. Using numerical simulations, the qualitative effect of some of the equivalent circuit elements on the frequency response will be studied. Finally, we look at a few case studies of perovskite solar cells that use different processing technologies and we attempt to match the models with experimental observations.

### 6.3 Discretization of the model

We will consider here a quasi-one dimensional solar cell of area  $A$  and thickness  $L$ , with the constraint that  $\sqrt{A} \gg L$  (assuming a square electrode), separated in  $n$  slabs of index  $j$  and of equivalent thickness  $l = L/n$ . Since we will work in the frequency space and consider all capacitors ideally, all time derivatives are equivalent to the  $90^\circ$  phase shift element  $i\omega$ . We restrict our study to the cases where a small light perturbation is applied over a comparatively large DC light bias, condition required for the linearization of some of the processes.

#### 6.3.1 Carrier transport and storage

Mass and carrier fluxes are assumed to answer to the drift-diffusion equation, such that the current of a carrier  $i$  at position  $x$  is writes:

$$J_i^{\text{charge}}(x) = -\sigma_i(x, t) \nabla(\mu_i^*(x) + \phi(x)) \quad (6.1)$$

Where  $\mu_i^*(x)$  is the chemical potential normalized by the electrical charge:  $\mu_i^* = \mu_i / (ez_i)$  of the carrier  $i$ ,  $\sigma_i$  its conductivity and  $\phi$  the electrostatic field. Note that the conductivity is written as position-dependent, as it is be expected from different materials, phases, in space-charge layers, across grain or phase boundaries on in regions with varying doping levels. In a medium dominated by diffusion rather by drift, this equation reduces to the well known equations known from nanoporous  $\text{TiO}_2$  transport equations. For the sake of simplicity, we will consider the conductivity as time-independent. This approximation holds fairly well provided that the additional charge carrier density induced by the AC component of the light bias is low. For electronic carriers in a p-n junction, equation 6.1 is no other than the gradient of the quasi-Fermi level of charge element  $i$

$$J_i(x) = -\sigma_i(x, t) \nabla(E_{f,i}^*(x)) \quad (6.2)$$

#### 6.3.2 Continuity equation

The continuity equation (equation 6.3) ensures that no carriers are lost. For electrons and holes, it includes a transport component, a generation component and a recombination

component that relate to the interaction of light and matter.

$$\frac{\partial}{\partial x} J_i^{\text{charge}}(x, t) = G_i(x, t) - J_i^{\text{rec}}(x, t) - e z_i \frac{\partial c_i(x, t)}{\partial t} \quad (6.3)$$

For charges without generation-recombination, equation 6.3 simply writes:

$$\frac{\partial}{\partial x} J_i^{\text{charge}}(x, t) = -e z_i \frac{\partial c_i(x, t)}{\partial t} \quad (6.4)$$

Where  $c_i$  is the volumetric concentration of the carrier  $i$ <sup>1</sup>.

When the chemical potential of the carrier can be thought as a dilute element, the concentration of species can be expressed using the expression of the chemical potential for dilute solutions:

$$\mu_i = \mu_i^0 + k_B T \ln(c_i) \quad (6.5)$$

which is nothing else that the Maxwell-Boltzmann expression of the chemical potential for ions but can also be valid for electrons and holes (described by the Fermi-Dirac distribution), provided that their concentration is not too high and that the temperature is not too low:

$$\bar{n}_i = \frac{g_i}{e^{\frac{\mu_i^0 - \mu_i}{k_B T} + 1}} \Big|_{e^{\frac{\mu_i^0 - \mu_i}{k_B T}} \gg 1} = \frac{g_i}{e^{\frac{\mu_i^0 - \mu_i}{k_B T}}} \quad (6.6)$$

Equation 6.3 can be recast using the following differential:

$$\frac{\partial \mu_i(x, t)}{\partial t} = \frac{\partial \mu_i^0}{\partial t} + \frac{k_B T}{c_i(x, t)} \frac{\partial c_i(x, t)}{\partial t} = \frac{k_B T}{c_i(x, t)} \frac{\partial c_i(x, t)}{\partial t} \quad (6.7)$$

For electrons and holes, it is customary to refer to the chemical potential with respect to the band edge minimum (in flat-band condition) with degeneracy  $N_{cb}$  or  $N_{vb}$ . We will use the term  $N_s$  to describe either.

$$\frac{\partial \mu_i(x, t)}{\partial t} = \frac{N_s k_B T}{c_i(x, t)} \frac{1}{N_s} \frac{\partial c_i(x, t)}{\partial t} \quad (6.8)$$

which is the exact same expression as equation 6.7.

The continuity equation becomes:

$$\frac{\partial}{\partial x} J_i^{\text{charge}}(x, t) = G_i(x, t) - J_i^{\text{rec}}(x, t) - \frac{(e z_i)^2 c_i(x, t)}{k_B T} \frac{\partial \mu_i^*(x, t)}{\partial t} \quad (6.9)$$

To express the recombination term as a function of the electrochemical potential, we need to start by rewriting the continuity equation as a steady-state component and a time-dependent

<sup>1</sup>It is common to use  $n_i$  to mean the exact same thing, called the carrier density. It is also normalized by the volumetric element and can be used interchangeably. The notation  $c_i$  comes the solid state ionics perspective, while  $n_i$  rather from a PV perspective

component. It can be considered that the perturbed charge carrier concentration is minimal with regards to the steady-state one:

$$\frac{\partial}{\partial x} \left( J_i^{\text{charge}}(x) + \delta J_i^{\text{charge}}(x, t) \right) = (G_i(x) + \delta G_i(x, t)) - (J_i^{\text{rec}}(x) + \delta J_i^{\text{rec}}(x, t)) - \frac{(ez_i)^2 c_i(x)}{k_B T} \frac{\partial (\mu_i^*(x) + \delta \mu_i^*(x, t))}{\partial t} \quad (6.10)$$

The time-dependent components of equation 6.10 can be extracted:

$$\frac{\partial}{\partial x} \delta J_i^{\text{charge}}(x, t) = \delta G_i(x, t) - \delta J_i^{\text{rec}}(x, t) - \frac{(ez_i)^2 c_i(x)}{k_B T} \frac{\partial \delta \mu_i^*(x, t)}{\partial t} \quad (6.11)$$

For ions, we assume no generation and recombination process, hence the continuity equation takes the simplest form:

$$\frac{\partial}{\partial x} \delta J_i^{\text{charge}}(x, t) = - \frac{(ez_i)^2 c_i(x)}{k_B T} \frac{\partial \delta \mu_i^*(x, t)}{\partial t} \quad (6.12)$$

### 6.3.3 Carrier generation

Carrier generation occurs when a photon is absorbed by the semiconductor, upon which an additional electron is placed in the conduction band and a hole in the valence band. This has the effect of splitting the Fermi level into two quasi-Fermi (one for the electrons, one for the holes) that are out of equilibrium. A small perturbation over a DC illumination therefore creates a displacement of the electrochemical potential of holes and electrons by  $\delta \tilde{\mu}_e^*$  and  $\delta \tilde{\mu}_h^*$ .

In equation 6.3, it was implicitly considered that the photon absorption is independent on carrier density. Aside from the Burstein-Moss effect[232, 233], which we will ignore here, this is a good approximation (plus, from an experimental perspective, we will use a 422 nm blue light as the perturbation and the absorption coefficient of the material is affected by the Burstein Moss shift only close to the optical band edge energy). The spatial dependence on the generation profile can be expressed as:

$$G(x, \nu) = (ez_i) I_0 \alpha(\nu) 10^{-\alpha(\nu)x} \quad (6.13)$$

Which can be re-expressed into a steady-state and perturbed component:

$$G(x, \nu, t) = (ez_i) \alpha(\nu) 10^{-\alpha(\nu)x} \left( I_0 + \delta I e^{i\omega t} \right) \quad (6.14)$$

where  $\alpha(\nu)$  is the absorption coefficient dependent on the incoming photon energy. Figure 6.1 shows the generation current as a function of thickness and the thickness within which 90 % and 99 % of the generation current occurs, for pristine  $\text{CH}_3\text{NH}_3\text{PbI}_3$ . Conveniently, for 422 nm photons, the penetration depth  $\lambda_x$  where  $x$  is the fraction of absorbed photon is quite small

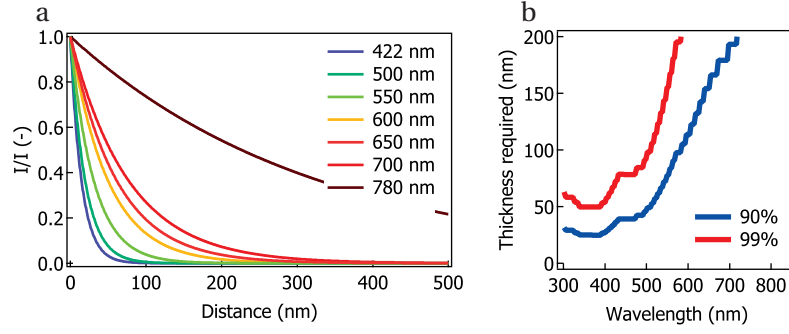


**Figure 6.1:** (a) Normalized generation current as a function of distance from the top of the sample for different wavelengths for pristine  $\text{CH}_3\text{NH}_3\text{PbI}_3$ . (b) Distance from the top of the sample at which 90 % and 99 % is absorbed

( $\lambda_{0.9} \sim 30$  nm), such that we can replace the generation current of equation 6.14 by a shallow surface generation, as it is expressed in equation 6.15. This has the advantage of replacing a volume generation (which should be numerically modeled as one current generator per element of the transmission line) by a single current source positioned in first decimated element of the transmission line model that represents the absorbing layer, as close as possible from the light source.

$$G(x, t) = ez_i \frac{\partial n_i}{\partial t} = \begin{cases} (ez_i) (I_0 + \delta I e^{i\omega t}) & x = 0 \\ 0 & x > 0 \end{cases} \quad (6.15)$$

- $I_0$ : large steady-state generation
- $\delta I(t)$ : small time-dependent perturbation

We can express the additional number of electrons (same treatment for holes) generated by the extra bit of light flux.

$$\begin{aligned} \delta n_0 + \delta n &= N_c \exp \frac{E_{f,e} + \delta E_{f,e} - E_c}{k_B T} \\ &= N_c \exp \frac{E_{f,e} - E_c}{k_B T} \exp \frac{\delta E_{f,e}}{k_B T} \\ &= n_0 \left( 1 + \frac{\delta E_{f,e}}{k_B T} \right) \end{aligned} \quad (6.16)$$

Where the time-dependent exponential term was linearized using a Taylor expansion, under the assumption that  $\delta E_{f,e} \ll k_B T$ . The steady-state component of equation 6.16 has no

frequency-dependent contribution and can be left out:

$$\delta E_{f,e}^* e^{i\omega t} = \frac{k_B T}{n_0} \delta I \quad (6.17)$$

The direct effect of light absorption is to bring additional carriers into the conduction and the valence band of the photo-absorber. In the small perturbation regime, it directly links to an increase of the electrochemical potential of the electrons and the decrease of the one of the holes and the surface generation current  $\delta I_0 e^{i\omega t}$ . However, in terms of equivalent circuit, the current source need not be expressed in terms of quasi-Fermi levels, as it is readily available as a constant value in the continuity equation. For numerical modeling, we will retain the approximation of the surface generation.

### 6.3.4 Carrier recombination

The recombination term  $R(x, t)$  can take various expressions, depending on the type of recombination that is considered. Generally though, recombination can be written as a function of hole and electron densities

$$J_{i,\text{net}}^{\text{rec}}(x, t) = G_{\text{therm.}}(x, t) - J_i^{\text{rec}}(x, t) = K(ez_i)^2 (pn - n_i^2) \quad (6.18)$$

Equation 6.18 can be re-written as a function of the quasi-Fermi level for holes and electrons

$$\begin{aligned} J_{i,\text{net}}^{\text{rec}}(x, t) &= -K(ez_i)^2 n_i^2 \left( \exp\left(\frac{E_{f,n}(x, t) - E_{f,p}(x, t)}{k_B T}\right) - 1 \right) \\ &= -K(ez_i)^2 n_i^2 \left( \exp\left(\frac{\tilde{\mu}_h(x, t) - \tilde{\mu}_e(x, t)}{k_B T}\right) - 1 \right) \end{aligned} \quad (6.19)$$

The exponential cannot be readily linearized because the difference of electrochemical potential is often larger than the thermal energy  $k_B T$ . Instead, we take advantage of the aforementioned quasi steady-state conditions to separate a small time-dependent term  $\delta\mu_i(x)$  and a time-independent term. Equation 6.19 turns into:

$$J_{i,\text{net}}^{\text{rec}}(x) + \delta J_i^{\text{rec}}(x, t) = -K(ez_i)^2 n_i^2 \left( \exp\left(\frac{\tilde{\mu}_h(x) - \tilde{\mu}_e(x)}{k_B T}\right) \exp\left(\frac{\delta\tilde{\mu}_h(x, t) - \delta\tilde{\mu}_e(x, t)}{k_B T}\right) - 1 \right) \quad (6.20)$$

If the perturbation from the equilibrium condition is small enough (lower than  $k_B T$ , or 25 meV), we can expand equation 6.20 into a Taylor series and clamp it after its first term:

$$J_{i,\text{net}}^{\text{rec}}(x) + \delta J_i^{\text{rec}}(x, t) = -K(ez_i)^2 n_i^2 \left( \exp\left(\frac{\tilde{\mu}_h(x) - \tilde{\mu}_e(x)}{k_B T}\right) \left( 1 + \frac{\delta\tilde{\mu}_h(x, t) - \delta\tilde{\mu}_e(x, t)}{k_B T} \right) - 1 \right) \quad (6.21)$$



Which can now be rearranged into a time-independent part (the steady-state recombination) and a time-dependent part (the perturbation recombination):

$$J_{i,\text{net}}^{\text{rec}}(x) + \delta J_i^{\text{rec}}(x, t) = -K(ez_i)^2 (pn - n_i^2) - \left( K(ez_i)^2 (pn) \frac{\delta \tilde{\mu}_h(x, t) - \delta \tilde{\mu}_e(x, t)}{k_B T} \right) \quad (6.22)$$

Owing to the linearization of equation 6.22, the recombination rate has now a linear dependence with the difference of chemical potential between electrons and holes. The resemblance to Ohm's law becomes clear at this point. When  $\tilde{\mu}_e^* = \tilde{\mu}_h^*$  then the system is in thermal equilibrium and no net recombination occurs. When  $\delta \tilde{\mu}_e^* = \delta \tilde{\mu}_h^* = 0$ , only the steady state recombination occurs the term  $\delta G_i(x, t) - \delta R_i(x, t)$  is null and there is no net recombination flux.

In this derivation, we used the relation between free carrier density and quasi-Fermi level, which is accurate for band-to-band recombination. For systems where carriers undergo first trapping, then recombination, a similar analysis can be made and a similar equation written between  $(\tilde{\mu}_i)_{\text{free}}$  and  $(\tilde{\mu}_i)_{\text{trapped}}$  for example.

Finally, by rewriting the time-dependent part of equation 6.22 in terms of resistances and fluxes:

$$\delta J_i^{\text{rec}}(x, t) = \frac{1}{\frac{k_B T}{(ez_i)^2 K pn}} \left( \delta \tilde{\mu}_h(x, t) - \delta \tilde{\mu}_e(x, t) \right) \quad (6.23)$$

The knowledge of the electron and hole concentration provides a direct read-out of the recombination constant  $K_{\text{rec}}$ .

### 6.3.5 Electronic and ionic charge storage

The last element in the continuity equation is  $\partial n_i(x, t) / \partial t$ , which we had already expressed in terms of the Maxwell-Boltzmann statistics. More generally, following ref. [234], a non-trivial recast of the partial differential can be done:

$$\frac{\partial c_i(x, t)}{\partial t} = \left( \frac{\partial c_i(x, t)}{\partial \mu_i} \right)_t \frac{\partial \mu_i}{\partial t} + \left( \frac{\partial c_i}{\partial t} \right)_{\mu_i} = \left( \frac{\partial c_i(x, t)}{\partial \mu_i} \right)_t \frac{\partial \mu_i}{\partial t} \quad (6.24)$$

Where all the cross-terms  $(\partial c_i / \partial \mu_j)_{i \neq j}$  are 0 (concentration of carrier  $i$  is independent on the chemical potential of carrier  $j$ ). The term  $(\partial c_i / \partial \mu_j)_{t=0}$  represents the capacity of the system to accept additional carriers  $j$  upon an increase of its chemical potential. This is analogous to the behavior of capacitor ( $J_{\text{charge}} = \partial Q / \partial t = C \cdot \partial V / \partial t$ ), for which the differential capacitance writes  $C = \partial Q / \partial V$ . By analogy, we write the chemical capacitance of a carrier  $i$  as (see ref. [234])

$$C_i^\delta = (z_i e)^2 \left( \frac{\partial \mu_i}{\partial c_i} \right)_{t=0}^{-1} \quad (6.25)$$

## Chapter 6. Intensity-modulated frequency response of perovskite solar cells

---

The continuity equation for electrons and holes, which was previously expressed in their specific form, can be written in a more general way:

$$\frac{\partial}{\partial x} J_i^{\text{charge}}(x, t) = G_i(x, t) - J_i^{\text{rec}}(x, t) - C_i^{\delta} \frac{\partial \mu_i^*(x, t)}{\partial t} \quad (6.26)$$

Assuming no generation or recombination for ions, the continuity equation for ions writes simply:

$$\frac{\partial}{\partial x} J_i^{\text{charge}}(x, t) = -C_i^{\delta} \frac{\partial \mu_i^*(x, t)}{\partial t} \quad (6.27)$$

Equations 6.26 and 6.27 contain a differential of the chemical potential with respect to time. The current flux is purely out of phase with the chemical potential, and represents a storage of charge carriers, whose magnitude is nothing other than the chemical capacitance. One must realize that there is no actual drop of the electrostatic potential across the capacitor, rather there is a drop in the chemical potential. The capacitor is there an entropic entity.

The chemical capacitance arising from the valence and the conduction can be determined by the Fermi-Dirac statistics:

$$C_{e, \text{on}}^{\delta} = (ez_i)^2 N_{\text{cb}} \frac{\partial \left( e^{\frac{\mu_i - E_c}{k_B T}} \right)}{\partial \mu_i} = \frac{(ez_i)^2 N_{\text{cb}}}{k_B T} e^{\frac{\mu_i - E_c}{k_B T}} \quad (6.28)$$

where

- $N_{\text{cb}}$  is the effective distribution of state at the conduction band
- $E_c$  is the position of the conduction band

The electronic chemical capacitance depends on the position of the Fermi level with regards to the conduction band minimum. The conduction band contribution to the chemical capacitance scales with the effective density of states  $N_s$ . In the case of a semi-conductor with an exponential distribution of trap states in the forbidden band of distribution  $g(\mu_e) = \frac{\alpha N_t}{k_B T} \exp(\alpha(\mu_e - E_c)/k_B T)$ , the chemical capacitance for the traps is written analogously:

$$C_{e, \text{trap}}^{\delta} = \frac{(ez_i)^2 \alpha^2}{k_B T} N_s e^{\frac{\alpha(\mu_e - E_c)}{k_B T}} \quad (6.29)$$

Both capacitances are in parallel, therefore:

$$C_{e, \text{tot}}^{\delta} = C_{e, \text{tot}}^{\delta} + C_{e, \text{trap}}^{\delta} \quad (6.30)$$

Without further knowledge of the trap state density in perovskites, it becomes difficult to estimate a value for the electronic component of the chemical capacitance. We can however give an estimate for the component of the conduction band. Assuming  $N_{\text{cb}} = 5 \times 10^{17} \text{cm}^{-3}$  and

an electron chemical potential 300 mV from the conduction band, the chemical capacitance for the electrons is merely in the order of  $1 \text{ nF cm}^{-2}$  (for a 200 nm thin film). The conduction band (and respectively valence band) capacitance is likely to be extremely low for high purity materials with few exposed surfaces. When the quasi-Fermi levels are far from the band minimum (conduction band) and maximum (valence band), the capacitance due to electronic trapping is dominant.

For ionic defects, calculating the chemical capacitance requires knowledge of the majority defects of the material. For example, considering the chemical capacitor arising from donor defects, we can write their chemical potential according to the dilute solution Boltzmann statistics

$$\mu_D = \mu_D^* + k_B T \ln N_D \quad (6.31)$$

Where  $N_D$  is the density of defects, such that

$$\frac{\partial \mu_i}{\partial N_D} = \frac{k_B T}{N_D} \quad (6.32)$$

Therefore, the chemical capacitance of the defects is directly proportional to their density:

$$C_{ion}^\delta = \frac{(ez)_i^2 N_D}{k_B T} \quad (6.33)$$

Which is equivalent to the results found in equation 6.9.

#### 6.3.6 Displacement capacitance

Finally, and this is the third thermodynamic equation describing the current flow is given by Maxwell's displacement current. It is unrelated to the transport of charged species. The displacement current occurs upon a change of the electrical field over time, and can be expressed as:

$$J_{\text{disp}}(x, t) = -\varepsilon_r(x, t)\varepsilon_0 \frac{\partial}{\partial t} \frac{\partial \phi(x, t)}{\partial x} \quad (6.34)$$

It can be considered that the permittivity is time and position independent, and the displacement flux can be expressed in the time-dependent, small perturbation regime:

$$\delta J_{\text{disp}}(x, t) = -\varepsilon_r \varepsilon_0 \frac{\partial}{\partial t} \frac{\partial (\delta \phi(x, t))}{\partial x} \quad (6.35)$$

Equation 6.35 is out of phase with the electrostatic potential variation. The storage of a displacement current (not charged species) depends on the gradient of the electrostatic field along the  $x$  direction and on the ability of the material oppose the applied electric field (the dielectric constant). It is equivalent to the description of an electrostatic capacitor.

### 6.4 Experimental procedure

In the IMVS/IMPS technique, a sine wave driven by a frequency response analyzer controls a voltage-controlled current source, which drives a laser diode. The phase and amplitude loss at this stage of the driver are not fundamentally important (although amplitude loss can be problematic in order to keep the small perturbation regime through the whole frequency window), if they are properly corrected. This correction can take the form of wide bandwidth photodiode (such as a low capacitance silicon reverse biased detector) which is fed into Y channel of the frequency response analyzer, across  $50\ \Omega$ . Typically, we used a 30% reflectance / 70% transmittance beamsplitter to provide a sufficiently strong reference signal. The transmitted portion of the beam is directed onto the device. Usually, a diffuser is added before the device such that the laser beam spreads into a broad Gaussian shape and illuminates the device uniformly. Commonly, an additional DC light bias of the same wavelength is provided by power LEDs and directed onto the device sideways.

The boundary conditions on the cell are enforced by the external circuit. They determine its working voltage and the charge extraction behavior. When the device under test (the photovoltaic cell) is loaded by a low impedance source and sink, there is no resistance to charge extraction except the one that is internal to the device. The transient response is therefore a photocurrent and the technique is called IMPS (intensity modulated photocurrent spectroscopy). When the cell is connected to a high impedance source, the cell gets automatically polarized according to the intersection between its  $j(V)$  curve and the current set-point (e.g. when the source is set to  $0\text{ A}$ , the device is polarized at open circuit). In this situation, the steady-state component of the photocurrent is extracted with a low impedance, but the AC component of the electron flux is blocked at the interface and must therefore recombine. In this case, the transient that is observed is a pure photo-voltage transient. Hence the technique is called, by analogy, IMVS (intensity modulated photovoltage spectroscopy).

Whether the impedance is high or low does not affect the DC electronic landscape in the device, but merely the behavior of the charges created by the perturbation. IMVS and IMPS can therefore be measured on any point of the  $j(V)$  curve in (but not limited to) the power-generating quadrant. Despite the fact that a zero impedance source or a high impedance source are built in fundamentally different ways, the steady-state electronic distribution is only determined by the potential across the leads and not by the external circuitry. Therefore, the IMPS and IMVS measured **at the same voltage** can be compared because they are two description of the same electrochemical system.

#### 6.4.1 Instrumentation

A common technique that is used to measure IMVS is to load a high resistance on the device, which is equivalent to actively forcing  $0\text{ A}$  current through the device. If the resistance is high enough, the cell is polarized in open-circuit condition.

Similarly, when a  $50\ \Omega$  resistor is loaded on the device, a near short-circuit condition is reached

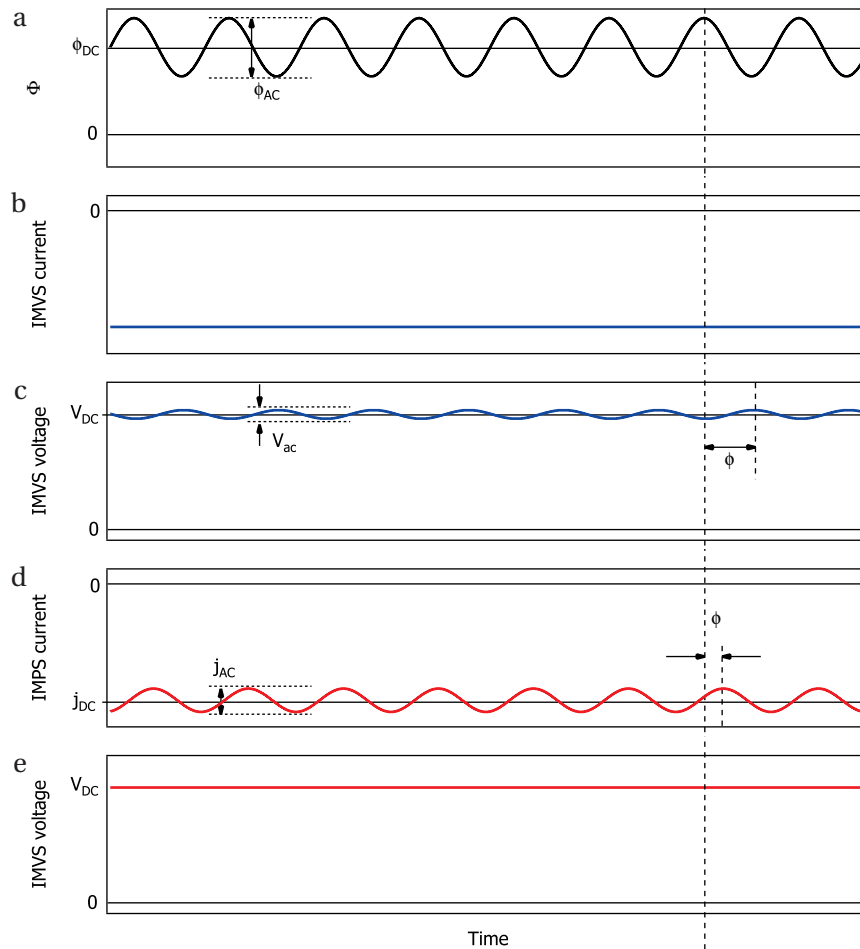


**Figure 6.2:** Schematic representation of an IMVS/IMPS data. (a) The excitation source, which comprises of a large DC component and a small AC component at a defined frequency. (b) The IMVS current. It is enforced by the external circuit and ideally is a steady-state value. (c) The IMVS voltage. It is the consequence of the AC illumination that splits the quasi-Fermi levels out of their steady-state. The voltage sine wave is described by an amplitude (in V) and a phase shift relative to the drive wave (in  $^{\circ}$ ). (d) The IMPS current. It is a consequence of the AC illumination that forces an additional current output on top of the steady-state current. The current sine wave is described by an amplitude (in A) and a phase shift relative to the drive wave (in  $^{\circ}$ ). (e) The IMPS voltage. It is enforced by the external circuit is ideally a steady-state value.

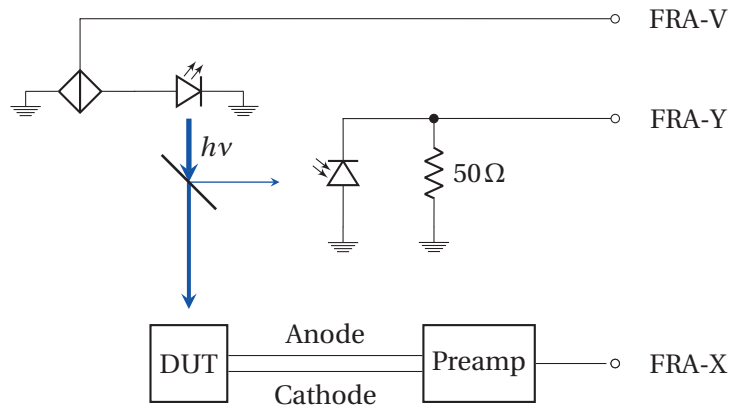


**Figure 6.3:** Schematics of an IMVS/IMPS experiment. DUT represents the solar under test, and the pre-amplifier is a home-built amplifier that defines the boundary conditions on the cell and amplifies its transient behavior. The FRA-X and FRA-Y outputs are directly fed into a high impedance frequency-response analyzer. The FRA-V input is provided by the frequency response analyzer and is used to drive the voltage-controlled current source that powers the laser diode

(depending on the DC current). By recording a voltage transient and converting it to current, a spectrum approaching the IMPS at short circuit can be recorded.

However, these techniques are restricted to a single working point ( $V_{oc}$  for IMVS and  $J_{sc}$  for IMPS) and using those two measurements to obtain a value for the collection efficiency would be clearly erroneous, due to the non-linearity of the device. In order to allow one to study the competition between transport and recombination, both the IMVS and IMPS **must** be evaluated at the same working voltage point.

To measure the intensity modulated spectra, some authors have proposed to load a variable resistance on the device, which biases the device at the crossing between the device  $j(V)$  curve and the resistance  $j(V)$  curve (a straight line from (0,0) with a slope that is the inverse of the resistance). However, the ability to load the cell at a single working point yet with different boundary conditions is lost, which results in a loss of information. We propose to maintain the contact impedance null or high while biasing the cell at any working point, allowing twice the information to be gained.

We now report very briefly on the design of the pre-amplifier shown in figure 6.3.

#### 6.4.1.1 IMPS driver

Measuring IMPS requires a low impedance source, such that the current perturbation can be extracted unhindered by the external circuitry. Such a source is easily realized using operational amplifiers (op-amp) in a closed-loop follower configuration. Because of its voltage feedback, the overall impedance of the amplifier in this topology can be as low a few milli-

ohms. A resistor can be placed in series to the op-amp to isolate the output stage from the capacitance of the cell and a potential instability, but it has to remain in the feedback loop to maintain the low output impedance. A careful selection of the amplifier has to be made, such that the output impedance remains low even at high frequencies ( $\leq 1$  MHz). The source can be connected to the cathode or the anode of the cell and should be capable of driving positive and negative voltages with respect to ground. The positive node of the amplifier should be connected to a precision digital to analog converter (DAC) capable of sourcing around  $\pm 2$  V. The IMPS experiment also requires a current readout. The other electrode of the DUT should be connected to a perfect current sink. It is not good enough to drop the current through a  $50 \Omega$  resistor and record the voltage transient, as it is commonly done in the literature: the resistor adds up to the intrinsic series resistance of the cell, shift the high frequency semi-circle to lower frequencies and potentially overshadows other spectral features. A transimpedance amplifier with a moderate transimpedance gain is the best available option to keep the impedance as low as possible. By grounding the positive node of the transimpedance amplifier, the negative node of the transimpedance amplifier (to which the device is connected) is at a virtual low impedance ground throughout the bandwidth of the amplifier. This topology has the advantage of directly yielding a current readout through the feedback resistor. This part of the design is critical, because the IMPS current readout should not have any phase lag even at high frequency. We designed the amplifier such that its phase shift is lower than  $2^\circ$  at 1 MHz. In addition, the input noise of the amplifier should remain low. An appropriate gain for this stage would be around  $500 \text{ V/A}$ , such that a 5 mA photocurrent is amplified to 2.5 V, well within the rails of a  $\pm 5$  V powered amplifier.

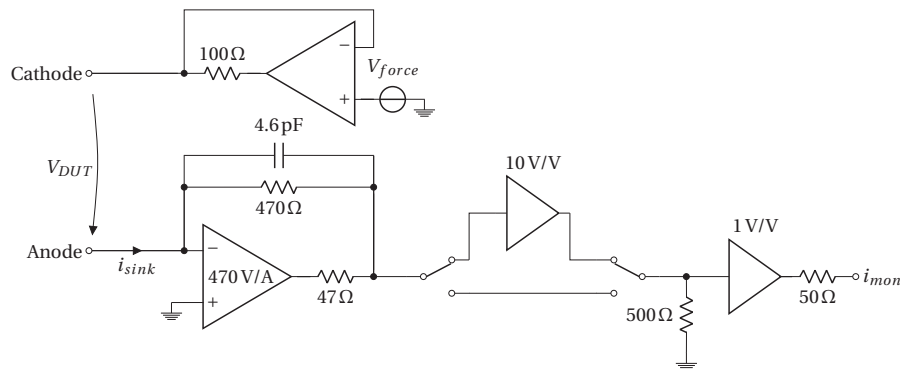


**Figure 6.4:** Bloc schematics of the cathode driver and the transimpedance amplifier

For low currents, such as when low DC illuminations are used, we decided to place an optional gain of  $10 \text{ V/V}$  amplifier, selectable through a relay. This amplifier should be wideband and would be switched on when currents lower than 0.25 mA are used. A final wideband line driver is used to buffer the signal into a  $50 \Omega$ -matched transmission line. A  $50 \Omega$  series resistor is used for the matching, but most frequency response analyzers have higher input impedance, which renders the effect of the series resistance negligible unless the impedance is voluntarily dropped close to the FRA input for noise immunity reasons. The whole gain chain should exhibit flat amplitude up and minimal phase shift up to 1 MHz.

6.4.1.2 Galvanostatic source

IMVS requires the use of a high impedance current source (a galvanostat). While designing the potentiostatic source was fairly straightforward, the galvanostatic source was significantly more involved. The transistor current mirror is the most commonly used topology, but can only source or sink current (not both). Alternatively, a MOSFET could be used within the feedback loop of an operational amplifier with a small resistor to the ground that sets the voltage to current gain, but is conditioned to the specification of the transistor (i.e. the leakage current limits the impedance of the source and the gate capacitance limits its speed). The Howland current pump is a good and simple alternative to both. Its schematics are shown in Figure 6.5. Variations of the standard topology have been proposed and thoroughly reviewed elsewhere[235]. A major advantage of the Howland current pump is that it can both source and sink current and is well adapted to drive a low impedance source such as a solar cell. A basic circuit analysis shows that when the resistances are matched, the current forced by the pump depends on the feedback resistors and the input voltage:  $I_{out} = -U_{in}/R_1$ .

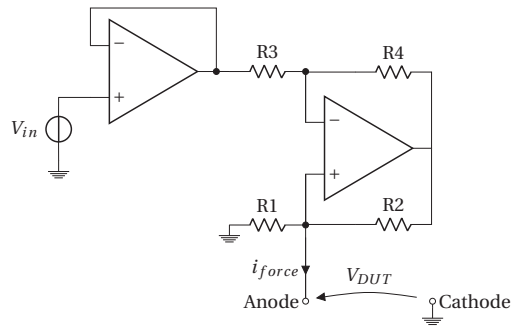


Figure 6.5: Bloc schematics of the Howland current pump

Its main drawback is that in order to source high currents with reasonable set point voltages, low feedback resistances have to be used (500 Ω in our case) which can significantly reduce the impedance of the current pump if the resistors are not tightly matched. The impedance of the Howland current pump can be expressed as  $Z_{out} \geq \frac{R1}{tolerance}$ . The output impedance of the DAC buffer adds up to the value of R3 and is frequency-dependent; hence the operational amplifier that drives the pump must be selected with care. Because the pump can source or sink current, one can connect to it either the anode or the cathode of the solar cell. The other electrode could be connected to the pseudo-ground of the transimpedance amplifier, but since a current readout is not necessary, it is better to ground it. The limited system impedance can be problematic to measure the IMVS spectrum of devices that show high impedance, typically around short circuit. However, most organic-inorganic perovskite cells have impedances below 100 kΩ, below what we expect for our implementation of the pump. In addition, at very low voltages in a galvanostatic mode, a small light perturbation or a small drift in the cell performance will anyway significantly shift the working voltage of the galvanostat and the quasi-steady state conditions are usually not respected anyway. Typically, we found that measurements below 500 mV are challenging.



### 6.4.1.3 Voltage buffering

In IMVS, the galvanostat provides a constant current through the cell but does not provide a direct voltage readout. In addition, in IMPS, because of the offset voltage at the negative node of the transimpedance amplifier, the anode of the solar cell might not be at exactly 0 V. A difference amplifier was connected directly between the anode and the cathode. The impedance and common-mode rejection ratio of the difference amplifier was increased by buffering the cathode and the anode by two high input impedance buffers, effectively turning it into a  $G = 1 \text{ VV}^{-1}$  instrument amplifier. The difference amplifier consisted of four 10 k $\Omega$  tightly matched resistors and a high speed, low distortion op amp that provides the buffered, ground references voltage. The output of the amplifier was fed through a relay (that allows the switching current monitoring for IMPS (through the output of the transimpedance amplifier) or voltage monitoring for IMVS). After the relay we placed the line driver (BUF634) and its series resistance, as was described earlier.

## 6.5 Assembling the equivalent circuit

Assuming that the variations in chemical potential and electric field are small, the time-dependence of the material properties can be replaced by their steady-state values. Therefore, the current fluxes due to the drift-diffusion of species and to electric field displacement can be expressed as a function of  $\delta\mu_i^*$  and  $\delta\phi$ , which retain their position-dependence:

$$\delta J_i^{\text{charge}}(x, t) = -\sigma_i(x) \frac{\partial}{\partial x} \delta\mu_i^*(x, t) \quad (6.36)$$

For ionic species that have no generation or recombination term, the continuity equation reads:

$$\frac{\partial}{\partial x} \delta J_i^{\text{charge}}(x, t) = -\frac{(z_i e)^2 c_i}{k_B T} \frac{\partial}{\partial t} \delta\mu_i^*(x, t) \quad (6.37)$$

The one for electrons and holes at  $x = 0$  reads:

$$\begin{aligned} \frac{\partial}{\partial x} \delta J_i^{\text{charge}}(0, t) = (ez_i) \delta I e^{i\omega t} - K_{\text{rec}}(0, t) \frac{pn(ez_i)^2}{k_B T} \left( \delta\mu_e^*(0, t) - \delta\mu_h^*(0, t) \right) \\ - \frac{(z_i e)^2 c_i}{k_B T} \frac{\partial}{\partial t} \delta\mu_i^*(0, t) \end{aligned} \quad (6.38)$$

And the one for electrons and holes at  $x \neq 0$  reads:

$$\begin{aligned} \frac{\partial}{\partial x} \delta J_i^{\text{charge}}(x, t) = -K_{\text{rec}}(0, t) \frac{pn(ez_i)^2}{k_B T} \left( \delta\mu_e^*(x, t) - \delta\mu_h^*(x, t) \right) \\ - \frac{(z_i e)^2 c_i}{k_B T} \frac{\partial}{\partial t} \delta\mu_i^*(x, t) \end{aligned} \quad (6.39)$$

$$\delta J_{\text{disp}}(x, t) = -\varepsilon_r(x)\varepsilon_0 \frac{\partial}{\partial x} \frac{\partial}{\partial t} \delta\phi(x, t) \quad (6.40)$$

Brumleve demonstrated that these coupled Nernst-Planck-Poisson equations can be mapped onto an equivalent electrical circuit answering to Kirchhoff's laws[236], made of ideal capacitors and resistors. The values of the components making the circuit have a physical meaning. Equation 6.36 shows a linear dependence between a current density and the drop in electrochemical potential across an element  $dx$ . It is the electrochemical equivalent of Ohm's law and the appropriate circuit element that it represents is a resistor placed between  $x$  and  $x + dx$ . In general, equations 6.37-6.39 account for the current difference between a node a position  $x$  and its neighbor at  $x + dx$  for a particular carrier. The elements implied by the continuity equation must therefore branch at each position  $x$  or the carrier rail and be placed in perpendicular to the  $x$ -coordinate.

The current differential that is common to equations 6.37-6.39 is out of phase with the perturbation of the chemical potential of the species  $i$ . Its expression is precisely that one of an ideal capacitor ( $I(t) = C \cdot dV(t)/dt$ . The potential difference across the capacitor is the chemical potential of the species (and not its electrochemical potential). One of the electrodes of the capacitor is at  $\delta\tilde{\mu}_i^*(x, t)$  and the second one at  $\delta\phi(x, t)$ . The generation term in equation 6.38 is a constant (for  $x = 0$ ). It is therefore best represented as an ideal current source, which bridges the electron and hole rail (the absorption process generates an electron and a hole, hence both rails should be affected). We note that the doping level of the semiconductor has no influence here<sup>2</sup>

The recombination term in equation 6.39 and 6.38 depends linearly on the difference in electrochemical potential between the electron and hole rail. Again, it takes a similar expression as Ohm's law  $I = V/R$ . The recombination term is therefore represented as a resistor bridging the electron and hole carrier rails. Finally, equation 6.40 yields an additional rail in  $x$ -coordinate (from the  $\frac{\partial}{\partial x}$  term). The displacement current is out of phase with the electrical potential, which gives rise to a capacitor. Interestingly, each position along this rail has the value  $\delta\phi(x, t)$ , which is exactly the difference between  $\tilde{\mu}_i^*$  and  $\mu_i^*$ . Therefore, each chemical capacitor at position  $x$  links each node  $x$  of the displacement rail.

It has been demonstrated in several instances that the equivalent circuit in figure 6.6 maps the physical reality of the charge carrier dynamics inside a material[234, 236, 237, 238, 239] and is equivalent to equations 6.36-6.40. The circuit elements of take physical meanings:

$$R_i(x) = \frac{1}{\sigma_i(x)} \frac{dx}{A} \quad (6.41)$$

---

<sup>2</sup>The lack of change of the electrochemical potential of a carrier, for example in the case of doped semiconductor, is the consequence of a large chemical capacitance. The generation term only describes the arrival of new charges. Whether they create an electrochemical potential response or not is irrelevant.

## 6.5. Assembling the equivalent circuit

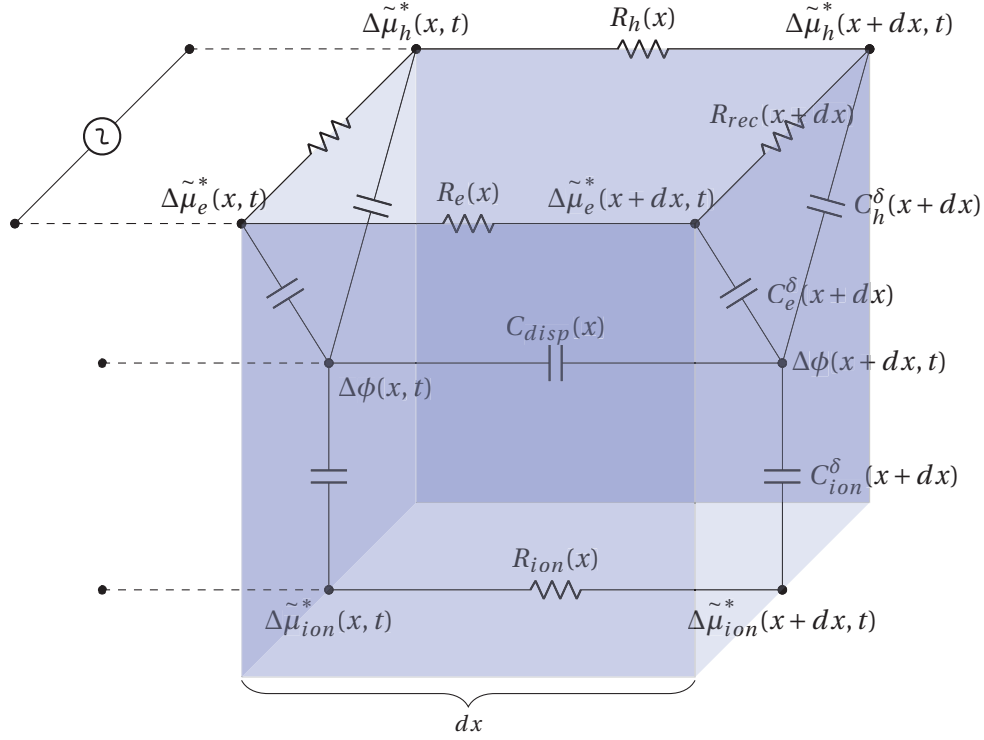


**Figure 6.6:** Differential resistors and capacitors obeying the set of equations for a slab of the model between  $x$  and  $x + dx$ . The two parallel rails at the top describe the flow of electrons and holes. They are cross-linked by current generation and recombination resistances (the first recombination resistance was omitted for clarity). The charges flow along the  $x$ -axis. The bottom rail is for one ionic charge carrier. The center rail is called the "displacement" rail in reference to Maxwell's equation of electrical displacement. The carrier branches are linked to the displacement branch through their chemical capacitances. All circuit elements can have time and position-dependence, but still respect Kirchoff's law of current and voltage.

$$C_{\text{disp}}(x) = \epsilon_r(x)\epsilon_0 \frac{A}{dx} \quad (6.42)$$

$$R_{\text{rec}}(x) = \frac{k_B T}{p n e^2 K_{\text{rec}}(x) A dx} \quad (6.43)$$

$$C_{\text{ion}}^\delta(x) = \frac{(e z_{\text{ion}})^2 N_D}{k_B T} A dx \quad (6.44)$$

$$C_{e/h}^\delta(x) = \frac{(e z_{e/h})^2 N_s}{k_B T} \exp\left(-z_{e/h} \left(\tilde{\mu}_e^* - E_{c/v}\right) / k_B T\right) A dx \quad (6.45)$$

## Chapter 6. Intensity-modulated frequency response of perovskite solar cells

---

Where  $A$  is the device area and  $dx$  is the thickness of a discrete slab. Considering a material of uniform conductivity and uniform dielectric constant, the total carrier transport resistance across the  $x$  dimension is given by:

$$R_i^{\text{tot}} = \int_0^L \frac{dx}{\sigma_i A} = \frac{L}{\sigma_i A} \quad (6.46)$$

Similarly, the total equivalent recombination resistance, assuming uniform electron and hole profile, can be calculated according to

$$R_{\text{rec}}^{\text{tot}} = \frac{k_B T}{p n e^2} \left( \int_0^L K_{\text{rec}} A dx \right)^{-1} = \frac{k_B T}{p n e^2} \frac{1}{K_{\text{rec}} \cdot AL} \quad (6.47)$$

Assuming that electro-neutrality prevails in the bulk, it can be shown that there is no net current flowing from the carrier rail through the displacement rail, but only in between the rails themselves. In this case, the capacitors along the displacement rail can be isolated into a single capacitor:

$$C_{\text{disp}}^{\text{tot}} = \left( \int_0^L \frac{1}{C_{\text{disp}}} \right)^{-1} = \frac{\epsilon_r \epsilon_0 A}{L} \quad (6.48)$$

It is not our purpose here to detail further the behavior of the bulk thermodynamics and the implications of the presented equations onto topics such as the chemical diffusion coefficient, the chemical capacitance or the impedance response of the transmission line. It is worth however looking more into details at the effects that can occur at the interfaces with other materials, whether they are metallic electrodes or other semiconductors.

In absence of a chemical picture of what process is exactly happening at the interface, generalization can be made. For example, in the Chang-Jaffé boundary condition[240, 241], the rate of charge transfer is proportional to the concentration gradient across the left-hand interface:

$$J_i^{\text{mass}}(t) = k_i \left( n_i^{\text{left}}(t) - n_i^{\text{right}}(t) \right) \quad (6.49)$$

where  $k_i$  is the rate of charge transfer and  $\delta c_i$  the drop of charge density across the interface. This is however not suitable for an equivalent circuit representation as it does not involve a flux and a drop of potential. It can however be recast by linearizing again the Fermi-Dirac statistics and the expression of the electrochemical potential:

$$J_i^{\text{charge}}(t) = \frac{(e z_i)^2 k_i n_i}{k_B T} \left( \tilde{\mu}_i^{\text{left}}(t) - \tilde{\mu}_i^{\text{right}}(t) \right) \quad (6.50)$$

The charge transfer dynamics across an interface can therefore be seen as a dispersive process that answers to Ohm's law. The charge transfer capacitance naturally arises from the mixing of the chemical capacitance and the displacement capacitance, but an additional capacitive effect can be added to describe the interface capacitance. In the case of a Schottky-type of

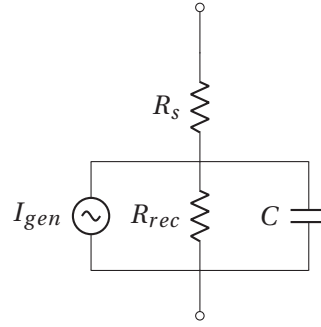


**Figure 6.7:** Basic equivalent circuit of a solar cell, including a dielectric capacitance, a transport resistance, a recombination resistance and a current source

contact, the capacitance follows:

$$C^\perp = \sqrt{\frac{q\epsilon_r\epsilon_0 N_d}{2(\phi_i - V_a)}} \quad (6.51)$$

Where  $N_d$  is the dopant concentration,  $\phi_i$  is the built-in potential of the junction,  $V_a$  is the additional applied potential.

### 6.5.1 Most basic equivalent circuit

IMVS and IMPS have been proven useful to quantify the rate of electron transport and recombination in the quasi-steady state regime of solar cells. Analytical derivations for the transfer function of both techniques have been derived for dye sensitized solar cells[242], but more generally it is based on the description of an equivalent circuit that the IMVS and IMPS analysis is done[243, 244, 245, 246]. The successful description of the circuit by transport and storage equations has been widely recognized. A basic model of a solar cell is shown in figure 6.7.

#### 6.5.1.1 Transport and recombination time constants

Where the capacitance can be of geometrical or the chemical origin,  $R_{rec}$  the recombination resistance and  $R_s$  the transport resistance. In those conditions, the IMVS and IMPS feature only one arc in the complex space, which take the following time constants:

$$\tau_{IMVS} = R_{rec}C \quad (6.52)$$

$$\tau_{IMPS} = \frac{R_{rec}R_s}{R_{rec} + R_s}C \quad (6.53)$$

### 6.5.1.2 The collection efficiency

The collection efficiency is defined as the ratio between the collection current and the recombination current. In the basic model of 6.7, it can be expressed as:

$$\eta_{cc} = \frac{j_{coll}}{j_{tot}} = \frac{j_{coll}}{j_{coll} + j_{rec}} = \frac{\frac{1}{R_s}}{\frac{1}{R_s} + \frac{1}{R_{rec}}} = \frac{R_{rec}}{R + R_{rec}} = 1 - \frac{\tau_{IMPS}}{\tau_{IMVS}} \quad (6.54)$$

Two aspects of this derivation should be commented:

- It relies on the fact that the IMVS and IMPS time constant take the form of equations 6.52 and 6.53. This is model-specific and we will that in the case of perovskite cells, it is clearly not true.
- Ohm's law has been used (it has been assumed that the voltage between each resistance is the same), which only holds true if the IMPS and IMVS are measured **at the same working voltage**.

The double layer capacitance responsible for the slow time component of the cell is between 4 and 5 orders of magnitude larger than the displacement capacitance. The capacitance takes values of tens of mFs, which is compatible with the values observed by . This magnitude of this capacitance is incompatible with the relative permittivity of  $\text{CH}_3\text{NH}_3\text{PbI}_3$  and its origin must be chemical. This capacitive element echoes the large low-frequency permittivity pointed out by Zarazua[247] and Juarez-Perez[248], simulated by Richardson [249] and explained further by Yang[63] and Almond[250]. This high apparent dielectric constant is nothing else than the result of the space-charge accumulation of ionic carriers at the interface with both the hole transporting or the electron transporting layer. We note that

### 6.5.2 Ionic transport in $\text{CH}_3\text{NH}_3\text{PbI}_3$

Experience shows that the simplistic model of figure 6.7 does not satisfactorily describe the behavior of perovskite solar cells. Unlike most other solar cell technologies, it is now accepted that the hybrid perovskite  $\text{CH}_3\text{NH}_3\text{PbI}_3$  is a mixed ionic-electronic conductor. Yang et al. have shown that iodine defects are carriers for ionic currents[63]. Direct observations of the slow polarization of perovskite films have been reported by Xiao et al.[251]. The large capacitance of perovskite solar cells was recognized, although its origin not explicitly cited[185]. Several authors have reported on the large, low-frequency permittivity of  $\text{CH}_3\text{NH}_3\text{PbI}_3$ [247, 248], which origin was assigned to the chemical capacitance by Yang[63]. Ionic currents due to mobile defects have been simulated by Richardson[249]. The activation barrier for vacancy-assisted iodine diffusion has been estimated between 0.1 V[252] and 0.6 eV[253]. In this work, we will make the reasonably accepted assumption that organic-inorganic perovskites ( $\text{CH}_3\text{NH}_3\text{PbI}_3$  and related permutations) are mixed electronic ionic conductors with a single ionic carrier that dominates the ionic conduction. The polarity and nature of this carrier has no influence

on our conclusions.

Mixed electronic ionic conductors have been thoroughly studied for their applications in intercalation batteries, fuel cells and electrochemical sensors. In applications like selective membranes, ionic conductivity is a feature that is by design, and the purpose is often the maximization of the ionic transport and reduction of the electronic transport to minimize leakage. However, ionic motion is often responsible for the degradation of dielectric materials, such as multi-layer ceramic capacitors (MLCCs), which are subjected to high DC fields for prolonged period of times (>100'000 hours). When applied to perovskite-based solar cells however, ionic transport is a side effect of the principal attractive features of the material, i.e. high absorption coefficient, slow recombination and high charge carrier mobility. When operated out of electrostatic equilibrium, the build-up of an internal stoichiometric polarization of mobile ionic species should occur internally of the perovskite layer. Whether it directly links to the reported long-term degradation of perovskite solar cells or not is unclear, but is certainly a likely candidate to explain the observed drop of efficiency over hundreds of hours of operation. In general, hybrid organic-inorganic perovskite solar cells remain poorly understood from an electrochemical perspective. It has been recognized for some time already that the electronic transport properties of the absorbing material are exceptional. In particular, the long charge carrier diffusion length is a key element in allowing high power conversion efficiencies to be reached[36, 37, 38]. But the slow time constant of the solar cell, resulting in significant hysteresis between the backward and forward direction  $j(V)$  sweep, remains to be clearly explained. Solar cells, like all electrochemical devices, can be studied by their small-signal ac electrical response, capable of providing valuable information on the transport, recombination and capacitance of the device, as a function of the Fermi-level difference between the cathode and the anode of the solar cell. However, standard solar cell impedance models do not account for the mixed-conductivity nature of the charge generation layer.

In the equivalent circuit of a perovskite solar cell, we are making use of one ionic branch in parallel to the electron and hole branch. The electrodes are considered purely selective for electrons, hence the ions can polarize across the film without participating to the current density in steady-state. At higher frequencies however, carriers from all branches can theoretically couple with each other, depending on the values of the chemical capacitance.

In the rest of this chapter, we discuss on the implications of the carrier system established in figure 6.6 onto the frequency response of perovskite solar cells.

### 6.5.3 Prior knowledge and working assumptions

Before trying to pin down the relevant equivalent circuit of perovskite solar cells, it is useful to inform the reader that is not accustomed to non-linear photovoltaic devices about a few of their steady-state properties.

- Under light and in DC condition, the electronic resistance of the cell is normally very

low. This is read from the  $j(V)$  characteristics of the cell at  $V_{oc}$ . Typically it is in the order of a few ohms. The series resistance includes at least the contact resistance, the substrate sheet resistance and the series resistance of the charge transport layers. It also includes a partition of the electron resistance and the hole resistance of the absorbing layer is added<sup>3</sup>. In any case, the transport of electrons and holes in the perovskite is likely to be below  $10 \Omega$ .

- The recombination resistance spans over a couple of orders of magnitude. At open circuit voltage, as seen in the previous point, it is generally quite low, around the value of the series resistance. At low voltage, the cell becomes a near-ideal current source and therefore, the recombination resistance increases drastically. Typically we can expect around 1-10 k $\Omega$  shunt resistance for good devices.
- The transport layers are selectively blocking. Each one is reversible for one electronic carrier (and blocking for the other one) and both are perfectly blocking for ions. Both interfaces can however be recombinative. So far, there has been no report of chemistry involving the electron transport layer ( $TiO_2$  or  $SnO_2$ ) or the hole transport layer (generally Spiro-MeOTAD) with iodine, methylammonium or lead.

### 6.6 Flat-film perovskite solar cells

From the point of view of a device modeling, flat hybrid perovskite cells are extremely attractive because they offer a uniform 1D structure comprising of two geometrically well defined charge transport layer that are selectively blocking for ions and an dense homogeneous material of uniform thickness, sandwiched between two conductive electrodes (the  $SnO_2$  front window and the Au counter electrode). From the perspective of the mixed ionic-electronic conductor, the model is greatly simplified by the fact that there is usually only one grain spanning across the whole active layer. If the grains are much larger than the device thickness, the lateral grain boundaries can also be ignored.

#### 6.6.1 Experimental dimensions

The area of a typical mesoscopic perovskite solar cell is defined by the dimension of the gold counter-electrode that is deposited by thermal evaporation, typically 0.5 cm x 0.5 cm (total area = 0.025 cm<sup>2</sup>). A cross-sectional SEM micrograph a typical flat film perovskite solar cell is shown in figure 6.8. The cell is typically made of a fluorine-doped tin oxide-coated glass used as a substrate, 10-20 nm thick layer  $SnO_2$ , ~320 nm  $CH_3NH_3PbI_3$  or  $CH_3NH_3PbI_xBr_{3-x}$ , ~150 nm Spiro-MeOTAD and finally between 60 nm and 100 nm of gold.

---

<sup>3</sup>The partitioning depends on the penetration of the light



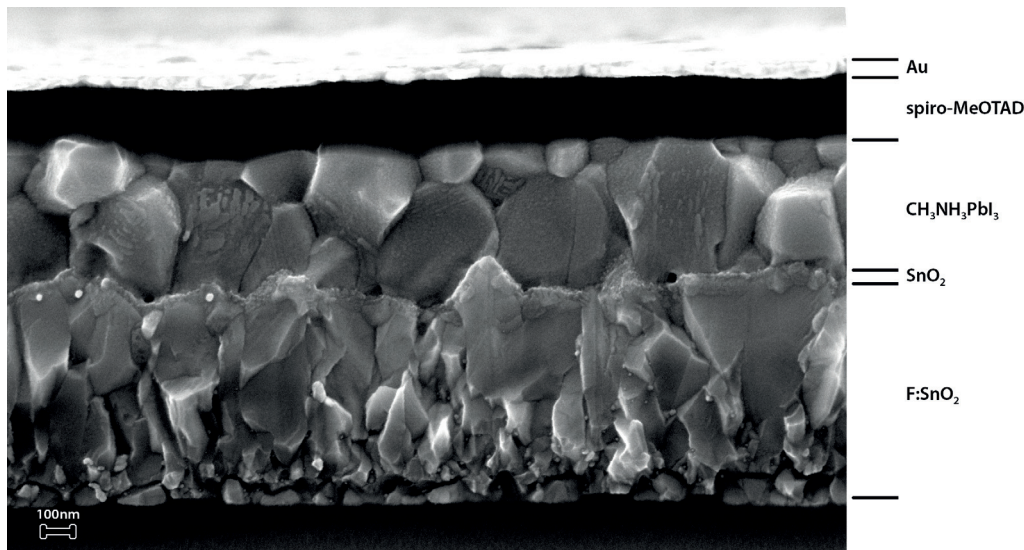


**Figure 6.8:** Cross-sectional scanning electron micrograph of a flat perovskite film using a  $\text{SnO}_2$  compact underlayer as an electron collector and Spiro-MeOTAD as a hole collector. The thickness of the perovskite is roughly 300 nm

### 6.6.2 The equivalent circuit

The equivalent circuit of a flat film perovskite solar cell can be drawn intuitively, accounting for the additional selective layers and electrodes and the associated charge transfer processes. The behavior of the MIEC photo-absorber is the same as the one described in section 6.5. Notably, we note the presence of the current source in the first slice of perovskite, describing the surface generation of electrons and holes.

However, the perovskite layer is traditionally sandwiched between the transport layer that behave differently from metal electrodes. The selectivity of the electron and hole transport layer are considered ideal, hence the transport of charges across the layers is described by a single rail. The interface are modeled using a lumped element that describes the charge transfer impedance. In the simplest approximation, it consists in a parallel combination of a resistor (charge transfer) and a capacitor (charge accumulation). Expressions for the value of such elements can be derived from various theories, such as Butler-Volmer or Chang-Jaffé transfer rates or the Schottky contact capacitance.

Recombination at the interface between the layers is to be expected. An additional lumped RC element in between the ETL and the hole transport rail of the perovskite, and between the HTL and the electron rail of the perovskite.

No direct recombination resistance between the two transport layer is included in the model, as there is simply no physical contact between the two.

The thermodynamic equations that were derived earlier fully apply to the transport layer, and give rise to a displacement capacitance, chemical capacitances and transport rates.

All those elements can be combined together into the full equivalent circuit of a perovskite solar cell, shown in figure 6.9.

## Chapter 6. Intensity-modulated frequency response of perovskite solar cells

---

The mass transport of ionic carriers is described with a set of resistors of equal value  $1/nR_{ion}^{\infty}$ . The hole and electron transport layers are perfectly blocking for ions, hence the ionic rail is disconnected from the rest of the circuit, but ionic carriers can still accumulate in the space-charge region. A double layer capacitor needs to be added between the transport layer and the ionic rail. We will later comment on the need for this double layer capacitor and its value. As it turns out, it is a key component of perovskite solar cell.

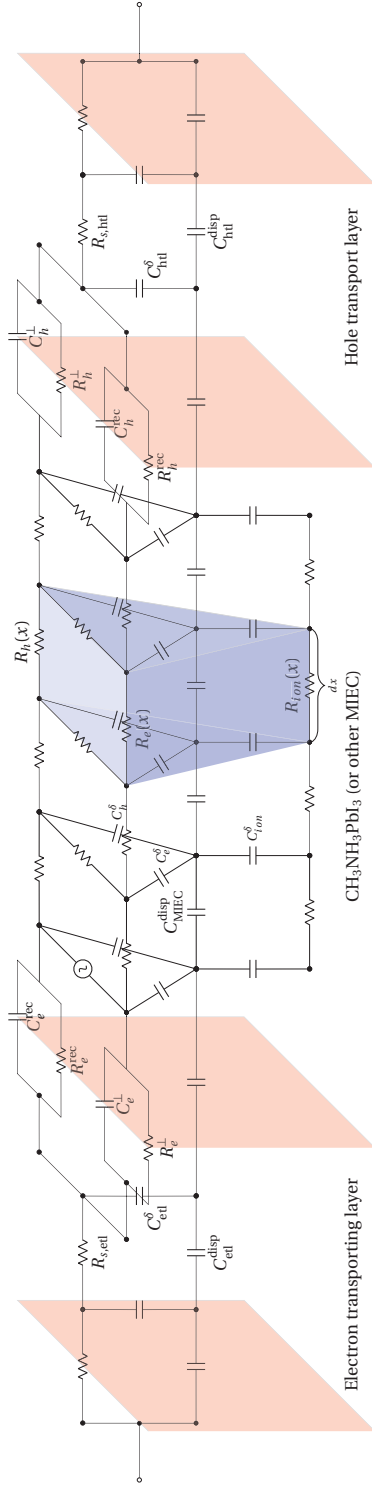


**Figure 6.9:** Full equivalent circuit of a flat perovskite solar cell, describing a metallic electrode, an electron selective transport layer, the perovskite absorber, a hole selective transport layer and another metallic electrode. The transmission line model for the ETL and HTL has been replaced by single elements for simplicity.

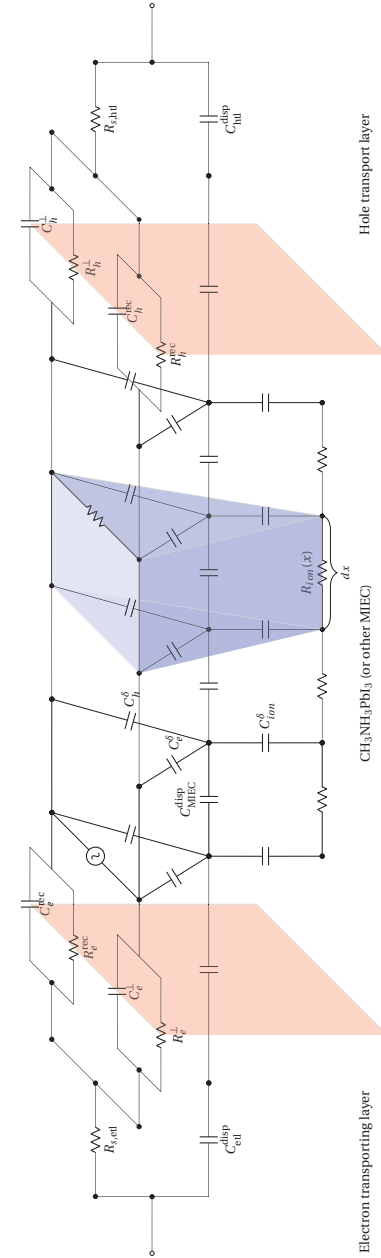


**Figure 6.10:** Simplified equivalent circuit of a flat perovskite solar cell. The simplification takes into account the fast transport of electrons and holes in the perovskite, the ideality of the contacts between the metallic electrodes and the transport layer, the small chemical capacitance and ideal selectivity of the transport layers

It is interesting to consider the simplifications that can be applied to the full circuit. Assuming that the Debye length is significantly smaller than the device thickness, the displacement rail does not charge away from the space-charge regions, and the displacement capacitor can be placed externally[234]. The chemical capacitance due to ions, electrons and holes are now connected as a three-terminal capacitor with a common node. The current induced by the chemical storage of charged species depends on the values of the chemical capacitors and the coupling between the rails on their relative value to each other. In the perovskite layer, the Debye length is approximately 1.5 nm[249], hence this approximation is reasonable. Interestingly, in an ideal IMPS experiment, this bulk capacitor has no influence on the signal, as it is placed externally to the cell. Dielectric effects in the space-charge regions are however possible. Second, it can be assumed that the electronic transport rate is limited by the interfaces and the transport layers. The electronic transport resistances in the perovskite can be ignored and the bulk recombination resistances bundled into a single one. We can further reduce the circuit by assuming an ideal interface between the metallic electrodes and the transport layers, which allows the removal of the lumped elements at these positions. Further ignoring the contribution of the transport layers to the chemical capacitance (which is likely to be untrue, but serves the purpose of the demonstration), the circuit reduces to the one in Figure 6.10

### 6.6.3 Simulations of the IMVS response

The measurement of the IMVS spectrum of a photovoltaic device should be realized under high-Z conditions. When no AC charges are allowed to escape from the device to the biasing circuitry, they must necessarily recombine. A difference in the electrochemical potential of the electronic carriers reaches the electrodes and is sensed as a photovoltage perturbation. The phase and amplitude of this perturbation can be directly linked to the carrier generation, motion and recombination that occur in the absorption and the transport layers. In the following section, we cover the main results arising from such numerical simulations under high-Z conditions, as well as ways to simplify the equivalent circuit in certain simple cases.

#### 6.6.3.1 Purely electronic conductor

The IMVS and IMPS spectra of a purely electronic conductor can be simulated by setting the transport resistance of the ionic rail extremely high. Omitting the interfacial recombination and the charge transfer impedance, a single semi-circle in the complex space best describes the IMVS response (figure 6.11). The DC amplitude of the arc is  $R_{rec}$  and its time constant, neglecting  $R_s$ , is given by  $\tau_{IMVS} = R_{rec}(C_{disp} + C_e^\delta \oplus C_h^\delta)$  (the parallel combination of the chemical and displacement capacitance). IMVS is therefore a very useful tool to determine readily the recombination resistance while minimizing interference from the transport effects (as long as  $R_{rec} \gg R_s$ ). Figure 6.12 shows the full numerical simulation of the IMVS response for various recombination resistances.

## 6.6. Flat-film perovskite solar cells

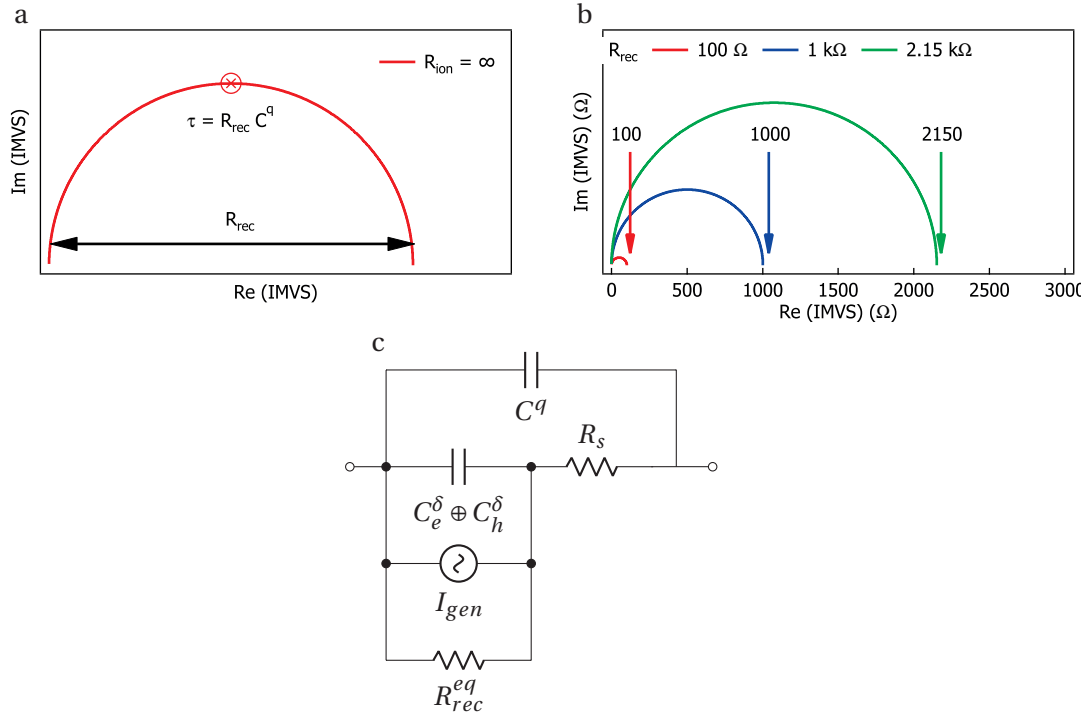


**Figure 6.11:** (a) Typical IMVS response for a p-i-n photovoltaic device with purely electronic conductivity. The dielectric capacitance of all other layers than the photocurrent generation layer have been omitted in this simplification. All interfaces are considered ideal. (b) IMVS response for various recombination resistances and (c) Possible simplification of the general equivalent circuit using the assumption of ideal interfaces (no transfer impedance, no recombination) and weak electron and hole chemical capacitance.

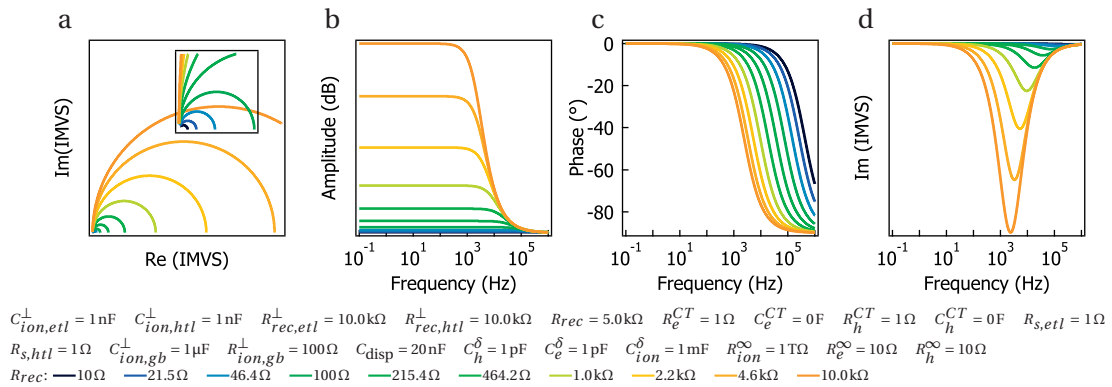


**Figure 6.12:** Numerical simulation of a purely electronic conductor generation layer between two ideal hole and electron transport layers for various recombination resistances. (a) Nyquist plot, (b) the amplitude (in dB) versus frequency, (c) the phase versus frequency and the imaginary response versus the frequency

### 6.6.3.2 Mixed ionic-electronic conductor

When the absorbing layer is also an ionic conductor, the IMVS spectrum becomes considerably more complicated and results can be highly sensitive of the choice of the circuit parameters.

## Chapter 6. Intensity-modulated frequency response of perovskite solar cells

In the case where the ionic conduction grain boundary-free and the electrodes are ideally blocking, the IMVS response usually features two semi-circles, provided that the ionic chemical capacitance is much larger than the dielectric capacitance and the electronic chemical capacitance. Alternatives to these conditions will be shown later.

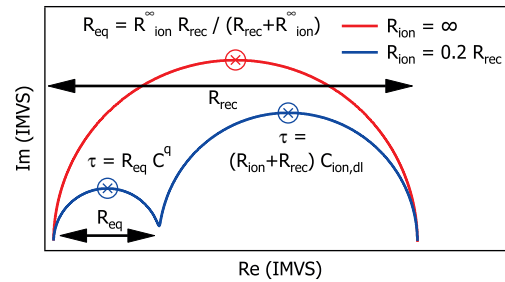


**Figure 6.13:** Typical IMVS response for a p-i-n photovoltaic device with mixed electronic-ionic conductivity and perfectly blocking electrodes. The dielectric capacitance of all other layers than the photocurrent generation layer have been omitted for clarity.

Because the electrodes are perfectly blocking for ionic carriers, the DC photovoltage is logically unaffected by the ionic resistance. However, at high frequency, the space-charge capacitance behaves as a short circuit and electrons can recombine through the ionic rail. This has the effect of splitting the single arc into two semi-circles. The high frequency one is formed of the equivalent parallel resistance  $R_{eq} = (R_{rec} R_{ion}^{\infty}) / (R_{rec} + R_{ion}^{\infty})$  and the dielectric capacitance. At low frequencies, the dielectric capacitor is open and the electronic relaxation occurs between the ionic space-charge capacitor, the ionic resistance and the recombination resistance. This leads to the appearance of the second semi-circle. The relative magnitude of the two circles obviously depends on the partition between the recombination and ionic transport resistances.

### 6.6.3.3 Effect of the chemical capacitance vs interfacial capacitance

Simply speaking, the effect of the bulk chemical capacitance and interfacial capacitance is synergic. They result in the shifting to lower or higher frequencies of the second semi circle only, as figure 6.15 shows (a-d for varying ionic chemical capacitance and e-h for the double layer capacitance). The capacitive behavior arising from the ionic charge storage can be separated into two components: one arising from the bulk storage and one from the interfacial storage [254]. The bulk chemical capacitance arises from the uptake and release of carriers upon changes in their chemical potential and scales the volume of the sample [255, 256]. The double layer capacitance is a three-terminal capacitance formed of the dielectric capacitance and chemical capacitance. It arises from the space-charge layer formed by the accumulation of ionic carriers close to the electrode (or, in our case, the transport layer) and its coupling with the dielectric of the material (it is therefore affected by the Debye length of the perovskite absorber). In the continuum model, its value is  $C_{ion}^{\perp} = \sqrt{C_{disp} C^{\delta}}$ , but owing to the non-

continuity of the system (discrete ion concentration, saturation effects, ...), it is usually fitted as an independent parameter. The double layer capacitance scales with the active surface area.

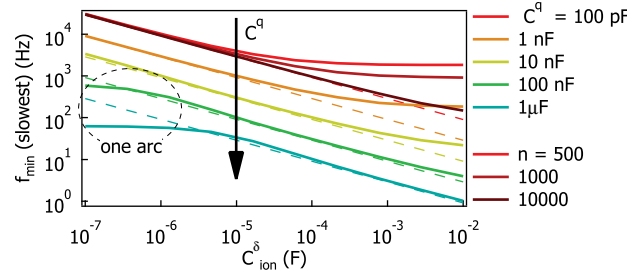


**Figure 6.14:** Solid lines: frequency at which the imaginary component of the semi-circle at low frequencies is maximum as a function of the dielectric capacitance  $C_{\text{disp}}$  and bulk chemical capacitance  $C_{\text{ion}}^{\delta}$ . Dark red lines: same simulation for  $C_{\text{disp}} = 100 \text{ pF}$  using 500, 1000 and 10000 discrete slabs. Dashed lines: corresponding frequency as predicted by 6.55. The deviations seen when  $C_{\text{ion}}^{\delta} \ll C_{\text{disp}}$  originate from the merging of the two semi-circles

First, let us consider a system without "artificial" double layer capacitance. In this case, two arcs can be resolved, provided that the chemical capacitance is larger than the dielectric capacitance (for equal  $R_{\text{rec}}$  and  $R_{\text{ion}}^{\infty}$ ). In the case where the chemical capacitance of the electrons and holes is negligible compared to the one of the ions, the frequency response arising from the stoichiometric polarization is not determined by the chemical capacitance, but by the diffuse layer capacitance it forms together with the dielectric capacitance:  $C_{\text{ion}}^{\perp} = \sqrt{C_{\text{disp}} C_{\text{ion}}^{\delta}}$ . We simulated the cell response for various values of displacement capacitance and bulk chemical capacitance. The frequency at which the imaginary component is maximum (in absolute value) was extracted from the simulation and displayed as solid lines in figure 6.14. In this simple case, a solution for this frequency can be given by

$$f_{\text{min}} = \frac{1}{2\pi \sqrt{C_{\text{disp}} C_{\text{ion}}^{\delta}}} \quad (6.55)$$

We stress that equation 6.55 is valid only if the electronic rails do not strongly couple with the ionic rail in the bulk, which implies that the two electronic chemical capacitances are low with regards to the ionic one. The results of this equation can be compared with the numerically calculated ones in figure 6.14 (dashed lines).<sup>4</sup>

This result is not perfectly equivalent to the one reported in the literature, where the term  $1/20C^{\delta}$  is missing[257]<sup>5</sup>. The difference arises from the inequality in the chemical potentials

<sup>4</sup>When the discretization uses 500 slabs, the correspondence is excellent unless the chemical capacitance is higher than the dielectric by more than 5 orders of magnitude (although we completely ignored the contribution of the electronic rails to  $C^{\delta}$ ). The deviation from the values predicted from equation 6.55 clearly indicates the breakdown of the numerical model, and better correspondence can be achieved by discretizing the model into thinner elements (1'000 and 10'000 slabs as shown in figure 6.14 in dark red).

<sup>5</sup>In ref. [257], the equivalent chemical capacitance was considered for a two rail system:  $C^{\delta} = (C_{\text{ion}}^{\delta -1} C_e^{\delta -1})^{-1}$ .

of the ions and the electrons. The effect of the electron and hole chemical capacitance on the IMVS frequency response will be shown later.

The effect of the diffuse layer capacitance simply adds up to the one naturally occurring from the coupling of  $C^\delta$  and  $C_{\text{disp}}$ , as figure 6.15e-h shows. It should be recalled that there are two double layer capacitances to be considered (at the electron transport layer interface and at the hole transport layer interface) and that they couple in series. The equivalent capacitance is such that the low frequency semi-circle has a maximum complex amplitude at:

$$f_{min} = \frac{1}{2\pi (R_{ion}^\infty + R_{rec}) \left( \frac{1}{(C_{\text{disp}} C_{ion}^\delta)^{0.5} + C_{ion,etl}^\perp} + \frac{1}{(C_{\text{disp}} C_{ion}^\delta)^{0.5} + C_{ion,etl}^\perp} \right)^{-1}} \quad (6.56)$$

When the ionic contribution to the chemical capacitance and the double layer capacitance are within the same order of magnitude as the dielectric capacitance, the bulk and the chemical relaxation have similar frequency responses and the two semi-circles can overlap into a single one, as it is shown in figure 6.15a-d.

The hypothesis we made by ignoring the charging of the transmission line by the electronic carriers is equivalent to saying that the device is limited by the contributions from the interfaces. All the ionic chemical capacitors and the double layer capacitance can be replaced to a single capacitive and resistive element. The capacitance has the value:

$$C_{dl,eq} = \left( \frac{1}{\sqrt{C_{\text{disp}} C_{ion}^\delta + C_{ion,etl}^\perp}} + \frac{1}{\sqrt{C_{\text{disp}} C_{ion}^\delta + C_{ion,etl}^\perp}} \right)^{-1} \quad (6.57)$$

and the ionic resistance combines into the sum of its  $n$  resistances that originate from the numerical discretization:

$$R_{ion}^{\text{total}} = \sum_1^n \frac{1}{n} R_{ion}^\infty = R_{ion}^\infty \quad (6.58)$$

An interesting situation occurs when the electronic charge transfer at the the interface with the hole transport and the electron transport layer is ideal ( $R^\perp = 0, C_{etl,htl}^\perp = 0$ ) and when the electronic resistance of the perovskite layer is negligible. In this case, we can further reduce the model to the simple equivalent circuit shown in Figure 6.16. Its complex impedance can be expressed by equation 6.59. With the aforementioned approximations, we observe that the current source is readily connected in series to the voltmeter through a circuitual element without imaginary impedance (the series resistance). Therefore, from equation 6.59, the IMVS response can be easily deduced (equation 6.60).

---

With the three electrode capacitance that we have in our model, such reduction cannot be made. Nevertheless, if both  $C_h^\delta$  and  $C_e^\delta$  are extremely low, the equivalent total chemical capacitance will also be extremely low. The term  $1/20C_e^\delta$  doesn't show up in the equation because we have automatically ignored it.



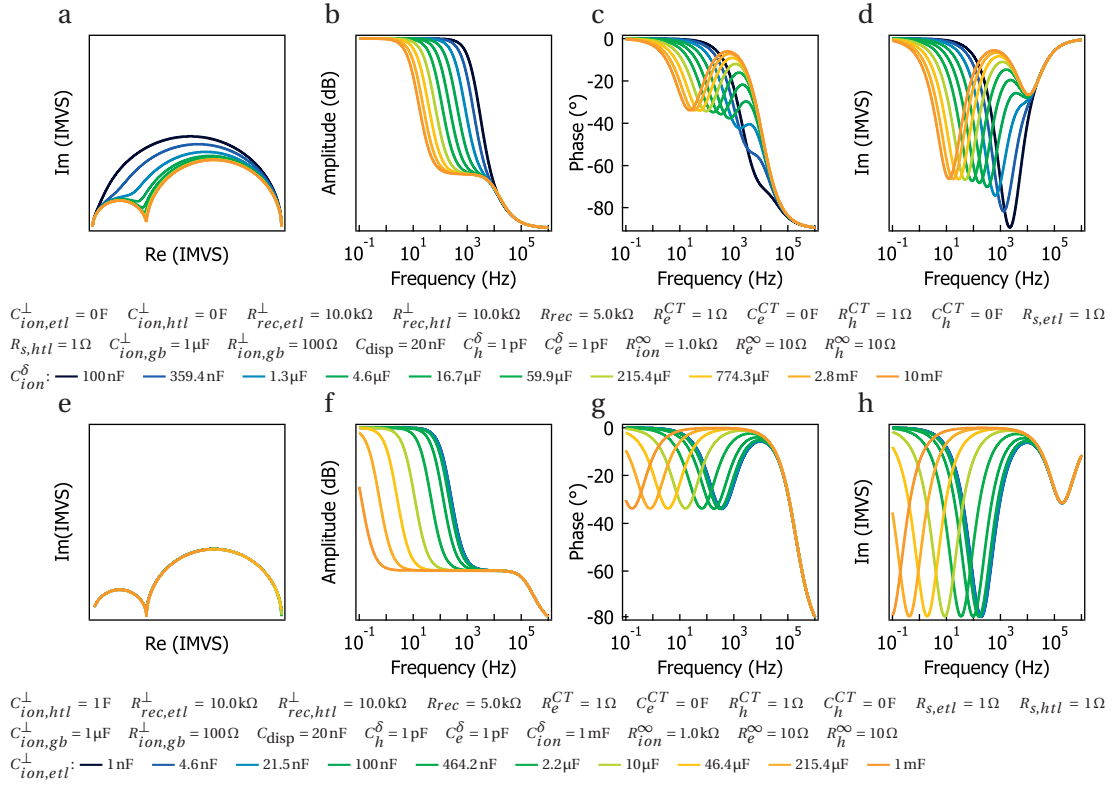


**Figure 6.15:** Numerical simulation of a mixed ionic-electronic conductor generation layer sandwiched between two ideal hole and electron transport layers, when the hole and electron chemical capacitance is negligible. (a-d) For varying the chemical capacitance (with  $C_{ion}^{\perp} = 0$  F) and (e-h) for varying the double layer capacitance (with  $C_{ion}^{\delta} = 10 \mu\text{F}$ ). (a,e) Nyquist plot, (b,f) the amplitude (in dB) versus frequency, (c,g) the phase versus frequency and (d,h) the imaginary response versus the frequency

$$Z_{reduced}(\omega) = R_s + \frac{1}{\frac{1}{R_{rec}^{eq}} + j\omega C_{disp} + \left(R_{ion}^{\infty} + \frac{1}{j\omega C^{eq}}\right)^{-1}}$$

$$\text{where } R_{rec}^{eq} = \left(\frac{1}{R_{rec}} + \frac{1}{R_{rec,htl}^{\perp}} + \frac{1}{R_{rec,etl}^{\perp}}\right)^{-1} \quad (6.59)$$

$$\text{and } C^{eq} = \left(\frac{1}{C^{\delta}/2 + C_{ion,etl}^{\perp}} + \frac{1}{C^{\delta}/2 + C_{ion,htl}^{\perp}}\right)^{-1}$$

$$IMVS(\omega) = \frac{Z_{reduced}(\omega) - R_s}{\Phi(\omega)} \quad (6.60)$$

The convergence between the two circuits is demonstrated in Figure 6.17, which depicts the error on the phase, amplitude and imaginary component of the IMVS resulting from

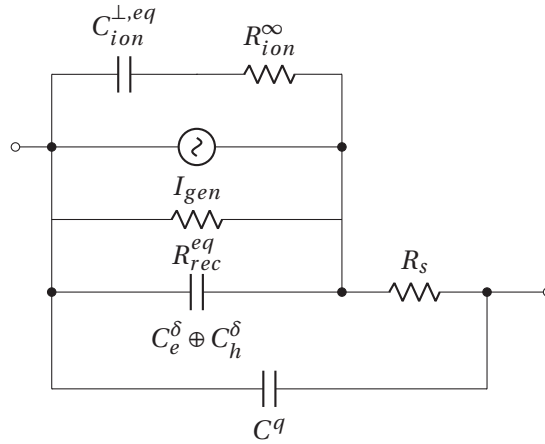


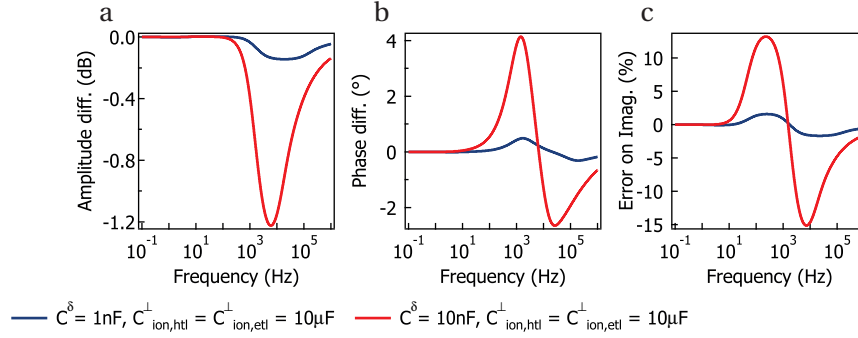
**Figure 6.16:** Reduced equivalent circuit in the case where  $C_{ion}^{\delta} \gg (C_e^{\delta} + C_h^{\delta})$  and neglecting the space charge elements affecting the electron injection. The transmission can then be omitted without compromise on the accuracy of the model. The equivalent recombination resistance  $R_{rec}^{eq}$  consists of the three recombinations (bulk and the two interfaces) in parallel, while the value  $C_{ion}^{\perp,eq}$  denotes the series combination of each  $C_{ion}^{\perp}$  in parallel with  $\sqrt{C_{ion}^{\delta} C_{disp}}$  (see equation 6.57. In this configuration, the parallel equivalent of the electronic and hole component of the chemical capacitance  $C_e^{\delta} \oplus C_h^{\delta} = \left(\frac{1}{C_e^{\delta}} + \frac{1}{C_h^{\delta}}\right)^{-1}$  appear in parallel to the dielectric capacitance.

those simplifications. We observe that the reduction of the model provides relatively good accuracy provided that the chemical capacitance remains much lower than the double layer capacitance for the ions. When its value is 0.1% of  $C_{ion}^{\perp}$ , the errors remain negligible, but become significant (around 10% error on the imaginary component) when it reaches 1% of  $C_{ion}^{\perp}$ . This approach, though making crude assumptions, is extremely appealing since it is the only instance where the IMVS response takes a simple analytical expression that can be readily inserted in a fitting routine.

We must highlight at this point a major approximation that is implicitly made when replacing the numerical discretization to a simple circuit such as the one in figure 6.16. When assembling the circuit we have assumed that each element is partitioned equally, i.e.  $R_{rec,j} = \frac{1}{n} R_{rec}$  (and similarly for each element). This clearly is not respected when the cell is under DC polarization or outside of thermal equilibrium (when there is a difference in the black body temperature of the cell and its environment). In this case, the electron and hole profile is such that the recombination resistance and the transport resistances must take a position-dependent partition that reflects the variations in charge carrier concentrations. The 0D approximation made here replaces the ionic transport resistance by the mean ionic transport resistance (averaged across the whole film), but clearly it will be higher in the region where ions accumulate. Similarly, the recombination resistance is an equivalent recombination resistance, which is dominated by the lowest one of the series (i.e. where the electrons and hole concentration is the highest). Experience shows however that the approximation still

yields excellent fitting and reflects accurately the general behavior of the solar cell, but the reader should be cautioned of the approximations entailed by the circuit simplification.

**Figure 6.17:** Error induced by the reduction of the equivalent circuit from the full circuit of Figure 6.9 to the one of Figure 6.16 on the (a) amplitude, (b) phase and, (c) imaginary component of the IMVS response of a cell.



#### 6.6.3.4 Effect of the recombination resistance

The recombination resistance is, with the transport resistance, the most critical parameter that describes the solar cell in steady-state. Its link to the collection efficiency is explicit and therefore strongly affects fill factor, the open circuit voltage and the power conversion efficiency of the solar cell. It is the ultimate goal of the device engineer to minimize the recombination current and hence maximize the recombination resistance. The physics of the solar cell dictates that the recombination resistance drops when the working voltage approaches the open circuit voltage of the cell. We can therefore simulate the IMVS response of the cell as a function of the recombination resistance with fixed ionic resistance and cross-check with experimental data. It is also worth reminding that the simplifications done when simplifying the electronic rail must hold, i.e. that  $R_{rec}$  remains significantly higher than the electronic transport resistance in the MIEC layer. In Figure 6.18, we show how the IMVS response is affected by a drop of the recombination resistance when  $R_{ion}^\infty = 1\text{k}\Omega$  (a to d)  $R_{ion}^\infty = 10\text{k}\Omega$  (e to h). The results can be interpreted in the sense of equation 6.60.

The high-frequency behaviour of the equivalent circuit of Figure 6.16 is accurately described by a  $-20\text{ dB/dec}$  low-pass filter, which  $-3\text{dB}$  corner frequency is (neglecting  $R_s$ ):

$$f_{-3\text{dB}} = \frac{1}{2\pi(C_{\text{disp}} + C_e^\delta \oplus C_h^\delta) \frac{R_{rec,eq}^\perp R_{ion}^\infty}{R_{rec,eq}^\perp + R_{ion}^\infty}} \quad (6.61)$$

which reduces elegantly - when  $R_{ion}^\infty \gg R_{rec,eq}^\perp$  - to:

$$f_{-3\text{dB}} = \frac{1}{2\pi(C_{\text{disp}} + C_e^\delta \oplus C_h^\delta) R_{rec,eq}^\perp} \quad (6.62)$$

which is equivalent to the situation where a single arc appears. Equation 6.62 can readily be used in the calculation of the collection efficiency, but experiments show that for most hybrid perovskite devices, the ionic resistance is not extremely high and two arcs are often observed. Therefore equation 6.62 can usually not be used as such. Instead, contributions from both semi-circles have to be accounted for, and it is best to perform a complex fit of equation 6.60 to readily distinguish recombination from ionic transport. We note the following phenomenological features that highlight the combinations between  $R_{rec}$  and  $R_{ion}^{\infty}$ :

- In the case where  $R_{rec} \ll R_{ion}^{\infty}$ , a single semi-circle describes the IMVS response (not observable from the Nyquist plot, but recognizable by the single feature in the phase plot and the amplitude plot). This does not mean that stoichiometric polarization does not take place, but rather that electrons feel a lower impedance through the direct recombination resistance than it does through the ionic branch (even when the impedance of  $C_{ion}^{\perp}$  is null, at high frequency). The amplitude of the semi-circle is too low for a feature to appear.
- On the other hand, when  $R_{rec,eq}^{\perp} = R_{ion}^{\infty}$ , the two arcs have the same magnitude because the parallel equivalent resistance formed of  $R_{rec,eq}^{\perp}$  and  $R_{ion}^{\infty}$  has exactly half the value of  $R_{rec,eq}^{\perp}$ .
- When  $R_{rec,eq}^{\perp} > R_{ion}^{\infty}$ , the second arc predominates. This situation is also illustrated when the ionic resistance is increased (Figure 6.18 c vs g) and the low frequency arc gains in amplitude at higher  $R_{rec}$  values, i.e. when it approaches the value of  $R_{ion}^{\infty}$  (it should not be forgotten that the effective recombination resistance is the parallel equivalent of the interfacial recombination and the bulk recombination).

### 6.6.3.5 Effect of the ionic resistance

The ionic resistance is proportional to the mobility and concentration of mobile defects. The nature of such defects is not the subject of this study but there is a consensus that iodide defects - vacancies or interstitials - are mobile. Under DC polarization, the defects accumulate on one side of the cell following the gradient of their electrochemical potential. Equivalent circuits do not provide direct solutions for this behavior, because they are being linearized during the calculation of their transfer function. We will for now retain the approximation that the defects are uniformly distributed. As we have discussed above, the value of the ionic resistance significantly weighs on the frequency response of mixed-conductor solar cells. This is further demonstrated in Figure 6.19, where  $R_{ion}^{\infty}$  is varied while keeping the recombination  $R_{rec}$  constant. The imaginary graph shows clearly that the ionic resistance couples strongly into the frequency response of both arcs. The Nyquist plot illustrates well that the recombination in steady-state condition remains constant (the x-intercept of the corresponding impedance response equals  $R_{rec,eq}^{\perp}$  and is independent of the value of  $R_{ion}^{\infty}$ ).

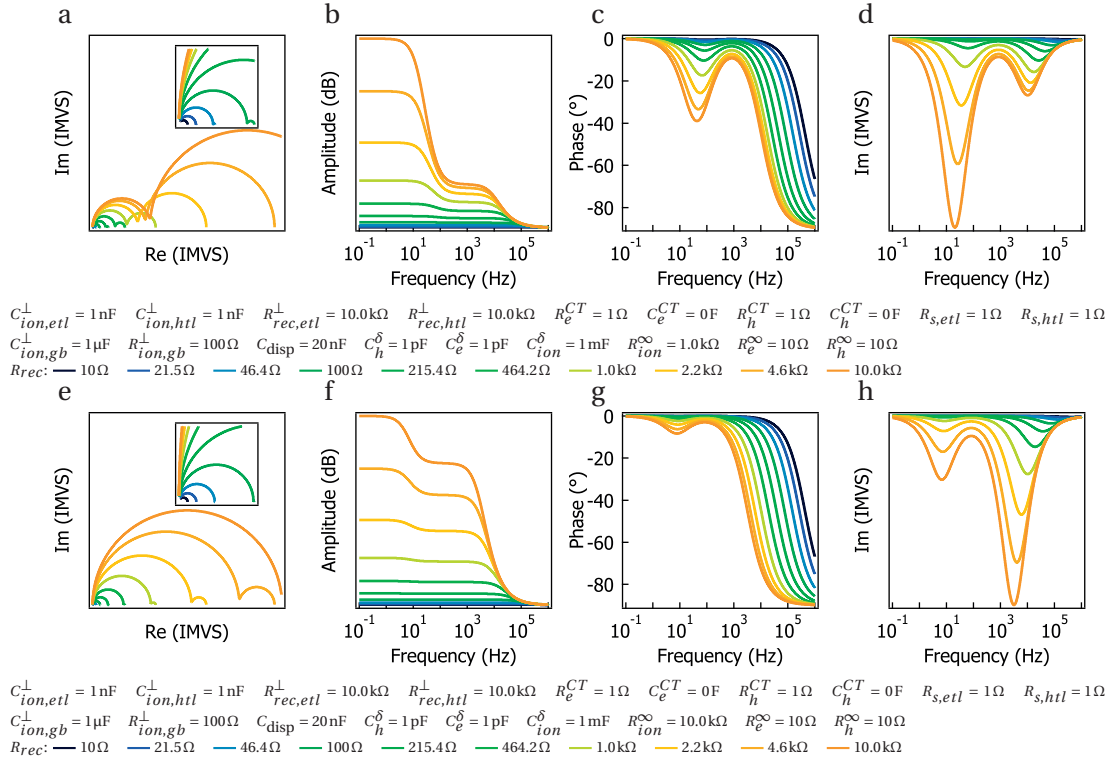


**Figure 6.18:** Numerical simulation of a mixed ionic-electronic conductor generation layer sandwiched between two ideal hole and electron transport layers, when the hole and electron chemical capacitance is negligible for various recombination resistances and when (a-d)  $R_{ion}^{\infty} = 1 \text{ k}\Omega$  and (e-h)  $R_{ion}^{\infty} = 10 \text{ k}\Omega$ . (a,e) Nyquist plot, (b,f) the amplitude (in dB) versus frequency, (c,g) the phase versus frequency and (d,h) the imaginary response versus the frequency

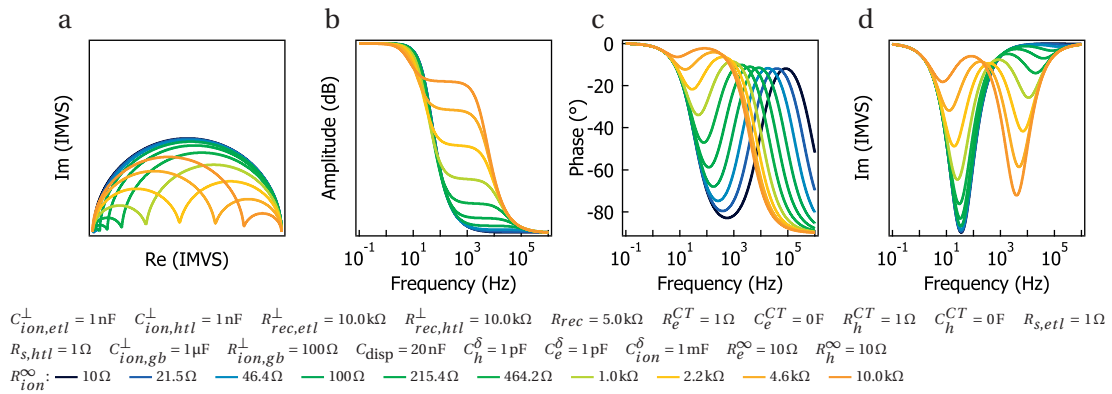


**Figure 6.19:** Numerical simulation of a mixed ionic-electronic conductor generation layer sandwiched between two ideal hole and electron transport layers, when the hole and electron chemical capacitance is negligible for various ionic resistances. (a) Nyquist plot, (b) the amplitude (in dB) versus frequency, (c) the phase versus frequency and (d) the imaginary response versus the frequency

6.6.3.6 Effect of the charge transfer RC elements

Experience shows that the model shown in 6.16 and described by equation 6.73 is often insufficient to describe the IMPS and IMVS response of most perovskite solar cells (see section 6.7.6). Proper corrections can be made by including the effect of the charge transfer impedance, in which case the equivalent circuit from figure 6.10 reduces to 6.20 (where neglected all interfacial recombinations). Unfortunately, there is no analytical solution for the AC transfer function for this circuit because the generation current source is buried within capacitive elements. One must therefore turn to numerical solving in order to simulate IMVS and IMPS response.

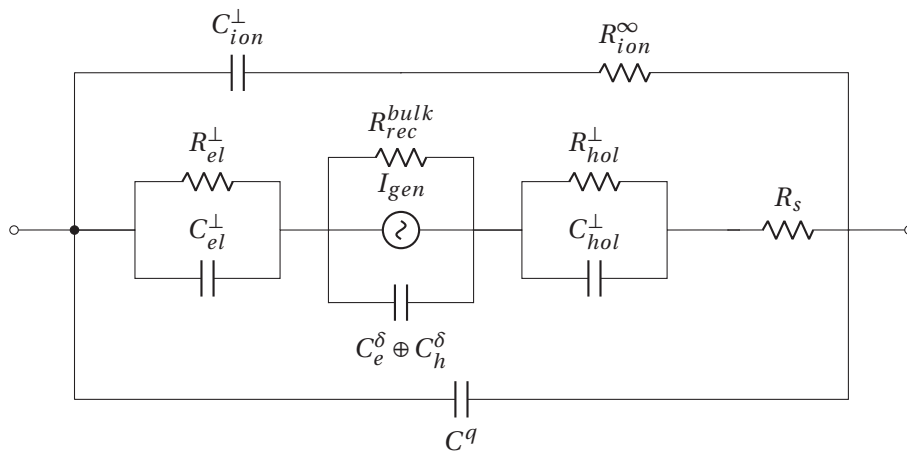


**Figure 6.20:** Reduced equivalent circuit in the case where the charge transfer impedance of the electrons and/or the holes cannot be ignored. The circuit is fitted through numerical simulation as no analytical expression exists. The interfacial recombination elements were omitted for clarity.

Figure 6.20 is the circuit we will use for all fitting procedures. Solving its AC characteristics requires far less computing time than the full transmission line. However, it features a higher number of components (10 in this case, 12 accounting for interfacial recombination) when compared to the one in figure 6.9. Let us consider the case where there is no capacitance at the interface. In this case there is a potential infinite set of  $(R^{CT}, R_{rec})$  that can describe the IMVS response and the fit cannot converge. In this situation, we must include the IMPS spectra and fit the two together. The IMPS spectra forces the value of the collection efficiency and therefore the ratio between  $R^{CT}$  and  $R_{rec}$ .

When the charge transfer impedance is small compared to the recombination resistance and the ionic resistance, the changes in the IMVS response are equally negligible. With respect to the displacement capacitor, the charge transfer resistance appears in series with the bulk recombination resistance and participates in shifting the high frequency semi-circle to lower frequencies  $(\tau = C \left( (R_{rec} + R^{CT})^{-1} + R_{ion}^{\infty -1} \right)^{-1})$ . With respect to the ion double layer

capacitance, it also adds up to the bulk recombination and participates in shifting the low frequency arc ( $\tau = C_{ion}^{\perp} (R_{rec} + R^{CT} + R_{ion}^{\infty})$ ).

In section 6.6.3.8 we will give the analytical expression for the DC value of the IMVS, as a function of the charge transfer resistance and the interfacial recombination. However, assuming no interfacial recombination, the DC value of the IMVS remains unchanged and equals

$$\lim_{f \rightarrow 0} \text{IMVS} = R_{rec} \quad (6.63)$$

The case where  $R_{rec,etl}^{\perp}$  (or  $R_{rec,htl}^{\perp}$ ) differs from infinity will be treated in section 6.6.3.8. We will show later that the charge transfer component has a significant influence over the performance of some perovskite solar cells. In fact, we will show that often, the transport resistance in the hole transporting and electron transporting layers are negligible.

When a double layer capacitance is added in parallel with the charge transfer resistance, an interesting situation occurs. There is now an RC element in series with a current source, which, for the first time in this study, sees a complex impedance between itself and the external circuit. If the RC element has the right resonant frequency, a negative loop can appear in the IMVS spectra. Figure 6.21 exemplifies such a situation, where 50 nF are added in parallel to a variable charge transfer resistance. In IMVS, this negative loop only occurs when there is a low impedance in series to it, such as the ionic branch or an interfacial recombination. In IMPS, the external circuit has a low impedance anyway and therefore such negative loops are more often observed.

### 6.6.3.7 The effect of the electron and hole chemical capacitance

So far we have considered the cases where the electronic contribution (from the electrons and the holes) to the chemical capacitance is minimal, such that  $C_{ion}^{\perp} \gg C^{\delta}$ . For highly disordered materials with a large trap state density, the electronic contribution to the total chemical capacitance may not be negligible, in which case we must consider the full transmission line behavior.

Increasing the electron chemical capacitance above  $C_{disp}$  leads to striking feature changes in the IMVS response. When  $C_{disp} \ll C_e^{\delta}$ , electrons and holes are allowed to trap on the transmission line, and two semi-circles describe the IMVS response: one describing the electrostatic relaxation of the electronic rail and one the chemical relaxation in the ionic rail. At steady-state, only the recombination resistance remains in all cases. At high frequency for  $C_e^{\delta} \ll C_{ion}^{\delta}$  (when the ionic concentration is higher than the electronic concentration), the space-charge capacitance in the ionic rail shorts, which gives rise to the high frequency arc. When  $C_e^{\delta} \sim C_{ion}^{\delta}$  or  $C_e^{\delta} \gg C_{ion}^{\delta}$ , the ionic rail strongly couples with the electronic rail and the ionic concentration follows a gradient across the whole film. In this regime, the chemical

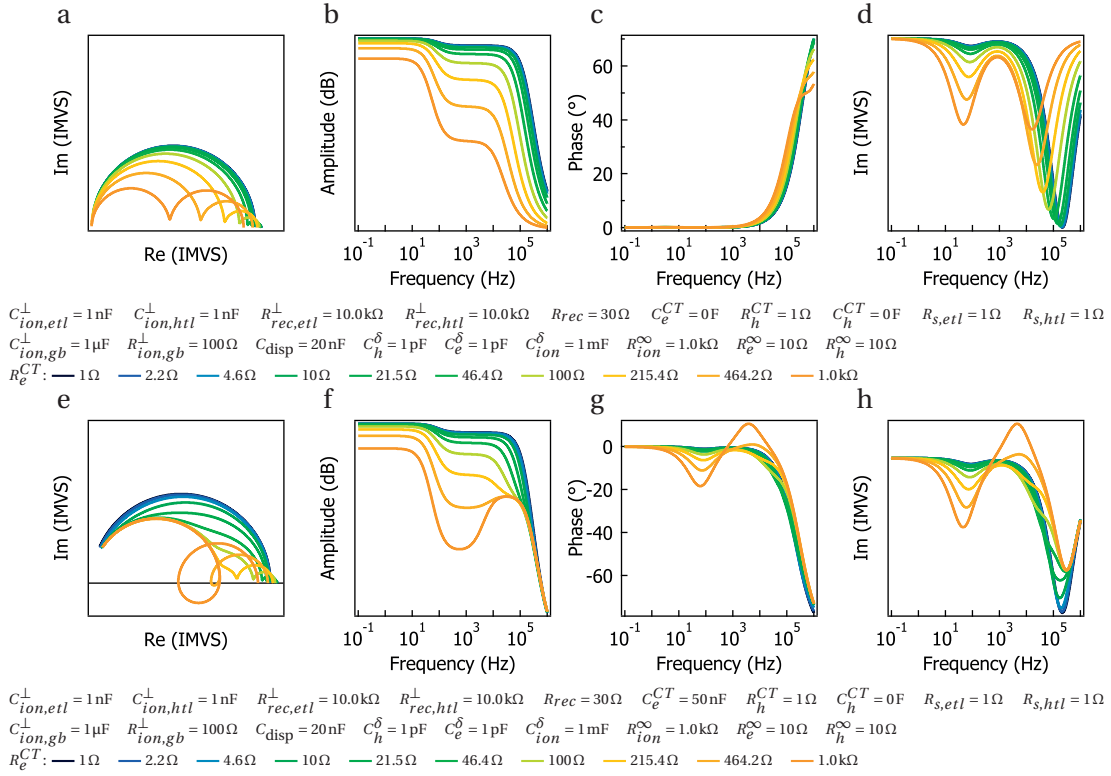


**Figure 6.21:** Numerical simulation of a mixed ionic-electronic conductor generation layer sandwiched between two ideal hole and electron transport layers, when the hole and electron chemical capacitance is negligible for various charge transfer resistance in the (a-d) low  $C^{CT}$  case and (e-h) high  $C^{CT}$  case (20 nF) (a,e) Nyquist plot, (b,f) the amplitude (in dB) versus frequency, (c,g) the phase versus frequency and (d,h) the imaginary response versus the frequency

relaxation of the electronic carriers determines the recombination rate, as opposed to the dielectric (bulk) relaxation.

We begin by pointing out that when both the electronic and hole contributions to the capacitance are high, the IMVS response is somewhat affected by either the electron or hole resistance but mostly limited by the recombination resistance that bridges the two rails. The recombination resistance (or a lower estimate of it) is easily determined by analyzing the  $j(V)$  curve. Assuming a electronic chemical capacitance of  $1\mu\text{ F}$  and  $C_{ion}^{\delta} = 1\text{ mF}$ ,  $C_{disp} = 20\text{ nF}$  and  $R_{rec} \approx 10\text{ k}\Omega$  (figure 6.22) two semicircles can still be seen because the interfacial capacitance  $C_{ion}^{\perp}$  ( $\approx 4.5\mu\text{ F}$  is still larger than  $C^{\delta}$  ( $\approx 1\mu\text{ F}$ ), but the high frequency arc has already significantly shifted to low frequencies ( $\approx 200\text{ Hz}$ ), which is much lower than our actual measurements. In general, numerical fittings will show that the electronic chemical capacitance is in the same order of magnitude or lower than the displacement capacitance. If we restrict our analysis to the case where  $C_{ion}^{\delta} \gg C_e^{\delta}$  and  $C_{ion}^{\delta} \gg C_h^{\delta}$ , we get again the simplified equivalent circuit shown in figure 6.16 (neglecting  $R_e^{\infty}$ ,  $R_h^{\infty}$  and  $Z^{CT}$ ). The electron and hole components of  $C^{\delta}$  now couple



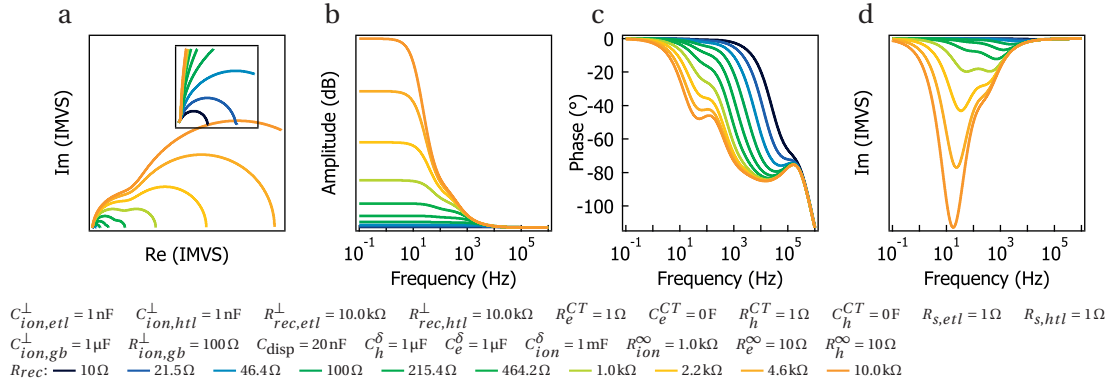


**Figure 6.22:** Numerical simulation of a mixed ionic-electronic conductor generation layer sandwiched between two ideal hole and electron transport layers, when the hole and electron chemical capacitance are equal to the ionic chemical capacitance, for various recombination resistances. (a) Nyquist plot, (b) the amplitude (in dB) versus frequency, (c) the phase versus frequency and (d) the imaginary response versus the frequency

in parallel to  $C_{\text{disp}}$ , but are in series with respect to each other, hence the  $\oplus$  denomination in figure 6.16. Figure 6.23 shows the results of numerical simulations for various values of  $C_e^\delta = C_h^\delta$  together with, in dashed line, the results of the numerical simulations from the circuit in figure 6.16 for the same input parameters.

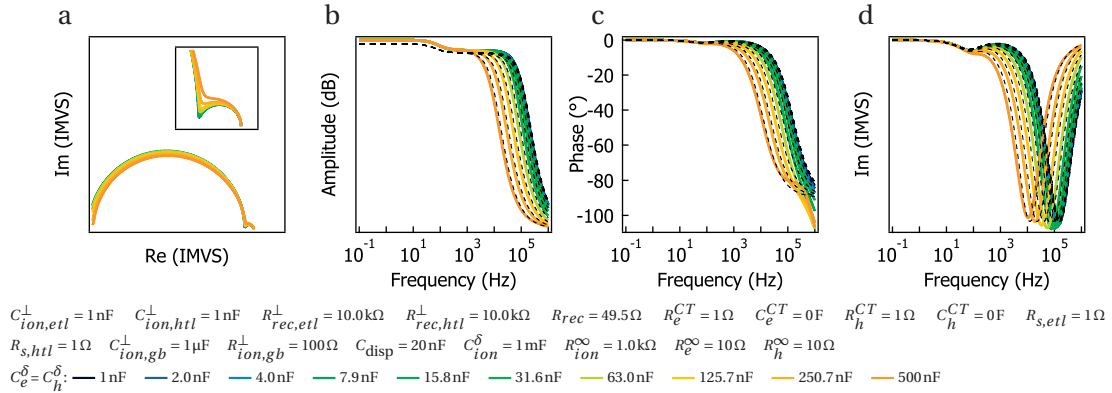


**Figure 6.23:** Numerical simulation of a mixed ionic-electronic conductor generation layer sandwiched between two ideal hole and electron transport layers, when the hole and electron chemical capacitance are of equal magnitude but much lower than the ionic chemical capacitance. The correspondence with the model of figure 6.16 is shown by the dashed black traces (a) Nyquist plot, (b) the amplitude (in dB) versus frequency, (c) the phase versus frequency and (d) the imaginary response versus the frequency. The small differences in the DC amplitude are due to the fact that we did not consider the interfacial recombination in the simulations of the simplified circuit.

In hybrid perovskite solar cells, it is believed that the contribution of the electronic component to the chemical capacitance is low compared to the ionic component. The low density of state of the valence band of  $\text{CH}_3\text{NH}_3\text{PbI}_3$  [258] suggests that the conduction band DoS is leading

the electronic contribution to the chemical capacitance. However, the electronic part of the chemical capacitance is not necessarily negligible with respect to  $C_{\text{disp}}$  and must be accounted for. Placing the electronic chemical capacitance in parallel to the current source, as it is shown in figure 6.16 and figure 6.20, accurately describes the simulated frequency response of the cell.

The high frequency response of the IMVS transfer function is dominated by the sum of the electronic relaxation of the carrier with the lowest chemical capacitance and the dielectric displacement capacitance. Deviations between the reference and the simplified circuit are evident at very high frequencies from the phase response. In the reference spectra, the phase drops below  $-90^\circ$  above 100 kHz, while it saturates at  $-90^\circ$  for the simplification of figure 6.16. This is due to the fact that the chemical capacitance and the dielectric capacitance are not purely in parallel as is simplified in figure 6.16, but there is a small charge transfer resistance  $2\ \Omega$  intercalated between to two.

In figure 6.24, we show the correspondence between the reference circuit of 6.10 and the one of figure 6.20, where contributions of the charge transfer resistance are accounted for. In the high frequency region, the phase shift dropping further than  $-90^\circ$  could be reproduced. Unfortunately, the convergence between the two models quickly fails when  $C_e^\delta \oplus C_h^\delta > C_{\text{disp}}$ , due to the coupling of the chemical capacitance with the displacement rail in the space-charge region. Correction for this effect could be accounted for in the charge transfer capacitance.

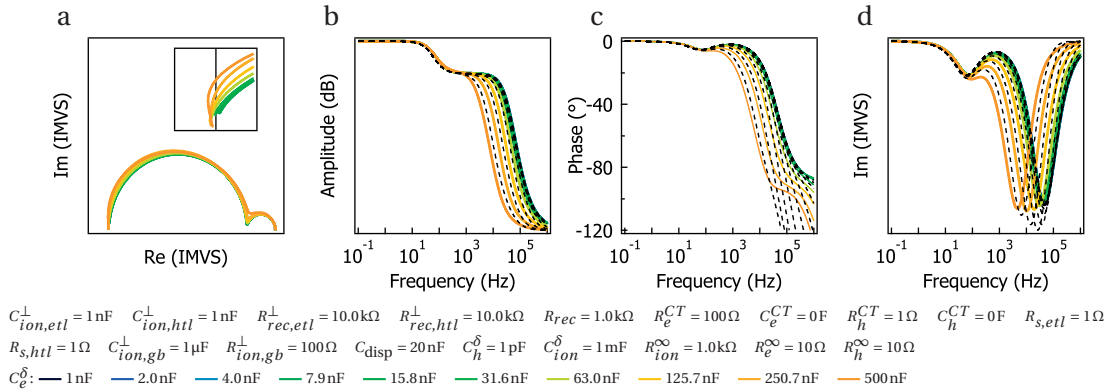


**Figure 6.24:** Numerical simulation of a mixed ionic-electronic conductor generation layer sandwiched between two ideal hole and electron transport layers, when the hole and electron chemical capacitance are of equal magnitude but much lower than the ionic chemical capacitance. The correspondence with the model of Figure 6.20 is shown in dotted black traces (a) Nyquist plot, (b) the amplitude (in dB) versus frequency, (c) the phase versus frequency and (d) the imaginary response versus the frequency

When there is significant coupling between the electronic rail and the ionic rail, a situation develops where the IMVS response can be described as a single-circle. This is shown in figure 6.25 (a-d), where the electronic component of the chemical capacitance is ramped from 1 pF to 1 mF. As it approaches the value of the ionic chemical capacitance (in this simulation, 1 mF), the two semi-circles merge together into a single one, whose magnitude is still strongly

influenced by the recombination resistance (figure 6.25(e-h)). Significant deformation of the semi-circle can occur, for example when the ionic resistance is in a similar order of magnitude as the recombination resistance (figure 6.25(i-l)). However, as we already mentioned, this situation does not seem to prevail in perovskite solar cells, where the electronic carriers couple very weakly to the displacement rail, owing to their low trap state density. We therefore decided not to push this analysis further.

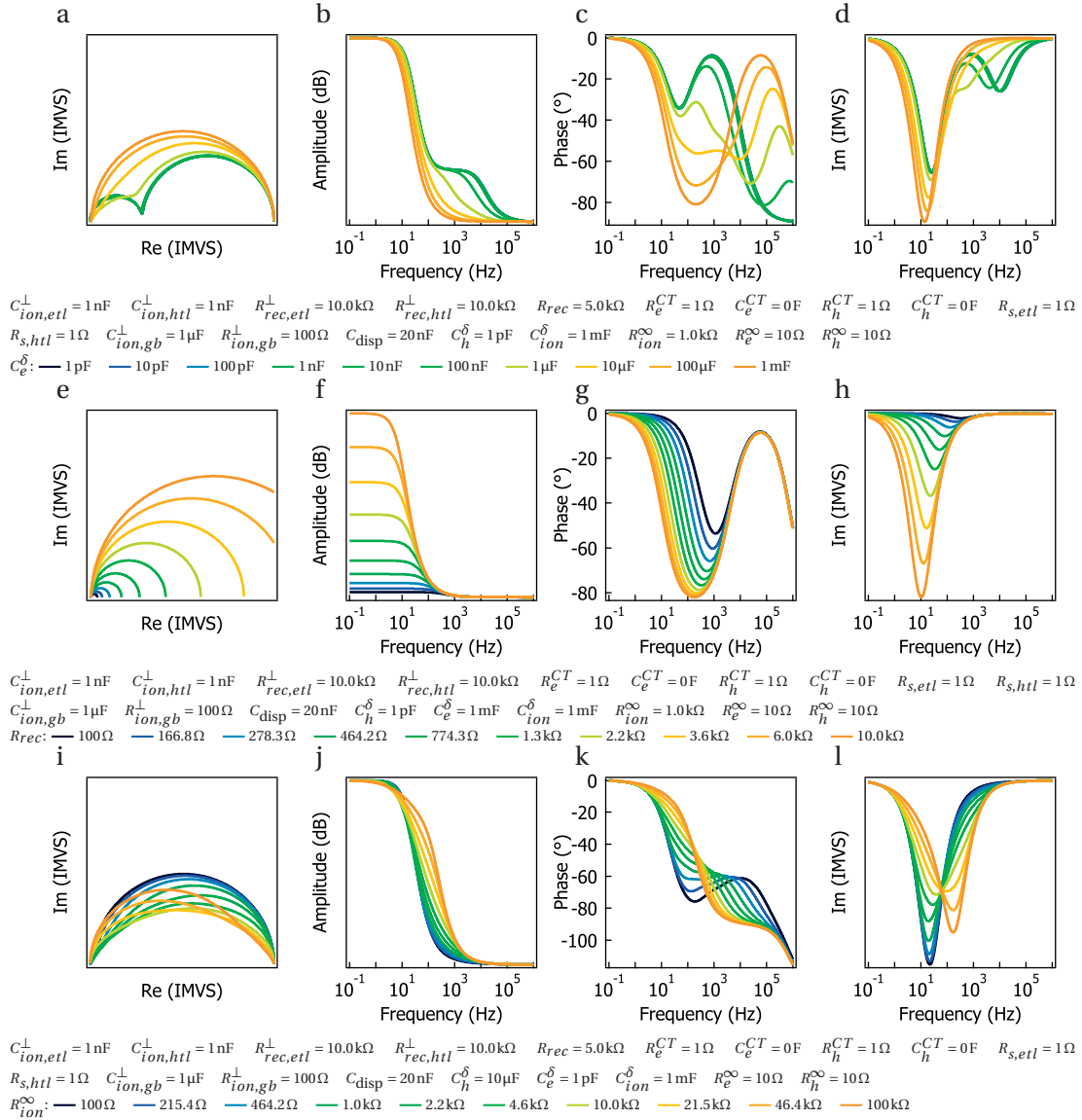


**Figure 6.25:** Numerical simulation of the IMVS response of a mixed ionic-electronic conductor generation layer sandwiched between two ideal hole and electron transport layers, when the hole chemical capacitance is negligible. (a-d) for varying electron chemical capacitance, (e-h) for varying recombination resistance and (i-l) for varying ionic resistance

### 6.6.3.8 Interfacial recombination

So far we have not treated the cases where the recombination is primarily interfacial, but accounted mostly for bulk recombination. If there is no charge transfer impedance, their effect on the IMVS spectra is the same and they cannot be differentiated.

Solving the steady-equation using the Kirchhoff laws of current and voltage for the circuit shown in figure 6.20 including interfacial recombination yields:

$$\lim_{f \rightarrow 0\text{Hz}} \text{IMVS} = \frac{1 - \frac{1}{1 + \frac{R_{rec,etl}^\perp}{R_e^{CT}}} - \frac{1}{1 + \frac{R_{rec,htl}^\perp}{R_h^{CT}}}}{\frac{1}{R_{rec}} + \frac{1}{R_e^{CT} + R_{rec,etl}^\perp} + \frac{1}{R_{rec,htl}^\perp + R_h^{CT}}} \quad (6.64)$$

Where the  $\perp$  sign stands for an interfacial component, and the subscripts *etl* and *htl* stand for electron transporting layer the hole transporting layer, respectively. When one of the interfacial recombination component is negligible (the resistance approaches infinity), equation 6.64 reduces to:

$$\begin{aligned} \lim_{f \rightarrow 0\text{Hz}} \text{IMVS} \left( R_{rec,etl}^\perp = \infty \right) &= \frac{1 - \frac{1}{1 + \frac{R_{rec,htl}^\perp}{R_h^{CT}}}}{\frac{1}{R_{rec}} + \frac{1}{R_{rec,htl}^\perp + R_h^{CT}}} \\ &= \frac{R_{rec,htl}^\perp}{\left( R_h^{CT} + R_{rec,htl}^\perp \right) \frac{1}{R_{rec}} + 1} \end{aligned} \quad (6.65)$$

When both interfacial recombinations are negligible, equation 6.64 reduces to:

$$\lim_{f \rightarrow 0\text{Hz}} \text{IMVS} \left( R_{rec,etl}^\perp = R_{rec,htl}^\perp = \infty \right) = R_{rec} \quad (6.66)$$

which properly expresses that only bulk recombination takes place. This situation is in accordance with the numerical simulations shown in figure 6.18. If all charge transfer impedances are null, equation 6.64 reduces to:

$$\lim_{f \rightarrow 0\text{Hz}} \text{IMVS} \left( R_e^{CT} = R_h^{CT} = 0 \right) = \left( \frac{1}{R_{rec,etl}^\perp} + \frac{1}{R_{rec,htl}^\perp} + \frac{1}{R_{rec}} \right)^{-1} \quad (6.67)$$

When one of the charge transfer component becomes very small with regards to the (for example  $R_e^{CT} \ll R_{rec,etl}^\perp$ ), equation 6.64 can be greatly simplified to:

$$\lim_{f \rightarrow 0\text{Hz}} \text{IMVS} \left( R_e^{CT} \ll R_{rec,etl}^\perp \right) = \frac{R_{rec,htl}^\perp}{\left( R_h^{CT} + R_{rec,htl}^\perp \right) \left( R_{rec} \parallel R_{rec,etl}^\perp \right)^{-1} + 1} \quad (6.68)$$

where the term  $R_{rec} \parallel R_{rec,etl}^\perp$  represents the equivalent parallel resistance made of  $R_{rec}$  and  $R_{rec,etl}^\perp$ . When the term  $(R_h^{CT} + R_{rec,htl}^\perp)$  is much smaller than  $R_{rec} \parallel R_{rec,etl}^\perp$ , equation 6.68 finally reduces to:

$$\lim_{f \rightarrow 0\text{Hz}} \text{IMVS} \left( R_e^{CT} \ll R_{rec,etl}^\perp \right) = \left( R_{rec} \parallel R_{rec,etl}^\perp \right) \frac{R_{rec,htl}^\perp}{R_h^{CT} + R_{rec,htl}^\perp} \quad (6.69)$$

The steady state IMVS value is proportional to the parallel resistance made of the bulk and the interfacial recombination. Allowing the interfaces to be recombinative strongly relaxes the model. When all five elements (the two CT resistances and the three recombinations) are fitting variables, the IMVS spectra becomes nondeterministic. Even when the charge transfer resistances are null, the steady-state IMVS value equals the parallel combination all three recombination processes, and it is impossible to resolve them separately.

In order to grasp the influence of the interfacial recombination, it is useful to simulate the frequency-dependent IMVS response of the cell as a function of the interfacial recombination. The added degree of freedom adds potential uncertainties on the other cell parameters. In figure 6.26, we show the influence of adding a recombinative interface behind a charge transfer resistance, while keeping the steady-state impedance constant (by making use of equation 6.65). We believe that the outcome of those measurements can induce uncertainties in the determination of ionic resistance, but such effects should be quite marginal in view of the rather small effect that 3 decades of  $R^{CT}$  have on the IMVS response.

There are three possible recombination pathways (1 bulk and 2 interfacial) in addition to two potential charge transfer impedances. Determining which of the three is the leading term is close to impossible by IMVS measurements. By coupling IMVS and IMPS together using precisely calibrated spectra, the collection efficiency can be fixed by the IMPS spectra. This can help in the determination of one of the charge transfer resistances but we must still rely in some simplification, i.e. assuming that one of the interfaces is non-limiting.

#### 6.6.4 Simulations of the IMPS response

The IMPS spectra of a photovoltaic device is acquired with the device connected to a low impedance biasing circuitry. Similarly to IMVS, IMPS can be recorded away from short circuit, but potentiostatic biasing is required (as opposed to galvanostatic biasing for IMVS). Photo-generated electrons can be extracted without hindrance, but undergo a competition between transport and recombination, which leads to a certain fraction of charges being lost in the process (as a reminder, in IMVS, all charges are lost by recombination). Similarly to the IMVS response, the IMPS response yields valuable information about the electronics of the cell, and in particular with regards to the transport properties of the electronic carriers.

The IMPS should be seen as an AC photocurrent loss measurement. After numerical correction,

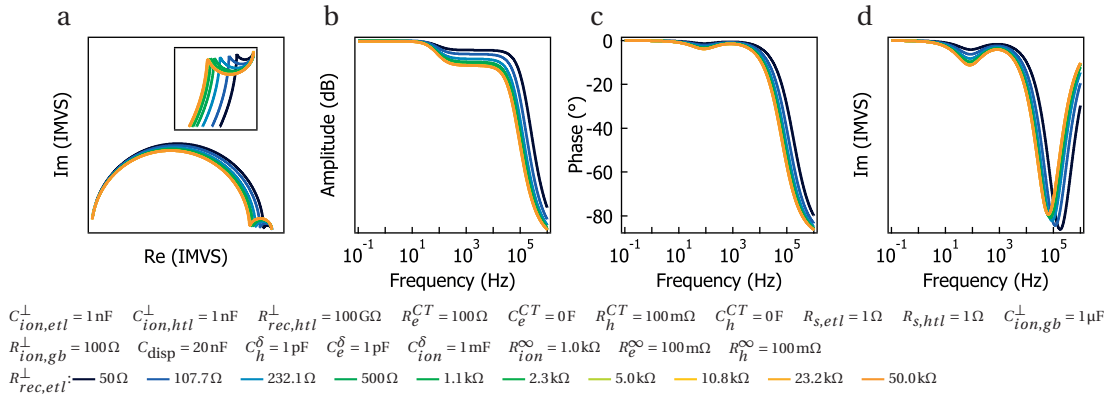


**Figure 6.26:** Numerical simulation of the IMVS response of a mixed ionic-electronic conductor generation layer sandwiched between two ideal hole and electron transport layers, for various partitions of the bulk and interfacial recombination. One of the interface was kept non-recombinative. The total recombination value was kept constant according to equation 6.65 for varying interfacial recombination resistance

the DC value of the IMPS spectra must be equal to the IQE (the product of the charge separation and the charge collection efficiency). For example, an IMPS value of 1 (in DC condition) means that all of the generated current is collected into the external circuit (no recombination). Because any electrochemical device has capacitive elements (displacement and entropic), the IMPS spectra appears in the complex space. For example, the capacitor in figure 6.16 is shorted at high frequency, hence all charges recombine and the IMPS value in the high frequency limit is null.

#### 6.6.4.1 Purely electronic conductor

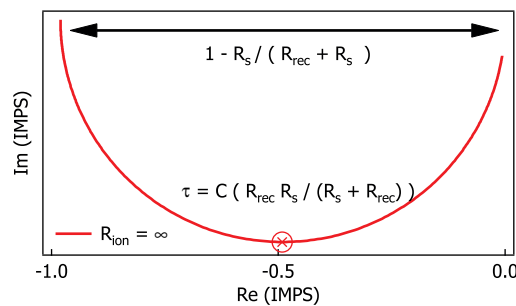


**Figure 6.27:** Typical IMPS response for a p-i-n photovoltaic device with purely electronic conductivity. The dielectric capacitance of all other layers than the photocurrent generation layer have been omitted for clarity.

For a simple circuit like the one shown in figure 6.16, which describes a basic, ideal solar cell without stoichiometric polarization, the IMPS spectra is described by a single semi-circle

(figure 6.27), which magnitude is nothing else than the collection efficiency:  $1 - R_s / (R_s + R_{rec})$ <sup>6</sup>. When  $R_s$  is close to 0 or when  $R_{rec} \gg R_s$ , the collection efficiency is close to unity. In the case where  $R_s \approx R_{rec}$  the DC value of the IMPS approaches 50%. When  $R_{rec} \ll R_s$ , the collection efficiency approaches 0.

In contrast with IMVS and AC impedance spectroscopy, the bulk capacitance has absolutely no effect on the IMPS response, due to its placement between the metallic electrodes. Instead, the high frequency response is dominated by the relaxation of the electronic chemical capacitances through the external circuit.

The influences that certain key elements of the full equivalent circuit have onto the IMPS spectra are now described in more details. Some of them echo the IMVS simulations but it is still worth looking into the principal effects that can be expected.

### 6.6.4.2 Mixed ionic-electronic conductor

Under illumination, the electronic conductivity of the absorbing MIEC increases drastically. Even though the MIEC could be primarily an ionic conductor in the dark, we expect it to become primarily an electronic conductor under light because of the sharp increase in electronic carrier density. This was the basis for the removal of all electronic resistances in the transmission line model (figure 6.10).

In IMVS, the impedance of the cell remained high, due to the high-Z biasing circuitry and the relatively high shunt resistance. The stoichiometric polarization could therefore easily be seen, especially at low voltages where  $R_{rec} \gg R_{ion}^\infty$ . In IMPS, a low frequency semi-circle originating from the ionic branch can also appear, but under the condition that the HTL and ETL resistance is in the same order of magnitude as the ionic resistance and that recombination is not much faster than the ionic resistance. If those conditions (which turn out to be respected for most PSCs), the IMPS spectra takes a shape similar to the one shown in figure 6.28.

The DC value of the IMPS ( $1 - R_s / (R_{rec} + R_s)$ ) is unaffected by the presence of the ionic branch, under the assumption that the electrodes are ideally blocking for ions (the ionic branch is behind a capacitor that has infinite impedance at low frequencies).

However the ionic branch induces another recombination pole at low frequencies, responsible for the appearance of the low frequency semi-circle. In this case, the high frequency semi-circle has a time constant of  $\tau = C(R_{rec}^{-1} + R_{ion}^{\infty -1} + R_s^{-1})^{-1}$  (the dielectric capacitor sees all resistances in parallel)<sup>7</sup>. At the intercept of the high frequency semi-circle with the real

<sup>6</sup>Neglecting charge transfer impedances and interfacial recombinations

<sup>7</sup>Provided that the ionic double layer capacitance is much larger than the dielectric capacitor (here bundled with the electronic component to the chemical capacitance in "C")

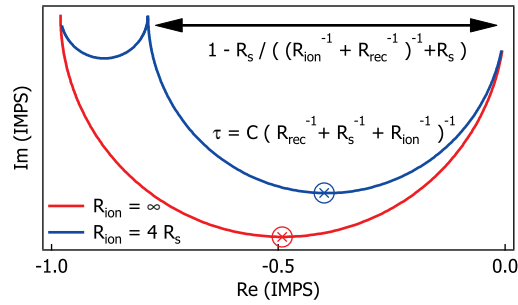


**Figure 6.28:** Typical IMPS response for a p-i-n photovoltaic device with mixed electronic-ionic conductivity (blue) and purely electronic conductivity (red) and perfectly blocking electrodes in the ionic branch. The dielectric capacitance of all other layers than the photocurrent generation layer have been omitted for clarity.

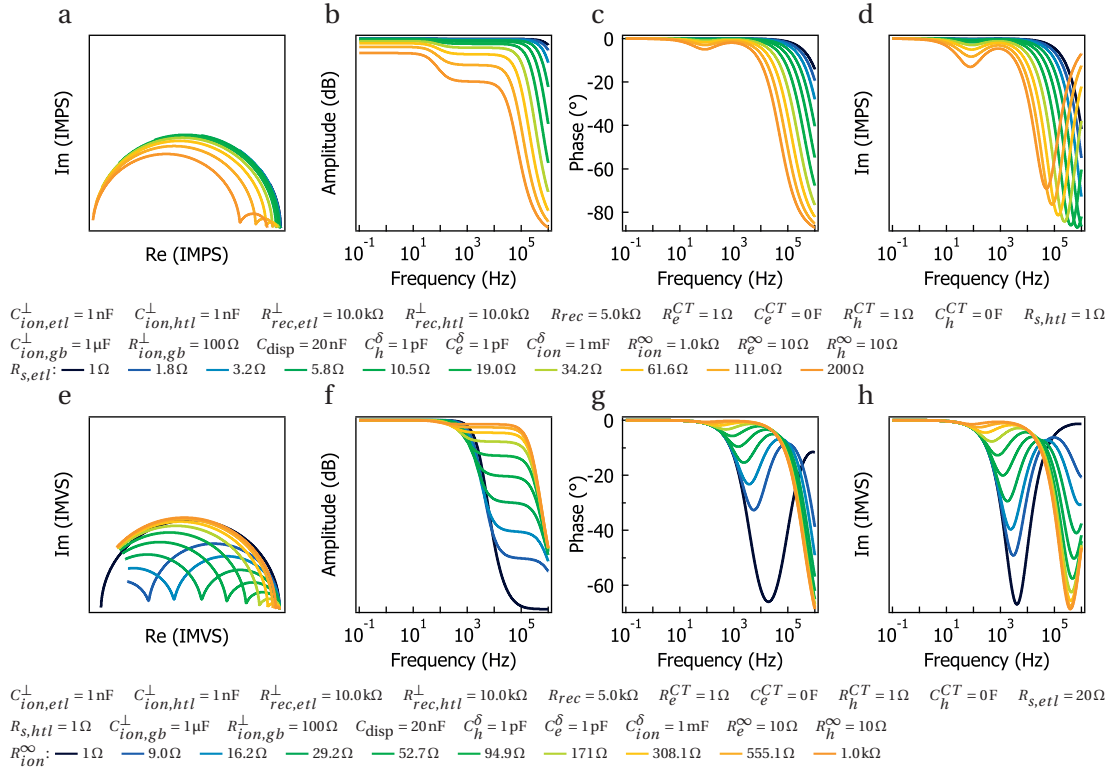
axis,  $C_{ion}^{\perp}$  is still shorted. Therefore, the magnitude of the high frequency semi-circle is determined by the amount of current flowing through the external circuit, in a competitive process with not only the direct recombination but also the recombination through the ionic branch, both as parallel processes. Hence the magnitude of the second semi-circle equals  $1 - R_s / ((R_{rec}^{-1} + R_{ion}^{-1})^{-1} + R_s)$ , which accounts for the parallel configuration of the ionic and recombination resistance.<sup>8</sup> Figure 6.29(a-d) shows the influence of the series resistance on a typical IMPS response. The higher the series resistance, the lower the frequency of the first semi-circle. In addition, for very high series resistance, the IMPS amplitude at steady-state drops, as larger amounts of recombination kick in.

Figure 6.29(e-h) depicts numerical simulations of IMPS spectra for various values of ionic resistance. We observe a large contribution of the ionic branch in the Nyquist plot when  $R_{ion}^{\infty}$  is lower or of equal magnitude as  $R_s$ , but vanishes quickly for higher ionic resistivities.

When the cumulated transport resistance of the hole transporting layer and the electron transport layer increases, the time constant of the high frequency semi-circle decreases accordingly (figure 6.29(e-h).) A high transport resistance is usually problematic, but only when it is compared with the recombination resistance. Significant losses occur when the IMPS cut-off frequency becomes dangerously close to the IMVS high frequency one. It is therefore a general aim to increase the transport rate and decrease the recombination rate, which are both values that can be read from the high frequency components of the IMVS and IMPS spectra. However, as we will show later, for efficient PSCs, the transport resistance is not the element that dictates the shape of the  $j(V)$  curve around the maximum power point.

<sup>8</sup>In this example, we assumed that the values of the capacitors were sufficiently different such that the complex components are fully decoupled. In practice this is of course not the case but this is only an example that aims at the understanding of the spectral features. In a real-life situation, we went through fitting of the full IMPS spectrum using the results of numerical simulations, which allows to perfectly decouple each component of the model.





**Figure 6.29:** Numerical simulation of the IMPS response of a mixed ionic-electronic conductor generation layer sandwiched between two ideal hole and electron transport layers, for (a-d) different series resistances and (e-h) different ionic resistances.

### 6.6.4.3 Effect of the charge transfer RC elements

Similarly to our description of the effect of  $Z^{CT}$  onto the IMVS response, the same phenomenological treatment can be applied to the IMPS transfer function.

One of the main prowess of IMPS is the ability to separate the charge transfer resistance from the series resistance. Let us consider the equivalent circuit shown in figure 6.20 as an example. Assuming  $C^{CT} \gg (C_e^\delta \oplus C_h^\delta)$ , the high frequency signal shorts through  $C^{CT}$ . The first arc is treated exactly in the same way as if there were no charge transfer impedance (see section 6.6.4.2), with a time constant  $\tau = C(R_{rec}^{-1} + R_{ion}^{-1} + R_s^{-1})^{-1}$ . Now, assuming  $C^{CT} \ll C_{ion}^\perp$ , the next IMPS feature occurs when the charge transfer capacitor stops shorting and becomes gradually open. In this case the electrons feel a higher impedance because they must flow through  $R^{CT}$  (and cannot flow through  $C^{CT}$  anymore). This adds a series resistance and drops the charge collection efficiency, which reflects as another intercept with the real axis. This crossing point is at a value **lower** than the previous (lower collection efficiency), which gives rise to the appearance of a negative loop (figure 6.30). Mathematically, the first intercept with the abscissa is given by  $1 - R_s / ((R_{rec}^{-1} + R_{ion}^{-1})^{-1} + R_s)$  (there is no influence of the charge transfer component) and the second intercept is given by  $R_{rec}R_{ion} / (R_s(R_{rec} + R_{CT} + R_{ion}) + R_{ion}(R_{CT} + R_{rec}))$ . In DC condition, the charge transfer resistance is simply in series with the HTL and ETL resistance,

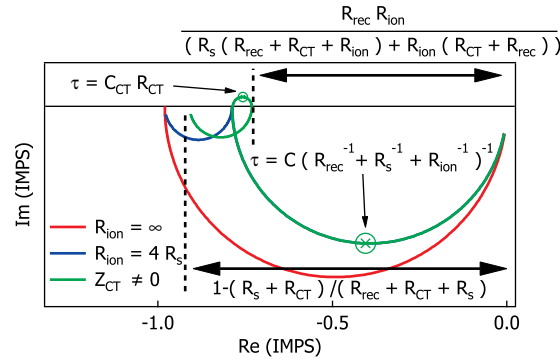


**Figure 6.30:** Typical IMPS response for a p-i-n photovoltaic device with purely electronic conductivity (red), mixed electronic-ionic conductivity (blue) and accounting for a complex charge transfer impedance (green). The electrodes in the ionic branch are considered perfectly blocking electrodes. The dielectric capacitance of all other layers than the photocurrent generation layer have been omitted for clarity.

hence the low frequency limit is give by:

$$\lim_{f \rightarrow 0\text{Hz}} \text{IMPS} = 1 - \frac{R_s + R_{CT}}{R_{rec} + R_{CT} + R_s} \quad (6.70)$$

The charge transfer impedance has a direct negative influence on the charge collection efficiency. We will show later that all PSCs we have measured have some degree of CT limitation which can seriously hamper their performance. It must be pointed out that in absence of further experiments, we cannot say whether the charge transfer is impeded at the ETL or the HTL side. When  $Z^{CT}$  is non-complex (lowly capacitive) we cannot distinguish the two charge transfers. However, when one of them is complex and shows up in the IMPS spectra, fitting the negative loop forces the determination of 1 CT element and the second CT element is naturally derived from the DC value of the IMPS spectra.

Figure 6.31 shows the effect of increases CT resistances (a-d) and capacitances (e-h) on simulated IMPS spectra. The small contribution to the ionic rail can be seen below 10 Hz. The effect of  $Z^{CT}$  appears as a positive "bump" or "shoulder" in the amplitude spectrum (Figure 6.31 b). The CT resonance occurs with the time constant of  $\tau = R^{CT} C^{CT}$  (in this case, between 100 Hz and 10 kHz) and appears as a **negative semi-circle**, as can be seen in the phase spectrum and imaginary part (Figure 6.31 c and d). The effect of varying the charge transfer capacitance has a similar effect (Figure 6.31 e-h) in that higher capacitances shift the pole to lower frequencies, but does not affect the arc amplitude (solely defined by  $R^{CT}$ ).

## 6.6. Flat-film perovskite solar cells

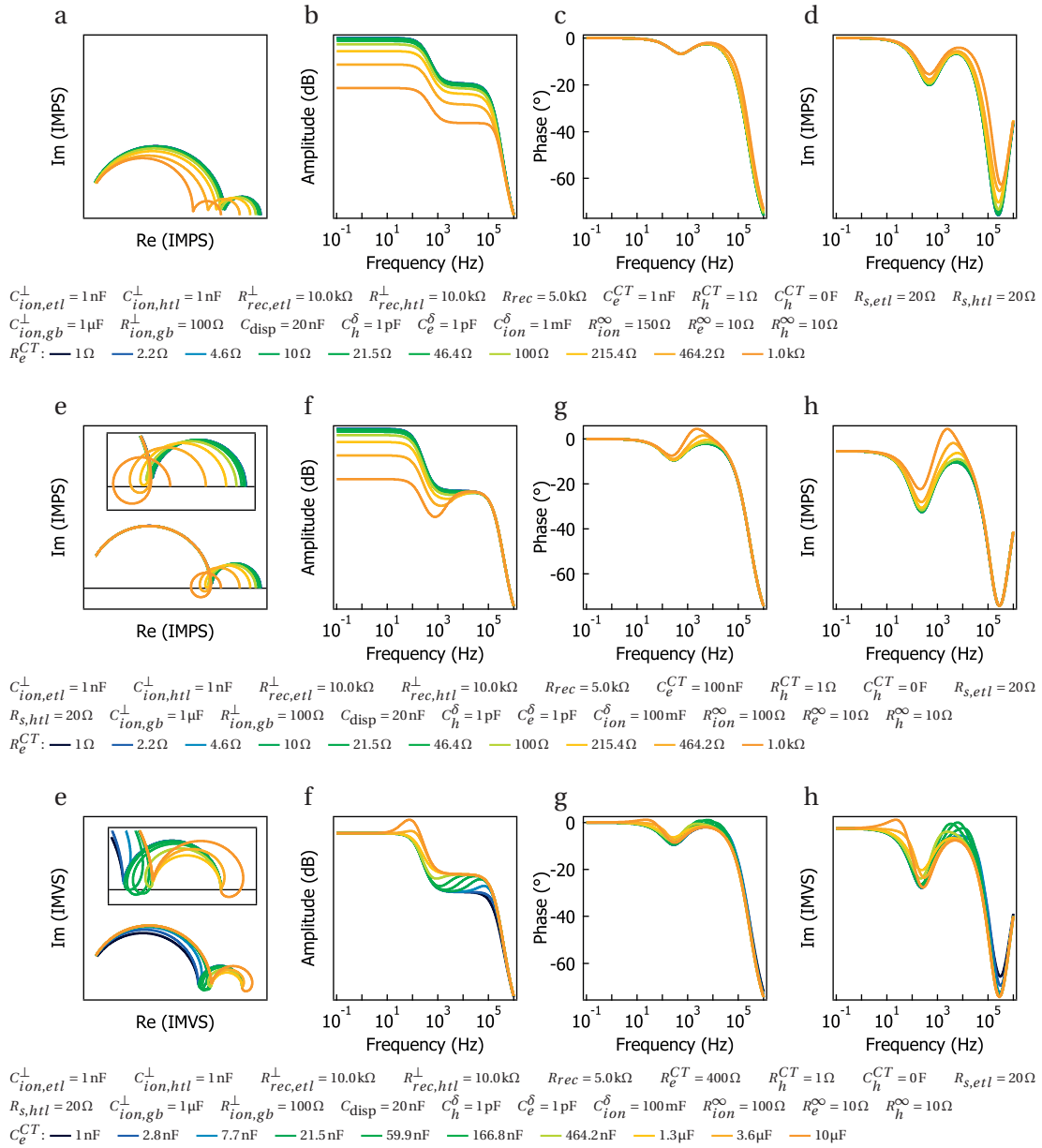


**Figure 6.31:** Numerical simulation of the IMPS response of a mixed ionic-electronic conductor generation layer sandwiched between two ideal hole and electron transport layers, with different charge transfer impedance conditions. (a-d) For varying  $R^{CT}$  with a negligible  $C^{CT}$ , (e-h) For varying  $R^{CT}$  with a significant  $C^{CT}$  (i-l) for varying  $C^{CT}$  with a fixed  $R^{CT}$

## 6.7 Results

### 6.7.1 Data treatment

Before fitting the IMVS and IMPS spectra, a rescaling factor must be applied to the real and imaginary part of the transfer function to normalize for the light flux and the generation current. Since we work with short wavelengths and considered a surface current generation, the result of both transfer function can be rescaled according to the measured IPCE and the measured cell reflectance losses (which is expressed as  $\eta_{lh}$ ) (equation 6.71.):

$$\text{IMVS}(\omega) = \text{IMVS}_{raw}(\omega) \frac{j_{ref}}{j_{generation}} = \text{IMVS}_{raw}(\omega) \frac{j_{ref} \text{IPCE}(0V) * \eta_{lh}}{\lim_{\omega \rightarrow 0} \text{IMPS}(0V)} \quad (6.71)$$

$$\text{IMPS}(\omega) = \text{IMPS}_{raw}(\omega) \frac{j_{ref}}{j_{generation}} = \text{IMPS}_{raw}(\omega) \frac{j_{ref} \text{IPCE}(0V) * \eta_{lh}}{\lim_{\omega \rightarrow 0} \text{IMPS}(0V)} \quad (6.72)$$

The charge profile and potential across the photovoltaic device is a function of light bias and biasing conditions, but not of the external circuit impedance (e.g. high-Z or low-Z). Therefore, IMPS and IMVS are complementary in the sense that for a same potential, the same components of the equivalent circuit have the same magnitude. IMPS and IMVS spectra therefore can be analyzed together. The resulting unit of the IMVS spectra is in  $\Omega$  while the IMPS spectra is unit-less and is always below 1. To compensate the non-deterministic nature of the circuit shown in figure 6.20, we generally fitted both the IMVS and the IMPS together, measured at the same potential. This allowed us to fit equivalent circuits with more circuit elements. We used a non-linear least square fitting (NLLSF) algorithm to optimize the input parameter set of the numerical model. At every iteration of the NLLSF loop, two numerical models representing the same equivalent circuit but with different boundary conditions were used to generate the IMPS and IMVS transfer function. The same input parameter set was used for both model, such that most degrees of freedom are heavily restricted.

Figure 6.32 shows the example of a the real and imaginary part of an IMVS and an IMPS spectra of a typical perovskite solar cell, fitted together to same circuit with different boundary conditions, using the same input parameter set. The residuals are displayed at the top of the graph, showing an excellent convergence of the fitting procedure.

#### 6.7.1.1 Implementation and procedure

Briefly, we used to Global Fit package provided with the IGOR Pro software to perform the coupled non-linear least square fitting of both the real and imaginary part of the IMVS spectra with a linked parameter set. The parameter values were the equivalent circuit descriptors (recombination resistance, series resistance, chemical capacitance, double layer capacitance, ...) and were used to assemble a SPICE equivalent model. The model was solved using the

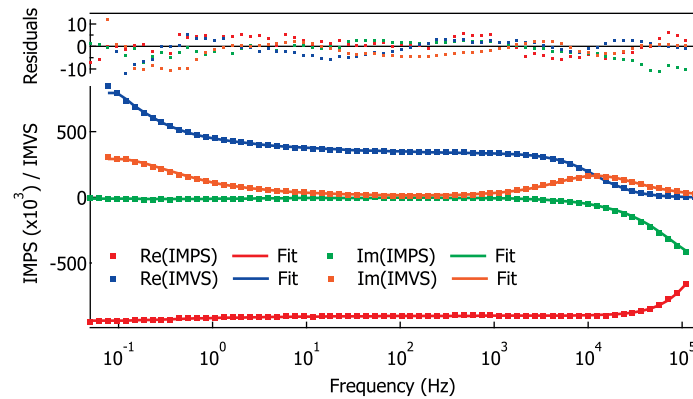


**Figure 6.32:** Global Fit of the IMVS and the IMPS real and imaginary part, fitted together to the circuit shown in figure 6.20. Both IMVS and IMPS spectra were acquired at 800 mV for a mesoscopic hybrid perovskite solar cell (its  $j(V)$  curve is shown in figure 6.35).

SPICE AC solver and read back as a phase and amplitude spectra by the Igor Pro homebuilt routines. After conversion into a real and imaginary component, the least squares were calculated and a new guess formulated. This iterative procedure, while extremely tedious, gives the unique opportunity to fit extremely complex IMVS and IMPS spectra for which only numerical solutions exist.

### 6.7.1.2 Non-deterministic situations

In section 6.6.3.8 we have briefly discussed the cases where no information about the recombination pathways is known: it can occur through the bulk or any of the two interfaces. This is extremely problematic with regards to the fitting procedure, as we cannot allow that multiple set of circuit element values lead to the same IMVS/IMPS spectra. **Therefore, we have decided to keep the interfaces as non-recombinative.** This is likely to be a major deviation from the reality and we realize it. But based on the result of the fit, we can arbitrarily recast the bulk recombination resistance into an interfacial one, using one of equations 6.64-6.68 and knowing its corresponding charge transfer component.

### 6.7.2 Typical IMVS spectra

The IMVS spectra of typical high efficiency perovskite solar cells is shown in figure 6.33 together with the results from its fit to equation 6.73. The qualitative shape of the IMVS response is representative of most standard mesoscopic and flat hybrid perovskite solar cells, as described in section 1.2.1 and 1.2.2. Previously, in section 6.6.3.7, we showed by numerical simulations (figure 6.25) that in the event of a large electronic chemical capacitance, a single IMVS arc should be observed. This is clearly not the situation here, hence this is a strong indication that the electrons and holes couple poorly with the ionic branch through a weak chemical capacitance. This justifies the simplification of the circuit in figure 6.9 to the one in figure 6.20.

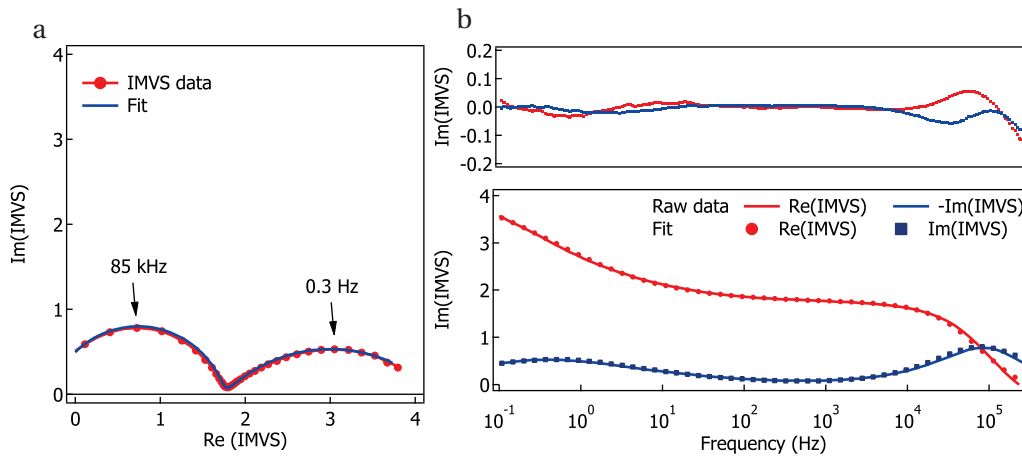


**Figure 6.33:** (a) Nyquist plot of the IMVS response of a mesoscopic (MA, FA, Cs) $\text{PbI}_x\text{Br}_{3-x}$ -based solar cell, measured at 980 mV. In red, the raw data. In blue, the fitted data to equation 6.73 using a constant phase element in place of the double layer capacitance in the ionic rail (b) Bottom: real and imaginary part (solid lines) of the same IMVS spectra with their respective fits (dots). Top: residuals of the fit.

The high-frequency arc describes the electrostatic relaxation of the dielectric capacitor into a combination of the recombination resistance and the ionic resistance (figure 6.13). The second semi-circle is at much lower frequencies (1 Hz-10 Hz)<sup>9</sup>. To account for the non-ideality of the double layer capacitance, we used a constant phase element instead of a normal capacitor in the fitting procedure.

In figure we 6.34, we show the imaginary part (a) and the phase (b) of the IMVS response of a typical flat film perovskite solar cell at different voltages. The fits to equation 6.73 are added in dashed line as a reference. The phase spectrum (figure 6.34b) shows that the frequency response of the first arc is strongly affected by the bias voltage. It is the consequence of the large variations of  $R_{rec}$ . Figure 6.13 lists the expected magnitudes and time constant of the IMVS semi-circles according to the circuit in figure 6.16. The amplitude of the first semi-circle is  $R_{eq} = R_{ion}^{\infty} R_{rec} / (R_{rec} + R_{ion}^{\infty})$  (the two resistors placed in parallel). The amplitude of the semi-circle is dominated by  $R_{rec}$  as long as  $R_{rec} \ll R_{ion}^{\infty}$ . In practice, it is not unusual for  $R_{rec}$  to be larger than  $R_{ion}^{\infty}$  at low bias and significantly smaller at high bias. We do not expect that the point at which the cross-over occurs has any specific physical meaning, but it can have a strong influence on the hysteresis of the solar cell. Also to be noted is the absence of negative-component in the complex plane. We showed in figure 6.21 that a negative loop can occur upon a complex charge transfer RC element along the electron or the hole rail. Its absence tells us that the electronic charge transfer process is ohmic. We will show later a counter-example to this situation. In the cases where the charge transfer resistance can be

<sup>9</sup>Its resonant frequency is in fact strongly influenced by the cell architecture. this will be covered in more details later

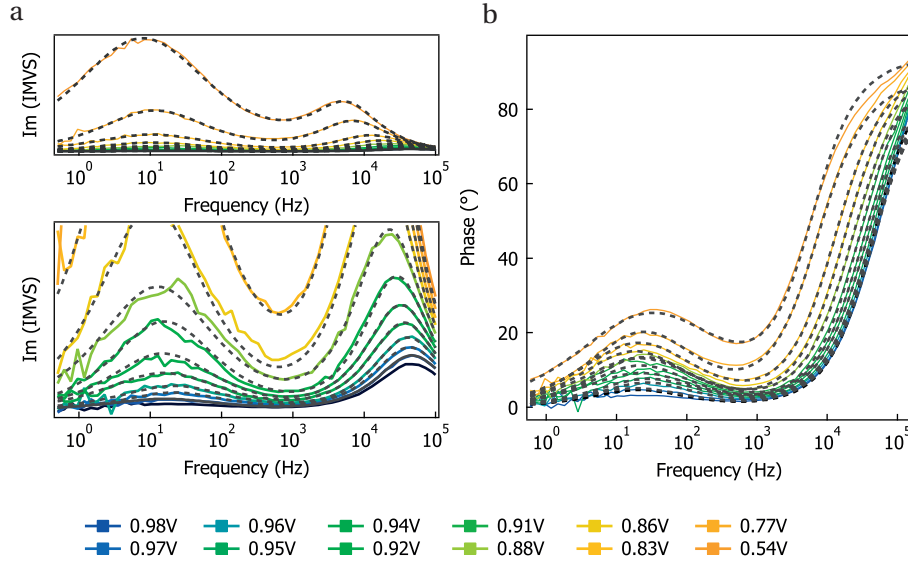


**Figure 6.34:** IMVS response of a flat film perovskite solar cells with SnO<sub>2</sub> electron transport layer. The cell was prepared according to [61]. The active layer is made of a SnO<sub>2</sub> compact layer (5-10 nm coated with a (MA, FA, Cs)PbI<sub>x</sub>Br<sub>3-x</sub> layer (~ 200 nm), a Spiro-MeOTAD hole transporting layer (~ 200 nm)

ignored, the IMVS spectra can be fitted using a complex fit to:

$$IMVS(\omega) = R_{fudge} + \frac{1}{\frac{1}{R_{rec}} + j\omega C_{disp} + \left( R_{ion}^{\infty} + \frac{1}{(j\omega)^n Q_{ion,dl}^{\perp}} \right)^{-1}} \quad (6.73)$$

where

- $R_{rec}$  is the equivalent recombination resistance, that includes the components from the interfacial recombination and the bulk recombination (see equation 6.68)
- $Q_{dl}$  is the CPE equivalent of the double layer capacitance
- $R_{ion}$  is the ionic resistivity
- $C_{disp}$  is the displacement capacitance
- $0 < n < 1$  is the CPE factor of the double layer capacitance
- $R_{fudge}$  is a purely instrumental factor used to correct the voltage offset on the output stage of the preamplifier

In general, we found that under a matched illumination comparable to  $400 \text{ W m}^{-2}$  (40% of the intensity of the nominal AM1.5G standard spectrum), the IMVS of flat solar cells generally fitted extremely well to equation 6.73. The CPE of the double layer capacitance usually takes

a value between 0.7 and 0.8. In Figure 6.35 we show the result of the IMVS fit to equation 6.73 as a function of the bias voltage. To the best of our knowledge, this is the first time that a voltage-dependent measurement is reported<sup>10</sup>.

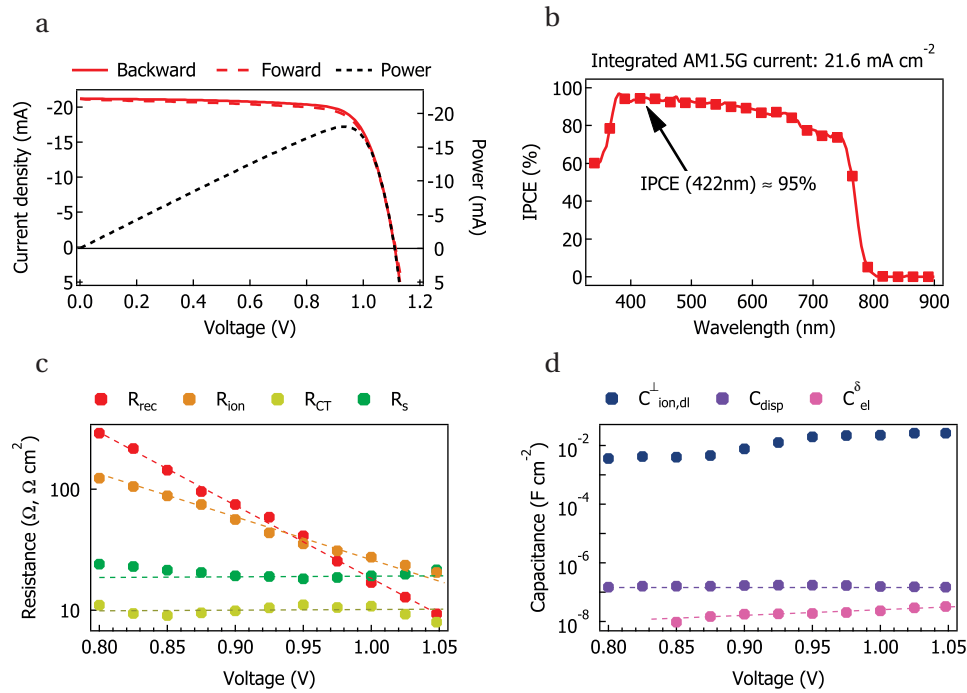


**Figure 6.35:** (a)  $j(V)$  of a typical mesoscopic solar cells, measured under a simulated AM1.5G solar irradiance of  $1000 \text{ W m}^{-2}$ , measured from  $V_{oc}$  to  $J_{sc}$  (solid red) and from  $J_{sc}$  to  $V_{oc}$  (dashed red). The solar cells parameters are: backward scan:  $V_{oc} = 1.11 \text{ V}$ ,  $J_{sc} = 21.2 \text{ mA cm}^{-2}$ ,  $FF = 76\%$ ,  $\eta = 18.01\%$ , forward scan:  $V_{oc} = 1.11 \text{ V}$ ,  $J_{sc} = 21.2 \text{ mA cm}^{-2}$ ,  $FF = 75\%$ ,  $\eta = 17.62\%$ . (b) Incident photon to current efficiency (IPCE) as a function of the wavelength. The integrated current matched fairly well the one short circuit measured by voltage sweep. The IPCE value at 422 nm was used to calibrate the IMPS measurement (using  $\eta_{lh} = 0.95$ ). (c) Series resistance (ETL, HTL, substrate, wires), ionic resistance, recombination resistance and charge transfer as a function of voltage, resulting from the fit of the IMVS (and IMPS) spectra to the model in figure 6.20. **The recombination, ionic and CT resistance have been scaled with the device area ( $\Omega \text{ cm}^2$ ). The series resistance has not ( $\Omega$ ).** (d) Ionic double layer capacitance, dielectric capacitance and (chemical capacitance) as a function of voltage, resulting from the same IMVS fit. All values have been scaled by the device area ( $\text{F cm}^{-2}$ ).

<sup>10</sup>It is technically possible to reach different voltages by using various light levels and loading a high resistance to the cell. While this approach has been used elsewhere, it affects the continuity equation in one more term (the generation). Therefore it cannot be ensured that the change in the value of the circuit components is uncorrelated to the light intensity



### 6.7.2.1 General observations

First, we note on the relative magnitude of the different circuit elements. The recombination rate and the ionic conductivity are usually of similar magnitude but do not have the same voltage dependence. In the case of the cell featured in figure 6.35, there is a cross-over between the two at around 950 mV. The cross-over between the two resistances originates from a change in the relative amplitude of the two IMVS arcs, as shown in figure 6.19 (a,d) and figure 6.18 (a,d). Practically, it means that at low voltages, the perturbation of light can take up to seconds to equilibrate into a photovoltage (for the larger part), due to the charging of the double layer capacitance. On the other hand, when  $R_{rec}$  dominates (when it is lower than  $R_{ion}^{\infty}$ ), the larger portion of the photovoltage equilibrates in the tens of kilohertz range.

### 6.7.2.2 Electronic components

The IMVS fit results notably in the determination of the bulk recombination resistance. In the example shown in figure 6.35, the recombination resistance drops from 290 to 9 between 800 mV and 1.05 V, in a quasi perfect exponential fashion (165 mV per decade). The recombination couples with the displacement capacitance in the high frequency region of the IMVS spectra. The displacement capacitance was remarkably constant throughout the whole voltage range. The value shown in figure 6.35d is normalized by the area, but in reality it should be scaled with the sample volume. Using equation 6.48 and a thickness of 200 nm, the real part of the relative dielectric permittivity of (MA, FA, Cs)PbI<sub>x</sub>Br<sub>3-x</sub> is approximately  $\epsilon_r \approx 39$ . We also note the small value of the electronic chemical capacitance that we placed in parallel to the current source in the model of figure 6.20. However, the value that we derived from the fit is at least a factor two lower than the dielectric capacitance. Except for an additional 90° phase shift at very high frequencies (that is anyway very faint in the case where  $R^{CT}$  is small), this element plays no role in the primary features of the IMVS spectra. At this stage, we cannot exclude an artifact from the measurement setup or from the fitting procedure.

To explain the behavior of the recombination resistance, we recall the proportionality between the recombination resistance and the charge density.

$$R_{rec} = \frac{a}{np} \quad (6.74)$$

Where  $a$  is a constant. Expressing the concentration of carriers in terms of electrochemical potentials, equation 6.74 rewrites

$$R_{rec} = \frac{a}{n_i^2 e^{-\frac{\tilde{\mu}_e - \tilde{\mu}_h}{k_B T}}} \quad (6.75)$$

By taking the base 10 logarithmic on both sides, we get:

$$\log R_{rec} = \log \left( \frac{a}{n_i^2} \right) + \log(e) \frac{1}{k_B T} (\tilde{\mu}_e - \tilde{\mu}_h) \quad (6.76)$$

and therefore:

$$\frac{\partial(\tilde{\mu}_e - \tilde{\mu}_h)}{\partial \log(R_{\text{rec}})} = \frac{k_B T}{\log(e)} \quad (6.77)$$

In the ideal scenario of bimolecular recombination, the voltage should increase by 56 mV for every decade of the recombination resistance. It is easy to show that in the case of mono-molecular recombination, the voltage should increase by the double, i.e. 112 mV per decade of the recombination resistance. In practice, the slope that we observe is closer to 165 mV per decade, which implies that recombination is neither bimolecular nor even mono-molecular, but it seems to be sub-mono-molecular. Comments on this value are for now out of the scope of this work.

### 6.7.2.3 Chemical components

The double layer capacitance responsible for the slow time component of the cell is between 4 and 5 orders of magnitude larger than the displacement capacitance. The capacitance takes values of tens of mFs, which is compatible with the values observed by Kim[185]. This magnitude of this capacitance is incompatible with the relative permittivity of  $\text{CH}_3\text{NH}_3\text{PbI}_3$  and its origin must be chemical. This capacitive element echoes the large low-frequency permittivity pointed out by Zarazua[247] and Juarez-Perez[248], simulated by Richardson [249] and explained further by Yang[63] and Almond[250]. This high apparent dielectric constant is nothing else than the result of the space-charge accumulation of ionic carriers at the interface with both the hole transporting or the electron transporting layer. We note that the capacitance is dictated by the lowest capacitance of the two interfaces and that at this stage we can give no indication with respect to the limiting one.

It is worth reflecting on the value of the double layer capacitance: at open circuit voltage under about  $400 \text{ W m}^{-2}$  irradiance, the capacitance reaches values to  $2 \text{ mF cm}^{-2}$ . Although it sounds extremely high, this value is not untypical of double layer capacitances that can be found in modern supercapacitors[259, 260] and close to the ones measured by Kim[185]. Using  $C_{ion}^\perp = \sqrt{C_{\text{disp}} C_{ion}^\delta}$ , assuming that the double layer chemical capacitances at both interfaces are equal and using the measured values for  $C_{ion}^\perp$  and  $C_{\text{disp}}$  at 800 mV, we find that the bulk chemical capacitance of  $\text{CH}_3\text{NH}_3\text{PbI}_3$  is equal to  $6.7 \text{ mF cm}^{-3}$ , which compares well to the value found by Yang et al.[63] of  $7.6 \text{ mF cm}^{-3}$ .

### 6.7.2.4 Light intensity variation

We observed a strong voltage dependence of both the ionic resistance (decreasing with voltage) and the double layer capacitance (increasing with voltage). Both vary with over one order of magnitude on a 250 mV span. This was similarly reported by Zarazua, who demonstrated the light activation of the real part of the dielectric constant at low frequency[247]. In the case of

perovskite solar cells, we already concluded that the measured capacitance belongs to the ionic rail mostly, and that the electronic component couples only weakly to the it through the chemical capacitance.

Figure 6.36 shows the variation of the IMVS fit parameters as a function of voltage (in galvanostatic mode) for another high-efficiency flat perovskite cell under two illumination conditions (yielding  $0.6 \text{ mA cm}^{-2}$  and  $7.9 \text{ mA cm}^{-2}$  of generation current). Both recombination and ionic resistance have dependence on the bias voltage and generation current, while the dielectric capacitance is almost unchanged (the small contribution of the electron chemical capacitance can hardly be seen here) and the ionic capacitance follows an upwards trend with voltage and generation.

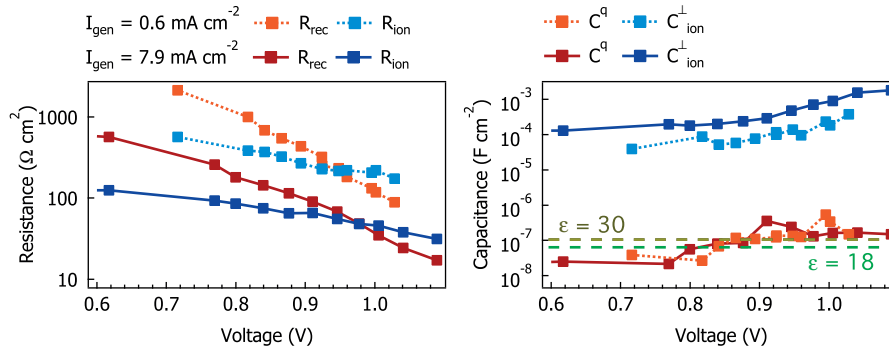


**Figure 6.36:** (left) resistance and (right) capacitance as results of the fit of the IMVS response of a state of the art flat perovskite solar cell with a  $\text{SnO}_2$  electron transporting layer to equation 6.73. The cell was biased galvanostatically at different currents to scan over the  $j(V)$  curve. The light intensity was varied by applying neutral density filters in front of the cell. The generation current was recorded for each point and the IMVS response corrected accordingly. Visual references for a displacement capacitance value for a material with  $\epsilon = 18$  and  $\epsilon = 30$  are added to the capacitance graph.

We also measured the IMVS response of a high-efficiency flat perovskite solar cell as a function of light bias by keeping the device under a zero current condition (open circuit voltage). Results are shown in figure 6.37. We observe that the value of the ionic resistance and capacitance are indeed dependent on the illumination intensity, and not uniquely on the bias voltage.

We can show that the decrease of ionic resistance is incompatible with the stoichiometric polarization:

$$R_{ion}^{\infty} = \frac{L}{A \cdot \sigma_{ion}} \quad (6.78)$$

Assuming that the total number of ionic carriers is constant and of constant mobility, but of

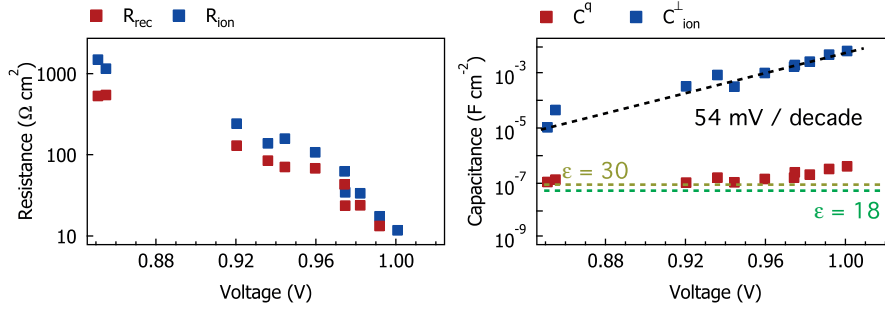


**Figure 6.37:** (left) resistance and (right) capacitance as results of the fit of the IMVS response of a state of the art flat perovskite solar cell with a SnO<sub>2</sub> electron transporting layer to equation 6.73. The cell was kept at open circuit voltage for the whole measurement. Light intensity was varied by applying neutral density filters in front of the cell. The generation current was recorded for each point and the IMVS response corrected accordingly. The expected displacement capacitance value for a material with  $\epsilon = 18$  and  $\epsilon = 30$  are added to the capacitance graph.

non-uniform distribution:

$$R_{ion}^{\infty} = \int_0^L \frac{dx}{A \cdot z_{ion} \cdot n_{ion}(x) \cdot \mu_{ion}} = \frac{1}{A \cdot \mu_{ion} \cdot z_{ion}} \int_0^L \frac{dx}{n_{ion}(x)} \quad (6.79)$$

The resistance is therefore limited by the depleted region in carriers, and should increase with the biasing of the device, rather than decreasing it.

Similarly, we recall the value of the chemical capacitance for ionic charges distributed uniformly across the film:

$$C_{ion}^{\delta} = \frac{(ez_{ion})^2 n_{ion}}{k_B T} A \cdot L \quad (6.80)$$

In the case of non-uniform ion concentration, the chemical capacitance takes exactly the same expression:

$$C_{ion}^{\delta} = \frac{(ez_{ion})^2}{k_B T} A \int_0^L n_{ion}(x) dx = \frac{(ez_{ion})^2 n_{ion}}{k_B T} A \cdot L \quad (6.81)$$

The stoichiometric polarization cannot explain the trends in ionic resistance and double layer ionic capacitance. Our results suggest that the ionic conductivity follows a similar correlation as the recombination resistance, which is dependent on the electronic carrier density (it decreases with light and bias). One hypothesis that could possibly explain the observed behavior is an increase in the mobile ionic defect concentration: the conductivity would decrease and the capacitance increase. One of the possible hypothesis would rely on the mass action law between ionic and electronic carriers:



Where an increase in hole concentration has a direct effect onto the concentration of iodide vacancies. Indeed we have

$$K = \frac{n_h}{a_{V_I} \cdot p_{I_2}^{\frac{1}{2}}} \quad (6.83)$$

Therefore we could express the chemical capacitance of the iodine vacancies using equation 6.33:

$$C_{ion}^{\delta} = \frac{(qz)^2}{k_B T} \frac{n_h}{K p_{I_2}^{\frac{1}{2}}} \quad (6.84)$$

Which expresses the linearity relationship between the hole density and the vacancy concentration. Equation 6.84 can be rewritten in terms of the hole electrochemical potential:

$$C_{ion}^{\delta} = \frac{(qz)^2}{k_B T} \frac{1}{K p_{I_2}^{\frac{1}{2}}} N_v e^{\frac{E_v - \tilde{\mu}_h^*}{k_B T}} \propto e^{\frac{\tilde{\mu}_h^* - E_v}{k_B T}} \quad (6.85)$$

and the ionic resistance rewrites:

$$R_{ion}^{\infty} = \frac{1}{\sigma_{ion}^{\infty}} = \frac{1}{\mu n_{ion} z} \propto \frac{1}{n_h} \propto e^{\frac{\tilde{\mu}_h^* - E_v}{k_B T}} \quad (6.86)$$

Equations 6.86 and 6.85 establish the exponential dependence of the chemical capacitance and resistance on the quasi-Fermi level of the holes. Voltage and illumination bias could, based on those relations, affect the ionic component of the chemical capacitance and its resistance, conditioned by the formation of a thermodynamic equilibrium with iodine gas (equation 6.82). The equilibration must be fast (faster than the measurement time) and to some extent reversible (measuring the cell at various potentials in various order does not affect the outcome of the measurement). These conditions are unfortunately unlikely to be satisfied. Similar defect chemistry equations might be more relevant with regards to the interaction of ionic and electronic carriers, but this now falls out of the scope of the present work.

### 6.7.3 Typical IMPS spectra

A typical IMPS spectra for a standard perovskite solar cell (mesoscopic or flat) is shown in figure 6.38. The real and imaginary part are typically rescaled such that the low frequency intercept of the IMPS spectra with the real axis - acquired at 0 V - matches the value of the internal quantum efficiency of the cell. The rescaling allows the proper scaling of the transport and recombination resistances such that expression 6.70 is respected.

Typically, the IMPS spectra features a large loop at very high frequency that reflects the

discharging of the dielectric capacitor into the external circuit through the series resistance. The exact magnitude and time constant of this arc were shown in figure 6.28 and 6.30. The IMPS usually features a second arc at low frequencies, often small in magnitude, which matches the relaxation of ionic carriers in the ionic rail. The magnitude of this arc depends on the relative values of  $R_{ion}^{\infty}$  and  $R_s$  (the lower  $R_s$ , the lower the magnitude of the semi-circle).

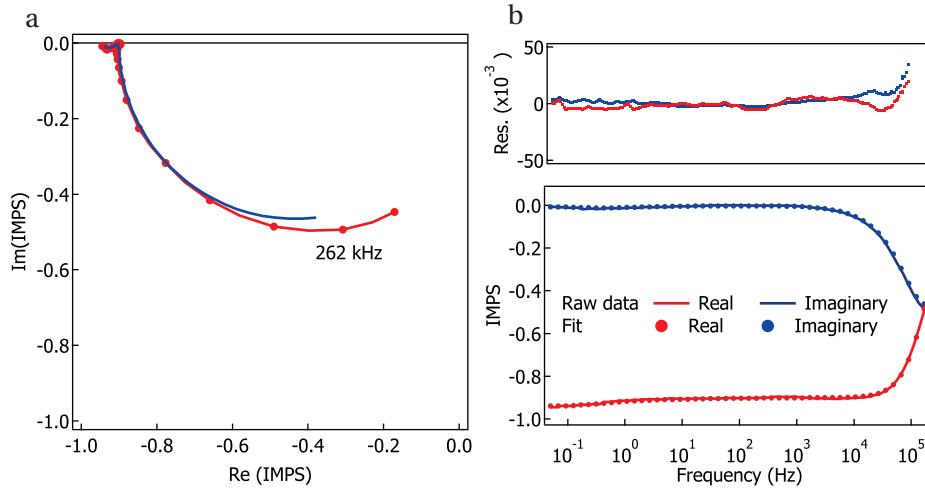


**Figure 6.38:** (a) Nyquist plot of the IMPS response of a perovskite cell using a  $\text{TiO}_2$  mesoporous electron extracting layer, measured at 800 mV. In red, the raw data. In blue, the fitted data to a the equivalent circuit shown in figure 6.20. (b) Real and imaginary part (bottom) of the same IMPS spectra with their respective fit (dots). Top: residuals of the fit.

#### 6.7.4 IMPS spectra with complex charge transfer components

We have explained using numerical simulations the behavior of a complex charge transfer impedance across the interface between the electron transporting layer and the hybrid perovskite layer, or between the hole transporting layer and the hybrid perovskite layer. In figure 6.39 we show as an example the IMPS spectra of a flat perovskite solar cell using a compact  $\text{TiO}_2$  underlayer which has been treated by LiTFSI. We observe a strong negative loop in the tens of kilohertz range and another small capacitive effect in the kink right after the loop (cf. the inset in figure 6.39). Those features are fitted extremely well by RC elements in series with the current source, as shown in the model of figure 6.20. Because the feature overlap with each other, a fitting is required to deconvolve the values of the components.

#### 6.7.5 Thickness dependence

We assembled two perovskite devices with different thickness of the  $\text{CH}_3\text{NH}_3\text{PbI}_3$  photo-absorbing layer that caps the  $\text{TiO}_2$  film ( $\sim 100$  nm and  $\sim 200$  nm) while keeping the same thickness of the  $\text{TiO}_2$  film constant ( $\sim 100$  nm). We measured  $j(V)$  characteristics and IPCE spectra for both cells (figure 6.40), as well as the IMVS and IMPS response, which were both

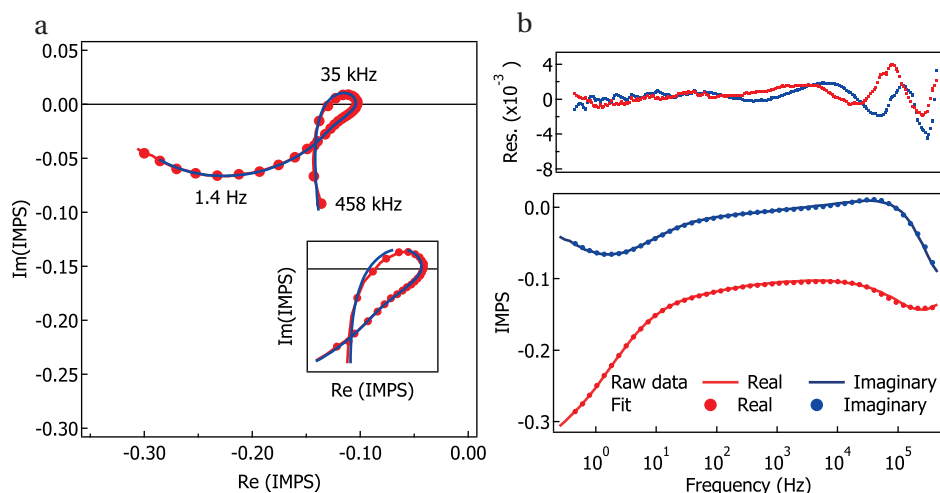


**Figure 6.39:** (a) Nyquist plot of the IMPS response of a perovskite cell using a  $\text{TiO}_2$  flat electron extracting layer treated with LiTFSI, measured at 800 mV. In red, the raw data. In blue, the fitted data to a the equivalent circuit shown in figure 6.20. The inset shows an enhanced view of the negative loop portion of the spectrum. (b) Real and imaginary part (bottom) of the same IMPS spectra with their respective fit (dots). Top: residuals of the fit.

numerically fitted to the circuit in 6.20. For the frequency-resolved measurements, we made sure that the same generation current is used in both cases.

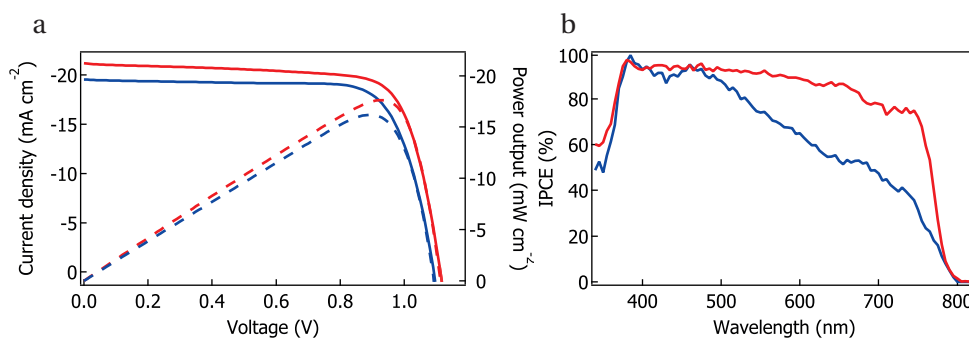


**Figure 6.40:** (a)  $j(V)$  curve of two typical mesoscopic perovskite solar cells with different thicknesses, measured under a simulated air mass 1.6 global spectrum of  $1000 \text{ W m}^{-2}$ . (b) IPCE response of the two same cells.

From the  $j(V)$  curve, the thin cell was slightly less efficient than the thick one (16.2% versus 17.6%), mostly owing to a lower photocurrent density ( $19.5 \text{ mA cm}^{-2}$  vs  $21.2 \text{ mA cm}^{-2}$ ) and a slightly lower open circuit voltage (1.09 V vs 1.11 V). The drop in photocurrent correlates well with the difference in the spectral response of the cell, where the red response of the thin cell is lower than the thick one, owing to a lack of absorption in this region of the solar spectrum. In both cases, we did not observe any significant  $j(V)$  hysteresis when the devices were scanned at  $20 \text{ mVs}^{-1}$ .

The results from the fitting of the IMVS and IMPS spectra are shown in Figure 6.41.

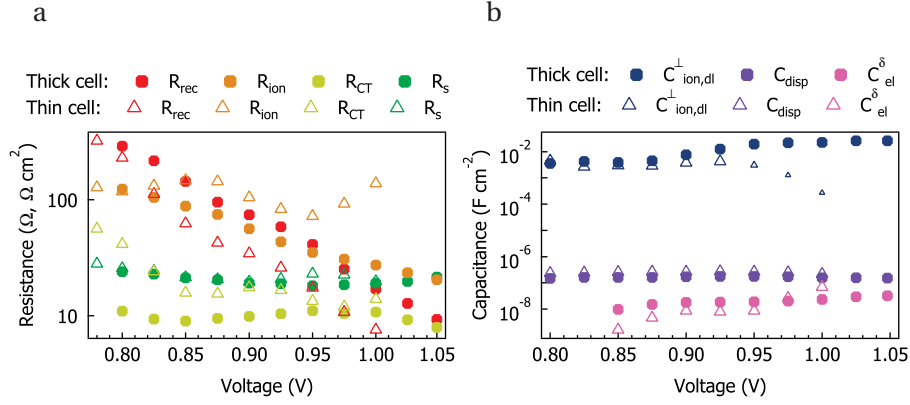


**Figure 6.41:** Results from the IMPS and IMVS fits for two devices assembled using a reported procedure[69]. (a) Series resistance (ETL, HTL, substrate, wires), ionic resistance, recombination resistance and charge transfer as a function of voltage, resulting from the fit of the IMVS (and IMPS) spectra to the model in figure 6.20. **The recombination, ionic and CT resistance have been scaled with the device area (Ω cm<sup>2</sup>). The series resistance has not (Ω).** (b) Ionic double layer capacitance, dielectric capacitance and (chemical capacitance) as a function of voltage, resulting from the same IMVS fit. All values have been scaled by the device area (F cm<sup>-2</sup>).

The following observations can be made:

- We observe a slight increase of the cell dielectric capacitance, by a factor 1.5. Recalling the expression of the displacement capacitance

$$C_{\text{disp}} = \epsilon_r \epsilon_0 \frac{A}{L} \quad (6.87)$$

where  $L$  is the cell thickness, this increase in the dielectric capacitance is only logical.

- Recombination in the thin cell is significantly faster than the thick cell. This explains the increase in open circuit voltage, but we see no obvious reason why the recombination should be thickness-dependent. The experiment should be repeated to confirm this hypothesis.
- The series resistance hasn't changed. In both cases it is around 20 Ω. This is not unexpected since the series resistance is given by the high frequency IMPS arc, which is nothing else than the dielectric capacitance discharging through the HTL and HTM layers.
- As for the surprising part, we observed completely different behavior of the ionic resistance and capacitance. We observe almost no ionic polarization at high voltage in



the thin device, owing to its large resistance. On the contrary, for the thick device, the variation of the ionic resistance with voltage is significantly more pronounced. At this stage we can only make a hypothesis: with a thinner crystalline capping layer, the ions have to transport through relatively more grain boundaries in the thin device that they do in the thick device. Provided that the grain boundaries have a higher impedance for ion transport, this could explain our observations. Different experiments should be performed to obtain a better idea of this behavior. The corresponding double layer capacitance at high voltage cannot be precisely estimated, because of the lack of low frequency feature at this potential ( $R_{ion}^{\infty} \gg R_{rec}$ ).

- If the double layer capacitance followed the continuum model:  $C_{ion}^{\perp} = \sqrt{C_{disp}C_{ion}^{\delta}}$ , there would be no thickness dependence ( $C_{disp} \propto 1/L$  and  $C_{ion}^{\delta} \propto L$ ). We see a slight decrease of the capacitance for the thinner cell, but it remains within the acceptable limits of the fitting model.

### 6.7.6 The p-type dopant in Spiro-MeOTAD

Traditionally, the HTM preparation involves the addition of a chemical dopant to increase the charge carrier density of the hole transporting layer. Doping of HTM is thought to be a key element in reaching low series resistance, by increasing the conductivity of the hole transporter:

$$\sigma_{HTM} = n_e \mu_u e + n_h \mu_h e \approx n_h \mu_h e \quad (6.88)$$

In a hole transporter, the term that relates to the holes leads the overall conductivity: in such p-type organic materials, holes usually have a higher mobility than electrons. Doping can also affect the mobility, such that the proportionality between conductivity and charge carrier concentration is not necessarily respected. The redox potential of a p-dopant should be more positive (a larger electron affinity) than the HTM, to allow electrons in the HOMO level of the HTM to be transferred to the dopant. The oxidation leaves behind a hole that participates in the conduction of charges in the HTM layer. However, other properties are also relevant, such as solubility properties: the solvent used to dissolve the dopant must have orthogonal solubility with the perovskite and miscibility with the solvent used to process the HTM (chlorobenzene, toluene, ...). In addition, weak absorption coefficients and chemical stability towards air, water and all the components of the solar cell are required. The most common dopant used in solid state dye sensitized solar cells and perovskite solar cells is FK209 (tris(2-(1H-pyrazol-1-yl)-4-tert-butylpyridine)cobalt(III) tri[bis(trifluoromethane)sulfonimide]). It is a  $Co^{3+}$  salt that reduces to the 2+ state in contact with Spiro-MeOTAD[131]. Other p-dopants, such as the copper-based bis(2,9-dimethyl-1,10-phenanthroline)copper(I/II) ( $[Cu(dmp)_2]^{1+/2+}$ ), have also been reported.

We have studied the influence of the dopant in terms of  $j(V)$  sweep, IMVS and IMPS response. It was expected that, owing to the higher carrier density in the HTM layer, we should observe a

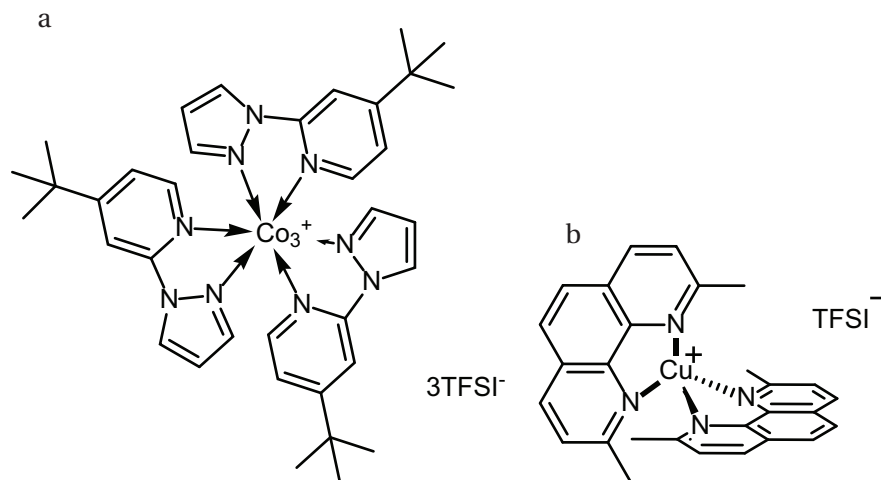


**Figure 6.42:** (a) Chemical structure of FK209. (b) Chemical structure of  $[\text{Cu}(\text{dmp})_2]\text{TFSI}_2$

lower resistance ( $R_{htm} \propto 1/\sigma_{htm}$ ) from the high frequency IMPS spectrum. In fact, in terms of  $j(V)$  characteristics, including the power conversion efficiency, we found no significant difference whether any dopant was used at all, let alone any differences between FK209 and  $[\text{Cu}(\text{dmp})_2]^{1+/2+}$ . The series resistances of the cells were extracted from the slope of the  $j(V)$  curve (measured at  $1000 \text{ W m}^{-2}$ ) around  $V_{oc}$ . In all three cases, they were between 4 and 5 ohms.

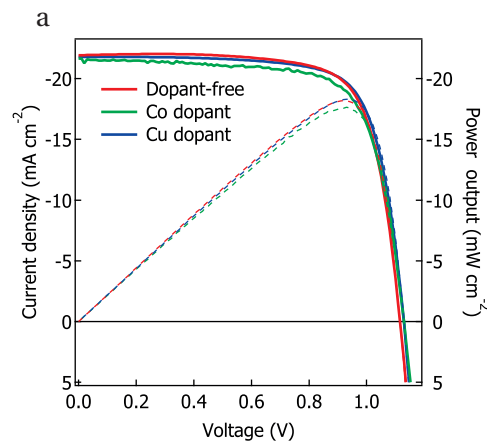


**Figure 6.43:**  $j(V)$  curve of the perovskite devices assembled using a reported procedure[100] with the following dopants in the HTM preparation: (red): dopant-free. Solar cell characteristics:  $V_{oc} = 1.12 \text{ V}$ ,  $J_{sc} = 21.9 \text{ mA cm}^{-2}$ ,  $\text{FF} = 0.74$ ,  $\text{PCE} = 18.18\%$ . (blue):  $[\text{Cu}(\text{dmp})_2]^{1+/2+}$ . Solar cell characteristics:  $V_{oc} = 1.13 \text{ V}$ ,  $J_{sc} = 21.8 \text{ mA cm}^{-2}$ ,  $\text{FF} = 0.74$ ,  $\text{PCE} = 18.29\%$ . (green): FK209. Solar cell characteristics:  $V_{oc} = 1.13 \text{ V}$ ,  $J_{sc} = 21.6 \text{ mA cm}^{-2}$ ,  $\text{FF} = 0.72$ ,  $\text{PCE} = 17.96\%$

In addition to the lack of change of resistivity from the  $j(V)$ , we did not detect any significant improvement in the HTL resistance measured from the IMPS spectra (figure 6.44a). In fact we observe quite the contrary. The series resistance is the dopant-free was slightly lower, by a

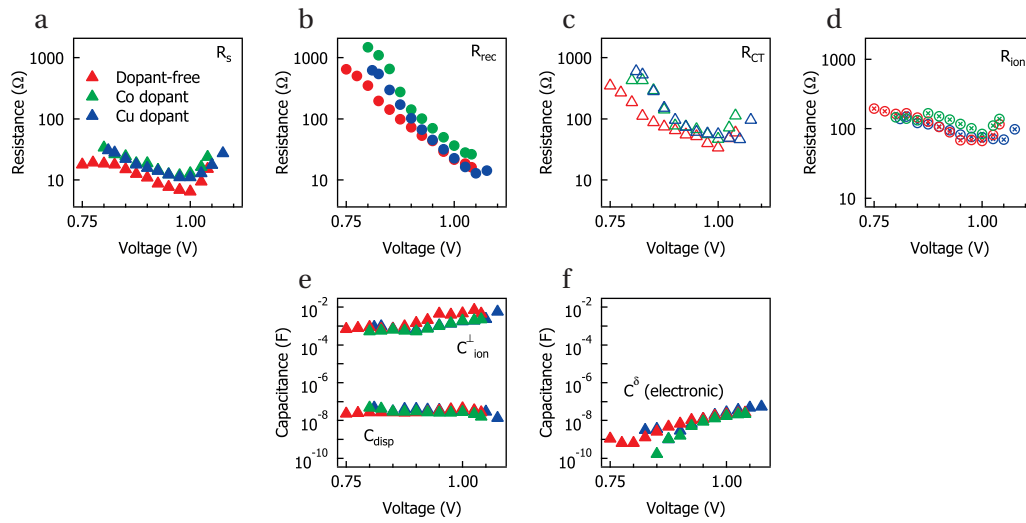


**Figure 6.44:** (a) Equivalent series resistance, (b) Equivalent recombination resistance, (c) Charge transfer resistance, (d) Ionic resistance, (e) Double layer capacitance on the ionic rail and displacement capacitance and (f) Electronic chemical capacitance, as a function of voltage for a typical mesoscopic solar cells containing with standard HTM preparation using (red) no dopant, (blue) Cu dopant and (green) Co dopant

few ohms. This can be related to an increase of the electron scattering in the hole transporter. The resistance measured from the high frequency IMPS semi-circle is the sum of the HTL, ETL and sheet resistance of the two electrodes. Therefore, the series resistance can very well be dominated by the ETL or the substrate resistance, especially in view of the low resistance we measured (maximum  $20 \Omega$ ). Alternatively, under high injection conditions, the doping level might create less carriers than the ones that are photo-generated, in which case there would be no change in the conductivity (this is unlikely to occur as we did not observe significant series resistance from dark  $j(V)$  measurements). Also, the photo-doping of Spiro-MeOTAD aided by the presence of LiTFSI could be sufficient to increase the HTM conductivity (see section 1.5.4) such that no additional effect from the dopant is seen.

In addition, the value of the transport resistance is not dominating the collection efficiency of the cell. Indeed, with the values of the HTL and ETL resistance that we measured, collection efficiencies significantly higher than the ones we measured should be obtained: the IPCE in the blue region (422 nm) does not exceed 85%. Accounting for the 5% from light reflection, there's still around 10% of photo-generated charges that are lost somewhere between the generation and their collection. We know that the HTL and ETL collection rate can not justify this drop (the recombination resistance is greater than the series resistance by over 2 orders of magnitude, which would mean a collection efficiency above 99%). The remainder of the losses must occur somewhere between inefficient generation, significant electron or hole transport resistance in the perovskite layer or charge transfer hindrance at this interface. In our modeled, they are all bundled in the charge transfer resistance.

### 6.7.7 The influence of the LiTFSI additive in Spiro-MeOTAD

We also assembled PSCs that did not contain the LiTFSI additive usually present in the HTM preparation. In typical PSC recipes, 50 mol% of with respect to the HTM is added. The effect of LiTFSI in perovskite solar cells is still unclear. It has been shown that it participates in the photo-oxidation of Spiro-MeOTAD (see section 1.5.4) and that it intercalates well in  $\text{TiO}_2$ , shifting the conduction band downwards. Also, as  $\text{Li}^+$  is an extremely mobile ion that can potentially screen the electric field and accumulate at interfaces, it could be argued that they are responsible for the slow response of perovskite cells. We assembled devices without LiTFSI, with 20% of the usual lithium concentration (10 mol% vs Spiro-MeOTAD) and standard devices (50 mol% vs Spiro-MeOTAD). The  $j(V)$  of the resulting device is shown in figure 6.45. Using pristine Spiro-MeOTAD as the HTM layer, we note the high series resistance of the cell. The short circuit current is also negatively affected by the absence of the additives, as is shown both in the  $j(V)$  curve and in the integrated IPCE response.

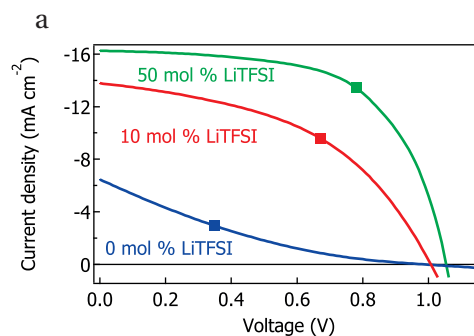


**Figure 6.45:**  $j(V)$  curve of the perovskite devices assembled using a reported procedure [100] using various concentrations of LiTFSI inside the HTM preparation. (blue) 0 mol%, (red) 10 mol% and (green) 50 mol% versus Spiro-MeOTAD.

We measured the IMVS and IMPS response for the three cells and show the results of the fit in figure 6.46. In absence of lithium and dopant, we found that the device series resistance became prohibitively high (around  $100 \Omega$ ). This is reflected in both the  $j(V)$  curve of the device and in the IMPS response (figure 6.47), where the high frequency semi-circle shifts to higher frequencies as the amount of LiTFSI is increased, corresponding to a lower resistance.

However, the increased series resistance in itself does not explain the low photocurrent of the device. We also detected a very significant charge transfer resistance, which does not manifest itself clearly in the IMPS spectra, but which has to be accounted for such that the IPCE of the cell matches with the DC value of the IMPS.

Overall, we found that recombination was unaffected by the presence of lithium. This explains that in all three cases a fair open circuit voltage was reached ( $> 1 \text{ V}$ ). Finally, we did not observe

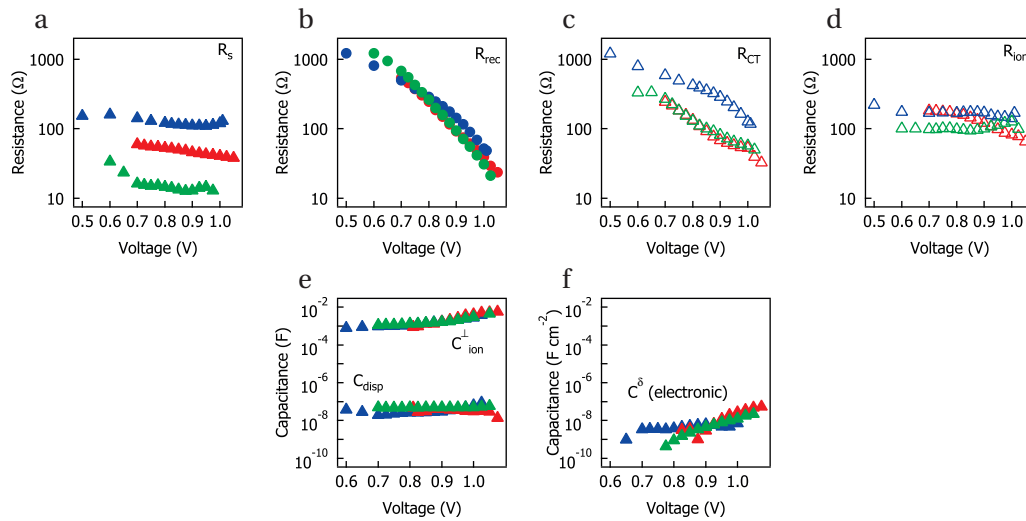


**Figure 6.46:** (a) Equivalent series resistance, (b) Equivalent recombination, (c) Charge transfer resistance and (d) Ionic resistance, (e) Double layer capacitance on the ionic rail and displacement capacitance and (f) Electronic chemical capacitance as a function of voltage for a mesoscopic solar cells containing various amounts of LiTFSI: (blue) 0 mol%, (red) 10 mol% and (green) 50 mol% versus Spiro-MeOTAD.

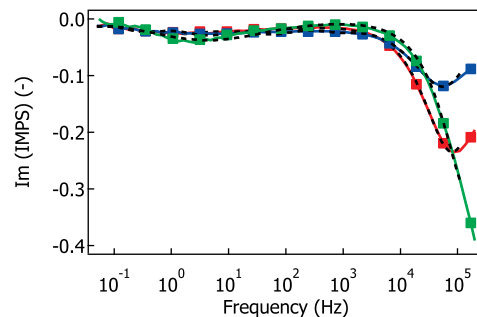


**Figure 6.47:** Imaginary component of the IMPS spectra of a perovskite devices assembled using a reported procedure[100] using various concentrations of LiTFSI inside the HTM preparation. (blue) 0 mol%, (red) 10 mol% and (green) 50 mol% versus Spiro-MeOTAD.

any significant change in the ionic conductivity. This confirms our hypothesis that the ionic conduction channel does not originate from  $Li^+$  but that it is indeed a feature of the perovskite layer itself.

## 6.8 Conclusion and outlook

In this chapter, we have presented the relevant equations that describe the behavior of electrically charged species inside a semiconductor. Notably, we have discussed their drift and diffusion, generation and recombination. When necessary, we have recast the equations such that they can be expressed as a function of electrochemical potentials. We show that the

## Chapter 6. Intensity-modulated frequency response of perovskite solar cells

---

equivalent circuit introduced by Jamnik can be extended to account for two electronic rails out of equilibrium. Based on the extended equivalent circuit, we re-introduce the intensity modulated photovoltage and photocurrent spectroscopy, methods that are heavily used to characterize 3<sup>rd</sup> generation solar cells. We performed a significant number of simulations of the two technique to allow us to qualitatively understand the experimental results. We then implemented a procedure that performs Levenberg-Marquart non-linear least square fitting using numerical simulations in the fitting iterations, such that values of various essential components, such as recombination and transport, can be calculated. We show that IMVS and IMPS spectra of perovskite solar cells can be very accurately described with only a few components in the equivalent circuit, and that the fits can be performed with little or no degrees of freedom. We also report on the fabrication of an electronic pre-amplifier that allows the measurement of IMVS and IMPS under potentiostatic and galvanostatic bias. This instrument allowed us to measure both spectra at the same working point. As a result, we performed complex fitting of both IMVS and IMPS together, using the same fitting parameters. We showed that even in this case, the resulting fits are exceptionally good. Finally, we demonstrate the usefulness of these techniques by studying a few practical cases.

However, this work is extremely far from being over. In fact, it opens a lot of perspectives for future work. Here are a few key points and ideas for future development:

- Based on the calculated values of the recombination resistance, series resistance, ionic resistance and all their associated capacitance, we should be able to reconstruct dynamically a  $j(V)$  curve.
- In our reduction of the full equivalent circuit with a transmission line to a circuit with 5 or 6 elements, we assumed that all resistors and capacitors along the transmission line have the same values. Under a steady-state bias, electronic and ionic carriers polarize across the device to oppose the electric field. This leads to a spatial distribution of conductivities and capacitances, which we did not account for. These effect can be corrected for iteratively solving the steady-state circuit and adapting the resistances according to the new carrier concentrations. The AC characteristics of the circuit could be simulated from the steady-state polarized model.
- Temperature-dependent measurements should be performed. We have performed such experiments in the past but were reluctant to report them here because they need some further interpretation.
- Systematic variations of the system under study could help us understand better the role of the charge transfer impedance and the type of recombination that occurs in perovskite solar cells.

# 7 Recycling of perovskite solar cells

*This chapter is an adaptation of a published article in a peer-reviewed journal[261]. It discusses a proof of concept for hybrid perovskite solar cells recycling and more generally the end of life of photovoltaic devices. It is partly based on a published article in a peer-reviewed journal. This work was done as an equal collaboration with Jeannette Kadro. All results were acquired together. We wish to thank Stéphane Thonney and Dr. Christophe Roussel for XRF measurements, Dr. Kurt Schenk for support of the XRD and Dr. Dongqin Bi and Dr. Fabrizio Giordano for providing some of the solar cells analysed in ESI-QTOF mass spectrometry.*

## 7.1 Motivation

Perovskite solar cells based on  $\text{CH}_3\text{NH}_3\text{PbI}_3$  and related materials have reached impressive efficiencies that, on a lab scale, can compete with established solar cell technologies, at least in short-term observations. Despite frequently voiced concerns about the solubility of the lead salts that make up the absorber material, several life cycle analyses have come to overall positive conclusions regarding environmental impact of perovskite solar cells (PSC) production. Their particularly short energy payback time (EBPT) in comparison to other established PV technologies makes them truly competitive. Several studies have identified valuable components such as FTO, gold and high temperature processes as the most significant contributors to the environmental impact of PSCs. Considering these findings, we have developed a rapid dismantling process allowing recovery of all major components, saving both raw materials, energy and production time in the fabrication of recycled PSCs. We demonstrate that the performance of PSC fabricated from recycled substrates can compete with that of devices fabricated from virgin materials.

## 7.2 Introduction

Despite unprecedented increases of reported energy conversion efficiencies for any type of novel solar energy harvesting technology, perovskite photovoltaic still comes with significant

challenges that require urgent addressing.[33] The tight regulation of hazardous substances in consumer products is one of them. The European Union is implementing policies phasing out hazardous substances - including lead - in consumer electronics, due to concerns of their long term exposure effects on humans and environment. Even so, stationary photovoltaic installations have been exempted from those regulations[262]. As a consequence, PSC solar farms or rooftop installation should be exempted from compliance with the RoHS. The challenges towards the realization of perovskite solar farms remain therefore mostly technical: long-term stability, encapsulation, fabrication of large-area modules and end-of-life processing.

### 7.2.1 The end-of-life of solar panels

Since the years 1990s, in the European Union, the cumulative photovoltaic installed capacity has jumped from a mere 2.3 GW to over 52 GW in 2016. Along with the strong increase of the installed capacity, a sharp increase of the quantity of photovoltaic waste is expected to occur as the first installations reach their end of life, somewhere after 20 to 30 years of operation. In 2016, only 0.6% of the total worldwide electronic waste was generated by photovoltaic waste (250 000 tons), but it is expected that those numbers will take new dimensions in the near future, with an estimate of a cumulated 60 to 80 million tons of waste by 2050[263]. In view of the expected problems that PV and more general electronic equipment waste will generate in the future, the European Commission has decided to act in 2003 already by introducing the directive on Waste of Electronic and Electrical Equipment (WEEE). For the first time, in 2014, the revised WEEE regulation includes photovoltaic installations[264]. Herein, we look more closely at the regulatory frameworks in place in the EU that regulate the waste streams of photovoltaic installations.

### 7.2.2 PV panel composition

While various PV technologies are under development in various research stages, the PV market is dominated mostly by the classical crystalline or multicrystalline silicon wafer-based technologies and by cadmium telluride thin film technologies. Both technologies contain hazardous substances in varying amounts. In particular, lead is present in the solder and back-electrode of silicon technologies, while cadmium, a known carcinogenic, is present in significant quantities in CdTe panels. While such hazardous materials are scientifically hardly avoidable in the making of the solar cell, they may affect the shipment, treatment, recovery and recycling of the final product. While it is beyond the scope of this report to decide on the hazardousness of photovoltaic waste, we point out several EU regulations and directives that are relevant in this matter.



### 7.2.3 Regulatory framework

The European Union has multiple regulatory documents that sets guidelines in the handling of waste streams, covering the disposal, treatment, recycling, shipment, recovery, ... In Table 7.1 we listed the main directives from the European Commission that cover one or multiple of those topics.

Directive / Regulation Number	Name	Comments	Hereafter named
2012/19/EU[264]2	on waste electrical and electronic equipment	Establishes the responsibility and various responsibilities of the user and producer in the WEEE collection, treatment, recovery, recycling and preparing for re-use.	WEEE Directive
1013/2006[265]	Shipment of waste	Notably describes the prohibition of the export of hazardous waste to some countries	Shipment of waste Directive
2008/98/EC[266]	Waste and repealing certain directives	Establishes the general framework of waste stream management within the EU	Waste directive
2011/65/EU[262]	on the restriction of the use of certain hazardous substances in electrical and electronic equipment	Restricts the use of certain hazardous materials in consumer electronics	RoHS Directive
1999/45/CE[267]	concerning the approximation of the laws, regulations and administrative provisions of the Member States relating to the classification, packaging and labeling of dangerous preparations	Details the thresholds above which a mixture of components containing hazardous impurities is considered hazardous	Hazardous compounds Directive
2000/532/EC[268]	replacing Decision 94/3/EC establishing a list of wastes pursuant to Article 1(a) of Council Directive 75/442/EEC on waste and Council Decision 94/904/EC establishing a list of hazardous waste pursuant to Article 1(4) of Council Directive 91/689/EEC on hazardous waste	Lists the codes for the 20 various waste categories, for the purpose of sorting, treatment and disposal	Hazardous waste Directive

**Table 7.1:** List of the main EU regulatory framework regulating the end-of-life of solar panels and the handling of their waste.

### 7.2.4 The Waste of Electrical and Electronic Equipment Directive

In the turn of the 21st century, it became clear that dealing with electronic and electrical waste would become problematic under the general regulatory framework of waste management in the EU. In an effort to address the growing problem, the Waste of Electronic and Electrical Equipment (WEEE) regulation (Directive 2002/96/EC) was enforced in the European Union. While attempting to regulate the various WEEE waste streams, it quickly turned out to be insufficient in view of the diversification and increasing volume of the waste. Under the impulse of the European Commission, the Directive was reviewed (2012/19/EU) 2 and, for the first time, regulated the end-of-life of PV panels. The revision entered into force on August 13th, 2012 and Member States had till February 14th, 2014 to transpose into law. Today, all Member States have transposed the WEEE Directive into national law (albeit with significant differences). As a result, the EU is the only jurisdiction regulating the end-of-life of photovoltaic devices. The revised WEEE Directive introduced the concept of extended-producer-responsibility principle and puts recycling and re-use as a core principle. The Directive shifts many responsibilities for recycling and recovery to the producer (which is defined in the sense of Article 2 of the Directive). Such responsibilities include the financing of the collection, recovery, recycling and preparing for re-use of the electronic waste. Producers need to report periodically on the quantity of panels taken back, sent for treatment and sent for recycling. The WEEE Directive requires statewide reporting regulations but some Member States like France go further by requiring reporting of the output stream from the recycling facilities. Last, PV producers have the duty to inform the various buyers that the generated waste should be eliminated through specific channels and not through household waste, that take-back is free-of-charge and of the various procedures to follow when discarding the waste. Producers are also required to provide the collection, recycling and preparing for re-use facilities with dismantling information regarding the procedures or the risks specific to their product

### 7.2.5 Financing

Under the WEEE directive, end-of-life PV panels may be classified as "WEEE from private households" or "WEEE from other users than private households", which are treated differently in the WEEE Directive with respect to the financing of the collection, recycling and disposal of PV waste. Unfortunately, the Directive is vague on what classifies a "WEEE from private household". Article 3 of the Directive states that "'WEEE from private households' means WEEE which comes from private households [...]" and has been interpreted differently by various Member States of the European Union. While France considers rooftop installations as "WEEE from private households" no matter the size of the PV array, the UK classifies them as "WEEE from other users than private households"1. When the photovoltaic module is considered a household item, the sales transaction is classified as Business to Customer (B2C) and in this case, the financing is the exclusive responsibility of the producer. WEEE from installations dating prior than August 2005 are labeled "historical" and under the WEEE Directive, the

## Chapter 7. Recycling of perovskite solar cells

---

financing of the recycling is to be borne by each producer coexisting on the market at the time of the recycling, proportionally to their market share. Because practically all major actors on the PV market were founded when the People's Republic of China decided in 2008 to grant massive credit loans at extremely low rates for the installation of new PV production facilities, those entities will have to bear the recycling and recovery costs of products which were not theirs in the first place, according to their market share within the EU. This ensures that historical waste is covered for, no matter if the actors on the market file for bankruptcy in the meantime or not. Such costs however can weaken an already vacillating market where energy prices are at an all-time low and PV companies are struggling to make profit. For more recent installations, producers are required to offer guarantees upon placing their product on the market that the costs of recycling are covered, through recycling insurances, blocked accounts or through a "participation by the producer in appropriate schemes for the financing of the management of WEEE". Producers are free to pay the recycling costs upfront (Pay As You Put, or PAYP) or to join collective compliance schemes. For example, in Germany, the law requires a 2 level financing to ensure that the end-of-life products will be covered for<sup>1</sup>. In the Level 1 financing scheme, current actors in the PV field cover the immediate costs of dismantling (Pay As You Go, PAYG), collection and recycling that occur for products included in the WEEE Directive but put on the market before its enactment. The producer bears the costs of the Level 1 scheme according to his market share, whether he decides to do it individually or through a collective scheme. This ensures that the total volume of WEEE PV waste is accounted for by the producers, following the WEEE Directive. The Level 2 financing ensures that there will be sufficient funding for recycling products put on the market on the day-to-day basis through securities. Normally, the Level 2 scheme is an extension of the Level 1, where each actor pay according to their market share when costs occur, but in addition have to pay premiums to a last-man-standing insurance that covers all costs in case all actors from the market were to disappear. The common fund pays for each cost of dismantling and is irrespective of which producer created them (it is the joint-and-several liability scheme, where producers accept to jointly bear the liability for the waste treatment of the products belonging to the category). For business to business (B2B) transactions, per Article 13 §2 of the WEEE Directive, the regulatory framework allows contractual terms to be established between parties which, in practice, is the most commonly adopted practice because it allows greater flexibility and cost-efficiency in the handling of the end-of-life of PV farms. The WEEE Directive prescribes that the costs are covered for, no matter who finances them. When no contract concerning the end-of-life is established and when the products were installed after August 2005, the same rule as the households products applies, i.e. the producers pays for recovery and recycling. If the installation dates from prior August 2005, and the product is replaced by another one with similar function (e.g. replacing a degraded panel in a solar farm), each EU Member States can regulate the financing differently. State laws could oblige the user and producer to share the financing of the decommissioning, or that either party covers it entirely. When old installations are not replaced (e.g. final decommissioning of a solar farm), the user party will bear the costs of recycling and is required to establish the necessary securities beforehand.

### 7.2.6 Collection the PV panels waste

Per article 5 of the WEEE Directive, the EU Member States shall ensure that, similarly to other electronic equipment waste, solar panels be collected separately from the household waste. The directive separates clearly the cases where private households or any other entity owns the installation. In this case, free-of-charge take-back of the installation needs to be ensured upon its end of life (which does not include dismantling costs), and the financing of the collection, treatment, recovery and "environmentally sound disposal" is to be handled by the producer. While the Directive does not specify individual collection rates for each branch of electronic waste, Article 7 §6 of the WEEE Directive urges the European Commission to report on specific deadlines and collection rates for PV panels by August 2015. No such reports have however been submitted and therefore the collection rate defined in Article 7 §1-2 apply, i.e. a collection of 45% (from 2016) and 65% (from 2019) per EEE weight basis averaged in the last three years, or 85% of the total EEE waste. In a growing market like the photovoltaic one, the 65% rule makes no sense because the average installed capacity in the last three years exceeds greatly the weight of solar panels that need to be recycled owing to their extended lifetime. Hence, in this case, the 85% rule of the total PV EEE waste would apply.

### 7.2.7 Waste treatment, recovery and recycling

Per article 8 §3 of the WEEE Directive, producers or third parties mandated by the producers are required to "set up systems to provide for the recovery of WEEE using best available techniques". Although Annex VII lists a minimum of treatments for specific waste, no particular one apply to PV panels. Per article 8 §4, the EU Commission can amend the Annex VII, but so far, has not done so for photovoltaic panels. The WEEE Directive supplements another waste Directive from the European Commission, the 2008/98/EC[266] that defines more specifically the treatment and recovery standards applicable to PV panels. Individual countries are allowed to implement more specific regulation. The recovery processes covers the dismantling of the panel into its constituents (e.g. the encapsulating glass, the rubber seals, the wiring, the EVA sheets and the photo-active material) in the sense of the article 3 of the waste Directive. Recycling of the panels, i.e. the reprocessing of the materials into new useful products, is treated separately. For PV panels, during the 3-year transition period extending till August 15th, 2018, 80% of PV panels are required to be recovered, and 70% prepared for re-use and recycled. After the transition period, 85% of them will have to be recovered, and 80% prepared for re-use or recycled. Recovery and recycling targets as laid out in Article 11 describe the weight percentage of waste entering the recovery and recycling chain relative to the total amount of collected waste for that category, but not with regards to the final quantity of materials resulting from recovery, preparing for re-use and recycling. In other words, in the sense of the WEEE directive, neither the quantity of recycled material nor the qualities of the output products are regulated. While this might change in future WEEE Directives (a technical draft on reporting is in preparation[269]), most countries already require reporting of targets with regards to the outcome of the recycling facilities. While the Directive clearly

## Chapter 7. Recycling of perovskite solar cells

---

aims at "reducing overall impacts of resource use and improving the efficiency of such use in accordance", there are no qualitative targets with regards to the value of the recycled product. For example, silicon wafers used in PV panels can be recovered and recycled into backfill for road constructions, which would be a significant loss of value in regards to its recycling into new PV arrays. However, per Article 8 paragraph 5 of the WEEE Directive, the EU commission has mandated standardization agencies to define standards that "shall reflect the state of the art" with regards to the treatment, recovery, recycling and preparing for re-use of electronic waste, including solar panels. The technical specification for PV panel recycling is under development and is to be made public by the end of 2016 by the European Committee for Electrotechnical Standardization CLC/TX.

### 7.2.8 Waste shipment

Export of EEE waste is permitted by article 10 of the Directive 2012/19/EU, provided it does not violate the Commission Regulation 1418/2007[270] and Regulation 1013/2006[265] on the shipment of waste. However, it is clear that the Article 36 of the shipment of hazardous waste to non-OECD decision countries (on the transboundary movements of waste) in accordance to the Basel Convention. The Directive lists clearly under Annex V lead in the solder and back-electrode of silicon panels (A1010 and A1020) and cadmium constituting CdTe solar cells and as part of CIGS solar cells (A1020) of the aforementioned regulation. In other words, exporting silicon, CdTe or CIGS solar panels to non-OECD decision countries, including China, should be forbidden in the sense of this article. The export of solar cell waste to OECD countries where the decision applies remains possible if in compliance with the shipment of waste regulation.

### 7.2.9 Waste disposal

The EU being the first entity worldwide to label PV panel waste as WEEE, there remains a debate whether the waste should be considered hazardous or not. The EU Directive 2012/19/EU applies without prejudice to the Directive 2008/98/EC on the regulation of waste[271]. However, PV panels clearly fall within the definition of electronic and electrical equipment: "'electrical and electronic equipment' or 'EEE' means equipment which is dependent on electric currents or electromagnetic fields in order to work properly and equipment for the generation, transfer and measurement of such currents and fields and designed for use with a voltage rating not exceeding 1 000 volts for alternating current and 1'500 volts for direct current." For solar cells that contain portions of lead in the solder or the back-electrode or cadmium as a constituent (CdTe) or as a window (CdS in CIGS solar cells), the handling and elimination of PV waste is regulated by the Directive 2008/98/EC of the European Union, which defines with the following: "'hazardous waste' means waste which displays one or more of the hazardous properties listed in Annex III", where Annex III of the aforementioned Directive lists adverse effects on health such as carcinogenic" and "toxic", which includes Cd in CdTe and Pb in lead solder in the sense of Annex VI of the Directive 67/548/EEC of 27 June 1967 that

lists the criterion for the "hazardous" label in case of mixed products and involve a list of medical tests that are out of the scope of this outlook. The quantity thresholds for a mixed product that contains hazardous impurities or additives above which the product is called "hazardous" are set in the 1999/45/CE Directive[267] (the hazardous compound Directive) in the Article 3, where thresholds of 0.1% by weight of carcinogenic or toxic with respect to the total weight are defined. The leachate test mentioned in the Directive 2008/98/EC (the waste directive) is often mentioned as the "main" criterion for the hazardous waste classification of PV waste, but the Annex III of the waste directive clearly states that hazardous also applies to the intrinsic risks posed by the material itself and not just its leachate. Together with the waste Directive 2008/98/EC, the List of Waste (LOW) defined in Decision 2000/532/CE[268] lists all waste codes with distinction between hazardous and non-hazardous wastes. Based on the list, relevant waste numbers for CdTe or a-Si devices could be 16 02 13 (discarded equipment containing hazardous substances) or 17 07 02 (Mixed construction and demolition waste or separated fractions containing dangerous substances). Under those codes, the Basel convention would therefore forbid the export of PV panel wastes to non OECD-decision countries.

### 7.2.10 Valuable device components of perovskite solar cells

The highest efficiencies for PSCs today are achieved with multi-layer devices comprised of a number of highly valuable components, such as gold, fluorine doped tin oxide (FTO) and mesoporous TiO<sub>2</sub>. [69] Their production not only contributes to the deprivation of important elements, but also is responsible for severe environmental impacts at the exploitation sites. In addition, gold value is subjected to strong price fluctuations due to market speculation and not directly tied to production volumes or scarcity factors.

Recently published studies have come to varying conclusions regarding the environmental impact of the production and disposal of PSCs.[272, 273, 274, 275] Some indicate that solvents (including chlorobenzene, diethyl ether, dimethyl sulfoxide and N,N-dimethylformamide) and the synthesis of CH<sub>3</sub>NH<sub>3</sub>I are among the main concerns.[275] Others argue that the overall impact is dominated by the gold and the transparent conductive oxide, used as the back and front contact, respectively.[274] It is, however, of common consensus that the lead content in the perovskite layer is not the main issue in terms of environmental impact of PSC production.[274, 275, 69, 276] Pb<sup>2+</sup>, in the form of the perovskite APbX<sub>3</sub>, content in the operational device can vary based on the device architecture but based on today's most efficient cells with perovskite layers of around 300 – 400nm thickness would amount to less than 1000 mgm<sup>-2</sup>. Recently published estimates on the potential of environmental pollution from damaged PSC panels have shown that the direct impact of lead leaking from damaged panels would be modest compared to potential damages from other anthropogenic lead sources, such as use of lead paint or lead smelting for car batteries.[277, 278] Calculations based on lab scale device efficiencies have shown that potential lead pollution from leaking PSCs would still be low compared to the amounts of lead released from to other energy conversion methods.

## Chapter 7. Recycling of perovskite solar cells

---

For example, lead emissions from a 1GW coal-power plants vary considerably based on lead content and quality of the coal burned but commonly range from 0.1t to 1t per year, and usually are not sequestered.[279] Hailegnaw et al. have estimated that a 1 GW solar field of PSCs would contain up to 30 t of Pb.[278] If lead contained in PSC solar panels is retrieved and recycled safely, PSC solar farms would allow a reduction of direct lead emissions. Certainly, measures to prevent large amounts of lead from damaged panels, for example as consequence of natural disasters such as earthquakes, floodings or wildfires, should still be considered and installations of large numbers of PSC panels in areas prone to such natural disasters or within the vicinity of important groundwater reserves might require special regulations. Aside from reliable encapsulation, development for safe recovery processes of the slightly water soluble lead salts ( $K_{sp} = 10^{-8}$  for  $\text{PbI}_2$  as opposed to  $10^{-27}$  for  $\text{CdTe}$ [280]) from PSC modules together with successful implementation of take-back-systems, such as already in place for  $\text{CdTe}$  solar panels, will be key to successfully bringing perovskite PV to the market.[281]

Substitution of lead by tin in organic-inorganic hybrid perovskites has been realized[34, 282, 8] and solar cells with power conversion efficiencies exceeding 6% have been reported,[283] but several studies have come to the conclusion that tin substitution is not advisable for numerous reasons. Leaving aside lower attained conversion efficiencies and the inherent instability of its 2+ oxidation state in air, organic tin compounds have also been found to be more environmentally harmful than their lead analogues.[272, 283] Tin based perovskite solar cells have been found to score higher in all environmental impact categories investigated as compared to their lead analogues in a recent study presenting an LCA including end-of-life scenarios of incineration or landfills, and thus will not be considered in this study.[272] Tin is a strategically highly critical metal as it is indispensable in a very broad range of applications in technology today, particularly in solders, alloys and coatings and it is used in sizable quantities as fluorine-doped tin oxide in PSCs. A small number of countries including China, Indonesia and Peru control more than 4/5 of the global production with no significant exploitation sites in Western Europe and North America.[284] Due to limited technological substitutability of tin, strongly geographically concentrated supply and risks associated to political instabilities in its main production countries and growing global tin demand, the metal has been assigned with a high material security index in a recent report.[285] Tin has recently been added to the European Commission's report on critical materials.[286]

So far, published LCAs confirm lead-based PSCs as environmentally friendly alternative to other PV technologies, particularly emphasizing their short energy payback times (EPBT) calculated based on lab-scale device efficiencies.[274] Based on such considerations, we developed a rapid and highly selective process allowing full recycling and/or recovery of the most precious components of a standard PSC device. We demonstrate that PSC devices can be easily dismantled in reverse order of fabrication and that materials can be extracted with high purity for direct reuse or further recycling. The process we introduce eliminates energy intensive processing steps such as sintering of the  $\text{TiO}_2$  in the fabrication of recycled devices, significantly reducing both fabrication time and energy input. Furthermore, sequestration of the lead salts contained in devices is achieved with a remarkable degree of segregation.



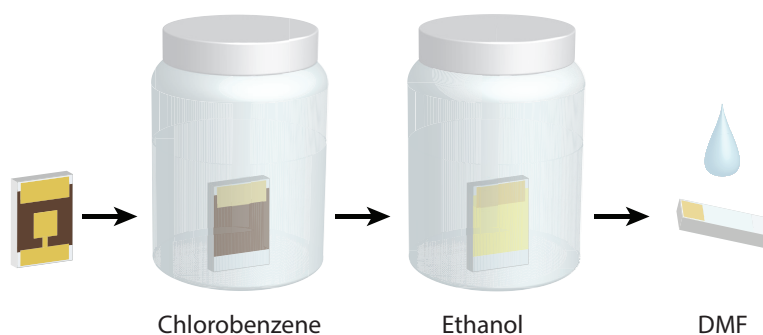


**Figure 7.1:** Schematic process outline: fully assembled PSCs are immersed into chlorobenzene, after complete dissolution of the HTM and cathode removal, EtOH is used to dissolve MAI, and small amounts of DMF are used to completely remove  $\text{PbI}_2$ .

Most importantly, we demonstrate that our high efficiency PSCs can be recycled at least twice without significant losses in performance. Recovery and reuse of the FTO-coated glass substrates with mesoporous  $\text{TiO}_2$  is desirable. Calculations based on devices of similar architecture as we use in this study the FTO substrate alone has been shown to contribute 40% to the overall carbon footprint of all materials embedded and its manufacturing consumes 36% of all primary energy of embedded materials.[274] In addition, the prolonged, high temperature associated to the  $\text{TiO}_2$  layers have been shown to contribute significantly to both carbon footprint and primary energy consumption of PSC fabrication.[287] Using a simple process, we show that FTO glass can be reused with little losses in performance. Gold being a scarce but technologically and economically highly valuable metal makes its recovery and recycling from used appliances particularly desirable. Its production and refining can have significant environmental impacts at exploitation and refining sites. Among normalized cradle-to-gate contributions of production of important metals, gold ranges second behind rhodium in terms of release of greenhouse gas emissions and toxic substances[288, 289] Aside from mitigating severe detrimental effects at the exploitation sites on eutrophication, acidification and land use, employing recycled gold can save up to 98% in energy required as opposed to use of newly mined material.[288, 290] Gong et al. have shown in their recently published LCA that extraction, refining and processing of the gold alone contributes up to 53% to the overall carbon footprint of all embedded materials.[274] During the review process of this publication, a paper describing a similar process to the one we are introducing here has been published using solar cells without mesoscopic layers.[291] We find it highly encouraging to see that sustainability and recycling of PSCs are receiving attention from many in the field. The entire dismantling process was carried out at room temperature in ambient conditions, A schematic outline is presented in figure 7.1. To remove the gold counter electrode, fully assembled (non-sealed) PSC devices were fully immersed into chlorobenzene in a round bottom flask with the gold cathode facing upwards. Due to the dissolution of the organic, doped hole transport layer a slight color change of the solvent can be observed while the counter electrode eventually peels off from the substrate completely. Gold removal was

typically completed within 2 – 5min. The collected gold was separated by decanting from the solvent and washed briefly with acetone, an aqueous solution of 20% HCl, and distilled water, successively. After complete removal of the gold cathode and the organic HTM, the hybrid perovskite absorber layers were removed in two steps, inverting the process for sequential deposition of  $\text{CH}_3\text{NH}_3\text{PbI}_3$  reported elsewhere[47]. Substrates were fully immersed into EtOH immediately following the chlorobenzene treatment. A vivid colour change from black to bright yellow can be observed as  $\text{CH}_3\text{NH}_3\text{I}$  dissolves into the solvent, leaving  $\text{PbI}_2$  behind. Upon completion,  $\text{PbI}_2$  was removed from the films by carefully dropping small amounts of DMF onto the surface of the substrate. As-treated substrates were carefully washed with EtOH to remove any remaining solvent and left to dry naturally. The entire dismantling process could typically be completed in less than 10 min. The  $\text{TiO}_2$  coated FTO substrates were then treated for 10 minutes by UV/ $\text{O}_3$  and reused without further heat treatment. The recycled substrates were processed again within 4-5 hours of the previous depositions. The same fabrication protocol described above and the same stock solutions were employed.

### 7.3 Results and discussion

The selectivity and completion of each of the three recycling steps was assessed by scanning electron microscopy, thin film X-ray diffraction, ICP-MS, mass spectrometry and X-ray fluorescence.

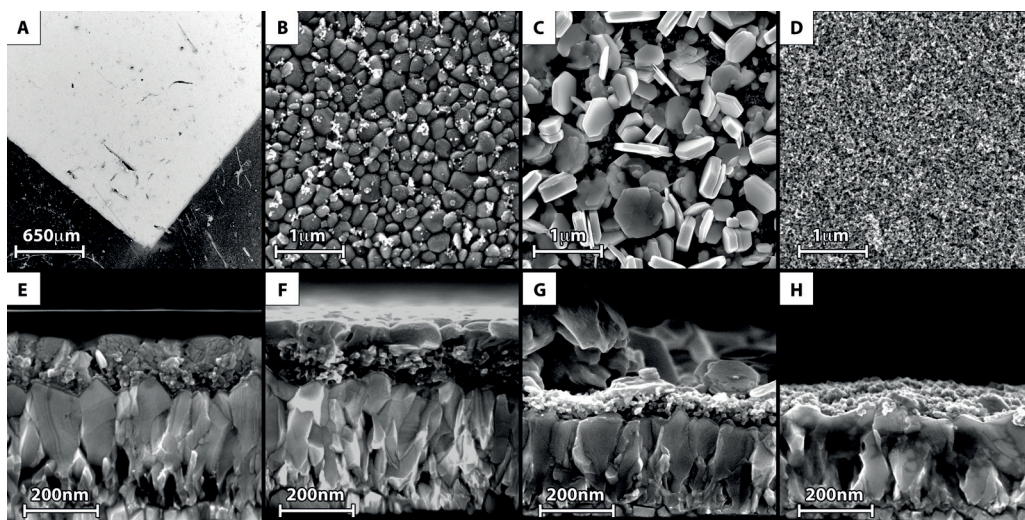
#### 7.3.1 Photoanode

Figure 7.2 shows top-view and cross-sectional SEM micrographs of the full device and after each recycling step and confirms the selectivity of each steps. It can clearly be seen that the perovskite absorber layer remains intact after cathode and HTM removal in chlorobenzene. Upon  $\text{CH}_3\text{NH}_3\text{I}$  dissolution in EtOH (Figure 7.2c and g), hexagonal structures typical of  $\text{PbI}_2$  are formed on the mesoporous  $\text{TiO}_2$  layer and appear to be completely absent after DMF treatment as (Figure 7.2d,h). Figure 7.2d shows a top-view image of the mesoporous  $\text{TiO}_2$  layer after removal of  $\text{PbI}_2$  in DMF. No indications for detrimental effects of the dismantling process such as delamination or scratching of the photoanode were observed; the  $\text{TiO}_2$  layer appears to remain completely intact.

Structural characterization by X-ray diffraction was carried out on twin samples analogous to those presented in Figure 7.2. The diffraction patterns presented in Figure 7.3 confirm the purity of each expected phase after the sequential solvent treatment steps.

#### 7.3.2 Back contact

Purity of the recovered gold was confirmed by X-ray fluorescence (XRF). No traces of lead were found on the material recovered from the chlorobenzene bath (see SI). The possibility of slight



**Figure 7.2:** top-view and cross sectional secondary electron micrographs of devices at all recycling stages (a and e): before recycling treatment (b and f): after chlorobenzene treatment, (c and g): after MAI dissolution, (d and h) after  $\text{PbI}_2$  removal

organic contaminations on the surface stemming from dissolved organic HTM cannot be completely be excluded due to detection limitations of XRF although we deem such remaining organic contaminations improbable as the recovered material is washed in acetone and HCl. As no foreign metal traces were found, it can be assumed that the recovered gold can be reused without extensive energy-intensive refining. Although all gold deposited on the HTM could be successfully recovered with high purity, the recovered material could not be used for fabrication of recycled devices due to purely practical reasons. Firstly, the amount of gold that is required to deposit a ca. 100 nm thick layer, (see experimental procedures) exceeds the amount of gold actually deposited (ca. 0.4 mg) on each device by several orders of magnitude in our evaporator. This is due to an unfavorable geometry of the experimental setup used and could be optimized on a larger scale. Collecting sufficient material for one single evaporation would require processing of at least 900 devices. Secondly, gold recovered in the recycling process remains in its original shape, that is, ca. 100 nm thick, freestanding films. Due to the low mass of these films, they would not withstand the suction produced in the evaporator during pumping and would be removed from the evaporation boat in the process of evacuating the machine.

### 7.3.3 Lead in solvents

Methanol, ethanol, 2-propanol, ethyl acetate and deionized water were used for the dissolution of the methylammonium iodide. The fastest observed conversion from  $\text{CH}_3\text{NH}_3\text{PbI}_3$  to  $\text{PbI}_2$  was achieved using MeOH, followed by deionized water, EtOH and isopropanol. Complete MAI dissolution in ethyl acetate could be achieved only after several hours, which was found too impractical for further consideration. EtOH was chosen for device recycling over MeOH,

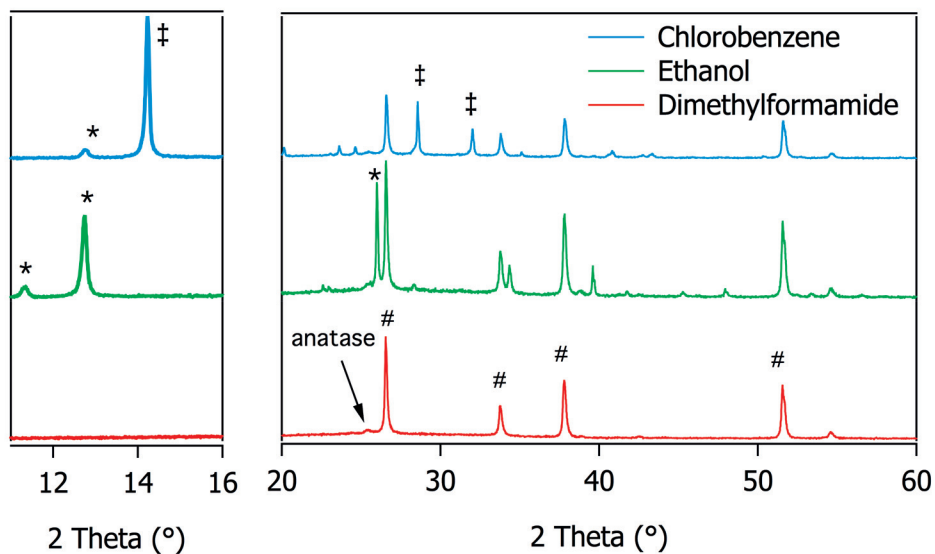


**Figure 7.3:** XRD patterns of substrates after each processing step. In blue, the original device stripped from gold and the HTM layer. In green, the device stripped from gold, the HTM layer and  $\text{CH}_3\text{NH}_3\text{I}$ . In red, the FTO substrate covered with the compact and mesoporous  $\text{TiO}_2$  layers. Characteristic peaks originating from the crystalline FTO substrate are denoted by #,  $\text{PbI}_2$  by \* and  $\text{CH}_3\text{NH}_3\text{PbI}_3$  by †

despite the slower dissolution considering its lower toxicity to workers and environment and reduced processing times due to higher drying rates as compared to water.

The remaining lead content in each solvent was assessed by ICP-MS to evaluate the process selectivity with respect to lead sequestering. Lead quantities are shown in Table 1.1 relative to the total lead content in the chlorobenzene, ethanol (water, isopropanol or methanol) and DMF. They underline the relative selectivity of each recycling step. Among the four solvents we have tested, water seems to perform with the highest selectivity. Only 0.14% of the total Pb amount could be detected, which is similar to the selectivity of chlorobenzene. After purification in Amberlite 120 IR, contents in the water dropped down to 0.03%, but in this case, lead sequestration by the resin may be limited by the slower uptake at extremely low concentrations (0.2 ppm). To confirm this, we prepared a saturated solution of  $\text{PbI}_2$  in water with a 30-fold molar excess of MAI. Following decanting and filtering, analysis by ICP-MS showed concentrations of  $43.5 \text{ ppm mL}^{-1}$ , which we believe is close to the upper dissolution limit of  $\text{PbI}_2$ , in particular since the large excess of  $\text{I}^-$  anions can help solubilize  $\text{PbI}_2$  by producing the soluble  $(\text{PbI}_4)_2^-$  complex, soluble in water. After lead removal by the resin for 16 h (1 g/30 mL), concentrations of lead down to  $0.44 \text{ ppm mL}^{-1}$  were recorded, which corresponds to a sequestration of 99%. 2-propanol showed the second best selectivity after water, with only 0.35% lead content in the solution. The slow dissolution of the MAI in 2-propanol (about 20 minutes) makes this solvent less appropriate. Then follows ethanol, with up to 3.4% Pb with respect to all extracted lead from the device. Finally, methanol showed the

Sample	Relative lead content
Chlorobenzene	0.09%
<b>Ethanol</b>	
EtOH	3.4%
DMF	96.5%
<b>Methanol</b>	
MeOH	7.1%
DMF	92.9%
<b>2-propanol</b>	
2-propanol	0.35%
DMF	99.6%
<b>Water</b>	
H <sub>2</sub> O	0.14%
DMF	99.8%
H <sub>2</sub> O (after purification)	0.03%

**Table 7.2:** Segregation efficiency of the solvents used in the recycling process. Lead content is reported with respect to the total amount of extracted lead. Solvent volumes were 5 mL for chlorobenzene, 5 mL for ethanol, methanol, water and isopropanol, and 0.5 mL for DMF.

poorest performance, with up to 7% Pb in the solvent with respect to the total Pb quantity.

Ion exchange resins such as Amberlite IR 120 can be used for purification of a range of organic solvents as well, including MeOH and IPA.[292, 293] An efficient, electrochemical process for lead recovery from PSC devices via electrodeposition of lead on lead using ethylene glycol with choline chloride as solvent has been demonstrated recently in a model experiment by Poll et al.[294]

#### 7.3.4 Fate of spiro-MeOTAD, dopants and additives

ESI-TOF mass spectrometry in positive and negative mode was carried out on samples of chlorobenzene, EtOH and DMF collected directly from each recycling step and resulting spectra are available in the Supplementary Information. Formic acid was used for protonation in the positive mode. *Spiro-MeOTAD*<sup>+</sup>. could be found neither in the ethanol nor in DMF, confirming the high selectivity of the process towards Spiro-MeOTAD extraction. TFSI<sup>-</sup> and what could possibly be (LiTFSI)H<sup>+</sup> was found in the chlorobenzene as well. Similar peaks were found in the EtOH and DMF, pointing at rather poor selectivity of the LiTFSI segregation. No iodide peak was found in the chlorobenzene, but appeared in the ethanol and DMF (negative mode). FK209 and TBP could not be found. It is possible that they appear as aggregates, such as the peak at m/z 217.1 observed in the ethanol and DMF, which is possibly (TBP)<sub>2</sub>H<sup>+</sup>.

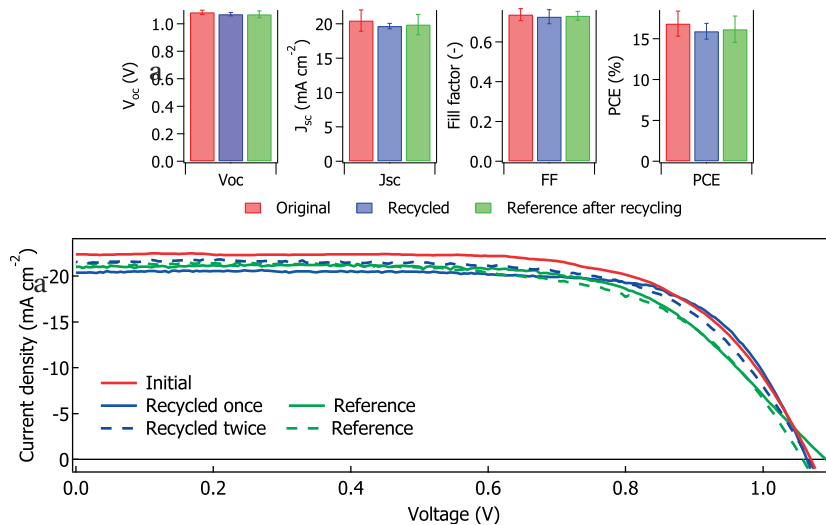


**Figure 7.4:** (a) Open circuit voltages, short circuit currents, fill factors and power conversion efficiencies for a 30 sample batch of perovskite solar cells before (red) and after (blue) recycling. Green bars represent the mean values of the reference cells assembled together with the recycled cells. (b) Typical  $j(V)$  characteristics of a device before and after recycling, reference devices are prepared from new materials.

### 7.3.5 Device performance

Table 7.3 shows the device performances for the recycled FTO/TiO<sub>2</sub> substrates reused into new solar cells. Efficiencies of 15-16% were obtained for recycled devices with short-circuit currents ranging between 19.7 and 21.5 mA cm<sup>-2</sup>, values for recycled devices as well as reference cells are given in Table 2. Open circuit voltages did not vary significantly between all of the tested devices. No significant drop in performance after recycling the substrates twice was observed, upon comparison to respective references (using fresh substrates) but overall small but noticeable drops in Jsc can be observed for recycled cells, possibly due to the perovskite crystallization being affected by residual solvents. All PV characteristics fall within the expected statistical deviation occurring within a batch of devices. Figure 7.4 shows the associated  $j$ - $V$  curves scaled artificially to 100 mW cm<sup>-2</sup> illumination intensity to allow for a fair comparison of the photocurrent density. Efficiencies obtained fall into the expected range for CH<sub>3</sub>NH<sub>3</sub>PbI<sub>3</sub> based cells with mesoporous TiO<sub>2</sub> scaffold, higher efficiencies are typically achieved with mixed-cation, mixed-halide perovskites.

## 7.4 Encapsulation

With perovskite PV still in the R&D stage, it is difficult to predict how perovskite PV modules will be designed for large-area applications if they meet the market. The geometry of the wiring as well as the use and design of rigid frames will greatly determine design and success of dismantling processes. To the best of our knowledge, there are no universally applied recycling

Sample description	Voc (V)	Jsc (mA cm <sup>-2</sup> )	Intensity (mW cm <sup>-2</sup> )	Fill factor (-)	Efficiency (%)
Reference initial	1.07	22.1	100	0.67	16.1
Recycled once	1.06	19.7	96.6	0.73	16.0
Reference 1st round	1.07	20.6	98	0.65	14.9
Recycled twice	1.07	21.5	99.6	0.67	15.0
Reference 2nd round	1.06	21.1	99.6	0.64	14.3

**Table 7.3:** IV characteristics of typical device before and after recycling, reference devices are prepared from new materials

processes for any type of PV modules today, but several processes have been developed on the lab scale and life-cycle analyses on silicon panel recycling including end-of-life stages have been undertaken.[295, 296, 297, 298, 299] Common encapsulation used in silicon PV panels for example, relies on laminates of glass and ethylene vinyl acetate sheets (EVA) with aluminum frames for increased stability. Frame and wiring can be detached manually and sealed edges could be cut off mechanically. The possibility of direct deposition of the working electrode on sturdy glass substrates could prove an advantage in mechanical processing as the devices can themselves provide considerable structural integrity, other than, for example, brittle silicon wafers. If scratches on the electrode surface are avoided in the dismantling process, it is unlikely for encapsulation to have a negative impact on the performance of recycled working electrodes as TiO<sub>2</sub> is both thermally and chemically highly stable, offering the possibility of both thermal as well as wet-chemical processing for removal of encapsulation residues. Overall, it will be imperative to develop encapsulation techniques specifically for PSC devices that not only protect the active materials from moisture, air and dust but also meet strict requirements for mechanical stability, (e.g., those defined in ASTM E1830-15 Standard Test Methods for Determining Mechanical Integrity of Photovoltaic Modules) but at the same time offer ease of dismantling.

## 7.5 Conclusion and outlook

In the European Union, recycling costs of photovoltaic panels are to be covered by the producer. But lead-containing waste can not simply be landfilled as it is currently done with silicon photovoltaics. Crushing the panel and using it as a backfill or similar downcycling processes might not be available for hazardous waste. In addition, solar cell producers might have a strong economic interest in re-using the most valuable components of the cell, i.e. the substrate and the back-contact. In this chapter, we have reported on a rapid and highly selective recycling process for hybrid perovskite photovoltaic devices. We have shown that the process is extremely selective with regards lead iodide, and that solvent contaminations can be reduced by a simple treatment with a resin. Valuable components could be extracted and collected for recycling into new PSCs or valued in other applications. By repeating the sequential recycling process, we demonstrated that efficiencies rivalling those obtained

## **Chapter 7. Recycling of perovskite solar cells**

---

using fresh substrates can be easily attained from reused substrates. Fabricating solar cells from recycled materials can drastically reduce both fabrication cost, time and environmental impact. Use of recovered materials will have a positive impact on environmental assessment of PSC technology and may make this technology even more competitive.



## 8 Conclusion

The various studies presented in this chapter treat various aspects of perovskite solar cells, including their fabrication, their characterization, their use for power applications and the treatment of their end-of-life. I have covered such broad topics in part because the field of perovskite solar cells has developed at an extremely fast pace in the last couple of years. Reporting high power conversion efficiencies was necessary and rewarding to myself and hopefully to the community. But the greater picture should not be forgotten. Therefore, I rapidly shifted my focus away from trying to boost the efficiency of PSCs. Rather, I attempted to focus my attention on the characterization of perovskite devices, including their power tracking and their frequency-resolved spectra. Last, with great concerns regarding the ecotoxicity and the durability of the solar cells, I have presented a proof-of-concept for the recycling of perovskite solar cells. In further details, the chapters presented in this thesis have covered the following:

- In chapter 2, I have reported on an efficient way to deposit  $\text{CH}_3\text{NH}_3\text{PbI}_3$  onto mesoscopic  $\text{TiO}_2$  substrates, using a two-step deposition technique that involves first the spin-coating of a  $\text{PbI}_2$  layer from a polar solvent, followed by a conversion reaction of the lead iodide into the perovskite structure  $\text{CH}_3\text{NH}_3\text{PbI}_3$  by dipping into in  $\text{CH}_3\text{NH}_3\text{I}$  solution in 2-propanol. The conversion reaction is extremely fast and proceeds to completion within less than 1 minute, thanks to the nanostructured nature of the  $\text{TiO}_2$  film. The sequential deposition technique allows an excellent coverage and conformity, as opposed to the classical deposition at the time, which involved spin-coating of the two perovskite precursors together. The better coverage and uniformity of  $\text{CH}_3\text{NH}_3\text{PbI}_3$  obtained by sequential deposition correlated well with the power conversion efficiency of the assembled devices. I have reported on a champion device, measured at 15% PCE, an absolute record at the time. Certified calibration for a similar cell was delivered at 14.14%, which is the first perovskite cell ever to be certified.

The formation of a capping layer made of  $\text{CH}_3\text{NH}_3\text{PbI}_3$  on top of the  $\text{TiO}_2$  film is critical in reaching high performance. The size of the crystals forming the capping layer can be tailored by varying the concentration of  $\text{CH}_3\text{NH}_3\text{I}$  in the 2-propanol solution. Optimization of the crystal size, such that light absorption was maximized was reported.

The issue of transport rate with respect to the recombination rate was also raised.

- In chapter 3, I reported on the fabrication of perovskite devices employing the mixed cations methylammonium and formamidinium, using the sequential deposition reported in chapter 2. While the perovskite  $\alpha\text{-CH}(\text{NH}_2)_2\text{PbI}_3$  is unstable and readily transforms into  $\delta\text{-CH}(\text{NH}_2)_2\text{PbI}_3$ , I showed that adding small amounts of methylammonium stabilizes the  $\alpha$ -phase of the final structure. By X-ray diffraction, it was clear that both cations can intercalate together in the perovskite structure, as in a solid solution. From an optical perspective,  $\alpha\text{-CH}(\text{NH}_2)_2\text{PbI}_3$  is attractive because it has a slightly smaller optimal band gap and allows photons further into the infrared to be harvested. Luckily, the optical band gap of  $\text{MA}_{0.6}\text{FA}_{0.4}\text{PbI}_3$  is extremely close to the one of  $\alpha\text{-CH}(\text{NH}_2)_2\text{PbI}_3$ , which allowed to assemble highly efficiency PSCs, surpassing the ones of both pristine  $\alpha\text{-CH}_3\text{NH}_3\text{PbI}_3$  and  $(\alpha, \delta)\text{-CH}(\text{NH}_2)_2\text{PbI}_3$ . We also show that the IQE of mixed-cation PSCs is higher than the one of pure  $\text{CH}_3\text{NH}_3\text{PbI}_3$ , which was related to the differences in lifetimes.
- In chapter 4, I reported on the surprising reactivity of the methylammonium lead halide perovskite with regards to the exchange of their halide component. It was shown that by dipping a  $\text{CH}_3\text{NH}_3\text{PbX}_3$  film into a solution of  $\text{CH}_3\text{NH}_3\text{Y}$  ( $\text{Y}=\text{Cl}, \text{Br}, \text{I} \neq \text{X}$ ), the halide X is exchanged by the halide Y within a matter of seconds to minutes. When the reaction occurs between Cl and Br or between Br and I, the perovskite structure exchanges the halides simultaneously, i.e. an intermediate of mixed halides is formed. When Cl is exchanged I or vice-versa, no evidence of mixed intercalation was found. We show a case-study where halide exchange was applied to perovskite nanowires, which can only be grown in the iodide form.
- In chapter 5, I reported on the maximum power tracking of perovskite solar cells in an effort to perform larger ageing studies. It was shown that the fast tracking of perovskite solar cells using well-established algorithms fails due to the large capacitance of PSCs. A strategy that efficiently stabilizes the tracking algorithm was proposed, using a simple hysteretic controller. I also reported on a very special property of perovskite solar cells: by forcing the solar cell to oscillate in forward bias, the cell produces a higher power output on average. This phenomenon was tentatively explained by dynamic transient photovoltage and transient photocurrent. The recombination rate during the backward scan was significantly lower than the one during the forward scan, which related to the increase in the collection efficiency.
- In chapter 6 I report on the study of the frequency response of perovskite solar cells. First, I show the equations that are relevant to carrier transport in semiconductors and their use in network thermodynamical circuits. The model was then extended to a three carrier system where two carriers are linked by thermodynamic equations of generation and annihilation. Based on this knowledge, a thermodynamic equivalent circuit of a perovskite solar cell under light was proposed. The frequency-response of the cell when it is subjected to sinusoidal perturbation of light was simulated for many different cases.

---

I then built an electronic pre-amplifier that allows voltage-dependent measurements of IMVS and IMPS. Quantitative fitting of some experimental data using numerical simulations was shown. Finally, I reported on a couple of case studies to showcase the effectiveness of frequency-resolved measurement techniques.

- Finally, in chapter 7, I report on a proof-of-concept to recycle perovskite solar cells. Using solvent orthogonality, I show that the cell can be disassembled in a similar procedure as its assembly. Notably, almost perfect lead sequestering can be achieved, avoiding the use of expensive separation techniques. The expensive and scarce components of the solar cell, i.e. the mesoscopic scaffold on the TCO glass and the gold could be reused without significant loss of efficiency.

In a time where the world needs more than ever to move away from fossil fuel energies, research in 3<sup>rd</sup> generation PV is a cornerstone of the energetic revolution. The stunning development of perovskite solar cells over the course of the last 5 years, with improvements in both the efficiency and the stability, is of great benefit to the photovoltaic community. I sincerely hope that this modest contribution will be of some use to one day move towards a commercialization of this technology. I believe that we are proceeding in the right direction. I do not know whether perovskite solar cells will be one day installed on my rooftop, but I am grateful to have had the opportunity to bring us one small step closer to this objective.



## 9 Methods summary

Chemicals and Reagents. Unless otherwise specified, all chemicals and reagents were purchased from Sigma-Aldrich, Dyesol or Dyenamo and solvents from Acros Organics and used without further purification. Spiro-MeOTAD was purchased from Merck KGaA.

### 9.1 Device fabrication

#### 9.1.1 Sequential deposition

*Procedure as used in chapter 2*

Patterned transparent conducting oxide substrates were coated with a TiO<sub>2</sub> compact layer by aerosol spray pyrolysis. A 350 nm thick mesoporous TiO<sub>2</sub> layer composed of 20 nm sized particles was then deposited by spin coating. The mesoporous TiO<sub>2</sub> films were infiltrated with PbI<sub>2</sub> by spin-coating a PbI<sub>2</sub> solution in DMF (462 mgmL<sup>-1</sup>) that was kept at 70 °C. After drying, the films were dipped in a solution of CH<sub>3</sub>NH<sub>3</sub>I in 2-propanol (10 mgmL<sup>-1</sup>) for 20 s and rinsed with 2-propanol. After drying, the HTM was deposited by spin-coating a solution of spiro-MeOTAD, 4-tert-butylpyridine, lithium bis(trifluoromethylsulphonyl)imide and tris(2-(1H-pyrazol-1-yl)-4-tert-butylpyridine)cobalt(III) bis(trifluoromethylsulphonyl)imide in chlorobenzene. Gold (80 nm) was thermally evaporated on top of the device to form the back contact.

For the fabrication of the best performing device, slightly modified conditions were used. First, PbI<sub>2</sub> was spin-cast for 5 s instead of 90 s and, second, the samples were subjected to a 'pre-wetting' by dipping in 2-propanol for 1–2s before being dipped in the solution of CH<sub>3</sub>NH<sub>3</sub>I and 2-propanol. For all measurements, devices were equipped with a 0.285 cm<sup>2</sup> metal aperture to define the active area.

*Procedure as used in chapter 3*

First, laser-etched FTO glass (NSG10, Nippon Sheet Glass) was cleaned by ultrasonication in an alkaline, aqueous washing solution for 30 min followed by rinsing with deionized water and isopropanol and UV/O<sub>3</sub> treatment for 30 min. A blocking TiO<sub>2</sub> layer was deposited by spin-

## Chapter 9. Methods summary

---

coating a room-temperature  $\text{TiCl}_4$  (2M) solution over the conductive glass (speed: 5000 r.p.m., acceleration: 2000 r.p.m.s<sup>-1</sup>, time: 20 s) followed by drying at 80 °C for approximately 20 min and cooling down to room temperature (~25 °C). The mesoporous  $\text{TiO}_2$  layer consisted of commercially available 20 nm-sized  $\text{TiO}_2$  nanoparticles (Dyesol 18NRT paste) in a colloidal suspension. The paste was diluted in ethanol (2:7, mass ratio) and stirred continuously. The film was spin-coated over the blocking layer (speed: 5000 r.p.m, acceleration: 2000 r.p.m.s<sup>-1</sup>, time: 20 s) followed by drying at 80 °C and 125 °C, sequentially. The films were then baked by gradual heating to 500 °C for 15 min under dry air flow. Upon cooling, the films were transferred in a dry-atmosphere glove box (< 1% relative humidity) for further manipulations.

$\text{PbI}_2$  was dissolved in N,N-dimethylformamide at a concentration of 582 mg mL<sup>-1</sup> (~ 1.26 mmol mL<sup>-1</sup> DMF) under continuous stirring at 80 °C and kept at this temperature during the whole procedure. The mesoporous  $\text{TiO}_2$  films were infiltrated by the  $\text{PbI}_2$  solution prior to spin-coating (speed: 6500 r.p.m, acceleration: 5000 r.p.m.s<sup>-1</sup>, time: 10 s) and drying at 80 °C for approximately 30 min. The films were dipped in a solution of  $\text{CH}_3\text{NH}_3\text{I}$ ,  $\text{H}_2\text{N}=\text{CHNH}_3\text{I}$  or a mixture thereof for 40 s prior to rinsing with pure isopropanol and spin coating to uniformly dry the film (speed: 2000 r.p.m, acceleration: 1000 r.p.m.s<sup>-1</sup>, time: 30 s). In the solution, the total iodide concentration was kept constant at 0.062 mol g<sup>-1</sup> 2-propanol regardless of the cation mixture. After spin-coating, the films were dried at 80 °C for 60 min before cooling down to room temperature (~25 °C) for further manipulation. The hole-transporting-material layer was deposited by spin coating (speed: 3000 r.p.m, acceleration: 2000 r.p.m.s<sup>-1</sup>, time: 20 s) from a solution containing 72.3 mg of (2,2',7,7'-tetrakis(N, N-di-p-methoxyphenylamine)-9,9-spirobifluorene) (spiro-MeOTAD), 28.8 µg of 4-tert-butylpyridine, 17.5 µL of a stock solution 520 mg mL<sup>-1</sup> lithium bis(trifluoromethylsulphonyl)imide in acetonitrile and 29 µL of a stock solution of 300 mg mL<sup>-1</sup> tris(2-(1H-pyrazol-1-yl)-4-tert-butylpyridine)cobalt(III) bis(trifluoromethylsulphonyl)imide in acetonitrile in 1 mL chlorobenzene. Finally, 100 nm of gold was thermally evaporated on top of the device to form the counter-electrode.

### *Procedure as used in chapter 5*

1.2 M  $\text{PbBr}_2$  precursor solution in DMF+DMSO mixture (1:1 volume ratio) was prepared by constant stirring at 60 °C for 30 min. 50 µL of the 1.2 M  $\text{PbBr}_2$  precursor solution was spin coated onto the mesoporous  $\text{TiO}_2$  films at 3000 r.p.m for 30 s. This was followed by annealing the films at 80 °C for 15 min. After cooling to room temperature, the  $\text{PbBr}_2$  films were dipped into isopropanol solution of FABr ( $50 \times 10^{-3}$  M) for 5 min at 60 °C, rinsed with 2-propanol for 5 s and dried at 80 °C for 30 min. Spiro-MeOTAD as HTM was deposited by spin coating 40 µL of the prepared solution at 4000 r.p.m for 30 s. The HTM solution was prepared by dissolving 72.3 mg (2,2',7,7'-tetrakis(N,N-di-p-methoxyphenylamine)-9,9-spirobifluorene) (spiro-OMeTAD), 17.5 µL of a stock solution of 520 mg mL<sup>-1</sup> bis(trifluoromethylsulphonyl)imide in acetonitrile, and 29 µL of a stock solution of 300 mg mL<sup>-1</sup> tris(2-(1H-pyrazol-1-yl)-4-tert-butylpyridine)cobalt(III) bis(trifluoromethylsulphonyl)imide in acetonitrile, and 28.8 µL 4-tert-butylpyridine in 1 mL chlorobenzene. The device fabrication was carried out under controlled atmospheric conditions with humidity <2%. Finally, device fabrication was completed by thermally evaporating 70 nm of gold layer as a back contact.

### 9.1.2 Single-step deposition

Fluorine-doped tin oxide (FTO) glass was etched to form the two detached electrodes with zinc powder and diluted hydrochloric acid. The glass was then cleaned by sonication in 2% Hellmanex solution. Thereafter, the glass substrates were rinsed with deionized water and Ethanol and dried with compressed air and subject to UV-O<sub>3</sub> treatment for 15 min. A compact hole blocking layer of TiO<sub>2</sub> was deposited onto the glass by spray pyrolysis. The precursor solution consisted of 600 μL of titanium diisopropoxide bis(acetylacetonate), 400 μL of acetylacetonate in 9 mL of ethanol, which was then sprayed with the carrier gas oxygen at 450 °C. A scaffold of mesoporous TiO<sub>2</sub> (m-TiO<sub>2</sub>) was deposited by spin coating a 1:5 (w/w) dispersion of TiO<sub>2</sub> with particle size of 30 nm in ethanol at 4000 r.p.m for 10 s to maintain a thickness of about 300 nm. The thus formed films were then heated upto 450 °C and sintered at that temperature for 30 min and allowed to cool to 100 °C. A surface treatment of the m-TiO<sub>2</sub> was carried out by spincoating a solution of 10 mg mL<sup>-1</sup> of bis(trifluoromethane)sulfonimide lithium salt in acetonitrile at 3000 r.p.m for 10 s. The substrates were then baked again by the procedure described above. The substrates were then baked again by the procedure described above. The cooled substrates were then used for the deposition of perovskite upon them. Upon cooling to room temperature, the perovskite layer was deposited in a dry air-filled glovebox by spin coating the perovskite precursor solution. For CH<sub>3</sub>NH<sub>3</sub>PbI<sub>3</sub> devices, the perovskite films were deposited from 1.22 M precursor solution of CH<sub>3</sub>NH<sub>3</sub>PbI<sub>3</sub> in anhydrous dimethylsulphoxide. For (FAPbI<sub>3</sub>)<sub>0.85</sub>(MAPbBr<sub>3</sub>)<sub>0.15</sub>, the solution consisted of H<sub>2</sub>N=CHNH<sub>3</sub>I (1 M), PbI<sub>2</sub> (1.1 M), CH<sub>3</sub>NH<sub>3</sub>Br (0.2 M) and PbBr<sub>2</sub> (0.2 M) in anhydrous dimethylformamide/ dimethylsulphoxide (4:1 (v:v)) solution. The perovskite solution was spin coated in a two-step program at 1000 r.p.m and 6000 r.p.m for 10 s and 30 s, respectively. During the second step, 120 μL of chlorobenzene was poured on the spinning substrate 10 s prior the end of the program. The substrates were then annealed at 100 °C for 1 h in a nitrogen-filled glove box. The HTM was subsequently deposited on the top of the perovskite layer by spin coating its solution at 4000 r.p.m for 20 s with a ramp of 2000 r.p.m s<sup>-1</sup>. To the prepared solution of 50 mg of Spiro-MeOTAD in 574 μL of CB, 20 μL of tert-butylpyridine, 11.4 μL of 1.8 M LiTFSI in acetonitrile and 4.9 μL of 0.25 M cobalt salt (FK 209) in acetonitrile were added as dopants. Finally, device fabrication was completed by thermally evaporating 70 nm of gold layer as a back contact.

## 9.2 Device characterization

### 9.2.1 Voltage sweep measurements

The  $j(V)$  characteristics were recorded by biasing an external potential bias to the cell while recording the current output using a digital source meter (Keithley Model 2400). The light source was a 450 W Xenon lamp (Oriol) equipped with a Schott K113 Tempax sunlight filter (Prazisions Glas & Optik GmbH) to match the emission spectra of the lamp to the AM1.5G standard. Before each measurement, the exact sun intensity was determined using a calibrated Si diode equipped with an infrared cut-off filter (KG-3, Schott).

### 9.2.2 IPCE response

IPCE spectra were recorded as a function of wavelength under a constant light bias of approximately 5 mW cm<sup>-2</sup> supplied by an array of white light-emitting diodes. The excitation beam coming from a 300 W xenon lamp (ILC Technology) was focused through a Gemini-180 double monochromator (Jobin Yvon Ltd) and chopped at approximately 2 Hz. The signal was recorded using a Model SR830 DSP Lock-In Amplifier (Stanford Research Systems). All measurements were conducted using a non-reflective metal aperture of 0.285 cm<sup>2</sup> or larger to define the active area of the device and avoid light scattering through the sides.

## 9.3 Kinetic measurements

### 9.3.1 Sequential deposition

Mesoporous TiO<sub>2</sub> films were deposited on microscopic glass slides and infiltrated with PbI<sub>2</sub> following the above-mentioned procedure. The samples were then placed vertically in a cuvette with a path length of 10 mm. The solution of CH<sub>3</sub>NH<sub>3</sub>I was then rapidly injected into the cuvette while either the photoluminescence or the optical transmission was monitored.

### 9.3.2 Halide exchange reactions

#### 9.3.2.1 Sample preparation

Fluorine-doped tin oxide (FTO) coated glass substrates (Tec 15, Pilkington or NSG10, Nippon Sheet Glass) were cleaned by ultrasonication in an alkaline, aqueous washing solution, rinsed with deionized water and ethanol and subjected to a UV/O<sub>3</sub> treatment for 30 minutes. A mesoporous Al<sub>2</sub>O<sub>3</sub> layer composed of 23 nm-sized nanoparticles was deposited by spin-coating at 5000 r.p.m for 10 seconds using a home-made Al<sub>2</sub>O<sub>3</sub> paste diluted in ethanol (2:7 weight ratio). After drying at 125 °C, the Al<sub>2</sub>O<sub>3</sub> films were gradually heated to 500 °C and baked for 15 minutes before cooling to room temperature. The resulting film was about 300 nm thick with 50 nm pores for a final porosity of 73%. CH<sub>3</sub>NH<sub>3</sub>PbCl<sub>3</sub>, CH<sub>3</sub>NH<sub>3</sub>PbBr<sub>3</sub> or CH<sub>3</sub>NH<sub>3</sub>PbI<sub>3</sub> were then deposited from a precursor solution at 70 °C by spin-coating onto the Al<sub>2</sub>O<sub>3</sub> films at either 2000 r.p.m (for SEM) or 5000 r.p.m (for all the other experiments) for 10 seconds followed by drying at 70 °C for 10 minutes. The precursor solution contained 0.5 M of PbX<sub>2</sub> and a 1.1 molar equivalent of CH<sub>3</sub>NH<sub>3</sub>X dissolved in either N,N-dimethylformamide (X=Br,I) or dimethylsulfoxide (X=Cl). Halide exchange reactions were performed by exposing the CH<sub>3</sub>NH<sub>3</sub>PbX<sub>3</sub> films to a 0.05 M solution of CH<sub>3</sub>NH<sub>3</sub>X (X=Cl,Br,I) in anhydrous 2-propanol. The MAI solution was typically saturated at such concentrations and was allowed to decant before use. All halide exchange reactions were performed under ambient conditions.



### 9.3.2.2 In situ photoluminescence

To monitor changes in photoluminescence during the halide exchange reaction, 8 x 20 mm  $\text{CH}_3\text{NH}_3\text{PbX}_3$  films were mounted in a quartz fluorescence cuvette and held steady at  $60^\circ$  by a home-crafted Teflon holder. A continuous solid-state blue-ray laser commercially available was directed onto the sample perpendicular to the cuvette window. The output signal was coupled through an optical fiber mounted at  $90^\circ$  from the indicated beam and recorded by an Ocean Optics USB2000+ spectrometer. At time  $t = 0$ , about 2 mL of a  $\text{CH}_3\text{NH}_3\text{X}$  solution (0.05 M in 2-propanol) was suddenly added into the cuvette. Each trace was integrated for 100 ms. The resulting (time, wavelength) intensity signal matrix was decomposed into singular values. Values below 5% of the highest were discarded and the signal matrix was reconstructed.

### 9.3.2.3 In situ absorbance

In situ absorbance measurements were carried out over a similar setup with a halogen lamp illuminating a quartz transmission cuvette in which the film was placed perpendicular to the incident beam. The transmitted light was coupled through an optical fiber and recorded by an Ocean Optics USB2000+ spectrometer. The resulting time x wavelength intensity matrix was decomposed into singular values. Values below 5% of the highest were discarded and the signal matrix was reconstructed. The transmitted light was converted into absorbance after subtraction of the shot noise of the CCD camera. The blank reference consisted of a similar FTO/ $\text{Al}_2\text{O}_3$  sample in 2-propanol.

## 9.4 Optical spectroscopy

### 9.4.1 Single pass absorption

Single-pass absorption measurements were conducted in transmission using a homemade setup equipped with a commercially available halogen lamp (20 W) chopped by a rotating wheel at about 10 Hz. The incident beam was restricted to an aperture of approximately  $0.05 \text{ cm}^2$  covered by the sample. The signal was filtered through a Gemini-180 double monochromator (Jobin Yvon Ltd) with 1.6 mm slit width and recorded using a Model SR830 DSP Lock-In Amplifier (Stanford Research Systems). The acquisition was averaged over 0.5 s per point and recorded every nanometer. Blank acquisitions were conducted over FTO-coated glass on which was deposited a blocking  $\text{TiO}_2$  layer and mesoporous  $\text{TiO}_2$  film deposited in similar conditions as the measured samples.

### 9.4.2 Photoluminescence

*As used in chapter 3*

Emission signals were recorded using a home-made photo-induced absorbance set-up used without bias light. A blue diode (460 nm) was flashed at 9 Hz by a Model SR830 DSP Lock-In

Amplifier (Stanford Research Systems). The light was filtered through a MODEL-BRAND interference filter. The sample was installed at 30° from the incoming light source, which was restricted to about 0.05 cm<sup>2</sup> covered by the sample. The photoluminescence signal was filtered by a Gemini-180 double monochromator (Jobin Yvon Ltd) with 0.8 mm slit width and recorded by the Lock-In Amplifier. Each point was recorded every nanometer for 8 seconds.

### 9.4.3 Scatter-free absorption spectra

*As used in chapter 3*

To measure absorption spectra, the samples were cut to fit size of the custom-made sample holder (13 x 12 mm) and placed in the center of an integration sphere. The measurements were conducted using a Jobin Yvon Ltd Spectrofluorometer. A 200 W Xe lamp was filtered through a monochromator (slit with 0.5 mm) and directed into the sphere. The incident beam was narrower than the aperture of the sample holder. The sample was set successively in and out of the incident beam path. The signal was recorded at 90° from the incoming light source through a monochromator scanning synchronously with the excitation monochromator. Signal amplification was performed by a photomultiplier.

### 9.4.4 Fluorescence lifetime measurements

Photoluminescence measurements were conducted with a Horiba Jobin Yvon Ltd spectrofluorometer equipped with the NanoLED® laser diode flashed at 100 kHz. The excitation wavelength was 406 nm. The photoluminescence signal was filtered through a cut-off filter (520 nm). The samples were mounted at 45° and the emission decay recorded at 90° from the incident beam path. The signal was filtered through a monochromator and recorded using a photomultiplier.

## 9.5 Water purification

A commercial ion-exchange resin was used to remove remaining lead contamination from H<sub>2</sub>O used for MAI dissolution. Amberlite IR 120 hydrogen form (Sigma Aldrich) was washed repeatedly in deionized water and EtOH and dried in a vacuum oven at 60 °C for 16h. 1 g dried resin was added per 30 mL solvent in a round-bottom flask and stirred at room temperature for 16h. The water was filtered using hydrophilized 0.2 µm PTFE syringe filters to remove Amberlite residues for analytical purposes.

## 9.6 ICP-MS

All lead assays were performed using an aqueous solution of tetrabutylammonium hydroxide (1% wt), Ethylenediaminetetraacetic acid disodium salt (NaEDTA, 1.25% wt) and bismuth nitrate (0.3 ppm or 0.6 ppm Bi) to provide an internal calibration. All lead contents were ex-

tracted from the integrated signal of  $^{208}\text{Pb}$  and  $^{209}\text{Bi}$ , calibrated using solutions of 0.05 ppm, 0.15 ppm and 0.3 ppm Pb and 0.3 ppm Bi. The lead source for the calibration standards was the same  $\text{PbI}_2$  as the one used for the devices, to avoid fluctuations in isotopic distributions. All measurements were done on an Agilent 7700x ICP-MS system and the same matrix was used for all the samples. Devices (2.5x1.5cm) were immersed into 10mL of anhydrous chlorobenzene in a round bottom flask, until the gold was removed and the HTM layer was dissolved. 5 mL of the resulting solution was pipetted out and dried by rotavapory evaporation. The remainder was dissolved into 0.5 mL of N,N-dimethylformamide and 10 mL of the aqueous solution described above. The same process was repeated for the dissolution of the organic component using ethanol, water, isopropanol or methanol.  $\text{PbI}_2$  was removed from the substrate by dropping 0.5 mL of N,N-dimethylformamide onto the substrate followed by dilution into 10 mL of the matrix. The resulting solution was further diluted 100 fold for ICP-MS measurements.

### 9.7 Structural characterization

X-ray powder diffractograms were recorded on an X'Pert MPD PRO (Panalytical) equipped with a ceramic tube (Cu anode,  $\lambda = 1.54060\text{\AA}$ ), a secondary graphite (002) monochromator and a RTMS X'Celerator (Panalytical). The measurements were done in the Bragg-Brentano geometry. The samples were mounted without further modification and the automatic divergence slit and beam mask were adjusted to the dimension of the films. A step size of  $0.002^\circ$  was chosen for an acquisition time of 7.5 min /  $^\circ$ . A baseline correction was applied to all X-Ray powder diffractograms to compensate for the broad feature arising from the glass substrate. The XRD measurements were focused on the  $13^\circ$  to  $16^\circ$  to probe the 110 reflection of the tetragonal structure.

### 9.8 X-ray fluorescence

XRF spectra were collected on a Fischerscope x-ray XAN with tungsten nickel anticathode.



# A Implementation of the IMVS / IMPS pre-amplifier

## A.1 Implementation of the anode sink

The transimpedance amplifier is the most critical part of the design. We selected the OPA847, which exhibits an extremely high gain bandwidth (3.9 GHz) and extremely low noise spectral density ( $0.85 \text{ nV}/\sqrt{\text{Hz}}$ ). A small gain resistance of  $47 \Omega$  was placed as close as possible from the output stage to isolate the op amp. A larger  $470 \Omega$  gain resistance was placed in the loop with a  $4.6 \text{ pF}$  compensation capacitance. Since the source capacitance of the solar cells is usually not defined, we selected a capacitor empirically for the solar cells we measured. It should be noted that a larger capacitance should further stabilize the op amp, but would come at the cost of bandwidth and phase lag. A digital switch (TS12A12511) was added between the DAC and the buffer, giving the option of the user to enable an external  $50 \text{ Ohm}$ -matched voltage set point through a BNC connector directly the board. The switch is controlled via the microprocessor that provides the board logic. After the switch, a low pass filter with a corner frequency at  $10 \text{ kHz}$  was added for noise-filtering purposes. All inputs and outputs were protected from overvoltage by Schottky diodes to  $\pm 5 \text{ V}$ . The output of the cathode driver is connected through a relay, to allow switching the cell to galvanostatic mode without changing the connections. The transimpedance signal was routed through a telecom relay (V23079) into either directly the output buffer or through an additional  $20 \text{ dB}$  gain stage (THS4303) with fixed gain and high bandwidth ( $1.8 \text{ GHz}$ ). The output of the first  $+20 \text{ dB}$  stage can be further amplified by another  $20 \text{ dB}$  through another relay, to amplify extremely low currents. To provide the output current necessary to drive a  $50 \text{ Ohm}$  line, a high current output line driver (BUF634) was added with  $50 \Omega$  in series. Because the BUF634 was not within the feedback loop of a previous stage, the offset voltage will introduce an additional error in the measurement, but affects the result independently of the frequency and thus is of no concern in this application.

Figure X: Cadsoft Eagle schematics of the transimpedance amplifier with two  $20 \text{ dB}$  post-amplifiers that can be enabled through relays.

### A.1.1 Numerical Simulation

The transimpedance amplifier and line driver make up the current amplification chain. The main criterion for frequency-resolved experiments is a minimal phase shift and amplitude loss over the experimental frequency span (DC-1MHz). The SPICE model depicted in Figure X was solved for the AC transfer characteristics. The phase shift and amplitude drops of the transimpedance amplifier and the amplitude loss of the cathode driver are shown in Figure X

Figure X: Numerical results of the SPICE simulation of the circuit shown in Figure X. (a) Phase shift of the transimpedance amplifier before (red) and after (blue) the BUF634 line driver. (b) Amplitude loss / gain of the same circuit. The simulation shows possible instability of the amplifier in the high frequency range, but in practice the 4.6pF compensation was enough to stabilize the OPA847. (c) Amplitude loss of the cathode driver in the closed-loop configuration with the 100Ohm isolation. The amplitude drop corresponds to the inability to drive the cell at high frequency, but only marginally (0.45dB at 1MHz)

Characterization

## A.2 Implementation of the cathode driver

For the cathode driver, we used the OPA820, which features a closed-loop output impedance below 0.1Ohm at 1MHz and is unity-gain stable. A 100  $\Omega$  series resistance was placed to isolate the output stage from the device. The voltage set-point was provided by a 16 bit DAC (8532) through a  $G = -1$  amplifier (OPA2234), as shown in Figure X.

Figure X: Cadsoft Eagle schematics of the potentiostatic driver

## A.3 Implementation of the Howland current pump

In Figure X, we show the implemented Howland current pump. The voltage set point was provided either by the second channel of the DAC (DAC8532) or by an external set point, selected through the same switch as the device driver (TS12A12511). A voltage follower (OPA820), which output impedance remains below 0.1Ohm at 1MHz, was used to drive the Howland current pump. With DAC voltages ranging from +2.5V to -2.5V and by setting the current range from 5mA to -5mA, the gain resistors were chosen at 511 Ohm with a tight matching of 0.05%. Therefore, the worst possible impedance, including the 0.1Ohm of the driver, should be around 300kOhm. Additional pads for a feedback capacitor were added to ensure the stability of the op amp, but usually found unnecessary in this application. We took advantage of the high bandwidth (100MHz) and high voltage power supply (+/- 12V) of the THS4031 as the current pump. When power a device at 1V with 5mA current, the driver must swing to at least 3.5V, which is close to the upper limit of most non rail-to-rail op amps. Therefore, using wider rails was found necessary. The output of the pump is directly connected

### **A.3. Implementation of the Howland current pump**

---

to the anode of the device through a relay, which routes the anode to either the pump or the transimpedance amplifier when IMPS is measured. Similarly to the cathode, the anode is protected by Schottky diodes to the  $\pm 5V$  power rails.





## B Fitting numerical simulations

When the devices cannot be simply described by equation 6.73 (because of interfacial recombination, charge transfer hindrance or due to a non-negligible chemical capacitance), their IMVS spectra can either be qualitatively explained by numerical simulations or can be quantitatively fitted to the result of such simulations.

### B.0.1 The constant phase element

Constant phase elements are often used instead of pure capacitors to describe non-ideal double layer capacitors. They often appear in the treatment of the impedance spectra of ionic cells[300] and are usually necessary to explain the impedance behavior of dye-sensitized solar cells[301, 302]. The impedance of a constant phase element is given by:

$$Z_{CPE} = \frac{1}{Q_0 (\omega i)^n} \quad (\text{B.1})$$

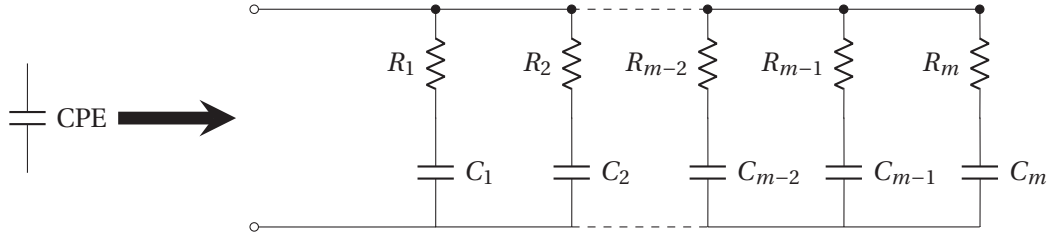
Where

- $n$  describes the phase of the CPE. When  $n = 1$ , the phase is  $90^\circ$  and CPE behaves as a perfect capacitor, while for  $n = 0$ , the phase is  $0^\circ$  and the CPE is a perfect resistor.
- $Q_0$  is frequency independent. When  $n = 1$  it is a capacitance.

While the transfer function of CPE elements is defined by equation B.1, the CPE does not exist as a basic SPICE element. Fortunately, CPEs can be simulated by an (ideally infinite) parallel set of capacitor-resistor in series[303], as shown in Figure B.1.

## Appendix B. Fitting numerical simulations

**Figure B.1:** Network model of a constant phase element, expanded into a parallel sum of  $m$  resistor-capacitor in series



The resistances and capacitors take the following values:

$$\begin{aligned} R_k &= R_1 a^{k-1} \\ C_k &= C_1 b^{k-1} \end{aligned} \quad (\text{B.2})$$

Where  $C_1$  and  $R_1$  are input parameter that can be chosen freely, to the extend that their time  $\tau = RC$  is smaller than the lowest time constant of interest for which the CPE should be emulated.  $0 \leq a \leq 1$  and  $0 \leq b \leq 1$  are parameter that, together, define the phase of the CPE:

$$\phi = 90 \frac{\log a}{\log ab} \quad (\text{B.3})$$

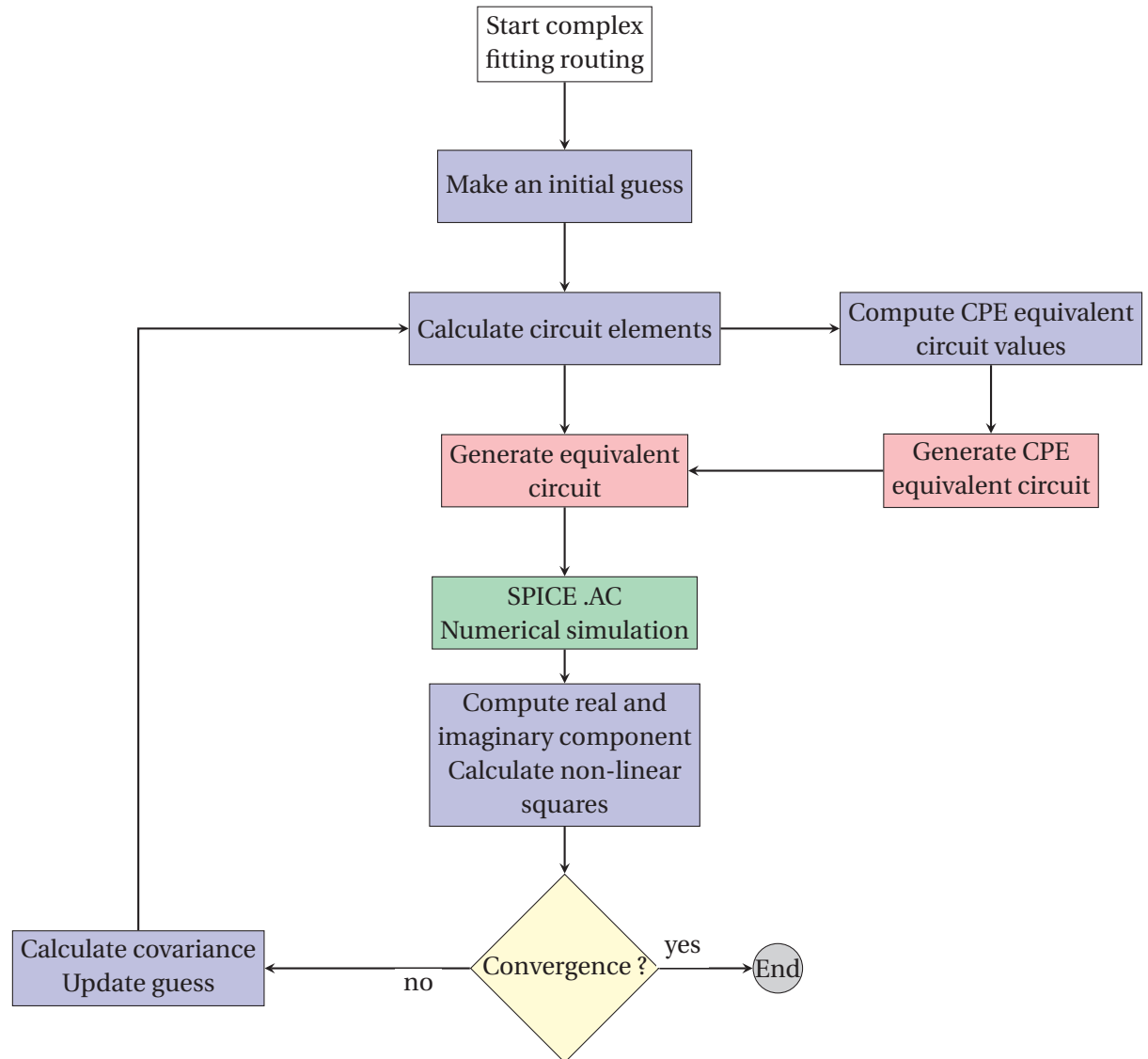
The special case of  $a = b$  describes a  $45^\circ$  phase. The input admittance of the equivalent circuit takes the value:

$$Y(j\omega) = \sum_{k=1}^m \frac{j\omega b^{k-1} C_1}{1 + j\omega (ab)^{k-1} R_1 C_1} \quad (\text{B.4})$$

For a given  $R_1$  and  $C_1$  that are arbitrarily chosen, the admittance is often far different from the target  $Q_0$ . In this case, after calculating the circuit admittance, a correction factor is applied to  $R_1$  and  $C_1$  to account for this deviation:

$$\begin{aligned} \text{scaling} &= Q_0^{\text{target}} / Y(1 \text{ rads}^{-1}) \\ R_1^{\text{new}} &= R_1 * \text{scaling} \\ C_1^{\text{new}} &= C_1 / \text{scaling} \end{aligned} \quad (\text{B.5})$$

**Figure B.2:** Flow-chart of the algorithm used in fitting numerical simulations. Blue blocks represent Igor PRO software code, red blocks a node.js script used to generate the SPICE input files and green the SPICE .AC run.





# C Implementation of the IMVS / IMPS pre-amplifier

## C.1 Implementation of the anode sink

The transimpedance amplifier is the most critical part of the design. We selected the OPA847, which exhibits an extremely high gain bandwidth (3.9 GHz) and extremely low noise spectral density ( $0.85 \text{ nV}/\sqrt{\text{Hz}}$ ). A small gain resistance of  $47 \Omega$  was placed as close as possible from the output stage to isolate the op amp. A larger  $470 \Omega$  gain resistance was placed in the loop with a  $4.6 \text{ pF}$  compensation capacitance. Since the source capacitance of the solar cells is usually not defined, we selected a capacitor empirically for the solar cells we measured. It should be noted that a larger capacitance should further stabilize the op amp, but would come at the cost of bandwidth and phase lag. A digital switch (TS12A12511) was added between the DAC and the buffer, giving the option of the user to enable an external  $50 \text{ Ohm}$ -matched voltage set point through a BNC connector directly the board. The switch is controlled via the microprocessor that provides the board logic. After the switch, a low pass filter with a corner frequency at  $10 \text{ kHz}$  was added for noise-filtering purposes. All inputs and outputs were protected from overvoltage by Schottky diodes to  $\pm 5 \text{ V}$ . The output of the cathode driver is connected through a relay, to allow switching the cell to galvanostatic mode without changing the connections. The transimpedance signal was routed through a telecom relay (V23079) into either directly the output buffer or through an additional  $20 \text{ dB}$  gain stage (THS4303) with fixed gain and high bandwidth ( $1.8 \text{ GHz}$ ). The output of the first  $+20 \text{ dB}$  stage can be further amplified by another  $20 \text{ dB}$  through another relay, to amplify extremely low currents. To provide the output current necessary to drive a  $50 \text{ Ohm}$  line, a high current output line driver (BUF634) was added with  $50 \Omega$  in series. Because the BUF634 was not within the feedback loop of a previous stage, the offset voltage will introduce an additional error in the measurement, but affects the result independently of the frequency and thus is of no concern in this application.

### C.2 Implementation of the cathode driver

For the cathode driver, we used the OPA820, which features a closed-loop output impedance below 0.1Ohm at 1MHz and is unity-gain stable. A 100  $\Omega$  series resistance was placed to isolate the output stage from the device. The voltage set-point was provided by a 16 bit DAC (8532) through a  $G = -1$  amplifier (OPA2234).

### C.3 Implementation of the Howland current pump

The voltage set point was provided either by the second channel of the DAC (DAC8532) or by an external set point, selected through the same switch as the device driver (TS12A12511). A voltage follower (OPA820), which output impedance remains below 0.1Ohm at 1MHz, was used to drive the Howland current pump. With DAC voltages ranging from +2.5V to -2.5V and by setting the current range from 5mA to -5mA, the gain resistors were chosen at 511 Ohm with a tight matching of 0.05%. Therefore, the worst possible impedance, including the 0.1Ohm of the driver, should be around 300kOhm. Additional pads for a feedback capacitor were added to ensure the stability of the op amp, but usually found unnecessary in this application. We took advantage of the high bandwidth (100MHz) and high voltage power supply (+/- 12V) of the THS4031 as the current pump. When power a device at 1V with 5mA current, the driver must swing to at least 3.5V, which is close to the upper limit of most non rail-to-rail op amps. Therefore, using wider rails was found necessary. The output of the pump is directly connected to the anode of the device through a relay, which routes the anode to either the pump or the transimpedance amplifier when IMPS is measured. Similarly to the cathode, the anode is protected by Schottky diodes to the +/- 5V power rails.

# D Design and assembly of the MPPT tracker

Solutions for multiple channels acquisition cards already exist and are widely available commercially. However, the cost of such instruments is usually prohibitive for large batches of solar cells, and offer capabilities beyond the requirements for long-term testing of solar cells (fast acquisition, wide voltage and current range, 24-bit resolution, ...). Standards ask for 1'000 hours of continuous uninterrupted testing under constant sunlight, which is clearly problematic when hundreds of devices have to be measured. The degradation pathways of 3rd generation solar cells, including perovskite cells, often remain under debate. In the case of hybrid organic-inorganic perovskites, humidity and solvent-induced degradation is often cited as the main problem, but other issues such as phase segregation, ion migration and crystallization are also likely to participate to the degradation of performances. Fixing such issues require large ageing facilities. A multi-channel ageing setup is an attractive solution because it allows the establishment of a statistical basis by parallel testing of various device architectures, testing conditions or packaging (sealing, sizing, ...). We report on a relatively inexpensive and elegant system that can replace most potentiostats or source-measuring units for the measurement and tracking of solar cells. Herein, we release the schematics, bill of material, cost estimate and microcontroller code.

When testing the stability of large modules with high photocurrent and high voltages, a buck-boost converter is usually required, such that the power output of the PV array is harvested by an external load (for DC loading) - typically a thermal resistance with a heat sink - or to an inverter, for DC/AC conversion. However provided that the device delivers small photocurrents (in our case, less than 60mA in total) and low voltages, the power generated can be easily dissipated into heat in the output stage of the driving unit. In our case, we chose an operational amplifier in follower configuration (OPA2192), placed within the feedback loop of the precision driver (INA2132), to compensate for drifts in temperature and non-unity gain. A digital to analog converter (DAC7563), interfaced by a microcontroller (ATMega328), sources the reference voltage that is driven by the output stage to the device. To sense the sinking or sourcing current, a small resistance ( $0.5\ \Omega$ ) is positioned in series with the device (high side), and the voltage drop across this resistor is amplified by a low-noise, high gain ( $200\ \text{VV}^{-1}$ )

## Appendix D. Design and assembly of the MPPT tracker

---

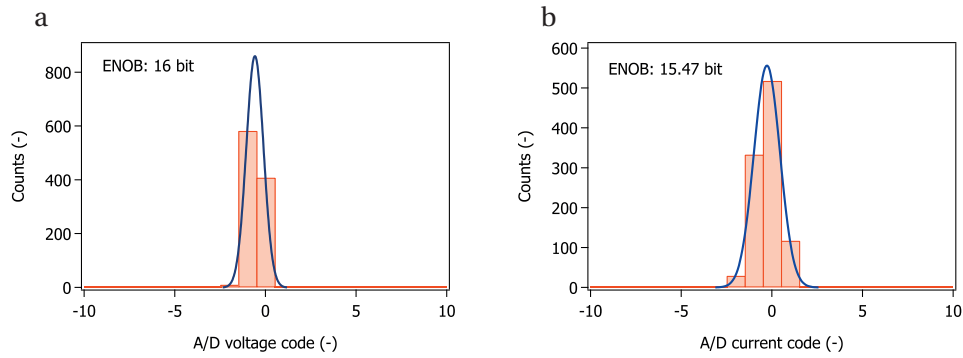
instrument amplifier (INA188) to feed into a 4th order Butterworth low-pass filter (OPA4722) that serves both anti-aliasing and high frequency noise removal. The cut-off frequency of the filter typically limits the sampling rate of the instrument and we set it arbitrarily to 500Hz so that it would settle within 1 bit resolution in roughly 1ms. The output of the filter is fed into a 16 bit  $\Sigma\Delta$  analog-to-digital converter (ADS1118) for the sampling, also interfaced by the microcontroller. The voltage across the device is directly buffered (OPA2188) into the low pass filter and sampled on a second channel of the ADC after appropriate level shifting. For cost saving, the 16 sensing lines (8 for current, 8 for voltage) are multiplexed (CD54HC4051) into the low pass filter and sampled by the same ADC. However, the drive line (DAC7563 DAC, INA2132 level shifter and OPA2191 output driver) are individual to each pair of cells (those three parts have two channel each), and therefore the voltage across each device is constantly maintained, even though not sample. In our case, the microcontroller is an inexpensive, open-source and easily programmable Arduino Nano, mounted onto the board. When all the devices are connected together, a bandwidth of about 3Hz can be achieved, typically limited by the Butterworth filter, the sampling rate of the ADC and the data transfer. Changing the -3dB pole of the Butterworth filter and using a faster ADC could easily achieve faster tracking. Using a 16bit analog to digital converter allowed us to read voltage up to 15.5 bit resolution and a 15 bit current resolution. The value of the series resistance, the gain of the INA and the (programmable) gain of the ADC allow wide tuning of the current range. The INA188 being of relatively low noise ( $12 \text{ V} \sqrt{\text{Hz}}^{-1}$ ) allow for large amplification. For this particular 16 bit resolution A/D converter with a Full-scale-range at  $\pm 2.048 \text{ V}$ , the input-referred RMS noise is  $62.5 \mu\text{V}$ . Therefore, a gain of

$$G = \frac{62.5}{0.012\sqrt{500}} = 233 \text{ VV}^{-1} \quad (\text{D.1})$$

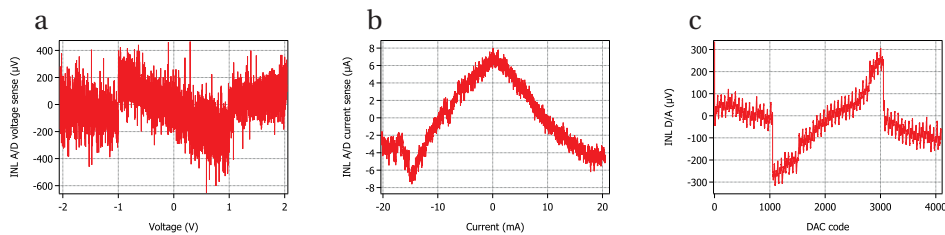
at the INA will remain within the boundaries of the A/D noise. A lower gain will reduce the system noise, but larger series resistance will have to be used to cover the same current range. Larger gains will begin to affect the effective number of bits (ENOB). Selecting a gain of  $200 \text{ VV}^{-1}$  and a current range of  $\pm 20 \text{ mA}$  sets the series resistance to  $0.5 \Omega$ , which creates a negligible voltage drop ( $5 \text{ mV}$  at  $10 \text{ mA}$ ) and can be compensated by the acquisition system. The effective number of bits for this configuration is shown in figure D.1.

Based on the noise figure, a resolution of about  $880 \text{ nA}$  can be achieved. In practice however, the non-linearity of the gain (INA, filter and ADC) will predominate. The integral non-linearity of the voltage sensing and current sensing is shown in figure D.2 (a,b). The INL of the current sensing reduces the resolution by 24 LSB, which brings the resolution to 11.4 ENOB. The accuracy of the voltage sensing could be greatly improved by fitting the calibration curve to the region of interest (negative currents, photovoltaic mode). The non-linearity of the voltage sensing stays under the resolution of the D/A converter, i.e.  $1 \text{ mV}$  and better resolution can not be expected without selecting a 14 or 16-bit DAC. The dynamic performances of the DAC drive



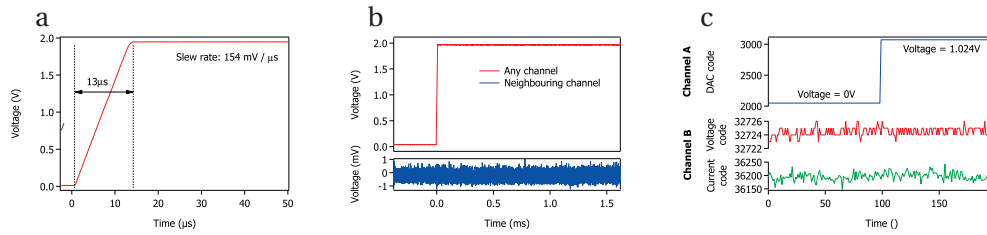


**Figure D.1:** Noise performance of the sensing lines. The ENOB resolution is calculated from the RMS noise of the analog to digital converter, obtained by approximating the histograms by a normal distribution (a) Voltage code histogram (N=1000 counts) for a typical sensing channel. The calculated effective number of bits was 16 (b) Current code histogram (N=1000 counts) for a typical sensing channel. The effective number of bit was 15.47.



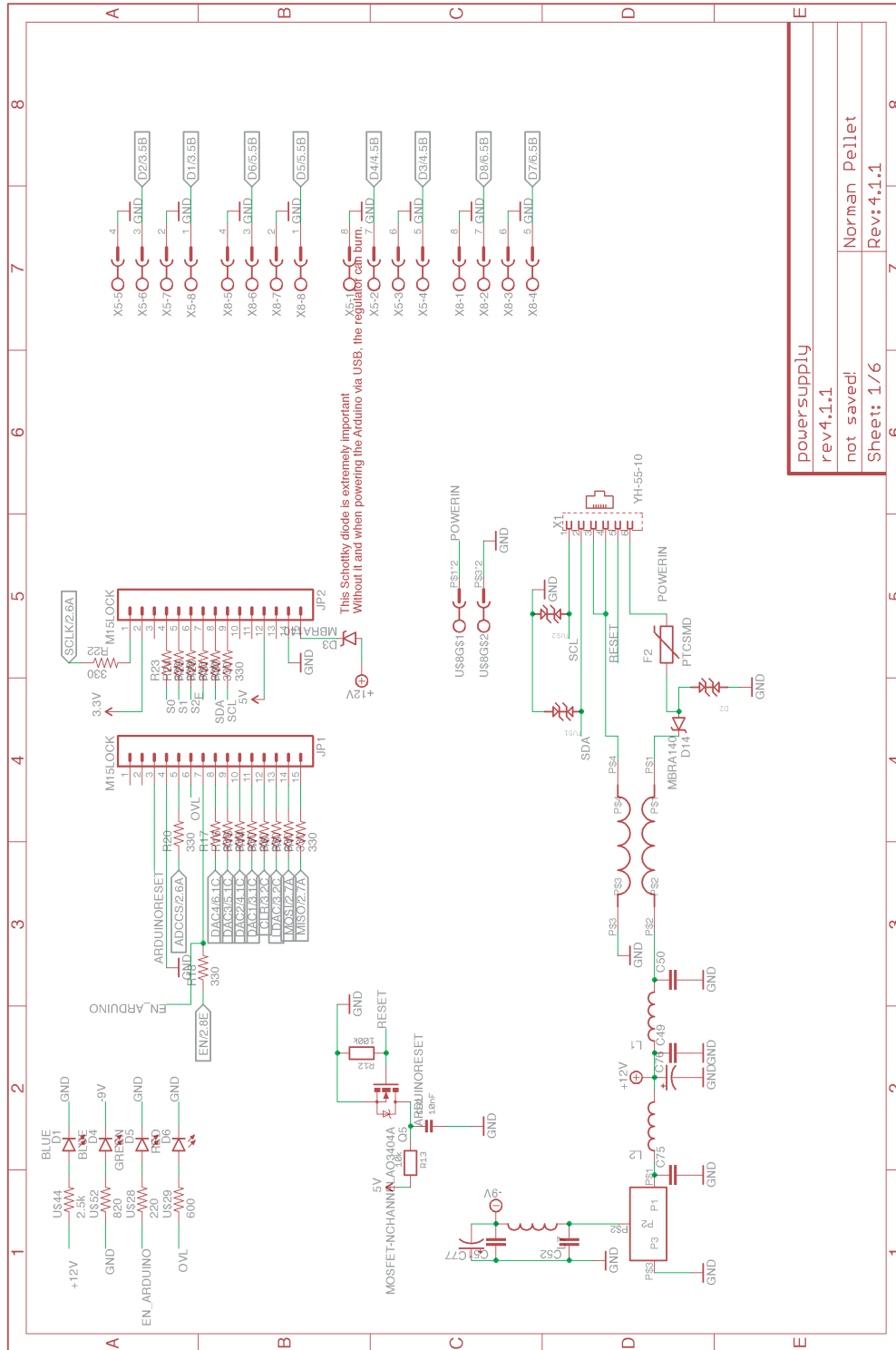
**Figure D.2:** Integral non-linearity (INL) of the (a) voltage sensing, (b) current sensing and (c) voltage driving. Obtained as the residuals of the fit through the whole ADC and DAC code range.

## Appendix D. Design and assembly of the MPPT tracker



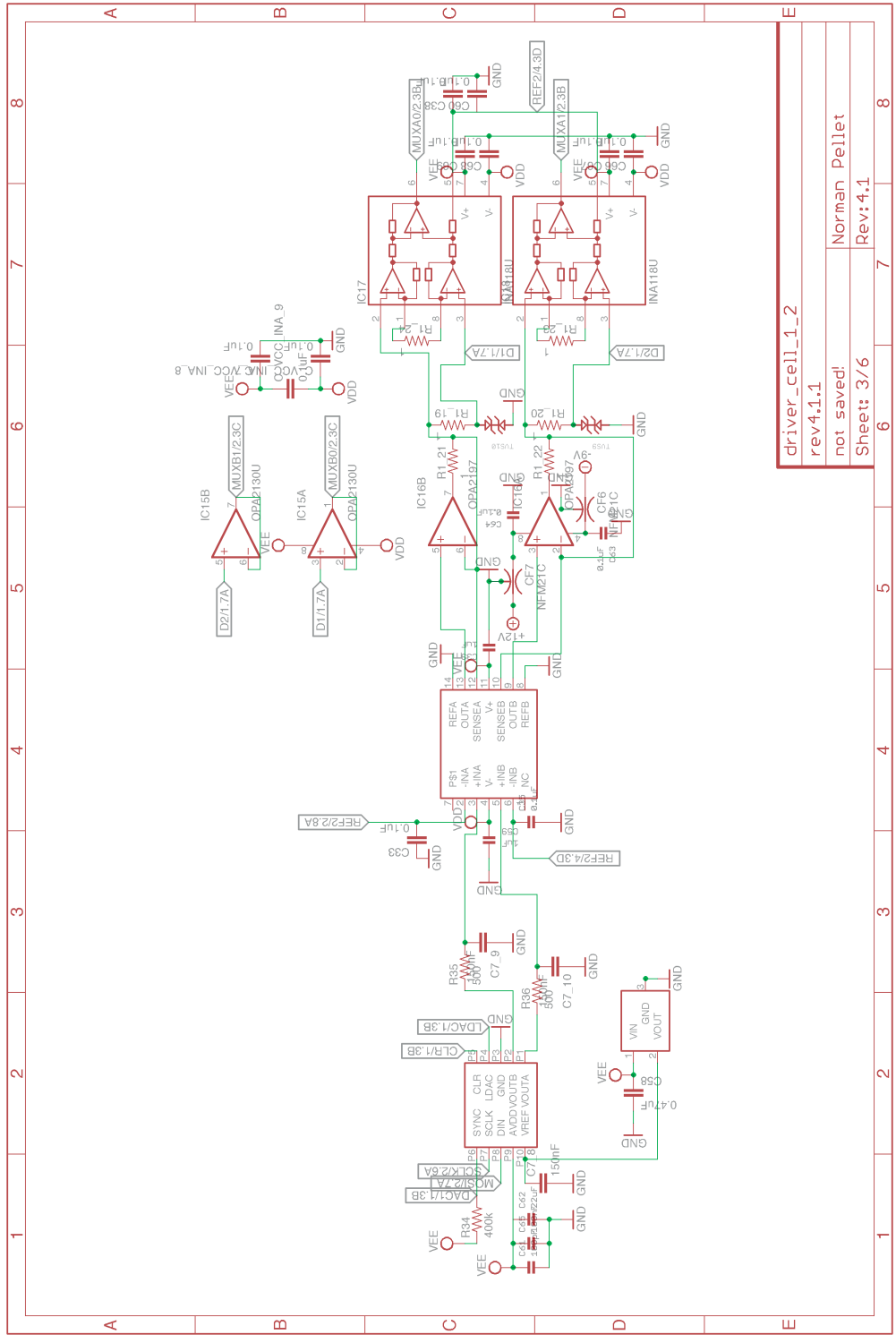
**Figure D.3:** Dynamic performances of the MPPT setup. (a) Large signal settling from code 2048 to 4096. (b) Drive line cross-talk between two neighboring channels. (c) Sense line cross-talk between two neighbouring channels

are shown in Figure D.3. Typical slew rates of  $0.15 \text{ V}\mu\text{s}^{-1}$  were recorded (Figure D.3a), limited by the INA2132 ( $0.1 \text{ V}\mu\text{s}^{-1}$  in the data sheet). The speed of the voltage step is deemed largely sufficient with regards to the frequency of the reading. Cross talks between two neighboring channels (using the same DAC, INA2132 and OPA2192) is shown in Figure D.3b. No significant perturbation of the voltage on the second channel was observed upon sudden voltage change in the first channel. Similarly, no significant perturbation in the sensing was observed (Figure D.3c)



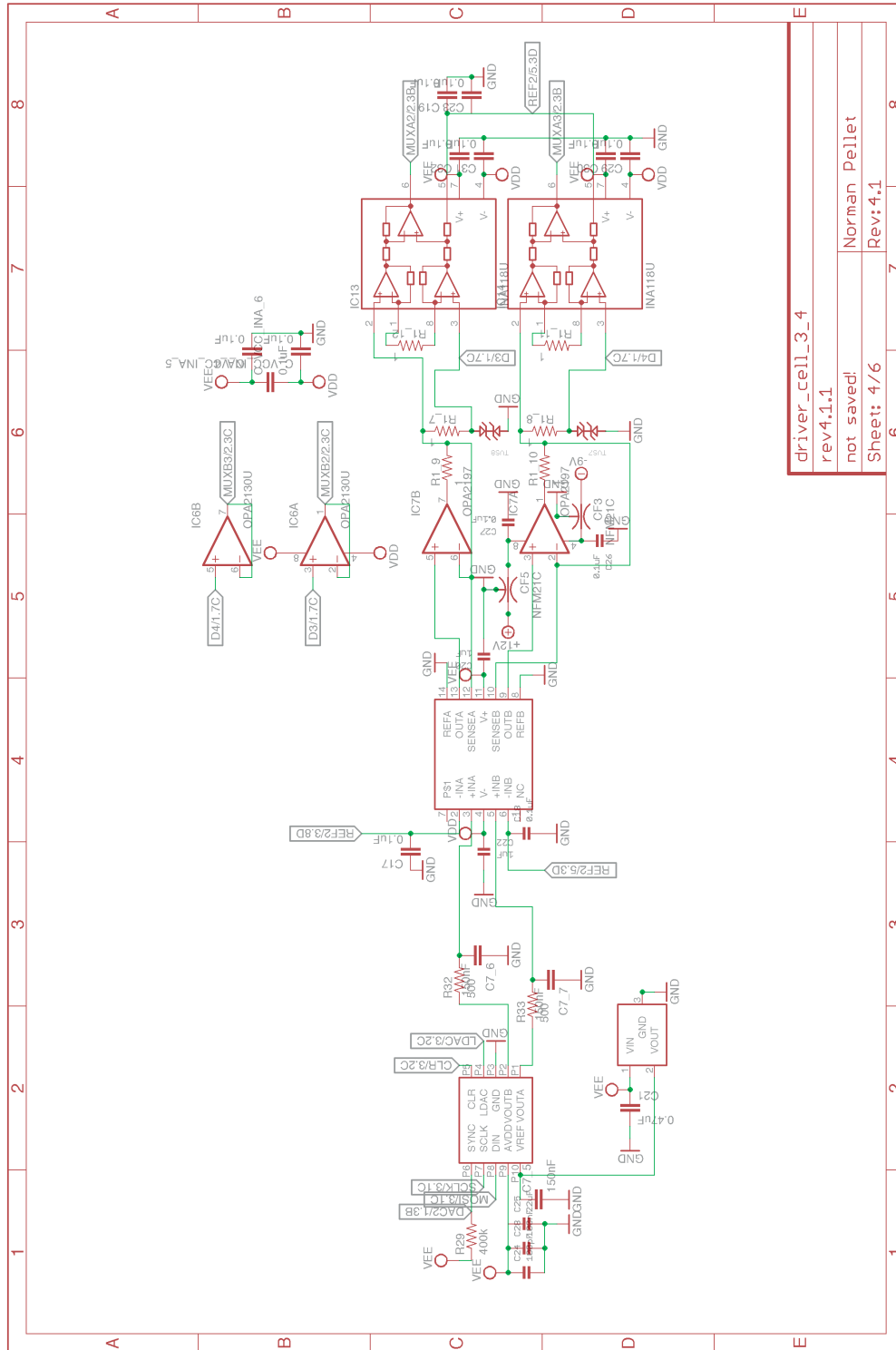
powersupply	
rev4.1.1	
not saved!	Norman Pellet
Sheet: 1/6	Rev: 4.1.1

Figure D.4: Schematics of the power block and digital signalisation



driver_cell_1_2	
rev4.1.1	
not saved!	
Sheet: 3/6	Rev: 4.1

Figure D.5: Schematics of the drive channels 1 and 2



driver_cell_3_4	
rev4.1.1	
not saved!	Norman Pellet
Sheet: 4/6	Rev: 4.1

Figure D.6: Schematics of the drive channels 3 and 4

# Appendix D. Design and assembly of the MPPT tracker

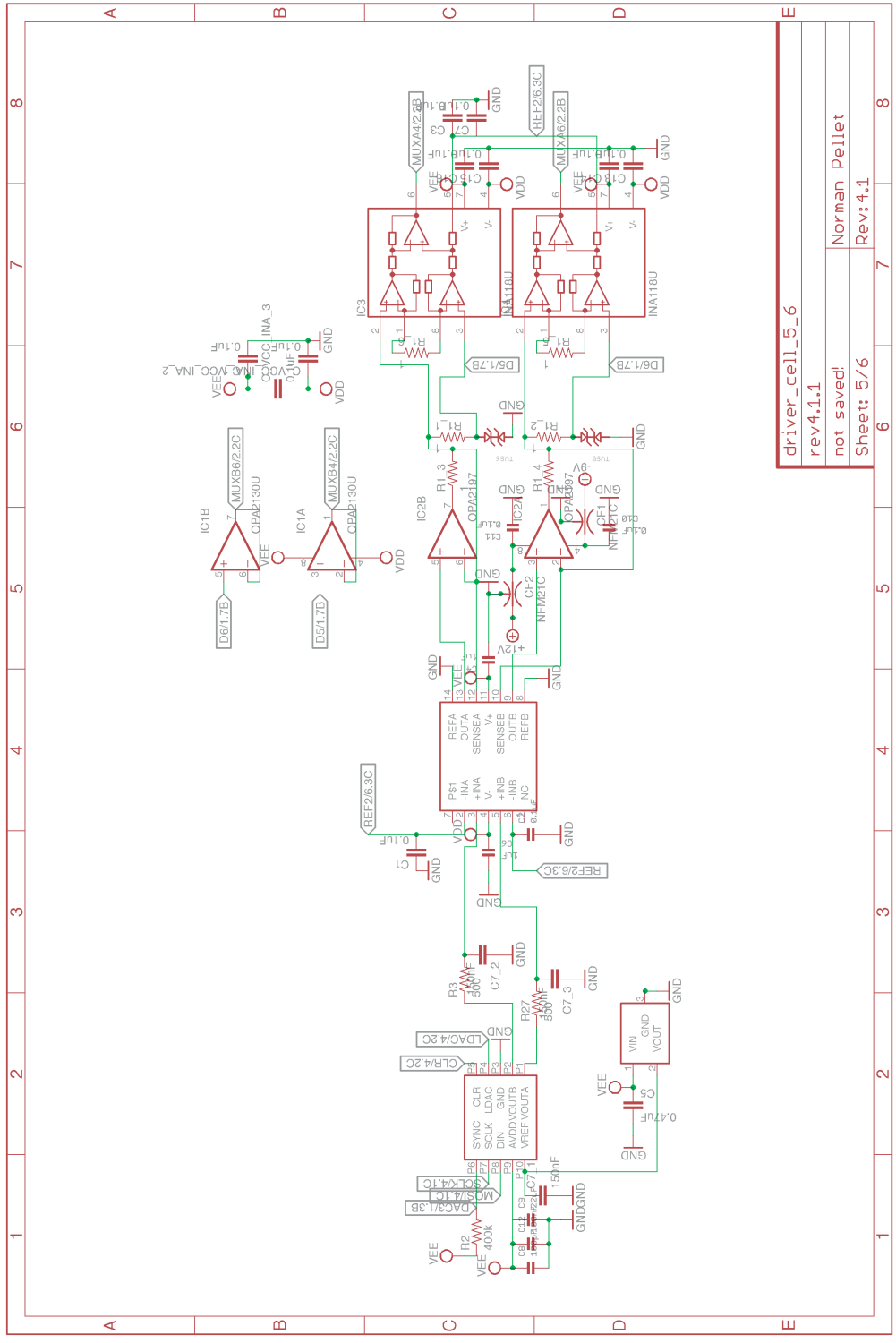
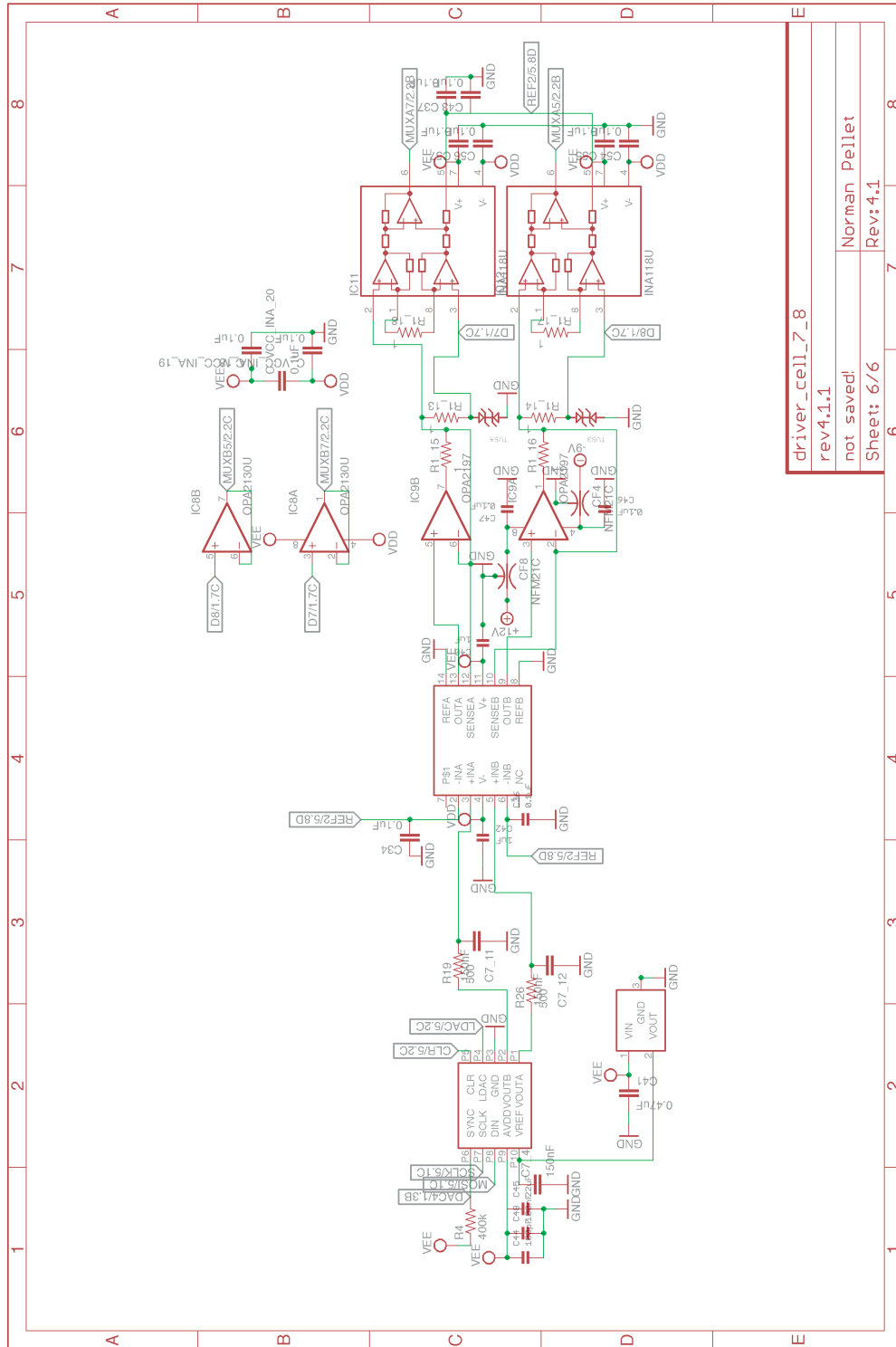


Figure D.7: Schematics of the drive channels 5 and 6



driver_cell_7_8	
rev4.1.1	
not saved	Norman Pellet
Sheet: 6/6	Rev: 4.1

Figure D.8: Schematics of the drive channels 7 and 8

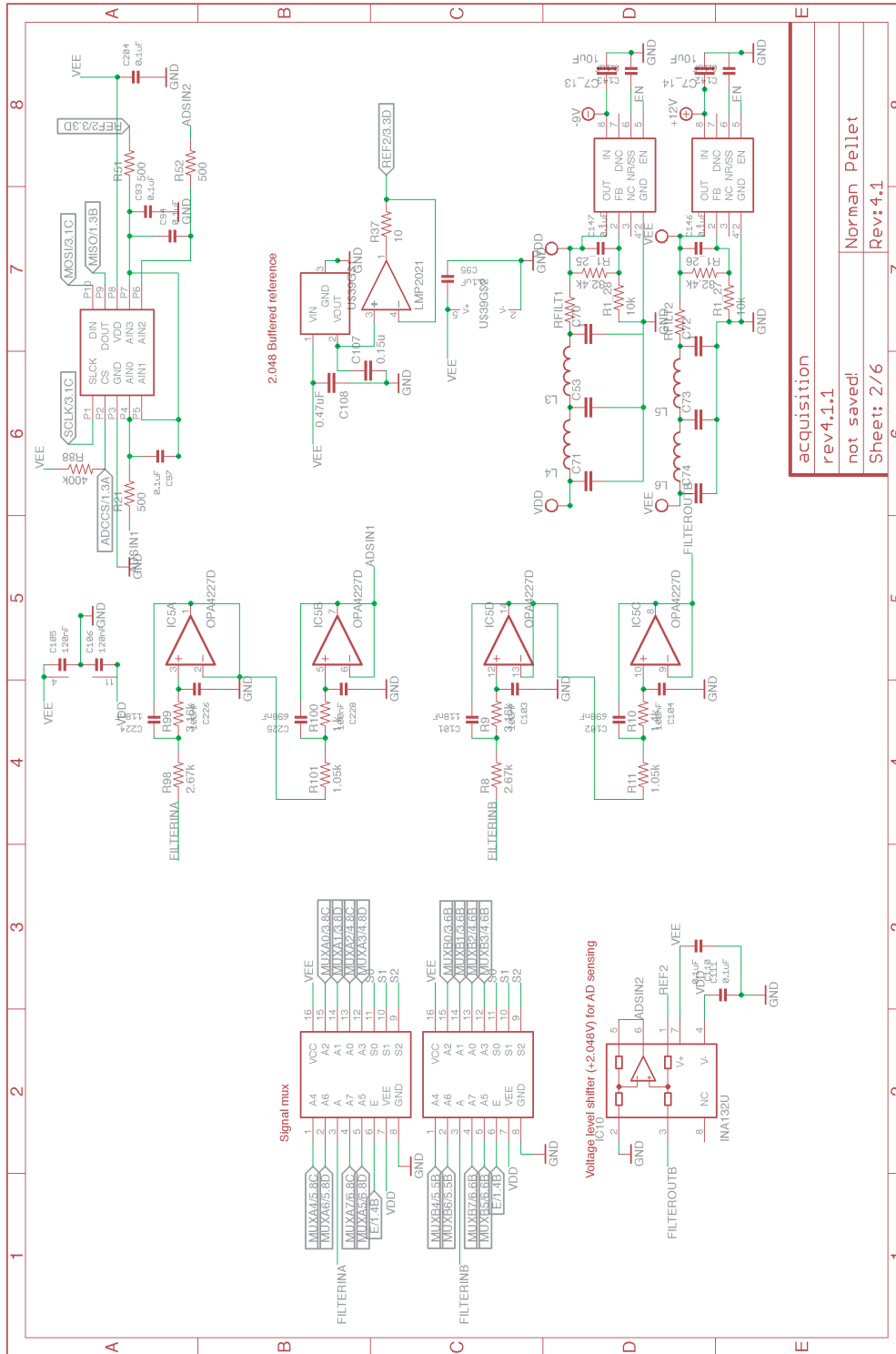


Figure D.9: Schematics of the multiplexed signal acquisition



Mouser No	Manufacturer	Desc.	Order Qty.
571-5520250-3	TE Connectivity	Modular Connectors / Ethernet Connectors 6/6 SIDE ENTRY	1
651-1757307	Phoenix Contact	Pluggable Terminal Blocks 8 Pos 5.08mm pitch Through Hole Header	2
595-TPS7A4901DGNR	Texas Instruments	LDO Voltage Regulators Vin 3-36V,150mA,High PSRR, LDO Reg	1
595-TPS7A3001DGNR	Texas Instruments	LDO Voltage Regulators - 3V to -36V,-200mA High PSRR, LDO Reg	1
490-P7805-Q24-S9-S	CUI Inc.	Non-Isolated DC/DC Converters dc-dc non-isolated, 0.5A, 11 32Vdc input, 9Vdc output, SIP	1
595-ADS1118IDGSR	Texas Instruments	Analog to Digital Converters - ADC 16B ADC w/Integrated MUX	1
926-LMP2021MFE/NOPB	Texas Instruments	Operational Amplifiers - Op Amps Zero Drift,Low Noise EMI Hardened Amp	1
667-ERJ-3EKF1001V	Panasonic	Thick Film Resistors - SMD 0603 1Kohms 1% AEC-Q200	2
755-ESR03EZPJ222	ROHM Semiconductor	Thick Film Resistors - SMD 0603 2K2ohm 5% Anti Surge AEC-Q200	1
667-ERJ-3GEYJ332V	Panasonic	Thick Film Resistors - SMD 0603 3.3Kohms 5% AEC-Q200	1
81-DLW5ATN501TQ2L	Murata	Common Mode Filters / Chokes 2000mA 5.0x3.6mm DCR0.040ohm+/-40%	1
651-1751163	Phoenix Contact	Fixed Terminal Blocks SPTA 1.5/2-5.08 2P 5.08MM	1

## Appendix D. Design and assembly of the MPPT tracker

---

595-CD74HC4051PWR	Texas Instruments	Multiplexer Switch ICs	2
595-DAC7563TDGSR	Texas Instruments	High Spd CMOS Analog Digital to Analog Converters - DAC 12bit Dual DAC with TTL IOs	4
595-INA2132UA	Texas Instruments	Differential Amplifiers	4
863-ESD9B5.0ST5G	ON Semiconductor	Dual Low Power Single-Supply TVS Diodes - Transient Voltage Suppressors BiDIRECTIONAL ESD PROTECTION	8
595-REF3020AIDBZT	Texas Instruments	Voltage References 2.048V 50ppm/DegC 50uA SOT23-3 Series	1
595-REF3040AIDBZT	Texas Instruments	Voltage References 4.096V 50ppm/DegC 50uA SOT23-3 Series	4
755-ESR03EZPJ100	ROHM Semiconductor	Thick Film Resistors - SMD 0603 10ohm 5% Anti Surge AEC-Q200	1
71-CRCW0402-100K-E3	Vishay	Thick Film Resistors - SMD 1/16watt 100Kohms 1%	1
667-ERJ-3EKF1051V	Panasonic	Thick Film Resistors - SMD 0603 1.05Kohms 1% AEC-Q200	2
652-CR0603FX-1401ELF	Bourns	Thick Film Resistors - SMD 1.4K 1% 1/10W	2
667-ERJ-3EKF3161V	Panasonic	Thick Film Resistors - SMD 0603 3.16Kohms 1% AEC-Q200	2
667-ERJ-3EKF2671V	Panasonic	Thick Film Resistors - SMD 0603 2.67Kohms 1% AEC-Q200	2
667-ERJ-3EKF4990V	Panasonic	Thick Film Resistors - SMD 0603 499ohms 1% AEC-Q200	11
71-CRCW0603-100K-E3	Vishay	Thick Film Resistors - SMD 1/10watt 100Kohms 1%	5

---

667-ERJ-3GEYJ103V	Panasonic	Thick Film Resistors - 2 SMD 0603 10Kohms 5% AEC-Q200
667-ERJ-3EKF3242V	Panasonic	Thick Film Resistors - 2 SMD 0603 32.4Kohms 1% AEC-Q200
71-CRCW0603-1-E3	Vishay	Thick Film Resistors - 2 SMD 1/10watt 1ohms 1%
667-ERJ-3GEY0R00V	Panasonic	Thick Film Resistors - 8 SMD 0603 Zero Ohms
667-ERA-3AEB2490V	Panasonic	Thin Film Resistors - 8 SMD 0603 249ohm 0.1% 25ppm
603-RL0603FR070R5L	Yageo	Current Sense Resistors 8 - SMD 0.500ohm 1% 1/10W
667-ERJ-3GEYJ331V	Panasonic	Thick Film Resistors - 17 SMD 0603 330ohms 5% AEC-Q200
621-2N7002K-7	Diodes Incorporated	MOSFET N-Channel 1
810-MLZ2012N220LT000	TDK	Fixed Inductors 22 UH 4 20%
963-CBC3225T220MR	Taiyo Yuden	Fixed Inductors 1210 3 22uH 351mOhms +/-20% 620mA
517-929974-01-15-RK	3M	Headers & Wire Housings 2 15 CON STR BRDMNT SKT
595-INA132UA/2K5	Texas Instruments	Differential Amplifiers 1 Low Pwr Single-Supply
595-OPA4227UA/2K5	Texas Instruments	Operational Amplifiers - 1 Op Amps High Prec Low Noise Oper Amplifier
595-INA188ID	Texas Instruments	Instrumentation Amplifiers 8 Hi-Sd Msmnt Cur- rent Shunt Mntr Crnt Otp
595-OPA2192IDR	Texas Instruments	Precision Amplifiers 36V 4 Precision Current Op Amp
595-OPA2188AIDR	Texas Instruments	Precision Amplifiers 4 LOW NOISE,RRO,36V ZERO-DRIFT OP AMP

## Appendix D. Design and assembly of the MPPT tracker

---

650-NANOC050F/13.2-2	TE Connectivity	Resettable Fuses - PPTC	1
		.5A 13.2V 100A I <sub>max</sub>	
625-SS26SHE3	Vishay	Schottky Diodes & Rectifiers	2
		2.0 Amp 60 Volt 40 Amp IFSM	
583-FM5819	Rectron	Schottky Diodes & Rectifiers	2
		V <sub>r</sub> /40V I <sub>o</sub> /1A T/R	
581-SMAJ12CA	AVX	TVS Diodes - Transient Voltage Suppressors	1
		12volts 400watts BiDirectional	
630-HSMG-C150	Broadcom Limited	Standard LEDs - SMD	1
		Green Diffused 572nm 8mcd	
630-HSMH-C150	Broadcom Limited	Standard LEDs - SMD	1
		Red Diffused 639nm 17mcd	
710-150120BS75000	Würth Electronics	Standard LEDs - SMD	2
		WL-SMCW SMD Mono TpVw Waterclr 1206 Blue	
81-NFM21CC222R1H3D	Murata	Feed Through Capacitors	8
		2200pF 50V 1A	
81-GRM155R61A684KE5D	Murata	Multilayer Ceramic Capacitors MLCC - SMD/SMT	2
		0402 0.68uF 10volts X5R 10%	
81-GRM155R60J124KE1D	Murata	Multilayer Ceramic Capacitors MLCC - SMD/SMT	4
		0.12uF 6.3Volts 10%	
710-885012205012	Würth Electronics	Multilayer Ceramic Capacitors MLCC - SMD/SMT	1
		WCAP-CSGP 10000pF 0402 10% 10V MLCC	
710-885012205055	Würth Electronics	Multilayer Ceramic Capacitors MLCC - SMD/SMT	4
		WCAP-CSGP 100pF 0402 10% 50V MLCC	

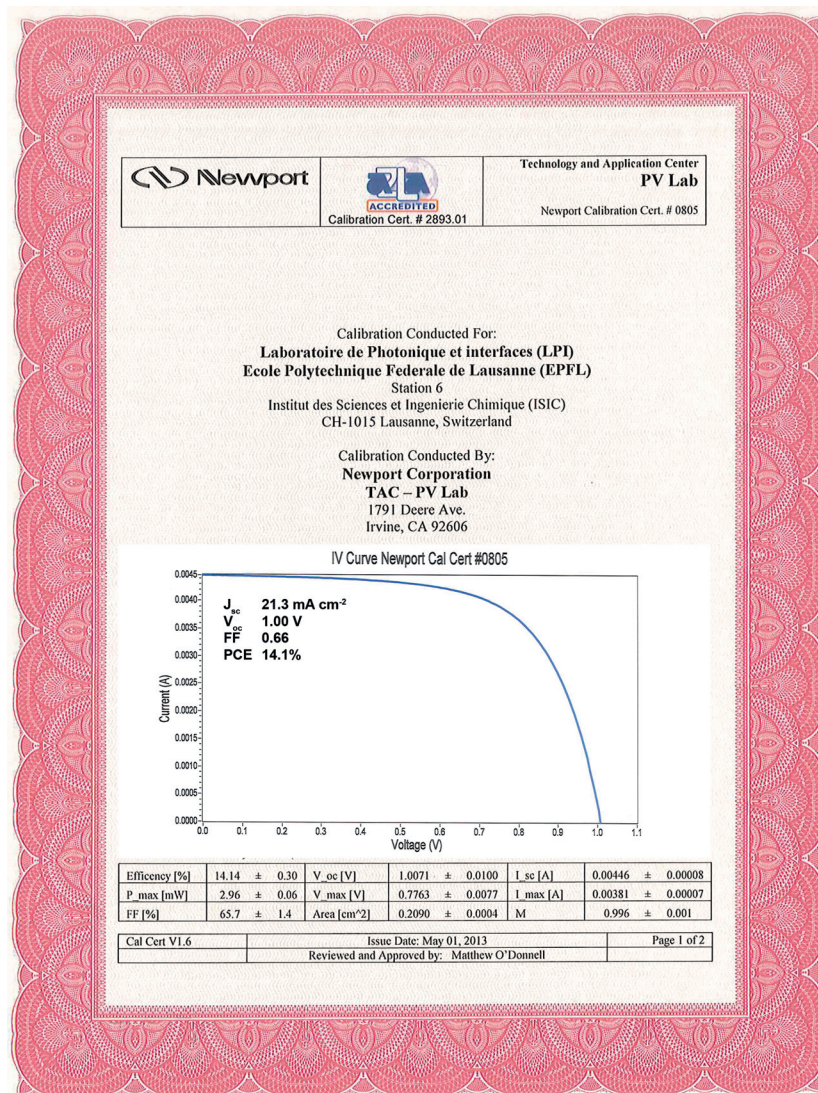
---

81-GRM21BR61C226ME4L	Murata	Multilayer Capacitors SMD/SMT	Ceramic MLCC 0805	17 - 22uF
				16volts X5R 20%
81-GRM155R61A474KE5D	Murata	Multilayer Capacitors SMD/SMT	Ceramic MLCC 0402	5 - 0.47uF
				10volts X5R 10%
81-GRM155R71C154KA2D	Murata	Multilayer Capacitors SMD/SMT	Ceramic MLCC 0402	14 - 0.15uF
				16volt X7R +/-10%
710-885012105018	Würth Electronics	Multilayer Capacitors SMD/SMT	Ceramic MLCC WCAP-CSGP	71 - 100000pF
				0402 20% 25V
667-EEE-1CA470WR	Panasonic	Aluminium Capacitors	Electrolytic - SMD	2 47uF
				16V

**Table D.1:** Bill of materials for a 8 channels board, exported from the Mouser supplier



# E Certificate of power conversion efficiency







# Acknowledgements

First of all I would like to thank my thesis director and supervisor, Prof. Michael Grätzel, for allowing me to perform my thesis in the laboratory of Photonics and Interfaces. Not only is Michael a accomplished scientist, he is also an excellent mentor, always ready to answer questions. Michael gave me total freedom in choosing the direction of my research and I am deeply grateful for that.

I also wish to thank my thesis co-director, Prof. Joachim Maier, for the scientific collaboration between the Max Planck Institute and EPFL. I am thankful for the knowledge and expertise that Prof. Maier and all the scientists and students at the Max Planck Institute have shared with me over those four years.

I am deeply grateful to all my colleagues at LPI for all the good times we have shared together and for supporting me scientifically throughout my thesis. In particular I would like to thank Julian, who introduced me to all the benefits of having barbecues and drinks after work. Not only was he a great friend, he was also a admirable scientific colleague. I must also not forget the memorable moments we had with Simon, Magda, Lauren and Tom. Life at LPI was definitely different after you left. I must also thank Fabrizio (and his really cool dog), for his amazing cooking skills and his knowledge on about everything relevant to solar cells; Marcel for our long and sometimes heated political discussions; Pascal for his expertise with the TiO<sub>2</sub> pastes and help with all of our outreach work; Paul for the laser etching of the substrates and for always having a solution to any problem; Thomas for his knowledge of impedance spectroscopy and who always managed to question my hypotheses; Aswani and Aravind, for our bowling nights and all the food they cooked; Amalie, who always shared the latest stories (scientific and not) with me; Marine, for pushing me to go climbing four times a week. I would like to address a very special thanks to Robin. He put me on the right scientific track and taught me all I needed to know about spectroscopy. I wouldn't be the same without him. I also would like to thank the team of the ISIC electronic workshop and mechanical workshop. Not only did they teach me a lot, they were always ready to fulfill my requests. Finally, I would like to acknowledge to Anders, Carole, Nazeer, Zakeer, Carmen, Heidi and Anne-Lene for all organizational matter and their assistance.

A final thanks to Jeannette, who proofread my thesis. She was the best support I could have hoped for.

Thank you all!



# Bibliography

- [1] International Energy Agency, “Key World Energy Statistics,” 2016.
- [2] Energimyndigheten Sweden, “Energiläget i siffror 2016,”
- [3] N. S. Lewis and D. G. Nocera, “Powering the planet: Chemical challenges in solar energy utilization,” *Proceedings of the National Academy of Sciences*, vol. 103, pp. 15729–15735, oct 2006.
- [4] International Energy Agency, “Snapshot of Global PV 1992–2014,” *Photovoltaic Power Systems Programme*, 2015.
- [5] J. Jean, P. R. Brown, R. L. Jaffe, T. Buonassisi, and V. Bulović, “Pathways for solar photovoltaics,” *Energy Environ. Sci.*, vol. 8, no. 4, pp. 1200–1219, 2015.
- [6] H. L. Wells, “Über die Cäsium- und Kalium-Bleihalogenide,” *Zeitschrift für anorganische Chemie*, vol. 3, no. 1, pp. 195–210, 1893.
- [7] C. K. MØLLER, “Crystal Structure and Photoconductivity of Cæsium Plumbohalides,” *Nature*, vol. 182, pp. 1436–1436, nov 1958.
- [8] J. L. Knutson, J. D. Martin, and D. B. Mitzi, “Tuning the band gap in hybrid tin iodide perovskite semiconductors using structural templating,” *Inorganic chemistry*, vol. 44, pp. 4699–705, jun 2005.
- [9] D. B. Mitzi and P. Brock, “Structure and optical properties of several organic-inorganic hybrids containing corner-sharing chains of bismuth iodide octahedra,” *Inorganic chemistry*, vol. 40, pp. 2096–104, apr 2001.
- [10] D. B. Mitzi, “Organic-inorganic perovskites containing trivalent metal halide layers: the templating influence of the organic cation layer,” *Inorganic chemistry*, vol. 39, pp. 6107–13, dec 2000.
- [11] K. Chondroudis and D. Mitzi, “Electroluminescence from an organic-inorganic perovskite incorporating a quaterthiophene dye within lead halide perovskite layers,” *Chemistry of materials*, vol. 11, pp. 3028–3030, nov 1999.

## Bibliography

---

- [12] D. B. Mitzi and K. Chondroudis, "Crystal Structure and Properties of Dye-Containing Organic-Inorganic Perovskites," *Molecular Crystals and Liquid Crystals Science and Technology. Section A. Molecular Crystals and Liquid Crystals*, vol. 356, pp. 549–558, feb 2001.
- [13] D. B. Mitzi, K. Chondroudis, and C. R. Kagan, "Design, Structure, and Optical Properties of Organic-Inorganic Perovskites Containing an Oligothiophene Chromophore.," *Inorganic chemistry*, vol. 38, pp. 6246–6256, dec 1999.
- [14] D. Mitzi, S. Wang, C. Feild, C. Chess, and A. Guloy, "Conducting layered organic-inorganic halides containing  $\langle 110 \rangle$ -oriented perovskite sheets," *Science*, vol. 267, pp. 1473–6, mar 1995.
- [15] D. B. Mitzi and K. Liang, "Preparation and Properties of  $(C_4H_9NH_3)_2EuI_4$ : A Luminescent Organic-Inorganic Perovskite with a Divalent Rare-Earth Metal Halide Framework," *Chemistry of Materials*, vol. 9, pp. 2990–2995, dec 1997.
- [16] K. Liang, D. B. Mitzi, and M. T. Prikas, "Synthesis and Characterization of Organic-Inorganic Perovskite Thin Films Prepared Using a Versatile Two-Step Dipping Technique," *Chemistry of Materials*, vol. 10, pp. 403–411, jan 1998.
- [17] Z. Xu, D. B. Mitzi, and D. R. Medeiros, " $[(CH_3)_3NCH_2CH_2NH_3]SnI_4$ : a layered perovskite with quaternary/primary ammonium dications and short interlayer iodine-iodine contacts.," *Inorganic chemistry*, vol. 42, pp. 1400–2, mar 2003.
- [18] D. B. Mitzi, "Thin-Film Deposition of Organic-Inorganic Hybrid Materials," *Chemistry of Materials*, vol. 13, pp. 3283–3298, oct 2001.
- [19] D. B. Mitzi, "Synthesis, Crystal Structure, and Optical and Thermal Properties of  $(C_4H_9NH_3)_2MI_4$  ( $M = Ge, Sn, Pb$ )," *Chemistry of Materials*, vol. 8, pp. 791–800, jan 1996.
- [20] Y. Lee, D. Mitzi, P. Barnes, and T. Vogt, "Pressure-induced phase transitions and templating effect in three-dimensional organic-inorganic hybrid perovskites," *Physical Review B*, vol. 68, p. 020103, jul 2003.
- [21] Z. Xu, D. B. Mitzi, C. D. Dimitrakopoulos, and K. R. Maxcy, "Semiconducting perovskites  $(2-XC_6H_4C_2H_4NH_3)_2SnI_4$  ( $X = F, Cl, Br$ ): steric interaction between the organic and inorganic layers.," *Inorganic chemistry*, vol. 42, pp. 2031–9, mar 2003.
- [22] D. Mitzi, "A Layered Solution Crystal Growth Technique and the Crystal Structure of  $(C_6H_5C_2H_4NH_3)_2PbCl_4$ ," *Journal of Solid State Chemistry*, vol. 145, pp. 694–704, jul 1999.
- [23] D. Mitzi and K. Liang, "Synthesis, Resistivity, and Thermal Properties of the Cubic Perovskite  $NH_2CH=NH_2SnI_3$  and Related Systems," *Journal of Solid State Chemistry*, vol. 134, pp. 376–381, dec 1997.

- [24] D. B. Mitzi, C. A. Feild, W. T. A. Harrison, and A. M. Guloy, "Conducting tin halides with a layered organic-based perovskite structure," *Nature*, vol. 369, pp. 467–469, jun 1994.
- [25] D. Mitzi, C. Dimitrakopoulos, J. Rosner, D. Medeiros, Z. Xu, and C. Noyan, "Hybrid Field-Effect Transistor Based on a Low-Temperature Melt-Processed Channel Layer," *Advanced Materials*, vol. 14, pp. 1772–1776, dec 2002.
- [26] S. Wang, D. B. Mitzi, C. A. Feild, and A. Guloy, "Synthesis and Characterization of [NH<sub>2</sub>C(I):NH<sub>2</sub>]<sub>3</sub>MI<sub>5</sub> (M = Sn, Pb): Stereochemical Activity in Divalent Tin and Lead Halides Containing Single .ltbbrac.110.rtbbrac. Perovskite Sheets," *Journal of the American Chemical Society*, vol. 117, pp. 5297–5302, may 1995.
- [27] D. B. Mitzi, "Synthesis, Structure, and Properties of Organic-Inorganic Perovskites and Related Materials," in *Progress in Inorganic Chemistry*, pp. 1–121, 2007.
- [28] K. Chondroudis and D. B. Mitzi, "The use of ionic salt dyes as amorphous, thermally stable emitting layers in organic light-emitting diodes," *Applied Physics Letters*, vol. 76, no. 1, p. 58, 2000.
- [29] D. B. Mitzi, C. D. Dimitrakopoulos, and L. L. Kosbar, "Structurally Tailored Organic-Inorganic Perovskites: Optical Properties and Solution-Processed Channel Materials for Thin-Film Transistors," *Chemistry of Materials*, vol. 13, pp. 3728–3740, oct 2001.
- [30] K. Chondroudis, D. B. Mitzi, and P. Brock, "Effect of Thermal Annealing on the Optical and Morphological Properties of (AETH)PbX<sub>4</sub> (X = Br, I) Perovskite Films Prepared Using Single Source Thermal Ablation," *Chemistry of Materials*, vol. 12, pp. 169–175, jan 2000.
- [31] D. Mitzi, C. Feild, Z. Schlesinger, and R. Laibowitz, "Transport, Optical, and Magnetic Properties of the Conducting Halide Perovskite CH<sub>3</sub>NH<sub>3</sub>SnI<sub>3</sub>," *Journal of Solid State Chemistry*, vol. 114, pp. 159–163, jan 1995.
- [32] K. R. Maxcy, R. D. Willett, D. B. Mitzi, and A. Afzali, "Tetrakis[(9-oxo-10-thioxanthene-2-yloxyethyl)ammonium] decaiodotriplumbate(II)," *Acta Crystallographica Section E Structure Reports Online*, vol. 59, pp. m364–m366, may 2003.
- [33] M. Grätzel, "The light and shade of perovskite solar cells," *Nature Materials*, vol. 13, pp. 838–842, aug 2014.
- [34] C. C. Stoumpos, C. D. Malliakas, and M. G. Kanatzidis, "Semiconducting tin and lead iodide perovskites with organic cations: phase transitions, high mobilities, and near-infrared photoluminescent properties.," *Inorganic chemistry*, vol. 52, pp. 9019–38, aug 2013.
- [35] T. Baikie, Y. Fang, J. M. Kadro, M. Schreyer, F. Wei, S. G. Mhaisalkar, M. Graetzel, and T. J. White, "Synthesis and crystal chemistry of the hybrid perovskite (CH<sub>3</sub>NH<sub>3</sub>)PbI<sub>3</sub> for solid-state sensitised solar cell applications," *Journal of Materials Chemistry A*, vol. 1, no. 18, p. 5628, 2013.

## Bibliography

---

- [36] G. Xing, N. Mathews, S. Sun, S. S. Lim, Y. M. Lam, M. Graetzel, S. Mhaisalkar, T. C. Sum, and M. Grätzel, “Long-range balanced electron- and hole-transport lengths in organic-inorganic  $\text{CH}_3\text{NH}_3\text{PbI}_3$ ,” *Science (New York, N.Y.)*, vol. 342, pp. 344–7, oct 2013.
- [37] S. D. Stranks, G. E. Eperon, G. Grancini, C. Menelaou, M. J. P. Alcocer, T. Leijtens, L. M. Herz, A. Petrozza, and H. J. Snaith, “Electron-hole diffusion lengths exceeding 1 micrometer in an organometal trihalide perovskite absorber,” *Science (New York, N.Y.)*, vol. 342, pp. 341–4, oct 2013.
- [38] Y. Zhao, A. M. Nardes, and K. Zhu, “Solid-State Mesostructured Perovskite  $\text{CH}_3\text{NH}_3\text{PbI}_3$  Solar Cells: Charge Transport, Recombination, and Diffusion Length,” *The Journal of Physical Chemistry Letters*, p. 140120101155009, jan 2014.
- [39] C. S. Ponseca, T. J. Savenije, M. Abdellah, K. Zheng, A. Yartsev, T. Pascher, T. Harlang, P. Chabera, T. Pullerits, A. Stepanov, J.-P. Wolf, and V. Sundström, “Organometal Halide Perovskite Solar Cell Materials Rationalized: Ultrafast Charge Generation, High and Microsecond-Long Balanced Mobilities, and Slow Recombination,” *Journal of the American Chemical Society*, vol. 136, pp. 5189–5192, apr 2014.
- [40] A. Kojima, K. Teshima, Y. Shirai, and T. Miyasaka, “Organometal halide perovskites as visible-light sensitizers for photovoltaic cells,” *Journal of the American Chemical Society*, vol. 131, pp. 6050–1, may 2009.
- [41] B. O’Regan and M. Grätzel, “A low-cost, high-efficiency solar cell based on dye-sensitized colloidal  $\text{TiO}_2$  films,” *Nature*, vol. 353, pp. 737–740, oct 1991.
- [42] J.-H. Im, C.-R. Lee, J.-W. Lee, S.-W. Park, and N.-G. Park, “6.5% efficient perovskite quantum-dot-sensitized solar cell,” *Nanoscale*, vol. 3, pp. 4088–93, oct 2011.
- [43] I. Chung, B. Lee, J. He, R. P. H. Chang, and M. G. Kanatzidis, “All-solid-state dye-sensitized solar cells with high efficiency,” *Nature*, vol. 485, pp. 486–489, may 2012.
- [44] H.-S. Kim, C.-R. Lee, J.-H. Im, K.-B. Lee, T. Moehl, A. Marchioro, S.-J. Moon, R. Humphry-Baker, J.-H. Yum, J. E. Moser, M. Grätzel, and N.-G. Park, “Lead iodide perovskite sensitized all-solid-state submicron thin film mesoscopic solar cell with efficiency exceeding 9%,” *Scientific reports*, vol. 2, p. 591, jan 2012.
- [45] M. M. Lee, J. Teuscher, T. Miyasaka, T. N. Murakami, and H. J. Snaith, “Efficient hybrid solar cells based on meso-superstructured organometal halide perovskites,” *Science (New York, N.Y.)*, vol. 338, pp. 643–7, nov 2012.
- [46] U. Bach, D. Lupo, P. Comte, J. E. Moser, F. Weissörtel, J. Salbeck, H. Spreitzer, and M. Grätzel, “Solid-state dye-sensitized mesoporous  $\text{TiO}_2$  solar cells with high photon-to-electron conversion efficiencies,” *Nature*, vol. 395, pp. 583–585, oct 1998.
- [47] J. Burschka, N. Pellet, S.-J. Moon, R. Humphry-Baker, P. Gao, M. K. Nazeeruddin, and M. Grätzel, “Sequential deposition as a route to high-performance perovskite-sensitized solar cells,” *Nature*, vol. 499, pp. 316–9, jul 2013.

- [48] P. Qin, S. Tanaka, S. Ito, N. Tetreault, K. Manabe, H. Nishino, M. K. Nazeeruddin, and M. Grätzel, "Inorganic hole conductor-based lead halide perovskite solar cells with 12.4% conversion efficiency," *Nature Communications*, vol. 5, may 2014.
- [49] S. Chavhan, O. Miguel, H.-J. Grande, V. Gonzalez-Pedro, R. S. Sánchez, E. M. Barea, I. Mora-Seró, and R. Tena-Zaera, "Organo-metal halide perovskite-based solar cells with CuSCN as the inorganic hole selective contact," *Journal of Materials Chemistry A*, vol. 2, p. 12754, jun 2014.
- [50] J. W. Jung, C.-C. Chueh, and A. K.-Y. Jen, "High-Performance Semitransparent Perovskite Solar Cells with 10% Power Conversion Efficiency and 25% Average Visible Transmittance Based on Transparent CuSCN as the Hole-Transporting Material," *Advanced Energy Materials*, vol. 5, p. 1500486, sep 2015.
- [51] S. Ye, W. Sun, Y. Li, W. Yan, H. Peng, Z. Bian, Z. Liu, and C. Huang, "CuSCN-Based Inverted Planar Perovskite Solar Cell with an Average PCE of 15.6%," *Nano Letters*, vol. 15, pp. 3723–3728, jun 2015.
- [52] J. H. Heo, S. H. Im, J. H. Noh, T. N. Mandal, C.-s. Lim, J. A. Chang, Y. H. Lee, H.-j. Kim, A. Sarkar, M. K. Nazeeruddin, M. Grätzel, and S. I. Seok, "Efficient inorganic–organic hybrid heterojunction solar cells containing perovskite compound and polymeric hole conductors," *Nature Photonics*, vol. 7, pp. 486–491, may 2013.
- [53] S. Ryu, J. H. Noh, N. J. Jeon, Y. Chan Kim, W. S. Yang, J. Seo, and S. I. Seok, "Voltage output of efficient perovskite solar cells with high open-circuit voltage and fill factor," *Energy & Environmental Science*, vol. 7, p. 2614, jun 2014.
- [54] N. J. Jeon, J. H. Noh, Y. C. Kim, W. S. Yang, S. Ryu, and S. I. Seok, "Solvent engineering for high-performance inorganic-organic hybrid perovskite solar cells.," *Nature materials*, jul 2014.
- [55] NREL, "Best Research-Cell Efficiencies," 2017.
- [56] A. Yella, L.-P. Heiniger, P. Gao, M. K. Nazeeruddin, and M. Grätzel, "Nanocrystalline rutile electron extraction layer enables low-temperature solution processed perovskite photovoltaics with 13.7% efficiency.," *Nano letters*, vol. 14, pp. 2591–6, may 2014.
- [57] M. Liu, M. B. Johnston, and H. J. Snaith, "Efficient planar heterojunction perovskite solar cells by vapour deposition.," *Nature*, vol. 501, pp. 395–8, sep 2013.
- [58] C. Roldán-Carmona, O. Malinkiewicz, A. Soriano, G. Mínguez Espallargas, A. Garcia, P. Reinecke, T. Kroyer, M. I. Dar, M. K. Nazeeruddin, and H. J. Bolink, "Flexible high efficiency perovskite solar cells," *Energy & Environmental Science*, vol. 7, no. 3, p. 994, 2014.
- [59] D. Liu and T. L. Kelly, "Perovskite solar cells with a planar heterojunction structure prepared using room-temperature solution processing techniques," *Nature Photonics*, vol. 8, pp. 133–138, dec 2013.

## Bibliography

---

- [60] Q. Chen, H. Zhou, Z. Hong, S. Luo, H.-S. Duan, H.-H. Wang, Y. Liu, G. Li, and Y. Yang, "Planar Heterojunction Perovskite Solar Cells via Vapor-Assisted Solution Process," *Journal of the American Chemical Society*, vol. 136, pp. 622–625, jan 2014.
- [61] E. H. Anaraki, A. Kermanpur, L. Steier, K. Domanski, T. Matsui, W. Tress, M. Saliba, A. Abate, M. Grätzel, A. Hagfeldt, and J.-P. Correa-Baena, "Highly efficient and stable planar perovskite solar cells by solution-processed tin oxide," *Energy Environ. Sci.*, vol. 9, no. 10, pp. 3128–3134, 2016.
- [62] J. P. Correa Baena, L. Steier, W. Tress, M. Saliba, S. Neutzner, T. Matsui, F. Giordano, T. J. Jacobsson, A. R. Srimath Kandada, S. M. Zakeeruddin, A. Petrozza, A. Abate, M. K. Nazeeruddin, M. Grätzel, and A. Hagfeldt, "Highly efficient planar perovskite solar cells through band alignment engineering," *Energy Environ. Sci.*, vol. 8, no. 10, pp. 2928–2934, 2015.
- [63] T.-Y. Yang, G. Gregori, N. Pellet, M. Grätzel, and J. Maier, "The Significance of Ion Conduction in a Hybrid Organic-Inorganic Lead-Iodide-Based Perovskite Photosensitizer," *Angewandte Chemie International Edition*, vol. 54, pp. 7905–7910, jun 2015.
- [64] E. L. Unger, E. T. Hoke, C. D. Bailie, W. H. Nguyen, A. R. Bowering, T. Heumüller, M. G. Christoforo, and M. D. McGehee, "Hysteresis and transient behavior in current–voltage measurements of hybrid-perovskite absorber solar cells," *Energy Environ. Sci.*, vol. 7, pp. 3690–3698, aug 2014.
- [65] L. Kavan, N. Tétreault, T. Moehl, and M. Grätzel, "Electrochemical Characterization of TiO<sub>2</sub> Blocking Layers for Dye-Sensitized Solar Cells," *The Journal of Physical Chemistry C*, vol. 118, pp. 16408–16418, jul 2014.
- [66] Y. Wu, X. Yang, H. Chen, K. Zhang, C. Qin, J. Liu, W. Peng, A. Islam, E. Bi, F. Ye, M. Yin, P. Zhang, and L. Han, "Highly compact TiO<sub>2</sub> layer for efficient hole-blocking in perovskite solar cells," *Applied Physics Express*, vol. 7, p. 052301, may 2014.
- [67] W. Ke, G. Fang, J. Wan, H. Tao, Q. Liu, L. Xiong, P. Qin, J. Wang, H. Lei, G. Yang, M. Qin, X. Zhao, and Y. Yan, "Efficient hole-blocking layer-free planar halide perovskite thin-film solar cells," *Nature Communications*, vol. 6, p. 6700, mar 2015.
- [68] A. K. Chandiran, A. Yella, M. T. Mayer, P. Gao, M. K. Nazeeruddin, and M. Grätzel, "Sub-Nanometer Conformal TiO<sub>2</sub> Blocking Layer for High Efficiency Solid-State Perovskite Absorber Solar Cells," *Advanced Materials*, vol. 26, pp. 4309–4312, jul 2014.
- [69] D. Bi, W. Tress, M. I. Dar, P. Gao, J. Luo, C. Renevier, K. Schenk, A. Abate, F. Giordano, J.-P. Correa Baena, J.-D. Decoppet, S. M. Zakeeruddin, M. K. Nazeeruddin, M. Grätzel, and A. Hagfeldt, "Efficient luminescent solar cells based on tailored mixed-cation perovskites," *Science Advances*, vol. 2, pp. e1501170–e1501170, jan 2016.



- [70] A. Yella, L.-P. Heiniger, P. Gao, M. K. Nazeeruddin, and M. Grätzel, "Nanocrystalline Rutile Electron Extraction Layer Enables Low-Temperature Solution Processed Perovskite Photovoltaics with 13.7% Efficiency," *Nano Letters*, vol. 14, pp. 2591–2596, may 2014.
- [71] J.-W. Lee, T.-Y. Lee, P. J. Yoo, M. Grätzel, S. Mhaisalkar, and N.-G. Park, "Rutile TiO<sub>2</sub>-based perovskite solar cells," *Journal of Materials Chemistry A*, vol. 2, no. 24, p. 9251, 2014.
- [72] H.-S. Kim, J.-W. Lee, N. Yantara, P. P. Boix, S. A. Kulkarni, S. Mhaisalkar, M. Grätzel, and N.-G. Park, "High Efficiency Solid-State Sensitized Solar Cell-Based on Submicrometer Rutile TiO<sub>2</sub> Nanorod and CH<sub>3</sub>NH<sub>3</sub>PbI<sub>3</sub> Perovskite Sensitizer," *Nano Letters*, vol. 13, pp. 2412–2417, jun 2013.
- [73] D.-Y. Son, J.-H. Im, H.-S. Kim, and N.-G. Park, "11% Efficient Perovskite Solar Cell Based on ZnO Nanorods: An Effective Charge Collection System," *The Journal of Physical Chemistry C*, vol. 118, pp. 16567–16573, jul 2014.
- [74] M. H. Kumar, N. Yantara, S. Dharani, M. Graetzel, S. Mhaisalkar, P. P. Boix, and N. Mathews, "Flexible, low-temperature, solution processed ZnO-based perovskite solid state solar cells," *Chemical Communications*, vol. 49, no. 94, p. 11089, 2013.
- [75] D. Bi, S.-J. Moon, L. Häggman, G. Boschloo, L. Yang, E. M. J. Johansson, M. K. Nazeeruddin, M. Grätzel, and A. Hagfeldt, "Using a two-step deposition technique to prepare perovskite (CH<sub>3</sub>NH<sub>3</sub>PbI<sub>3</sub>) for thin film solar cells based on ZrO<sub>2</sub> and TiO<sub>2</sub> mesostructures," *RSC Advances*, vol. 3, no. 41, p. 18762, 2013.
- [76] M. A. Green, A. Ho-Baillie, and H. J. Snaith, "The emergence of perovskite solar cells," *Nature Photonics*, vol. 8, pp. 506–514, jun 2014.
- [77] S. D. Stranks and H. J. Snaith, "Metal-halide perovskites for photovoltaic and light-emitting devices," *Nature Nanotechnology*, vol. 10, pp. 391–402, may 2015.
- [78] J.-H. Im, H.-S. Kim, and N.-G. Park, "Morphology-photovoltaic property correlation in perovskite solar cells: One-step versus two-step deposition of CH<sub>3</sub>NH<sub>3</sub>PbI<sub>3</sub>," *APL Materials*, vol. 2, p. 081510, aug 2014.
- [79] G. Grancini, S. Marras, M. Prato, C. Giannini, C. Quarti, F. De Angelis, M. De Bastiani, G. E. Eperon, H. J. Snaith, L. Manna, and A. Petrozza, "The Impact of the Crystallization Processes on the Structural and Optical Properties of Hybrid Perovskite Films for Photovoltaics," *The Journal of Physical Chemistry Letters*, vol. 5, pp. 3836–3842, nov 2014.
- [80] M. I. Dar, N. Arora, P. Gao, S. Ahmad, M. Grätzel, and M. K. Nazeeruddin, "Investigation Regarding the Role of Chloride in Organic–Inorganic Halide Perovskites Obtained from Chloride Containing Precursors," *Nano Letters*, vol. 14, pp. 6991–6996, dec 2014.
- [81] N. Pellet, J. Teuscher, J. Maier, and M. Grätzel, "Transforming Hybrid Organic Inorganic Perovskites by Rapid Halide Exchange," *Chemistry of Materials*, vol. 27, pp. 2181–2188, mar 2015.

## Bibliography

---

- [82] J.-H. Im, I.-H. Jang, N. Pellet, M. Grätzel, and N.-G. Park, "Growth of CH<sub>3</sub>NH<sub>3</sub>PbI<sub>3</sub> cuboids with controlled size for high-efficiency perovskite solar cells.," *Nature nanotechnology*, aug 2014.
- [83] M. R. Leyden, L. K. Ono, S. R. Raga, Y. Kato, S. Wang, and Y. Qi, "High performance perovskite solar cells by hybrid chemical vapor deposition," *J. Mater. Chem. A*, vol. 2, no. 44, pp. 18742–18745, 2014.
- [84] H. Zhou, Q. Chen, and Y. Yang, "Vapor-assisted solution process for perovskite materials and solar cells," *MRS Bulletin*, vol. 40, pp. 667–673, aug 2015.
- [85] O. Malinkiewicz, A. Yella, Y. H. Lee, G. M. Espallargas, M. Graetzel, M. K. Nazeeruddin, and H. J. Bolink, "Perovskite solar cells employing organic charge-transport layers," *Nature Photonics*, vol. 8, pp. 128–132, dec 2013.
- [86] M. Liu, M. B. Johnston, and H. J. Snaith, "Efficient planar heterojunction perovskite solar cells by vapour deposition.," *Nature*, vol. 501, pp. 395–8, sep 2013.
- [87] C. Momblona, O. Malinkiewicz, C. Roldán-Carmona, A. Soriano, L. Gil-Escrig, E. Bandiello, M. Scheepers, E. Edri, and H. J. Bolink, "Efficient methylammonium lead iodide perovskite solar cells with active layers from 300 to 900 nm," *APL Materials*, vol. 2, p. 081504, aug 2014.
- [88] J. Teuscher, A. Ulianov, O. Müntener, M. Grätzel, and N. Tétreault, "Control and Study of the Stoichiometry in Evaporated Perovskite Solar Cells," *ChemSusChem*, vol. 8, pp. 3847–3852, nov 2015.
- [89] C. Gao, J. Liu, C. Liao, Q. Ye, Y. Zhang, X. He, X. Guo, J. Mei, and W. Lau, "Formation of organic–inorganic mixed halide perovskite films by thermal evaporation of PbCl<sub>2</sub> and CH<sub>3</sub>NH<sub>3</sub>I compounds," *RSC Adv.*, vol. 5, no. 33, pp. 26175–26180, 2015.
- [90] G.-X. Liang, P. Fan, J.-T. Luo, D. Gu, and Z.-H. Zheng, "A promising unisource thermal evaporation for in situ fabrication of organolead halide perovskite CH<sub>3</sub>NH<sub>3</sub>PbI<sub>3</sub> thin film," *Progress in Photovoltaics: Research and Applications*, vol. 23, pp. 1901–1907, dec 2015.
- [91] G. Longo, L. Gil-Escrig, M. J. Degen, M. Sessolo, and H. J. Bolink, "Perovskite solar cells prepared by flash evaporation," *Chem. Commun.*, vol. 51, no. 34, pp. 7376–7378, 2015.
- [92] X. Li, D. Bi, C. Yi, J.-D. Decoppet, J. Luo, S. M. Zakeeruddin, A. Hagfeldt, and M. Gratzel, "A vacuum flash-assisted solution process for high-efficiency large-area perovskite solar cells," *Science*, jun 2016.
- [93] G. E. Eperon, S. D. Stranks, C. Menelaou, M. B. Johnston, L. M. Herz, and H. J. Snaith, "Formamidinium lead trihalide: a broadly tunable perovskite for efficient planar heterojunction solar cells," *Energy & Environmental Science*, vol. 7, no. 3, p. 982, 2014.

- [94] J. H. Noh, S. H. Im, J. H. Heo, T. N. Mandal, and S. I. Seok, "Chemical management for colorful, efficient, and stable inorganic-organic hybrid nanostructured solar cells.," *Nano letters*, vol. 13, pp. 1764–9, apr 2013.
- [95] S. A. Kulkarni, T. Baikie, P. P. Boix, N. Yantara, N. Mathews, and S. Mhaisalkar, "Band-gap tuning of lead halide perovskites using a sequential deposition process," *J. Mater. Chem. A*, vol. 2, pp. 9221–9225, mar 2014.
- [96] G. Xing, N. Mathews, S. S. Lim, N. Yantara, X. Liu, D. Sabba, M. Grätzel, S. Mhaisalkar, and T. C. Sum, "Low-temperature solution-processed wavelength-tunable perovskites for lasing.," *Nature materials*, vol. 13, pp. 476–80, may 2014.
- [97] E. T. Hoke, D. J. Slotcavage, E. R. Dohner, A. R. Bowring, H. I. Karunadasa, and M. D. McGehee, "Reversible photo-induced trap formation in mixed-halide hybrid perovskites for photovoltaics," *Chem. Sci.*, vol. 6, no. 1, pp. 613–617, 2015.
- [98] J. H. Kim, P.-W. Liang, S. T. Williams, N. Cho, C.-C. Chueh, M. S. Glaz, D. S. Ginger, and A. K.-Y. Jen, "High-Performance and Environmentally Stable Planar Heterojunction Perovskite Solar Cells Based on a Solution-Processed Copper-Doped Nickel Oxide Hole-Transporting Layer," *Advanced Materials*, vol. 27, pp. 695–701, jan 2015.
- [99] N. Pellet, P. Gao, G. Gregori, T.-Y. Yang, M. K. Nazeeruddin, J. Maier, and M. Grätzel, "Mixed-organic-cation perovskite photovoltaics for enhanced solar-light harvesting.," *Angewandte Chemie (International ed. in English)*, vol. 53, pp. 3151–7, mar 2014.
- [100] M. Saliba, T. Matsui, J.-Y. Seo, K. Domanski, J.-P. Correa-Baena, M. K. Nazeeruddin, S. M. Zakeeruddin, W. Tress, A. Abate, A. Hagfeldt, and M. Grätzel, "Cesium-containing triple cation perovskite solar cells: improved stability, reproducibility and high efficiency," *Energy Environ. Sci.*, 2016.
- [101] R. J. Sutton, G. E. Eperon, L. Miranda, E. S. Parrott, B. A. Kamino, J. B. Patel, M. T. Hörantner, M. B. Johnston, A. A. Haghighirad, D. T. Moore, and H. J. Snaith, "Bandgap-Tunable Cesium Lead Halide Perovskites with High Thermal Stability for Efficient Solar Cells," *Advanced Energy Materials*, vol. 6, apr 2016.
- [102] Z. Li, M. Yang, J.-S. Park, S.-H. Wei, J. J. Berry, and K. Zhu, "Stabilizing Perovskite Structures by Tuning Tolerance Factor: Formation of Formamidinium and Cesium Lead Iodide Solid-State Alloys," *Chemistry of Materials*, vol. 28, pp. 284–292, jan 2016.
- [103] J. Burschka, *High performance solid-state mesoscopic solar cells*. PhD thesis, 2013.
- [104] H. J. Snaith and M. Grätzel, "Enhanced charge mobility in a molecular hole transporter via addition of redox inactive ionic dopant: Implication to dye-sensitized solar cells," *Applied Physics Letters*, vol. 89, p. 262114, dec 2006.
- [105] R. Schölin, M. H. Karlsson, S. K. Eriksson, H. Siegbahn, E. M. J. Johansson, and H. Rensmo, "Energy Level Shifts in Spiro-OMeTAD Molecular Thin Films When Adding Li-TFSI," *The Journal of Physical Chemistry C*, vol. 116, pp. 26300–26305, dec 2012.

## Bibliography

---

- [106] U. B. Cappel, T. Daeneke, and U. Bach, "Oxygen-Induced Doping of Spiro-MeOTAD in Solid-State Dye-Sensitized Solar Cells and Its Impact on Device Performance," *Nano Letters*, vol. 12, pp. 4925–4931, sep 2012.
- [107] A. Abate, T. Leijtens, S. Pathak, J. Teuscher, R. Avolio, M. E. Errico, J. Kirkpatrick, J. M. Ball, P. Docampo, I. McPherson, and H. J. Snaith, "Lithium salts as "redox active" p-type dopants for organic semiconductors and their impact in solid-state dye-sensitized solar cells," *Physical Chemistry Chemical Physics*, vol. 15, no. 7, p. 2572, 2013.
- [108] C. D. Bailie, M. G. Christoforo, J. P. Mailoa, A. R. Bowring, E. L. Unger, W. H. Nguyen, J. Burschka, N. Pellet, J. Z. Lee, M. Grätzel, R. Noufi, T. Buonassisi, A. Salleo, and M. D. McGehee, "Semi-transparent perovskite solar cells for tandems with silicon and CIGS," *Energy Environ. Sci.*, vol. 8, no. 3, pp. 956–963, 2015.
- [109] J. Jang, H.-G. Im, J. Jin, J. Lee, J.-Y. Lee, and B.-S. Bae, "A Flexible and Robust Transparent Conducting Electrode Platform Using an Electroplated Silver Grid/Surface-Embedded Silver Nanowire Hybrid Structure," *ACS Applied Materials & Interfaces*, vol. 8, pp. 27035–27043, oct 2016.
- [110] J. Werner, C.-H. Weng, A. Walter, L. Fesquet, J. P. Seif, S. De Wolf, B. Niesen, and C. Ballif, "Efficient Monolithic Perovskite/Silicon Tandem Solar Cell with Cell Area >1 cm<sup>2</sup>," *The Journal of Physical Chemistry Letters*, vol. 7, pp. 161–166, jan 2016.
- [111] P. Löper, S.-J. Moon, S. Martín de Nicolas, B. Niesen, M. Ledinsky, S. Nicolay, J. Bailat, J.-H. Yum, S. De Wolf, and C. Ballif, "Organic–inorganic halide perovskite/crystalline silicon four-terminal tandem solar cells," *Phys. Chem. Chem. Phys.*, vol. 17, no. 3, pp. 1619–1629, 2015.
- [112] V. M. Goldschmidt, "Die Gesetze der Krystallochemie," *Die Naturwissenschaften*, vol. 14, pp. 477–485, may 1926.
- [113] G. E. Eperon, S. D. Stranks, C. Menelaou, M. B. Johnston, L. M. Herz, and H. J. Snaith, "Formamidinium lead trihalide: a broadly tunable perovskite for efficient planar hetero-junction solar cells," *Energy & Environmental Science*, vol. 7, no. 3, p. 982, 2014.
- [114] Y. Fu, H. Zhu, A. W. Schrader, D. Liang, Q. Ding, P. Joshi, L. Hwang, X.-Y. Zhu, and S. Jin, "Nanowire Lasers of Formamidinium Lead Halide Perovskites and Their Stabilized Alloys with Improved Stability," *Nano Letters*, vol. 16, pp. 1000–1008, feb 2016.
- [115] J.-h. Im, J. Chung, S.-j. Kim, and N.-g. Park, "Synthesis , structure , and photovoltaic property of a nanocrystalline 2H perovskite-type novel sensitizer (CH<sub>3</sub>CH<sub>3</sub>NH<sub>3</sub>)PbI<sub>3</sub>," *Nanoscale Research Letters*, vol. 7, no. 1, pp. 1–7, 2012.
- [116] G. Niu, X. Guo, and L. Wang, "Review of recent progress in chemical stability of perovskite solar cells," *J. Mater. Chem. A*, vol. 3, no. 17, pp. 8970–8980, 2015.

- [117] A. D. Raw, J. a. Ibers, and K. R. Poeppelmeier, "Syntheses and structure of hydrothermally prepared CsNiX<sub>3</sub> (X=Cl, Br, I)," *Journal of Solid State Chemistry*, vol. 192, pp. 34–37, aug 2012.
- [118] H. Tanaka, K. Iio, and K. Nagata, "Magnetic properties of Rb<sub>1-x</sub>K<sub>x</sub>NiCl<sub>3</sub>, RbVBr<sub>3</sub> and CsNiI<sub>3</sub>," *Journal of Magnetism and Magnetic Materials*, vol. 104-107, pp. 829–830, feb 1992.
- [119] T. I. Li, G. D. Stucky, and G. L. McPherson, "The crystal structure of CsMnCl<sub>3</sub> and a summary of the structures of RMX<sub>3</sub> compounds," *Acta Crystallographica Section B Structural Crystallography and Crystal Chemistry*, vol. 29, pp. 1330–1335, jun 1973.
- [120] G. L. McPherson, J. E. Wall, and A. M. Hermann, "Electrical, magnetic, and spectroscopic properties of cesium nickel triiodide," *Inorganic Chemistry*, vol. 13, pp. 2230–2233, sep 1974.
- [121] G. L. McPherson, L. J. Sindel, H. F. Quarls, C. B. Frederick, and C. J. Doumit, "Preparation and solid-state properties of cesium triiodovanadate, cesium triiodochromate, and cesium triiodomanganate," *Inorganic Chemistry*, vol. 14, pp. 1831–1834, aug 1975.
- [122] J. F. Ackerman, G. M. Cole, and S. L. Holt, "Invited Review The Physical Properties of Some Transition Metal Compounds of the ABX<sub>3</sub> Type," *Inorganica Chimica Acta*, vol. 8, pp. 323–343, 1974.
- [123] G. L. McPherson, W.-m. Heung, and J. J. Barraza, "Coupled Pairs of Chromion(III) Ions in Crystals of CsMgCl<sub>3</sub>, CsMgBr<sub>2</sub>, and CsCdBr<sub>3</sub>. A Case of Charge Compensation Induced Pair Formation," *Journal of the American Chemical Society*, vol. 100, no. 2, pp. 469–475, 1978.
- [124] B. J. Beberwyck and A. P. Alivisatos, "Ion exchange synthesis of III-V nanocrystals.," *Journal of the American Chemical Society*, vol. 134, pp. 19977–80, dec 2012.
- [125] J. M. Luther, H. Zheng, B. Sadtler, and A. P. Alivisatos, "Synthesis of PbS nanorods and other ionic nanocrystals of complex morphology by sequential cation exchange reactions.," *Journal of the American Chemical Society*, vol. 131, pp. 16851–7, nov 2009.
- [126] H. Li, M. Zanella, A. Genovese, M. Povia, A. Falqui, C. Giannini, and L. Manna, "Sequential cation exchange in nanocrystals: preservation of crystal phase and formation of metastable phases.," *Nano letters*, vol. 11, pp. 4964–70, nov 2011.
- [127] P.A. Beckmann, "A review of polytypism in lead iodide," *Crystal Research and Technology*, vol. 45, pp. 455–460, may 2010.
- [128] R. F. Warren and W. Y. Liang, "Raman spectroscopy of new lead iodide intercalation compounds," *Journal of Physics: Condensed Matter*, vol. 5, pp. 6407–6418, aug 1993.

## Bibliography

---

- [129] N. Preda, L. Mihut, M. Baibarac, I. Baltog, and S. Lefrant, "A distinctive signature in the Raman and photoluminescence spectra of intercalated  $\text{PbI}_2$ ," *Journal of Physics: Condensed Matter*, vol. 18, pp. 8899–8912, oct 2006.
- [130] G. Gurina and K. Savchenko, "Intercalation and formation of complexes in the system of lead(II) iodide–ammonia," *Journal of Solid State Chemistry*, vol. 177, pp. 909–915, mar 2004.
- [131] J. Burschka, A. Dualeh, F. Kessler, E. Baranoff, N.-L. Cevey-Ha, C. Yi, M. K. Nazeeruddin, and M. Grätzel, "Tris(2-(1H-pyrazol-1-yl)pyridine)cobalt(III) as p-type dopant for organic semiconductors and its application in highly efficient solid-state dye-sensitized solar cells.," *Journal of the American Chemical Society*, vol. 133, pp. 18042–5, nov 2011.
- [132] G. Juška, K. Arlauskas, M. Viliūnas, and J. Kočka, "Extraction Current Transients: New Method of Study of Charge Transport in Microcrystalline Silicon," *Physical Review Letters*, vol. 84, pp. 4946–4949, may 2000.
- [133] W. Shockley and H. J. Queisser, "Detailed Balance Limit of Efficiency of p-n Junction Solar Cells," *Journal of Applied Physics*, vol. 32, no. 3, p. 510, 1961.
- [134] I. Borriello, G. Cantele, and D. Ninno, "Ab initio investigation of hybrid organic-inorganic perovskites based on tin halides," *Physical Review B*, vol. 77, p. 235214, jun 2008.
- [135] X. Hong, T. Ishihara, and A. Nurmikko, "Dielectric confinement effect on excitons in  $\text{PbI}_{4-n}\text{X}_n$ -based layered semiconductors," *Physical Review B*, vol. 45, no. 12, pp. 6961–6964, 1992.
- [136] E. Mosconi, A. Amat, M. K. Nazeeruddin, M. Grätzel, and F. De Angelis, "First-Principles Modeling of Mixed Halide Organometal Perovskites for Photovoltaic Applications," *The Journal of Physical Chemistry C*, vol. 117, pp. 13902–13913, jul 2013.
- [137] J. M. Kadro, K. Nonomura, D. Gachet, M. Grätzel, and A. Hagfeldt, "Facile route to freestanding  $\text{CH}_3\text{NH}_3\text{PbI}_3$  crystals using inverse solubility," *Scientific Reports*, vol. 5, p. 11654, jun 2015.
- [138] E. D. Palik, *Handbook of optical constants of solids Volume 1*. 1985.
- [139] A. A. Petrov, N. Pellet, J.-Y. Seo, N. A. Belich, D. Y. Kovalev, A. V. Shevelkov, E. A. Goodilin, S. M. Zakeeruddin, A. B. Tarasov, and M. Graetzel, "New Insight into the Formation of Hybrid Perovskite Nanowires via Structure Directing Adducts," *Chemistry of Materials*, vol. 29, pp. 587–594, jan 2017.
- [140] J.-H. Im, J. Luo, M. Franckevičius, N. Pellet, P. Gao, T. Moehl, S. M. Zakeeruddin, M. K. Nazeeruddin, M. Grätzel, and N.-G. Park, "Nanowire Perovskite Solar Cell," *Nano Letters*, vol. 15, pp. 2120–2126, mar 2015.

- [141] B. E. McCandless, L. V. Moulton, and R. W. Birkmire, "Recrystallization and sulfur diffusion in CdCl<sub>2</sub>-treated CdTe/CdS thin films," *Progress in Photovoltaics: Research and Applications*, vol. 5, pp. 249–260, jul 1997.
- [142] S. A. Ringel, A. W. Smith, M. H. MacDougal, and A. Rohatgi, "The effects of CdCl<sub>2</sub> on the electronic properties of molecular-beam epitaxially grown CdTe/CdS heterojunction solar cells," *Journal of Applied Physics*, vol. 70, pp. 881–889, jul 1991.
- [143] N. Armani, G. Salviati, L. Nasi, A. Bosio, S. Mazzamuto, and N. Romeo, "Role of thermal treatment on the luminescence properties of CdTe thin films for photovoltaic applications," *Thin Solid Films*, vol. 515, pp. 6184–6187, may 2007.
- [144] A. Romeo, D. Bätzner, H. Zogg, and A. Tiwari, "Recrystallization in CdTe/CdS," *Thin Solid Films*, vol. 361-362, pp. 420–425, feb 2000.
- [145] A. Dualeh, N. Tétreault, T. Moehl, P. Gao, M. K. Nazeeruddin, and M. Grätzel, "Effect of Annealing Temperature on Film Morphology of Organic-Inorganic Hybrid Perovskite Solid-State Solar Cells," *Advanced Functional Materials*, vol. 24, pp. 3250–3258, jun 2014.
- [146] F. Liu, Q. Dong, M. K. Wong, A. B. Djurišić, A. Ng, Z. Ren, Q. Shen, C. Surya, W. K. Chan, J. Wang, A. M. C. Ng, C. Liao, H. Li, K. Shih, C. Wei, H. Su, and J. Dai, "Is Excess PbI<sub>2</sub> Beneficial for Perovskite Solar Cell Performance?," *Advanced Energy Materials*, vol. 6, p. 1502206, apr 2016.
- [147] E. Mosconi, G. Grancini, C. Roldán-Carmona, P. Gratia, I. Zimmermann, M. K. Nazeeruddin, and F. De Angelis, "Enhanced TiO<sub>2</sub>/MAPbI<sub>3</sub> Electronic Coupling by Interface Modification with PbI<sub>2</sub>," *Chemistry of Materials*, vol. 28, pp. 3612–3615, jun 2016.
- [148] A. Clearfield, "Role of ion exchange in solid-state chemistry," *Chemical Reviews*, vol. 88, pp. 125–148, jan 1988.
- [149] D. H. Son, S. M. Hughes, Y. Yin, and A. Paul Alivisatos, "Cation exchange reactions in ionic nanocrystals.," *Science (New York, N.Y.)*, vol. 306, pp. 1009–12, nov 2004.
- [150] M. V. Kovalenko, D. V. Talapin, M. A. Loi, F. Cordella, G. Hesser, M. I. Bodnarchuk, and W. Heiss, "Quasi-seeded growth of ligand-tailored PbSe nanocrystals through cation-exchange-mediated nucleation.," *Angewandte Chemie (International ed. in English)*, vol. 47, pp. 3029–33, jan 2008.
- [151] B. Sadtler, D. O. Demchenko, H. Zheng, S. M. Hughes, M. G. Merkle, U. Dahmen, L.-W. Wang, and A. P. Alivisatos, "Selective facet reactivity during cation exchange in cadmium sulfide nanorods.," *Journal of the American Chemical Society*, vol. 131, pp. 5285–93, apr 2009.
- [152] R. D. Robinson, B. Sadtler, D. O. Demchenko, C. K. Erdonmez, L.-W. Wang, and A. P. Alivisatos, "Spontaneous superlattice formation in nanorods through partial cation exchange.," *Science (New York, N.Y.)*, vol. 317, pp. 355–8, jul 2007.

## Bibliography

---

- [153] Q. Yao, I. U. Arachchige, and S. L. Brock, "Expanding the repertoire of chalcogenide nanocrystal networks: Ag(2)Se gels and aerogels by cation exchange reactions.," *Journal of the American Chemical Society*, vol. 131, pp. 2800–1, mar 2009.
- [154] C. Dong and F. C. J. M. van Veggel, "Cation exchange in lanthanide fluoride nanoparticles.," *ACS nano*, vol. 3, pp. 123–30, jan 2009.
- [155] Z. Zhang, S. Dai, X. Fan, D. A. Blom, S. J. Pennycook, and Y. Wei, "Controlled Synthesis of CdS Nanoparticles inside Ordered Mesoporous Silica Using Ion-Exchange Reaction," *The Journal of Physical Chemistry B*, vol. 105, pp. 6755–6758, jul 2001.
- [156] J. Park, H. Zheng, Y.-w. Jun, and A. P. Alivisatos, "Hetero-epitaxial anion exchange yields single-crystalline hollow nanoparticles.," *Journal of the American Chemical Society*, vol. 131, pp. 13943–5, oct 2009.
- [157] L. Dloczik and R. Könenkamp, "Nanostructure Transfer in Semiconductors by Ion Exchange," *Nano Letters*, vol. 3, pp. 651–653, may 2003.
- [158] Y. Tsujimoto, K. Yamaura, and T. Uchikoshi, "Extended Ni(III) oxyhalide perovskite derivatives: Sr<sub>2</sub>NiO<sub>3</sub>X (X = F, Cl).," *Inorganic chemistry*, vol. 52, pp. 10211–6, sep 2013.
- [159] T. A. Kodenkandath, J. N. Lalena, W. L. Zhou, E. E. Carpenter, C. Sangregorio, A. U. Falster, W. B. Simmons, C. J. O'Connor, and J. B. Wiley, "Assembly of MetalAnion Arrays within a Perovskite Host. Low-Temperature Synthesis of New Layered CopperOxyhalides, (CuX)LaNb<sub>2</sub>O<sub>7</sub>, X = Cl, Br," *Journal of the American Chemical Society*, vol. 121, pp. 10743–10746, nov 1999.
- [160] T. A. Kodenkandath, A. S. Kumbhar, W. L. Zhou, and J. B. Wiley, "Construction of Copper Halide Networks within Layered Perovskites. Syntheses and Characterization of New Low-Temperature Copper Oxyhalides," *Inorganic Chemistry*, vol. 40, pp. 710–714, feb 2001.
- [161] L. Viciu, G. Caruntu, N. Royant, J. Koenig, W. L. Zhou, T. A. Kodenkandath, and J. B. Wiley, "Formation of MetalAnion Arrays within Layered Perovskite Hosts. Preparation of a Series of New Metastable Transition-Metal Oxyhalides, (MCl)LaNb<sub>2</sub>O<sub>7</sub> (M = Cr, Mn, Fe, Co)," *Inorganic Chemistry*, vol. 41, pp. 3385–3388, jul 2002.
- [162] L. Viciu, T. A. Kodenkandath, and J. B. Wiley, "Construction of a double-layered tetrahedral network within a perovskite host: Two-step route to the alkali-metal-halide layered perovskite, (LixCl)LaNb<sub>2</sub>O<sub>7</sub>," *Journal of Solid State Chemistry*, vol. 180, pp. 583–588, feb 2007.
- [163] J. J. Choi, X. Yang, Z. M. Norman, S. J. L. Billinge, and J. S. Owen, "Structure of methylammonium lead iodide within mesoporous titanium dioxide: active material in high-performance perovskite solar cells.," *Nano letters*, vol. 14, pp. 127–33, jan 2014.



- [164] M. Hirasawa, T. Ishihara, T. Goto, K. Uchida, and N. Miura, "Magnetoabsorption of the lowest exciton in perovskite-type compound (CH<sub>3</sub>NH<sub>3</sub>)PbI<sub>3</sub>," *Physica B: Condensed Matter*, vol. 201, pp. 427–430, jul 1994.
- [165] K. Tanaka, T. Takahashi, T. Ban, T. Kondo, K. Uchida, and N. Miura, "Comparative study on the excitons in lead-halide-based perovskite-type crystals CH<sub>3</sub>NH<sub>3</sub>PbBr<sub>3</sub> CH<sub>3</sub>NH<sub>3</sub>PbI<sub>3</sub>," *Solid State Communications*, vol. 127, pp. 619–623, sep 2003.
- [166] P. Docampo, F. Hanusch, S. D. Stranks, M. Döblinger, J. M. Feckl, M. Ehrensperger, N. K. Minar, M. B. Johnston, H. J. Snaith, and T. Bein, "Solution Deposition-Conversion for Planar Heterojunction Mixed Halide Perovskite Solar Cells," *Advanced Energy Materials*, pp. n/a–n/a, may 2014.
- [167] H. Deng, D. Dong, K. Qiao, L. Bu, B. Li, D. Yang, H.-E. Wang, Y. Cheng, Z. Zhao, J. Tang, and H. Song, "Growth, patterning and alignment of organolead iodide perovskite nanowires for optoelectronic devices," *Nanoscale*, vol. 7, no. 9, pp. 4163–4170, 2015.
- [168] P. Zhu, S. Gu, X. Shen, N. Xu, Y. Tan, S. Zhuang, Y. Deng, Z. Lu, Z. Wang, and J. Zhu, "Direct Conversion of Perovskite Thin Films into Nanowires with Kinetic Control for Flexible Optoelectronic Devices," *Nano Letters*, vol. 16, pp. 871–876, feb 2016.
- [169] M. Spina, M. Lehmann, B. Náfrádi, L. Bernard, E. Bonvin, R. Gaál, A. Magrez, L. Forró, and E. Horváth, "Microengineered CH<sub>3</sub>NH<sub>3</sub>PbI<sub>3</sub> Nanowire/Graphene Phototransistor for Low-Intensity Light Detection at Room Temperature," *Small*, vol. 11, pp. 4824–4828, oct 2015.
- [170] Q. Hu, H. Wu, J. Sun, D. Yan, Y. Gao, and J. Yang, "Large-area perovskite nanowire arrays fabricated by large-scale roll-to-roll micro-gravure printing and doctor blading," *Nanoscale*, vol. 8, no. 9, pp. 5350–5357, 2016.
- [171] H. Zhu, Y. Fu, F. Meng, X. Wu, Z. Gong, Q. Ding, M. V. Gustafsson, M. T. Trinh, S. Jin, and X.-Y. Zhu, "Lead halide perovskite nanowire lasers with low lasing thresholds and high quality factors," *Nature Materials*, vol. 14, pp. 636–642, apr 2015.
- [172] A. Fu and P. Yang, "Organic–inorganic perovskites: Lower threshold for nanowire lasers," *Nature Materials*, vol. 14, pp. 557–558, may 2015.
- [173] A. B. Wong, M. Lai, S. W. Eaton, Y. Yu, E. Lin, L. Dou, A. Fu, and P. Yang, "Growth and Anion Exchange Conversion of CH<sub>3</sub>NH<sub>3</sub>PbX<sub>3</sub> Nanorod Arrays for Light-Emitting Diodes," *Nano Letters*, vol. 15, pp. 5519–5524, aug 2015.
- [174] E. Horváth, M. Spina, Z. Szekrényes, K. Kamarás, R. Gaal, D. Gachet, and L. Forró, "Nanowires of Methylammonium Lead Iodide (CH<sub>3</sub>NH<sub>3</sub>PbI<sub>3</sub>) Prepared by Low Temperature Solution-Mediated Crystallization," *Nano Letters*, vol. 14, pp. 6761–6766, dec 2014.

## Bibliography

---

- [175] D. Shen, X. Yu, X. Cai, M. Peng, Y. Ma, X. Su, L. Xiao, and D. Zou, "Understanding the solvent-assisted crystallization mechanism inherent in efficient organic–inorganic halide perovskite solar cells," *J. Mater. Chem. A*, vol. 2, pp. 20454–20461, oct 2014.
- [176] X. Guo, C. McCleese, C. Kolodziej, A. C. S. Samia, Y. Zhao, and C. Burda, "Identification and characterization of the intermediate phase in hybrid organic–inorganic MAPbI<sub>3</sub> perovskite," *Dalton Trans.*, vol. 45, no. 9, pp. 3806–3813, 2016.
- [177] M. O. Reese, S. A. Gevorgyan, M. Jørgensen, E. Bundgaard, S. R. Kurtz, D. S. Ginley, D. C. Olson, M. T. Lloyd, P. Morvillo, E. A. Katz, A. Elschner, O. Haillant, T. R. Currier, V. Shrotriya, M. Hermenau, M. Riede, K. R. Kirov, G. Trimmel, T. Rath, O. Inganäs, F. Zhang, M. Andersson, K. Tvingstedt, M. Lira-Cantu, D. Laird, C. McGuinness, S. J. Gowrisanker, M. Pannone, M. Xiao, J. Hauch, R. Steim, D. M. DeLongchamp, R. Rösch, H. Hoppe, N. Espinosa, A. Urbina, G. Yaman-Uzunoglu, J.-B. Bonekamp, A. J. van Breemen, C. Girotto, E. Voroshazi, and F. C. Krebs, "Consensus stability testing protocols for organic photovoltaic materials and devices," *Solar Energy Materials and Solar Cells*, vol. 95, pp. 1253–1267, may 2011.
- [178] G. Kakavelakis, D. Konios, E. Stratakis, and E. Kymakis, "Enhancement of the Efficiency and Stability of Organic Photovoltaic Devices via the Addition of a Lithium-Neutralized Graphene Oxide Electron-Transporting Layer," *Chemistry of Materials*, vol. 26, pp. 5988–5993, oct 2014.
- [179] M. Marszalek, F. D. Arendse, J.-D. Decoppet, S. S. Babkair, A. A. Ansari, S. S. Habib, M. Wang, S. M. Zakeeruddin, and M. Grätzel, "Ionic Liquid-Sulfolane Composite Electrolytes for High-Performance and Stable Dye-Sensitized Solar Cells," *Advanced Energy Materials*, vol. 4, p. 1301235, apr 2014.
- [180] R. Harikisun and H. Desilvestro, "Long-term stability of dye solar cells," *Solar Energy*, vol. 85, pp. 1179–1188, jun 2011.
- [181] A. G. Kontos, T. Stergiopoulos, V. Likodimos, D. Milliken, H. Desilvesto, G. Tulloch, and P. Falaras, "Long-Term Thermal Stability of Liquid Dye Solar Cells," *The Journal of Physical Chemistry C*, vol. 117, pp. 8636–8646, may 2013.
- [182] M. I. Asghar, K. Miettunen, J. Halme, P. Vahermaa, M. Toivola, K. Aitola, and P. Lund, "Review of stability for advanced dye solar cells," *Energy & Environmental Science*, vol. 3, no. 4, pp. 418–426, 2010.
- [183] W. Chen, Y. Wu, Y. Yue, J. Liu, W. Zhang, X. Yang, H. Chen, E. Bi, I. Ashraful, M. Gratzel, and L. Han, "Efficient and stable large-area perovskite solar cells with inorganic charge extraction layers," *Science*, vol. 350, pp. 944–948, nov 2015.
- [184] W. Tress, N. Marinova, T. Moehl, S. M. Zakeeruddin, M. K. Nazeeruddin, and M. Grätzel, "Understanding the rate-dependent J–V hysteresis, slow time component, and aging in CH<sub>3</sub>NH<sub>3</sub>PbI<sub>3</sub> perovskite solar cells: the role of a compensated electric field," *Energy Environ. Sci.*, vol. 8, no. 3, pp. 995–1004, 2015.

- [185] H.-S. Kim, I.-H. Jang, N. Ahn, M. Choi, A. Guerrero, J. Bisquert, and N.-G. Park, "Control of I – V Hysteresis in CH<sub>3</sub>NH<sub>3</sub>PbI<sub>3</sub> Perovskite Solar Cell," *The Journal of Physical Chemistry Letters*, vol. 6, pp. 4633–4639, nov 2015.
- [186] S. Jain and V. Agarwal, "A New Algorithm for Rapid Tracking of Approximate Maximum Power Point in Photovoltaic Systems," *IEEE Power Electronics Letters*, vol. 2, pp. 16–19, mar 2004.
- [187] N. D'Souza and L. Lopes, "An Intelligent Maximum Power Point Tracker Using Peak Current Control," in *IEEE 36th Conference on Power Electronics Specialists*, pp. 172–177, IEEE, 2005.
- [188] T. Tafticht and K. Agbossou, "Development of a MPPT method for photovoltaic systems," in *Canadian Conference on Electrical and Computer Engineering 2004 (IEEE Cat. No.04CH37513)*, pp. 1123–1126, IEEE.
- [189] M.-L. Chiang, C.-C. Hua, and J.-R. Lin, "Direct power control for distributed PV power system," in *Proceedings of the Power Conversion Conference-Osaka 2002 (Cat. No.02TH8579)*, vol. 1, pp. 311–315, IEEE, 2002.
- [190] O. Waszynek, "Dynamic Behavior of a Class of Photovoltaic Power Systems," *IEEE Transactions on Power Apparatus and Systems*, vol. PAS-102, pp. 3031–3037, sep 1983.
- [191] C.-C. Hua and Jong-Rong Lin, "Fully digital control of distributed photovoltaic power systems," in *ISIE 2001. 2001 IEEE International Symposium on Industrial Electronics Proceedings (Cat. No.01TH8570)*, vol. 1, pp. 1–6, IEEE, 2001.
- [192] Y. Jung, G. Yu, J. Choi, and J. Choi, "High-frequency DC link inverter for grid-connected photovoltaic system," in *Conference Record of the Twenty-Ninth IEEE Photovoltaic Specialists Conference, 2002.*, pp. 1410–1413, IEEE.
- [193] A. Al-Amoudi, "Optimal control of a grid-connected PV system for maximum power point tracking and unity power factor," in *Seventh International Conference on Power Electronics and Variable Speed Drives*, vol. 1998, pp. 80–85, IEE, 1998.
- [194] N. Femia, G. Petrone, G. Spagnuolo, and M. Vitelli, "Optimization of Perturb and Observe Maximum Power Point Tracking Method," *IEEE Transactions on Power Electronics*, vol. 20, pp. 963–973, jul 2005.
- [195] K. Chomsuwan, P. Prisuwan, and V. Monyakul, "Photovoltaic grid-connected inverter using two-switch buck-boost converter," in *Conference Record of the Twenty-Ninth IEEE Photovoltaic Specialists Conference, 2002.*, pp. 1527–1530, IEEE.
- [196] L. Zhang, "Real-time maximum power point tracking for grid-connected photovoltaic systems," in *8th International Conference on Power Electronics and Variable Speed Drives*, vol. 2000, pp. 124–129, IEE, 2000.

## Bibliography

---

- [197] Wenkai Wu, N. Pongratananukul, Weihong Qiu, K. Rustom, T. Kasparis, and I. Batarseh, "DSP-based multiple peak power tracking for expandable power system," in *Eighteenth Annual IEEE Applied Power Electronics Conference and Exposition, 2003. APEC '03.*, vol. 1, pp. 525–530, IEEE.
- [198] K. Hussein, "Maximum photovoltaic power tracking: an algorithm for rapidly changing atmospheric conditions," *IEE Proceedings - Generation, Transmission and Distribution*, vol. 142, no. 1, p. 59, 1995.
- [199] K. Kobayashi, I. Takano, and Y. Sawada, "A study on a two stage maximum power point tracking control of a photovoltaic system under partially shaded insolation conditions," in *2003 IEEE Power Engineering Society General Meeting (IEEE Cat. No.03CH37491)*, pp. 2612–2617, IEEE, 2003.
- [200] G. Yu, Y. Jung, J. Choi, I. Choy, J. Song, and G. Kim, "A novel two-mode MPPT control algorithm based on comparative study of existing algorithms," in *Conference Record of the Twenty-Ninth IEEE Photovoltaic Specialists Conference, 2002.*, pp. 1531–1534, IEEE, 2002.
- [201] K. Irisawa, T. Saito, I. Takano, and Y. Sawada, "Maximum power point tracking control of photovoltaic generation system under non-uniform insolation by means of monitoring cells," in *Conference Record of the Twenty-Eighth IEEE Photovoltaic Specialists Conference - 2000 (Cat. No.00CH37036)*, pp. 1707–1710, IEEE, 2000.
- [202] Yeong-Chau Kuo, Tsorng-Juu Liang, and Jiann-Fuh Chen, "Novel maximum-power-point-tracking controller for photovoltaic energy conversion system," *IEEE Transactions on Industrial Electronics*, vol. 48, pp. 594–601, jun 2001.
- [203] A. Brambilla, M. Gambarara, A. Garutti, and F. Ronchi, "New approach to photovoltaic arrays maximum power point tracking," in *30th Annual IEEE Power Electronics Specialists Conference. Record. (Cat. No.99CH36321)*, vol. 2, pp. 632–637, IEEE, 1999.
- [204] Tae-Yeop Kim, Ho-Gyun Ahn, Seung Kyu Park, and Youn-Kyun Lee, "A novel maximum power point tracking control for photovoltaic power system under rapidly changing solar radiation," in *ISIE 2001. 2001 IEEE International Symposium on Industrial Electronics Proceedings (Cat. No.01TH8570)*, vol. 2, pp. 1011–1014, IEEE.
- [205] M. Slonim and L. Rahovich, "Maximum power point regulator for 4 kW solar cell array connected through inverter to the AC grid," in *IECEC 96. Proceedings of the 31st Intersociety Energy Conversion Engineering Conference*, vol. 3, pp. 1669–1672, IEEE, 1996.
- [206] N. Femia, G. Petrone, G. Spagnuolo, and M. Vitelli, "Optimization of Perturb and Observe Maximum Power Point Tracking Method," *IEEE Transactions on Power Electronics*, vol. 20, pp. 963–973, jul 2005.

- [207] K. Hussein, I. Muta, T. Hoshino, and M. Osakada, "Maximum photovoltaic power tracking: an algorithm for rapidly changing atmospheric conditions," *IEE Proceedings - Generation, Transmission and Distribution*, vol. 142, no. 1, pp. 59–64, 1995.
- [208] B. Wilamowski and Xiangli Li, "Fuzzy system based maximum power point tracking for PV system," in *IEEE 2002 28th Annual Conference of the Industrial Electronics Society. IECON 02*, pp. 3280–3284, IEEE, 2002.
- [209] A. Mahmoud, H. Mashaly, S. Kandil, H. El Khashab, and M. Nashed, "Fuzzy logic implementation for photovoltaic maximum power tracking," in *Proceedings 9th IEEE International Workshop on Robot and Human Interactive Communication. IEEE RO-MAN 2000 (Cat. No.00TH8499)*, pp. 155–160, IEEE, 2000.
- [210] M. Simoes, N. Franceschetti, and M. Friedhofer, "A fuzzy logic based photovoltaic peak power tracking control," in *IEEE International Symposium on Industrial Electronics. Proceedings. ISIE'98 (Cat. No.98TH8357)*, vol. 1, pp. 300–305, IEEE, 1998.
- [211] T. Senjyu and K. Uezato, "Maximum power point tracker using fuzzy control for photovoltaic arrays," in *Proceedings of 1994 IEEE International Conference on Industrial Technology - ICIT '94*, pp. 143–147, IEEE, 1994.
- [212] R. Hilloowala and A. Sharaf, "A rule-based fuzzy logic controller for a PWM inverter in photo-voltaic energy conversion scheme," in *Conference Record of the 1992 IEEE Industry Applications Society Annual Meeting*, pp. 762–769, IEEE, 1992.
- [213] T. Hiyama, S. Kouzuma, and T. Imakubo, "Identification of optimal operating point of PV modules using neural network for real time maximum power tracking control," *IEEE Transactions on Energy Conversion*, vol. 10, pp. 360–367, jun 1995.
- [214] A. Hussein, K. Hirasawa, Jinglu Hu, and J. Murata, "The dynamic performance of photovoltaic supplied dc motor fed from DC-DC converter and controlled by neural networks," in *Proceedings of the 2002 International Joint Conference on Neural Networks. IJCNN'02 (Cat. No.02CH37290)*, pp. 607–612, IEEE, 2002.
- [215] Kyoungsoo Ro and S. Rahman, "Two-loop controller for maximizing performance of a grid-connected photovoltaic-fuel cell hybrid power plant," *IEEE Transactions on Energy Conversion*, vol. 13, no. 3, pp. 276–281, 1998.
- [216] J. Enslin and D. Snyman, "Simplified feed-forward control of the maximum power point in PV installations," in *Proceedings of the 1992 International Conference on Industrial Electronics, Control, Instrumentation, and Automation*, pp. 548–553, IEEE, 1992.
- [217] A. Kislovski and R. Redl, "Maximum-power-tracking using positive feedback," in *Proceedings of 1994 Power Electronics Specialist Conference - PESC'94*, pp. 1065–1068, IEEE, 1994.

## Bibliography

---

- [218] P. Midya, P. Krein, R. Turnbull, R. Reppa, and J. Kimball, "Dynamic maximum power point tracker for photovoltaic applications," in *PESC Record. 27th Annual IEEE Power Electronics Specialists Conference*, vol. 2, pp. 1710–1716, IEEE, 1996.
- [219] T. Esum, J. Kimball, P. Krein, P. Chapman, and P. Midya, "Dynamic Maximum Power Point Tracking of Photovoltaic Arrays Using Ripple Correlation Control," *IEEE Transactions on Power Electronics*, vol. 21, pp. 1282–1291, sep 2006.
- [220] D. Logue and P. Krein, "Observer-based techniques in ripple correlation control applied to power electronic systems," in *2001 IEEE 32nd Annual Power Electronics Specialists Conference (IEEE Cat. No.01CH37230)*, vol. 4, pp. 2014–2018, IEEE, 2001.
- [221] T. Esum, J. Kimball, P. Krein, P. Chapman, and P. Midya, "Dynamic maximum power point tracking of photovoltaic arrays using ripple correlation control," *IEEE Transactions on Power Electronics*, vol. 21, pp. 1282–1291, sep 2006.
- [222] E. Dallago, D. G. Finarelli, U. P. Gianazza, A. L. Barnabei, and A. Liberale, "Theoretical and Experimental Analysis of an MPP Detection Algorithm Employing a Single-Voltage Sensor Only and a Noisy Signal," *IEEE Transactions on Power Electronics*, vol. 28, pp. 5088–5097, nov 2013.
- [223] M. Azab, "A New Maximum Power Point Tracking for Photovoltaic Systems ," sep 2008.
- [224] B. C. O'Regan, P. R. F. Barnes, X. Li, C. Law, E. Palomares, and J. M. Marin-Beloqui, "Optoelectronic Studies of Methylammonium Lead Iodide Perovskite Solar Cells with Mesoporous TiO<sub>2</sub> : Separation of Electronic and Chemical Charge Storage, Understanding Two Recombination Lifetimes, and the Evolution of Band Offsets during J–V Hysteresis," *Journal of the American Chemical Society*, vol. 137, pp. 5087–5099, apr 2015.
- [225] P. R. F. Barnes, K. Miettunen, X. Li, A. Y. Anderson, T. Bessho, M. Grätzel, and B. C. O'Regan, "Interpretation of optoelectronic transient and charge extraction measurements in dye-sensitized solar cells," *Advanced materials (Deerfield Beach, Fla.)*, vol. 25, pp. 1881–922, apr 2013.
- [226] A. M. Latham, C. R. Sullivan, and K. M. Odame, "Performance of photovoltaic maximum power point tracking algorithms in the presence of noise," *IEEE Energy Conversion Conference and Exposition*, 2010.
- [227] F. Zhang, W. Shi, J. Luo, N. Pellet, C. Yi, X. Li, X. Zhao, T. J. S. Dennis, X. Li, S. Wang, Y. Xiao, S. M. Zakeeruddin, D. Bi, and M. Grätzel, "Isomer-Pure Bis-PCBM-Assisted Crystal Engineering of Perovskite Solar Cells Showing Excellent Efficiency and Stability," *Advanced Materials*, p. 1606806, feb 2017.
- [228] G. Schlichthörl, S. Y. Huang, J. Sprague, and A. J. Frank, "Band Edge Movement and Recombination Kinetics in Dye-Sensitized Nanocrystalline TiO<sub>2</sub> Solar Cells: A Study by Intensity Modulated Photovoltage Spectroscopy," *The Journal of Physical Chemistry B*, vol. 101, pp. 8141–8155, oct 1997.

- [229] E. Ponomarev and L. Peter, "A generalized theory of intensity modulated photocurrent spectroscopy (IMPS)," *Journal of Electroanalytical Chemistry*, vol. 396, pp. 219–226, oct 1995.
- [230] L. Dloczik, O. Ieperuma, I. Lauermann, L. M. Peter, E. A. Ponomarev, G. Redmond, N. J. Shaw, and I. Uhlendorf, "Dynamic Response of Dye-Sensitized Nanocrystalline Solar Cells: Characterization by Intensity-Modulated Photocurrent Spectroscopy," *The Journal of Physical Chemistry B*, vol. 101, pp. 10281–10289, dec 1997.
- [231] P. E. de Jongh and D. Vanmaekelbergh, "Investigation of the Electronic Transport Properties of Nanocrystalline Particulate TiO<sub>2</sub> Electrodes by Intensity-Modulated Photocurrent Spectroscopy," *The Journal of Physical Chemistry B*, vol. 101, pp. 2716–2722, apr 1997.
- [232] K. G. Saw, N. M. Aznan, F. K. Yam, S. S. Ng, and S. Y. Pung, "New Insights on the Burstein-Moss Shift and Band Gap Narrowing in Indium-Doped Zinc Oxide Thin Films," *PLOS ONE*, vol. 10, p. e0141180, oct 2015.
- [233] M. Feneberg, S. Osterburg, K. Lange, C. Lidig, B. Garke, R. Goldhahn, E. Richter, C. Netzel, M. D. Neumann, N. Esser, S. Fritze, H. Witte, J. Bläsing, A. Dadgar, and A. Krost, "Band gap renormalization and Burstein-Moss effect in silicon- and germanium-doped wurtzite GaN up to 10<sup>20</sup> cm<sup>-3</sup>," *Physical Review B*, vol. 90, p. 075203, aug 2014.
- [234] J. Jamnik and J. Maier, "Generalised equivalent circuits for mass and charge transport: chemical capacitance and its implications," *Physical Chemistry Chemical Physics*, vol. 3, no. 9, pp. 1668–1678, 2001.
- [235] T. Instruments, "AN-1515 A Comprehensive Study of the Howland Current Pump," 2008.
- [236] T. R. Brumlev and R. P. Buck, "Transmission line equivalent circuit models for electrochemical impedances," *Journal of Electroanalytical Chemistry and Interfacial Electrochemistry*, vol. 126, pp. 73–104, sep 1981.
- [237] J. R. Macdonald, "Electrical Response of Materials Containing Space Charge with Discharge at the Electrodes," *The Journal of Chemical Physics*, vol. 54, pp. 2026–2050, mar 1971.
- [238] J. Ross Macdonald, "The impedance of a galvanic cell with two plane-parallel electrodes at a short distance," *Journal of Electroanalytical Chemistry and Interfacial Electrochemistry*, vol. 32, pp. 317–328, oct 1971.
- [239] G. Barker, "Aperiodic equivalent electrical circuits for the electrolyte solution The ideally polarizable electrode and the ion and its atmosphere," *Journal of Electroanalytical Chemistry and Interfacial Electrochemistry*, vol. 41, pp. 201–211, jan 1973.
- [240] H. Chang and G. Jaffé, "Polarization in Electrolytic Solutions. Part I. Theory," *The Journal of Chemical Physics*, vol. 20, pp. 1071–1077, jul 1952.

## Bibliography

---

- [241] J. R. Macdonald, "Theory of space-charge polarization and electrode-discharge effects," *The Journal of Chemical Physics*, vol. 58, pp. 4982–5001, jun 1973.
- [242] R. Kern, R. Sastrawan, J. Ferber, R. Stangl, and J. Luther, "Modeling and interpretation of electrical impedance spectra of dye solar cells operated under open-circuit conditions," *Electrochimica Acta*, vol. 47, pp. 4213–4225, oct 2002.
- [243] L. Bay and K. West, "An equivalent circuit approach to the modelling of the dynamics of dye sensitized solar cells," *Solar Energy Materials and Solar Cells*, vol. 87, pp. 613–628, may 2005.
- [244] W. Chen, Y. Qiu, and S. Yang, "A new ZnO nanotetrapods/SnO<sub>2</sub> nanoparticles composite photoanode for high efficiency flexible dye-sensitized solar cells," *Physical Chemistry Chemical Physics*, vol. 12, no. 32, p. 9494, 2010.
- [245] W. Liu, L. Hu, S. Dai, L. Guo, N. Jiang, and D. Kou, "The effect of the series resistance in dye-sensitized solar cells explored by electron transport and back reaction using electrical and optical modulation techniques," *Electrochimica Acta*, vol. 55, pp. 2338–2343, feb 2010.
- [246] Y. Li, G. Wang, K. Pan, B. Jiang, C. Tian, W. Zhou, and H. Fu, "NaYF<sub>4</sub>:Er<sup>3+</sup>/Yb<sup>3+</sup>–graphene composites: preparation, upconversion luminescence, and application in dye-sensitized solar cells," *Journal of Materials Chemistry*, vol. 22, no. 38, p. 20381, 2012.
- [247] I. Zarazua, J. Bisquert, and G. Garcia-Belmonte, "Light-Induced Space-Charge Accumulation Zone as Photovoltaic Mechanism in Perovskite Solar Cells," *The Journal of Physical Chemistry Letters*, vol. 7, pp. 525–528, feb 2016.
- [248] E. J. Juarez-Perez, R. S. Sanchez, L. Badia, G. Garcia-Belmonte, Y. S. Kang, I. Mora-Sero, and J. Bisquert, "Photoinduced Giant Dielectric Constant in Lead Halide Perovskite Solar Cells," *The Journal of Physical Chemistry Letters*, vol. 5, pp. 2390–2394, jul 2014.
- [249] G. Richardson, S. E. J. O’Kane, R. G. Niemann, T. A. Peltola, J. M. Foster, P. J. Cameron, and A. B. Walker, "Can slow-moving ions explain hysteresis in the current–voltage curves of perovskite solar cells?," *Energy Environ. Sci.*, vol. 9, no. 4, pp. 1476–1485, 2016.
- [250] D. P. Almond and C. R. Bowen, "An Explanation of the Photoinduced Giant Dielectric Constant of Lead Halide Perovskite Solar Cells," *The Journal of Physical Chemistry Letters*, vol. 6, pp. 1736–1740, may 2015.
- [251] Z. Xiao, Y. Yuan, Y. Shao, Q. Wang, Q. Dong, C. Bi, P. Sharma, A. Gruverman, and J. Huang, "Giant switchable photovoltaic effect in organometal trihalide perovskite devices," *Nature Materials*, vol. 14, pp. 193–198, dec 2014.
- [252] J. M. Azpiroz, E. Mosconi, J. Bisquert, and F. De Angelis, "Defect migration in methylammonium lead iodide and its role in perovskite solar cell operation," *Energy Environ. Sci.*, vol. 8, no. 7, pp. 2118–2127, 2015.



- [253] C. Eames, J. M. Frost, P. R. F. Barnes, B. C. O'Regan, A. Walsh, and M. S. Islam, "Ionic transport in hybrid lead iodide perovskite solar cells," *Nature Communications*, vol. 6, p. 7497, jun 2015.
- [254] C. Chen, D. Chen, W. C. Chueh, and F. Ciucci, "Modeling the impedance response of mixed-conducting thin film electrodes," *Physical Chemistry Chemical Physics*, vol. 16, no. 23, p. 11573, 2014.
- [255] W. Lai and S. M. Haile, "Impedance Spectroscopy as a Tool for Chemical and Electrochemical Analysis of Mixed Conductors: A Case Study of Ceria," *Journal of the American Ceramic Society*, vol. 88, pp. 2979–2997, nov 2005.
- [256] M. E. Lynch and M. Liu, "Investigation of sheet resistance in thin-film mixed-conducting solid oxide fuel cell cathode test cells," *Journal of Power Sources*, vol. 195, pp. 5155–5166, aug 2010.
- [257] J. Jamnik and J. Maier, "Treatment of the Impedance of Mixed Conductors Equivalent Circuit Model and Explicit Approximate Solutions," *Journal of The Electrochemical Society*, vol. 146, no. 11, p. 4183, 1999.
- [258] J. Endres, D. A. Egger, M. Kulbak, R. A. Kerner, L. Zhao, S. H. Silver, G. Hodes, B. P. Rand, D. Cahen, L. Kronik, and A. Kahn, "Valence and Conduction Band Densities of States of Metal Halide Perovskites: A Combined Experimental–Theoretical Study," *The Journal of Physical Chemistry Letters*, vol. 7, pp. 2722–2729, jul 2016.
- [259] Z. Peng, J. Lin, R. Ye, E. L. G. Samuel, and J. M. Tour, "Flexible and Stackable Laser-Induced Graphene Supercapacitors," *ACS Applied Materials & Interfaces*, vol. 7, pp. 3414–3419, feb 2015.
- [260] H.-C. Chien, W.-Y. Cheng, Y.-H. Wang, and S.-Y. Lu, "Ultrahigh Specific Capacitances for Supercapacitors Achieved by Nickel Cobaltite/Carbon Aerogel Composites," *Advanced Functional Materials*, vol. 22, pp. 5038–5043, dec 2012.
- [261] J. M. Kadro, N. Pellet, F. Giordano, A. Ulianov, O. Müntener, J. Maier, M. Grätzel, and A. Hagfeldt, "Proof-of-concept for facile perovskite solar cell recycling," *Energy Environ. Sci.*, vol. 9, no. 10, pp. 3172–3179, 2016.
- [262] European Parliament, "Directive 2011/65/EU of the European Parliament and of the Council of 8 June 2011 on the restriction of the use of certain hazardous substances in electrical and electronic equipment (RoHS)," *Official Journal of the European Union*, vol. 54, no. 1 July, pp. 88–110, 2011.
- [263] International Renewable Energy Agency, "End-Of-Life Management of Solar Photovoltaic Panels," 2016.
- [264] European Parliament, "Directive 2012/19/EU of the European Parliament and of the Council of 4 July 2012 on waste electrical and electronic equipment (WEEE)," 2012.

## Bibliography

---

- [265] European Commission, "Regulation (EC) No 1013/2006 of the European Parliament and of the Council of 14 June 2006 on shipments of waste," 2006.
- [266] European Parliament, "Directive 2008/98/EC of the European Parliament and of the Council of 19 November 2008 on waste and repealing certain Directives," 2008.
- [267] European Parliament, "Directive 1999/45/EC of the European Parliament and of the Council of 31 May 1999 concerning the approximation of the laws, regulations and administrative provisions of the Member States relating to the classification, packaging and labelling of dangerous," 1999.
- [268] European Commission, "Commission Decision of 3 May 2000 replacing Decision 94/3/EC establishing a list of wastes pursuant to Article 1(a) of Council Directive 75/442/EEC on waste and Council Decision 94/904/EC establishing a list of hazardous waste pursuant to Article 1(4) of C," 2000.
- [269] "Committee for the "Adaptation to Scientific and Technical Progress and Implementation of the Directives on Waste Established Under Article 39 of Directive 2008/98/EC" Directive 2012/10/EU on Waste From Electrical and Electronic Equipment (WEEE). Summary," 2015.
- [270] European Commission, "Commission Regulation (EC) No 1418/2007 of 29 November 2007 concerning the export for recovery of certain waste listed in Annex III or IIIA to Regulation (EC) No 1013/2006 of the European Parliament and of the Council to certain countries to which the OECD," 2007.
- [271] "Consultation on the review of the Hazardous Properties,"
- [272] L. Serrano-Lujan, N. Espinosa, T. T. Larsen-Olsen, J. Abad, A. Urbina, and F. C. Krebs, "Tin- and lead-based perovskite solar cells under scrutiny: An environmental perspective," *Advanced Energy Materials*, vol. 5, no. 20, pp. 1–5, 2015.
- [273] N. Espinosa, L. Serrano-Luján, A. Urbina, and F. C. Krebs, "Solution and vapour deposited lead perovskite solar cells: Ecotoxicity from a life cycle assessment perspective," *Solar Energy Materials and Solar Cells*, vol. 137, pp. 303–310, jun 2015.
- [274] J. Gong, S. B. Darling, and F. You, "Perovskite photovoltaics: life-cycle assessment of energy and environmental impacts," *Energy Environ. Sci.*, vol. 8, no. 7, pp. 1953–1968, 2015.
- [275] J. Zhang, X. Gao, Y. Deng, B. Li, and C. Yuan, "Life Cycle Assessment of Titania Perovskite Solar Cell Technology for Sustainable Design and Manufacturing," *ChemSusChem*, vol. 8, pp. 3882–3891, nov 2015.
- [276] A. Babayigit, D. Duy Thanh, A. Ethirajan, J. Manca, M. Muller, H.-G. Boyen, and B. Conings, "Assessing the toxicity of Pb- and Sn-based perovskite solar cells in model organism *Danio rerio*," *Scientific Reports*, vol. 6, p. 18721, jan 2016.

- [277] D. Fabini, "Quantifying the Potential for Lead Pollution from Halide Perovskite Photovoltaics," *The Journal of Physical Chemistry Letters*, vol. 6, pp. 3546–3548, sep 2015.
- [278] B. Hailegnaw, S. Kirmayer, E. Edri, G. Hodes, and D. Cahen, "Rain on Methylammonium Lead Iodide Based Perovskites: Possible Environmental Effects of Perovskite Solar Cells," *The Journal of Physical Chemistry Letters*, vol. 6, pp. 1543–1547, may 2015.
- [279] United States Environmental Protection Agency, "Technical Note – Estimating Lead (Pb) Emissions from Coal Combustion Sources," tech. rep., 2011.
- [280] D. R. Lide, ed., *CRC Handbook of Chemistry and Physics*, vol. 84. 84th ed., 2003.
- [281] Photovoltaic Solar Energy Department-National Renewable Energy Centre Fundacion Chile, "First Solar CdTe Photovoltaic Technology : Environmental , Health and Safety Assessment Final Report," tech. rep., 2013.
- [282] Y. Takahashi, R. Obara, Z.-Z. Lin, Y. Takahashi, T. Naito, T. Inabe, S. Ishibashi, and K. Terakura, "Charge-transport in tin-iodide perovskite CH<sub>3</sub>NH<sub>3</sub>SnI<sub>3</sub>: origin of high conductivity," *Dalton transactions (Cambridge, England : 2003)*, vol. 40, pp. 5563–8, may 2011.
- [283] N. K. Noel, S. D. Stranks, A. Abate, C. Wehrenfennig, S. Guarnera, A.-a. Haghighirad, A. Sadhanala, G. E. Eperon, S. K. Pathak, M. B. Johnston, A. Petrozza, L. M. Herz, and H. J. Snaith, "Lead-free organic–inorganic tin halide perovskites for photovoltaic applications," *Energy & Environmental Science*, vol. 7, p. 3061, may 2014.
- [284] J. R.L.Moss, E.Tzimas, H.Kara, P.Willis, "European Commission-Critical Metals in Strategic Energy Technologies: Assessing Rare Metals as Supply-Chain Bottlenecks in Low-Carbon Energy Technologies," tech. rep., 2011.
- [285] Oakdene Hollins, "Material Security," tech. rep., 2008.
- [286] European Commission: Ad hoc working group on defining critical raw materials, "Report on critical raw materials for the EU," Tech. Rep. May, 2014.
- [287] J. Gong, B. Darling, and F. You, "Perovskite Photovoltaics : Life-Cycle Assessment of Energy and Environmental Impacts Supporting Information," *Energy & Environmental Science*, no. 847, pp. 1–22, 2015.
- [288] UNEP, "Environmental Risks and Challenges of Anthropogenic Metals Flows and Cycles," tech. rep., 2013.
- [289] UNEP, "Assessing the Environmental Impacts of Consumption and Production," tech. rep., 2010.
- [290] "Ecoinvent V2.2."

## Bibliography

---

- [291] A. Binek, M. L. Petrus, N. Huber, H. Bristow, Y. Hu, T. Bein, and P. Docampo, "Recycling Perovskite Solar Cells To Avoid Lead Waste," *ACS Applied Materials & Interfaces*, vol. 8, pp. 12881–12886, may 2016.
- [292] G. W. Bodamer, R. Kunin, and H. Co, "Behavior of Ion Exchange Resins in Solvents Other Than Water-Swelling and Exchange Characteristics," *Industrial and Engineering Chemistry*, vol. 45, no. 11, 1953.
- [293] Z. Hubicki and D. Koodynsk, "Selective Removal of Heavy Metal Ions from Waters and Waste Waters Using Ion Exchange Methods," in *Ion Exchange Technologies*, InTech, nov 2012.
- [294] C. G. Poll, G. W. Nelson, D. M. Pickup, A. V. Chadwick, D. J. Riley, and D. J. Payne, "Electrochemical recycling of lead from hybrid organic–inorganic perovskites using deep eutectic solvents," *Green Chem.*, vol. 18, no. 10, pp. 2946–2955, 2016.
- [295] C. E. Latunussa, F. Ardente, G. A. Blengini, and L. Mancini, "Life Cycle Assessment of an innovative recycling process for crystalline silicon photovoltaic panels," *Solar Energy Materials and Solar Cells*, vol. 156, pp. 101–111, nov 2016.
- [296] S. Kang, S. Yoo, J. Lee, B. Boo, and H. Ryu, "Experimental investigations for recycling of silicon and glass from waste photovoltaic modules," *Renewable Energy*, vol. 47, pp. 152–159, nov 2012.
- [297] V. M. Fthenakis, "End-of-life management and recycling of PV modules," vol. 28, pp. 1051–1058, 2000.
- [298] T. Doi, I. Tsuda, H. Unagida, A. Murata, K. Sakuta, and K. Kurokawa, "Experimental study on PV module recycling with organic solvent method," vol. 67, 2001.
- [299] W. Berger, F.-g. Simon, K. Weimann, and E. A. Alsema, "A novel approach for the recycling of thin film photovoltaic modules," *Resources, Conservation and Recycling*, vol. 54, pp. 711–718, aug 2010.
- [300] M. Shoar Abouzari, F. Berkemeier, G. Schmitz, and D. Wilmer, "On the physical interpretation of constant phase elements," *Solid State Ionics*, vol. 180, pp. 922–927, jun 2009.
- [301] Q. Wang, J.-E. Moser, and M. Grätzel, "Electrochemical Impedance Spectroscopic Analysis of Dye-Sensitized Solar Cells," *The Journal of Physical Chemistry B*, vol. 109, pp. 14945–14953, aug 2005.
- [302] A. Hauch and A. Georg, "Diffusion in the electrolyte and charge-transfer reaction at the platinum electrode in dye-sensitized solar cells," *Electrochimica Acta*, vol. 46, pp. 3457–3466, aug 2001.
- [303] J. Valsa and J. Vlach, "RC models of a constant phase element," *International Journal of Circuit Theory and Applications*, pp. 59–67, oct 2011.

# Norman Pellet

**Date of birth:** 07.03.1990 (St-Aubin, NE, Switzerland)

**E-mail:** norman.pellet@gmail.com

## Higher Education

### **PHD, LABORATORY OF PHOTONICS AND INTERFACES, EPFL - MAX PLANCK INSTITUTE FOR SOLID STATE RESEARCH, GERMANY, 2013 - 2017**

Worked on the design and the development of hybrid organic-inorganic perovskite and their application into high performance solar cells, with an emphasis on their characterization.

### **MASTER THESIS, PHYSICAL BIOSCIENCE DIVISION, LAWRENCE BERKELEY NATIONAL LABORATORY, 2012**

Synthesis of oligoaromatic molecular wires behaving as rectifying charge transport molecules. Synthesis and characterization of metal oxide nanomaterials and their use in water splitting.

### **Master degree, Swiss Federal institute of technology, 2010-2012**

Master in Chemistry and Molecular Sciences

### **Bachelor degree (y. 3), Nanyang Technological University, Singapore, 2009-2010**

School of Physical and Mathematical Science

### **Bachelor degree (y. 1 - 2), Swiss federal Institute of technology, 2007-2009**

School of Chemistry and Chemical Engineering.

## Professional experience

### **IT developer, SERVICE of Cheminformatics, Swiss Federal institute of technology - 2011 - 2012**

Coding of a javascript based modular data visualization systems.

### **SENIOR FRONT SIDE developer, Precidata SaRL, Switzerland, 2010-2012**

Development of interactive information systems aiming at visualizing efficiently and conveniently real-time data.

## Additional skills

**Languages:** French (native), English (fluent), German (basic)

**Programming:** C, C++, Javascript (+NodeJS), PHP, Java, XHTML, CSS, Python

**Electronics:** Analog systems, microcontroller-based architectures

## List of publications

### As first or equal author

- [1] N. Pellet, P. Gao, G. Gregori, T.-Y. Yang, M. K. Nazeeruddin, J. Maier, and M. Grätzel, "Mixed-organic-cation perovskite photovoltaics for enhanced solar-light harvesting.," *Angew. Chem. Int. Ed. Engl.*, vol. 53, no. 12, pp. 3151–7, Mar. 2014.
- [2] N. Pellet, J. Teuscher, J. Maier, and M. Grätzel, "Transforming Hybrid Organic Inorganic Perovskites by Rapid Halide Exchange," *Chem. Mater.*, Jan. 2015.
- [3] J. Burschka, N. Pellet, S.-J. Moon, R. Humphry-Baker, P. Gao, M. K. Nazeeruddin, and M. Grätzel, "Sequential deposition as a route to high-performance perovskite-sensitized solar cells.," *Nature*, vol. 499, no. 7458, pp. 316–9, Jul. 2013.
- [4] J. M. Kadro, N. Pellet, F. Giordano, A. Ulianov, O. Müntener, J. Maier, M. Grätzel, and A. Hagfeldt, "Proof-of-concept for facile perovskite solar cell recycling," *Energy Environ. Sci.*, vol. 9, no. 10, pp. 3172–3179, 2016.
- [5] N. Pellet, F. Giordano, Ibrahim M. Dar, G. Gregori, S. M. Zakeeruddin, J. Maier, M. Grätzel, "Hill climbing hysteresis of perovskite-based solar cells: a maximum power point tracking investigation" *Progress in Photovoltaics: Research and Applications*, Accepted

### As a collaborator

- [6] Y. Saygili, M. Söderberg, N. Pellet, F. Giordano, Y. Cao, A. B. Muñoz-García, S. M. Zakeeruddin, N. Vlachopoulos, M. Pavone, G. Boschloo, L. Kavan, J.-E. Moser, M. Grätzel, A. Hagfeldt, and M. Freitag, "Copper Bipyridyl Redox Mediators for Dye-Sensitized Solar Cells with High Photovoltage," *J. Am. Chem. Soc.*, vol. 138, no. 45, pp. 15087–15096, Nov. 2016.
- [7] N. Arora, M. I. Dar, M. Abdi-Jalebi, F. Giordano, N. Pellet, G. Jacopin, R. H. Friend, S. M. Zakeeruddin, and M. Grätzel, "Intrinsic and Extrinsic Stability of Formamidinium Lead Bromide Perovskite Solar Cells Yielding High Photovoltage," *Nano Lett.*, vol. 16, no. 11, pp. 7155–7162, Nov. 2016.
- [8] X. Zhang, Y. Xu, F. Giordano, M. Schreier, N. Pellet, Y. Hu, C. Yi, N. Robertson, J. Hua, S. M. Zakeeruddin, H. Tian, and M. Grätzel, "Molecular Engineering of Potent Sensitizers for Very Efficient Light Harvesting in Thin-Film Solid-State Dye-Sensitized Solar Cells," *J. Am. Chem. Soc.*, vol. 138, no. 34, pp. 10742–10745, Aug. 2016.
- [9] T.-Y. Yang, G. Gregori, N. Pellet, M. Grätzel, and J. Maier, "The Significance of Ion Conduction in a Hybrid Organic-Inorganic Lead-Iodide-Based Perovskite Photosensitizer," *Angew. Chemie Int. Ed.*, vol. 54, no. 27, pp. 7905–7910, Jun. 2015.

[10] J.-H. Im, J. Luo, M. Franckevičius, N. Pellet, P. Gao, T. Moehl, S. M. Zakeeruddin, M. K. Nazeeruddin, M. Grätzel, and N.-G. Park, "Nanowire Perovskite Solar Cell," *Nano Lett.*, vol. 15, no. 3, pp. 2120–2126, Mar. 2015.

[11] C. D. Bailie, M. G. Christoforo, J. P. Mailoa, A. R. Bowring, E. L. Unger, W. H. Nguyen, J. Burschka, N. Pellet, J. Z. Lee, M. Grätzel, R. Noufi, T. Buonassisi, A. Salleo, and M. D. McGehee, "Semi-transparent perovskite solar cells for tandems with silicon and CIGS," *Energy Environ. Sci.*, vol. 8, no. 3, pp. 956–963, 2015.

[12] J.-H. Im, I.-H. Jang, N. Pellet, M. Grätzel, and N.-G. Park, "Growth of CH<sub>3</sub>NH<sub>3</sub>PbI<sub>3</sub> cuboids with controlled size for high-efficiency perovskite solar cells," *Nat. Nanotechnol.*, Aug. 2014.

[13] P. Qin, S. Paek, M. I. Dar, N. Pellet, J. Ko, M. Grätzel, and M. K. Nazeeruddin, "Perovskite Solar Cells with 12.8% Efficiency by Using Conjugated Quinolizino Acridine Based Hole Transporting Material," *J. Am. Chem. Soc.*, vol. 136, no. 24, pp. 8516–8519, Jun. 2014.

[4] H. A. Harms, N. Tétreault, N. Pellet, M. Bensimon, and M. Grätzel, "Mesoscopic photosystems for solar light harvesting and conversion: facile and reversible transformation of metal-halide perovskites," *Faraday Discuss.*, vol. 176, pp. 251–269, 2014.

## List of patents

Burschka J.; Pellet, N.; Nazeeruddin, M. K.; Grätzel, M.; Ahmad, S. High performance perovskite sensitized mesoscopic solar cells, EP13166720.6

Pellet, N.; Giordano F.; Zakeeruddin, S. M.; Grätzel, M.; Maximum power point tracking algorithm for Photovoltaic devices in presence of hysteresis, In filing

